



The
University
Of
Sheffield.

Microstructural evaluation in structural steels containing dilute niobium concentrations

By:

Bhushan D Rakshe

A thesis submitted in partial fulfilment of the requirements for the degree of
Doctor of Philosophy

The University of Sheffield
Faculty of Engineering
Department of Material Science and Engineering

Submission Date

March 2020

This page is internationally left blank

Dedication

This thesis is dedicated with love and the deepest gratitude:

To my parents, Vasudha Rakshe and Dattatray Rakshe;

To my wife and soul mate, Anjali;

To my daughter and sunshine of my life, Abhira and

To all known and unknown helping hands who showed me the "path of knowledge".

This page is internationally left blank

Acknowledgements

I gratefully acknowledge the financial support of the Engineering and Physical Research Council (EPSRC) and CBMM, Brazil for the project. I am thankful to Faculty of Engineering for awarding me a Vice Chancellor's Indian Scholarship. I owe a great debt of gratitude to the support infrastructure and dedication of the members of staff at the Advanced Metallic System CDT who helped me at every stage of the Ph.D. Special thanks to my CDT cohort colleague from both Sheffield and Manchester for their support and kind friendship.

I am thankful to my immediate supervisors Prof. Eric J Palmiere and Dr. Jitendra Patel for their advice, valuable guidance and general support during my Ph.D. program. Both supported me in many ways over last five years, not only academically but also financially and personally. They have patiently helped me in refining my ideas, experiments, results and ensured a smooth sailing till the completion of the project. Eric gave me a full freedom to set my own experiments plans and goals, helping me to develop as an independent researcher. I cherished long hours of discussions with him on various technical and non-technical topics. I am grateful to his guru mantra "Believe in what you see." Jit being my mentor and critic has constantly steered my work towards being substantial.

I am indebted to Mr. Braja Mishra for granting me the study leave and generous financial support to undertake this endeavour. I sincerely thank my colleagues at Ferro Tech India Pvt Ltd. who encouraged me to take this challenge and supported me throughout this journey. I am thankful to my primary and secondary school teachers for their kindness, constant encouragement and showing me the right path of life.

My appreciation goes to Sorby Centre staff for the training and technical help on electron microscopy and microanalysis work. I appreciate the kind support of Dr. Peng Gong (PDRA) for TEM data analysis and high-resolution imaging of fine precipitates. Special thanks to Dean Haylock for the training on the TMC machine and bearing all troubles from me for the last four years. I want to especially thank Eduardo, Marta, Luis, Daniel, Carl, Nick and other colleague in G8 office for the helpful discussions and joyful company.

I am thankful to immediate family members and friends for their support over the last four years. My father is not around to see this, but I am sure he would have been immensely proud of me. I am grateful to my wife, Anjali Rakshe for her constant support and external pressure to reach logical conclusion at the end. She fully covered all my family responsibility, especially with our daughter, without her this Ph.D. would not have been possible.

This page is internationally left blank

Abstract

The thermomechanical processing of microalloyed steels has been instrumental in the successful development of HSLA steel plate and strip products with enhanced property combinations. Microalloying additions of niobium (Nb) have the most potent effect in retarding the static recrystallisation of austenite during interpass times by solute drag and precipitate pinning mechanism. However, published research on the use of Nb in carbon steel long products ($C \geq 0.20$ wt.%) is somewhat limited due to the low solubility of Nb in austenite at such carbon levels. Such steels represent well over 50 % of overall world steel consumption primarily intended for the construction sector and therefore represent an essential area for cost efficiencies.

This research aimed to understand the influence of dilute niobium concentrations (50-200 ppm) on microstructural evaluation in structural steels. The investigation involved three low carbon steels with varying Nb concentration at constant C (0.20%) and N (0.007%) levels. Isothermal double-hit deformation technique led to the determination of $T_{5\%}$ and $T_{95\%}$ (beginning and end of recrystallisation, respectively) as a function of strain and interpass time.

The results indicate that the $T_{5\%}$ increases with increasing Nb supersaturation in austenite at a rate of 40°C per 0.006% Nb supersaturation for a true strain $\epsilon=0.40$. The Nb supersaturation ratio ≥ 6 resulted in an unrecrystallised microstructure at respective $T_{5\%}$ for all tested steels. A high, localised strain-induced precipitation of Nb(CN) was observed at the austenite subgrain boundaries. This translated into higher values for local precipitate pinning force (F_{PIN}), which were significantly higher than one predicted from equilibrium thermodynamics. The critical F_{PIN} for retardation of static recrystallisation was found to be 1.8 MPa at respective $T_{5\%}$ for each steel.

The present study has contributed to advancing our knowledge of the interplay between solute supersaturation and volume fraction of Nb(CN) precipitation. Even the lowest addition of 66 ppm Nb could retard the recrystallisation at certain rolling conditions and raised $T_{5\%}$ temperature over base steel composition. It is possible to develop a viable TMCP deformation schedule to best benefit from dilute Nb additions. The better control of austenite microstructure will improve the mechanical properties of existing low value-added products through ferrite grain refinement. The dilute Nb additions might permit the reduction in other substitutional alloying elements such as Mn as the Nb provides a more strengthening effect at low cost.

This page is internationally left blank

Nomenclature

a	Activity in Raoultian standard state
A	Surface area of newly formed phase or precipitate
APFIM	Atom probe analysis/field ion microscopy
b	Burgers vector
B-N	Baker-Nutting orientation relationship
C_0	Initial composition of solute
CCR	Conventional controlled rolling
CHR	Conventional hot rolling
DB	Deformation bands
D_i	Initial austenite grain size
DRCR	Dynamic recrystallisation controlled rolling
E	Modulus of elasticity
f_v	Precipitate volume fraction
F_{PIN}	Particle pinning force
F_{RXN}	Driving force for recrystallization
FIM	Field ion microscopy
G	Molar Gibbs free energy
H	Molar enthalpy
HSLA	High Strength Low Alloy
HSS	High strength steels
k_s	Solubility product of compound
K-S	Kurdjumov-Sachs orientation relationship
l	Average austenite subgrain boundary intercept distance
L	Mean austenite grain intercept length
MAE	Microalloying elements
N_s	Number of particles per unit area

N_v	Number of particles per unit volume
Nb(CN)	Niobium carbonitride precipitate
PSC	Plane Strain Compression
P_s	Actual precipitation-start time
P_{Ns}	Start of precipitation in deformed austenite
P_{Os}	Start of precipitation in undeformed austenite
PF_s	Polygonal ferrite start temperature
PF_f	Polygonal ferrite finish temperature
Q_{rex}	Apparent activation energy
QST	Quenching and self-tempering
r	Precipitate radius
r^*	Critical radius for precipitation
r_c	Critical particle size below which austenite grain boundaries are fully pinned
R	Ideal gas constant or amount of reduction
R_f	Finish of recrystallization in microalloyed steels
R_{Nf}	Finish of recrystallization in plain carbon steels
R_o	Mean radius of austenite grain
R_s	Start of recrystallization in microalloyed steels
R_{Ns}	Start of recrystallization in plain carbon steels
RCR	Recrystallization controlled rolling
Rebar	Steel reinforcing bar
S	Molar entropy
S_v	Effective interfacial area per unit volume
S_v^{GB}	Grain boundary surface area per unit volume
S_v^{DB}	Deformation bands and twist boundaries surface area per unit volume
SEG	Segregation event
SEM	Scanning electron microscopy
SGB	Austenite subgrain boundary

SIP	Strain-induced precipitate
t_p	Time-to-peak stress for dynamically recrystallized austenite
T_{DIS}	Dissolution temperature of compound precipitate
T_e	Equilibrium solvus and transformation temperature
T_{GC}	Austenite grain coarsening temperature
T_{nr} / T_{RXN}	Austenite recrystallization-stop temperature
$T_{5\%}$	Temperature corresponding to beginning of austenite recrystallisation (5%)
$T_{95\%}$	Temperature corresponding to end of austenite recrystallisation (95%)
T_s	Solutionising temperature
T_ϵ	Deformation temperature
TB	Twin boundaries
TEM	Transmission electron microscopy
TMCP	Thermomechanical controlled processing
V	Volume of newly formed phase or precipitate
V_h	Volume of unconstrained hole in a strained matrix
WF_S	Widmanstätten ferrite start temperature
WF_F	Widmanstätten ferrite finish temperature
X	Mole fraction of solute
X_A	Fractional softening parameter of austenite
z	Ratio of the radii of growing grains to matrix grains
Z	Zener-Hollomon parameter
α	Low carbon martensite
γ	Activity coefficient in Raoultian standard state
δ	Volume misfit parameter
ΔG^*	Critical free energy for nucleation (activation energy)
ΔG_{het}^*	Activation energy for heterogeneous nucleation
ΔG_{hom}^*	Activation energy for homogeneous nucleation

ΔG_n	Free energy change per mole of precipitate
ΔG_s	Increase in strain energy per unit volume of precipitate
ΔG_{TOT}	Total free energy at equilibrium
ΔG_v	Free energy change per unit volume of precipitate (driving force for precipitation)
ΔT	Degree of undercooling
$\Delta \rho$	Change in dislocation density associated with the migration of the recrystallization front into deformed austenite
ϵ	True strain
$\dot{\epsilon}$	True strain rate
ϵ_c^R	Critical strain for onset of dynamic recrystallization
ϵ_c^r	Critical strain for onset of dynamic recovery
ϵ_p	Strain to peak stress
ϵ_{ss}	Amount of true strain corresponding to steady-state stress
θ	Contact angle between phases
λ	Interparticle spacing
μ	Shear modulus of matrix
γ	Interfacial energy between matrix and precipitate or true stress
Σ	Solute supersaturation
Φ	Particle diameter

Table of Contents

DEDICATION	I
ACKNOWLEDGEMENTS.....	III
ABSTRACT	V
NOMENCLATURE	VII
TABLE OF CONTENTS	XI
CHAPTER 1 INTRODUCTION	1
CHAPTER 2 LITERATURE REVIEW	5
2.1 STRUCTURAL STEELS.....	5
2.1.1 Market Statistics	6
2.1.2 Process Overview	8
2.1.3 High Strength Structural Steels	12
2.2 MICROALLOYING AND STRENGTH.....	16
2.2.1 Role of microalloying element.....	18
2.2.2 Structure-property relationship.....	20
2.2.3 Applications.....	22
2.3 THERMOMECHANICAL PROCESSING	24
2.3.1 Microstructure Control and Significance of S_v	24
2.3.2 Recrystallisation Controlled Rolling	28
2.3.3 Conventional Controlled Rolling	32
2.3.4 Dynamic Recrystallisation Controlled Rolling (DRCR).....	37
2.4 AUSTENITE RECRYSTALLISATION AND GRAIN GROWTH	39
2.4.1 Dynamic Microstructural Changes.....	39
2.4.2 Static Microstructural Changes	45
2.4.3 Grain Growth.....	51

2.5 FUNDAMENTALS OF Nb MICROALLOYING	53
2.5.1 Solute Drag.....	53
2.5.2 Nb(CN) Precipitation	54
2.5.3 Nb(CN) Pinning Force Models	63
2.6 HOT DEFORMATION OF MICROALLOYED AUSTENITE	65
2.6.1 Recrystallisation Stop Temperature ($T_{RXN}/ T_{5\%}$).....	65
2.6.2 RPTT Diagram	69
2.6.3 F_{RXN} vs. F_{PIN}	72
2.7. LABORATORY SIMULATION	73
2.7.1 Mechanical Testing Methods	73
2.7.2 PSC + Double-Hit Tests	74
2.7.3 Fraction Softening Analysis	75
2.8. KNOWLEDGE GAP	77
2.9. SUMMARY OF LITERATURE REVIEW	78
CHAPTER 3 AIMS AND OBJECTIVES	81
3.1 PROJECT AIM	81
3.2 PROJECT OBJECTIVES	81
CHAPTER 4 EXPERIMENTAL PROCEDURE	83
4.1. MATERIAL ALLOY DESIGN AND PROCESSING.....	83
4.2. GRAIN COARSENING STUDIES	84
4.3. STATIC SOFTENING STUDIES	85
4.3.1 PSC Specimen.....	85
4.3.2 Test Plan.....	86
4.3.3 Fraction Softening Analysis.....	88
4.4. TRANSFORMATION BEHAVIOUR STUDIES	88
4.5. MICROSTRUCTURAL STUDIES.....	89
4.5.1 Metallography Preparation.....	90
4.5.2 Chemical Etching	91

4.5.3 TEM Characterisation	92
4.6. QUANTITATIVE METALLOGRAPHY	94
4.6.1. Grain Size: Linear Intercept Method.....	94
4.6.2. Mean Aspect Ratio	96
4.6.3. Surface Area per Unit Volume.....	96
4.6.4. Recrystallised volume fraction.....	97
4.6.5. Determination of Precipitate Radius	97
4.7. MECHANICAL TESTING.....	98
4.7.1. Micro-hardness testing	98
4.7.2. Compression Testing.....	99
CHAPTER 5 RESULTS	101
5.1 AUSTENITE GRAIN COARSENING BEHAVIOUR.....	101
5.2 STATIC SOFTENING BEHAVIOUR OF AUSTENITE	107
5.2.1 High-Temperature Flow Curves	108
5.2.2 Fractional Softening Behaviour	116
5.2.3 Nb Supersaturation in Austenite	121
5.2.4 Microstructural Observation: Optical	125
5.3 NB(CN) PRECIPITATION: QUANTITATIVE TEM	145
5.3.1 Thin Foils	145
5.3.2 Extraction Replicas	150
5.4 TRANSFORMATION BEHAVIOUR OF AUSTENITE.....	161
5.4.1 Dilatometry	161
5.4.2 Microstructure Observations	164
5.4.3 Mechanical Properties.....	168
CHAPTER 6 DISCUSSION	171
6.1 GRAIN COARSENING OF AUSTENITE.....	171
6.2 STATIC RECRYSTALLISATION OF AUSTENITE	172
6.2.1 Solution Treatment.....	172

6.2.2 Recrystallisation Driving Force (F_{RXN})	176
6.2.3 Fractional Softening Parameter	177
6.2.4 Recrystallisation Processing Window	179
6.2.5 Nb Supersaturation, $[Nb]_{ss}$	183
6.2.6 Nb Supersaturation Ratio, $[Nb]_{SSR}$	185
6.2.7 Optical Microstructure Studies	186
6.3 NB(CN) PRECIPITATION IN AUSTENITE.....	188
6.3.1 Crystallography of Precipitation	188
6.3.2 Precipitate Location	191
6.3.3 Size and Distribution of Nb(CN)	192
6.3.4 Precipitate Volume Fraction	195
6.3.5 Nb(CN) Pinning Forces.....	197
6.3.6 Relationship between F_{PIN} and F_{RXN}	200
6.4 MICROSTRUCTURE MODELLING.....	203
6.4.1 Model for predicting microstructure	203
6.4.2 RPTT Diagram	208
6.4.3 Strain-induced Precipitation Model	214
6.5 TRANSFORMATION BEHAVIOUR OF AUSTENITE.....	220
6.5.1 Allotriomorphic Ferrite Nucleation.....	220
6.5.2 Widmanstätten Ferrite	221
6.5.3 Mechanical Properties	222
CHAPTER 7 APPLICATION TO COMMERCIAL PROCESSING.....	225
7.1 HEAVY SECTIONS (BEAM-IPE AND CRANE RAIL)	226
7.2 LIGHT OR MEDIUM SECTIONS (EQUAL ANGLE AND CHANNEL - PFC)	229
7.3 REBAR.....	230
CHAPTER 8 CONCLUDING REMARKS	231
CHAPTER 9 SCOPE FOR FUTURE WORK	235
REFERENCES	237

APPENDIX A PLANE STRAIN COMPRESSION (PSC) TESTING.....	249
A.1 TMTS ARCHITECTURE AND CONTROL SYSTEM.....	250
A.2 TEST CONTROL AND FEATURES.....	252
A.3 MEASUREMENT OF FLOW STRESS	253
A.4 INHOMOGENEOUS PSC DEFORMATION	255
APPENDIX B TEM SAMPLE PREPARATION.....	257

Chapter 1

Introduction

The parallel development of microalloying technology and TMCP since the 1960s has enabled the development of today's high strength steel with excellent toughness. The physical metallurgical aspects of both are widely researched and reported in various journal papers [1-5], conference proceedings [6-8], and several books [9-10]. The principle goal of TMCP is to produce a fine ferrite grain size and non-equilibrium transformation products after accelerated cooling. The resulting microstructure refinement gives rise to high strength and low-temperature toughness properties. These mechanical properties improvements are achieved only because of synergy that exists between the recrystallisation retarding effects of the niobium (Nb) microalloying element and the hot deformation processing variables.

Figure 1.1 illustrates the influence of Nb microalloying addition on three critical temperatures of hot deformation of austenite. The undissolved Nb(CN) precipitates delays the austenite grain growth during the soaking; therefore, retaining fine-grained austenite before the start of hot rolling (T_{GC}). The solute drag and strain-induced precipitation of Nb(CN) either delays or slows down the recrystallisation kinetics of austenite during hot rolling (T_{RXN}). Finally, the solute Nb in austenite solution retards the ferrite nucleation during phase transformation (A_{r3}).

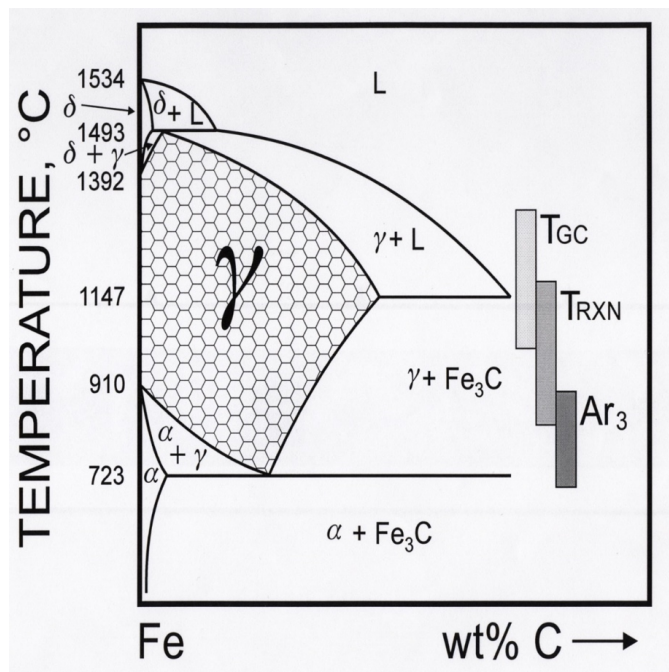


Figure 1.1 Influence of Nb addition on three critical temperatures of austenite processing (adapted from ref [11]).

Each year about 100 million tonnes of steel is thermomechanically processed. If the “value-added” of this approach is to say \$100 per tonne, then thermomechanical processing contributes \$10 billion a year to the overall economy of the world. In looking forward to the future, it seems inevitable that the application of TMCP in the metal processing industry will continue to increase. Several factors have contributed to the success of TMCP technology and to bring it at this advanced stage.

The first is our increased understanding of the individual metallurgical phenomena that make up TMCP, which allowed us to develop a quantitative relationship based on physical or empirical-based modelling. We can now do an offline simulation reasonably predicting the effect of deformation variables on recrystallisation and precipitation kinetics, grain size, and mechanical properties in the finished steel product. A second factor is the gradual application of the TMCP principles to more categories of commercially available steel grades and products. Once successful process control and methods are in place for our highest value-added products, the natural tendency will be to extend their use to lower value-added products.

About half of the steel produced worldwide goes into the building and infrastructure sector. In 2018, the steel consumption in the construction industry was 873 million tonnes, representing 51% of overall steel consumption [12]. Even with the advancement in physical metallurgy, a significant portion of structural steels consists of conventional plain C-Mn steels of low to medium carbon content with yield strengths of 250-300 MPa.

The construction industry is facing significant challenges in developing sustainable structures using a cost-effective method. The structural engineering community is actively considering the use of new high strength steel (HSS) grades, better building components, and composite structures to overcome challenges in the construction segment. HSS has a higher load-bearing capacity due to its higher yield strength compared to equivalent mild steel grade, which reduces the weight of the structure. A cost-saving in a range of 10-30% is possible through weight reduction and associated benefits [13-14]. Nb microalloying addition adds significant value to HSS production by improving strength, toughness, and weldability of steel with a cost addition of just 0.5% over plain C-Mn steel.

The basic understanding of the effect of Nb addition in structural steels long product is still incomplete, despite the numerous investigations and progress made in TMCP for flat products. There is still debate about the interaction between recrystallisation and precipitation behaviour for long products. The structural steels typically have high carbon content (0.20-0.30%C), which limits the solubility of Nb in austenite. The higher soaking temperatures are required to dissolve all Nb into austenite solution. The finish rolling temperature is generally above 950°C for the majority of the structural steel long products. At this temperature, very little precipitation of Nb(CN) is expected to occur, and consequently, no TMCP synergy exists for austenite conditioning.

Some anecdotal evidence suggests that even dilute Nb additions (< 200 ppm) have a beneficial effect on the mechanical properties of structural steel long products [15-17]. The small Nb addition retarded the static recrystallisation under certain rolling conditions for some steel products [18-19]. However, some of these study lacks detailed analysis and therefore need for a systematic study to validate and quantify the influence of dilute Nb concentrations to mechanical properties of structural steels. In particular, the role of dilute Nb on austenite microstructure evaluation during thermomechanical processing needs to be examined.

The present study was primarily designed to investigate the influence of dilute Nb microalloying additions (50-200 ppm) on static restoration behaviour of structural steels to gain better control of microstructural changes occurring during deformation. The study will propose an optimal processing route, and alloy design for structural steels to best benefit from dilute Nb additions. The development of cost-effective structural steels with the dilute Nb concept can meet modern requirements for many civil engineering applications.

The relevant work in the literature on Nb microalloying and TMCP technology was identified and reviewed for low carbon steel flat products. The knowledge was utilised for identifying the areas in which the current understanding is limited for structural steels long products. The experimental program based on plane strain compression testing was designed to simulate applicable industrial rolling conditions.

Hot deformation studies were performed to analyse the recrystallisation and precipitation kinetics of microalloyed austenite. The fractional softening analysis allowed the determination of the recrystallisation processing window as a function of constant pass strain for all steel composition. The Nb(CN) precipitation in deformed austenite has been quantified with electron microscopy to determine the grain boundary pinning forces. Finally, the recrystallisation driving forces and precipitation pinning forces were compared to understand the influence of Nb supersaturation on static softening.

The influence of dilute Nb concentration on austenite microstructure evaluation is discussed in the context of thermomechanical processing. The finding from macroscopic flow behaviour has been validated with extensive microstructure characterisation. The dilute Nb concentrations (50-200 ppm) strongly inhibited the static recrystallisation of austenite for different rolling conditions as a function of Nb supersaturation in austenite and associated strain-induced Nb(CN) precipitation.

This page is internationally left blank

Chapter 2

Literature Review

2.1 Structural Steels

The construction industry is vital for any robust economy not only due to its direct influence on overall economic development but also being one of the largest employment sectors. In 2014, the construction industry contributed around £103 billion to the UK economy, which was 6.5 % of total economic output. It employed 2.1 million people in Q1 2015, 6.2 % of UK total jobs [20]. If we look at overall Europe, it employs around 26 million workers in 2018, which highlights the importance of the construction industry for the economic development of the entire region [21].

Steel is one of the most important structural material used in the construction industry under various forms and shapes, i.e., beams, rebar, and plates. The popularity of steels for construction is due to its ability to get different shapes by hot rolling and excellent joining capability by on-site welding and mechanical joining techniques [22]. Figure 2.1 shows the example of typical hot rolled sections produced from billet and blooms casts in a typical steel mill [23].

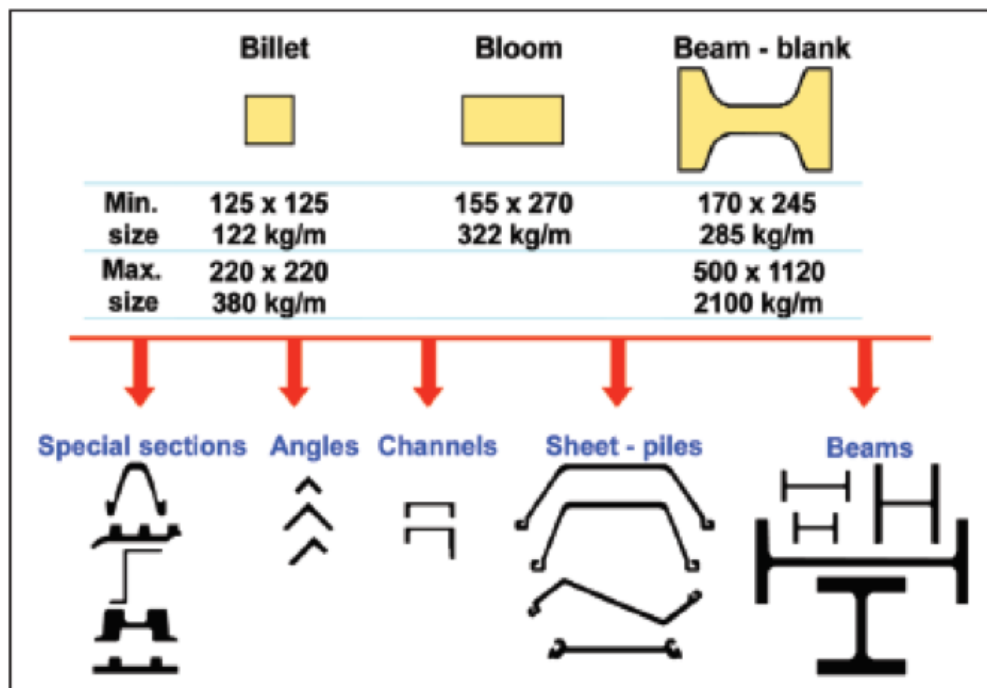


Figure 2.1 Example of typical hot rolled sections (adapted from ref [23])

2.1.1 Market Statistics

About half of the steel produced worldwide goes into the building and infrastructure sector. In 2018, the steel consumption in the construction industry was 873 million tonnes, representing 51% of overall steel consumption [12]. Figure 2.2 illustrates the consumption statistics released by the World Steel Association. Even with the advancement in physical metallurgy, a significant portion of these structural steels is plain C-Mn steels of medium and high carbon content with a yield strength of 250-300 MPa.

There will be 2.7 billion more people by the year 2050 as the world population is continuously increasing. The population growth is driving rapid urbanisation of cities due to the migration of people from rural areas. The buildings and infrastructure will continue to grow worldwide to accommodate this rapid urbanisation and replacement of aging infrastructure. The strong demand for structural steels will continue as it being the preferred choice of material along with concrete. Indeed, world steel consumption is expected to be 2,800 million tonnes by the year 2050 [12]. The major steel producers around the world are now working in close partnership with the structural engineering community to accomplish goals of sustainable and energy-efficient construction.

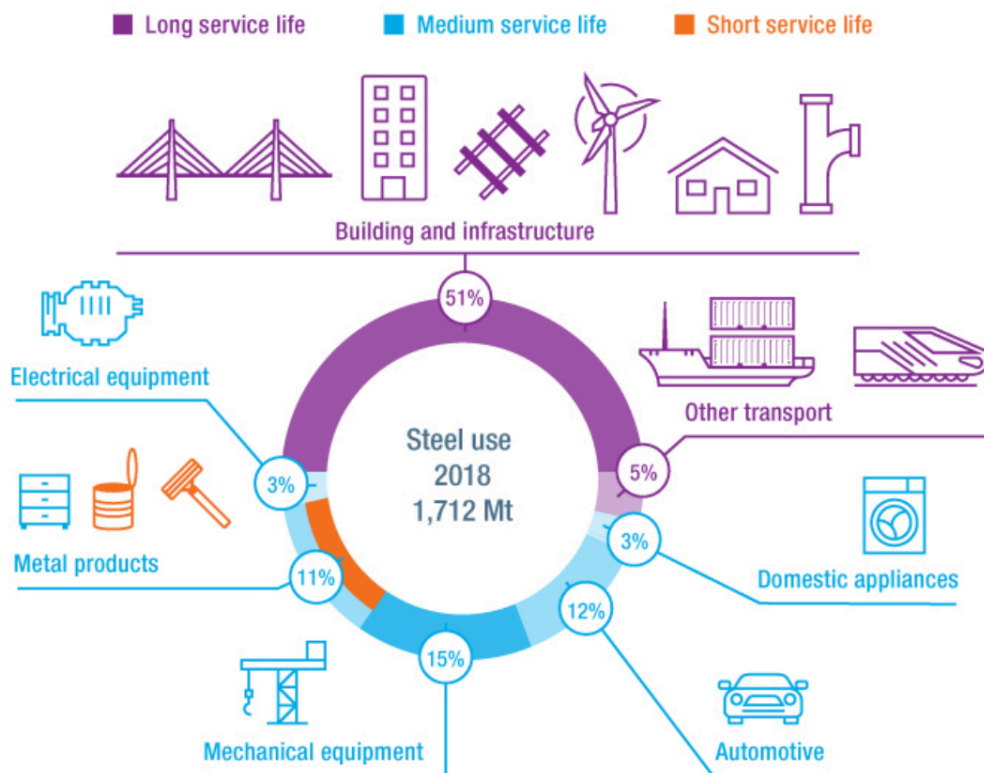


Figure 2.2 Global Steel Consumption in the year 2018 (adapted from ref [12])

Table 2.1 presents the EU finished steel production by product throughout 2011-2017. In the year 2017, long products production was 39 % of the total hot rolled steel production, 154 million tonnes [24]. The section and rebar constitute significant portion steel used for the construction sector.

Table 2.1 EU finished steel production by product category (adapted from ref [24]), all quantities in '000 metric tonnes

Year	2011	2012	2013	2014	2015	2016	2017
Total Hot Rolled	161,516	152,663	150,496	152,338	150,991	150,404	153,857
of which flat products	97,086	92,602	92,836	94,336	92,437	92,200	94,809
Quarto Plate	13,175	12,350	11,021	11,551	10,936	10,573	10,953
Hot Rolled Wide Strip	82,151	78,729	80,358	81,281	80,024	79,941	82,073
Other flat products	1,760	1,523	1,457	1,504	1,477	1,686	1,783
of which long products	64,430	60,061	57,660	58,003	58,554	58,204	59,048
Wire Rod	22,452	20,652	20,138	20,159	20,825	20,451	21,221
Rebars	15,037	14,644	13,172	13,020	12,763	13,191	12,487
Merchant Bars	14,568	12,447	12,562	13,058	12,774	12,319	12,930
Heavy Sections	9,335	9,300	8,584	8,590	8,894	9,401	9,605
Other long products	3,038	3,018	3,204	3,176	3,298	2,842	2,805

Figure 2.3 illustrates the steel consumption by various sectors in the year 2017. The steel consumption in the construction sector was highest (43 million tonnes) and constituted around 35% of overall steel consumption [24]. The steel consumption in the construction sector (35%) for the EU is lower compared to the global average (51%), but that is reasonable considering the developed economy.

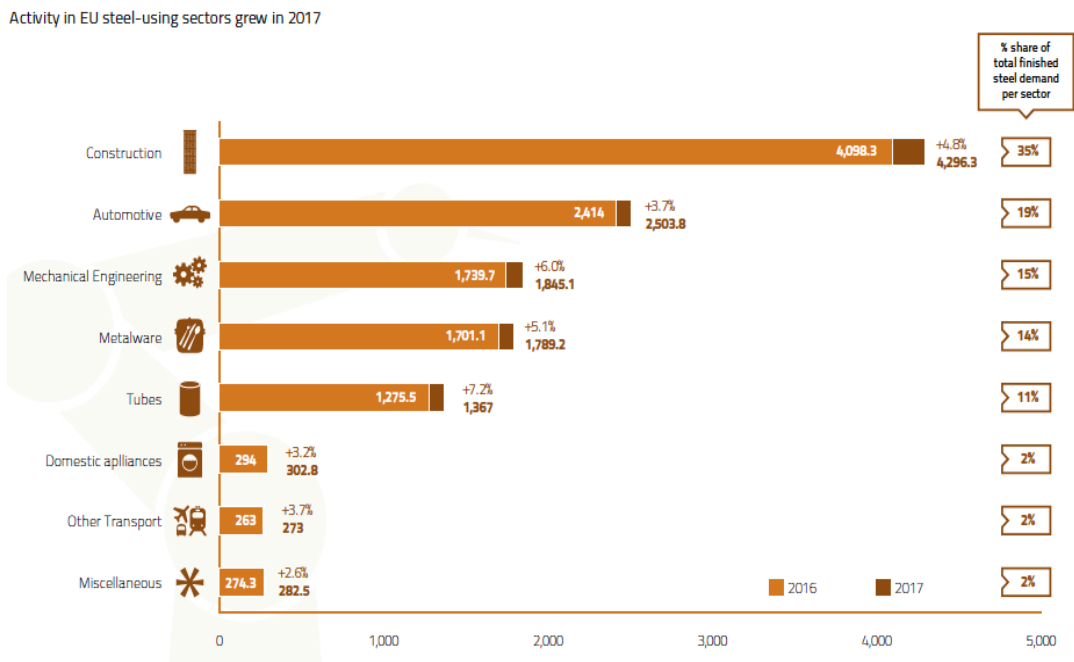


Figure 2.3 EU steel consumption by various sector in the year 2017 (adapted from ref [24])

2.1.2 Process Overview

The steel input for hot rolling differs in form and shape (i.e., blooms, billets, or ingots) depending on the process route and the finished product shape. The cast steel undergoes repeated compressive deformation (temperature ranging from 1050-1300°C) between electrically powered rollers to achieve the desired shape and size. The rolling process also controls the metallurgical properties of the finished product.

2.1.2.1 Section Mill

The design of section mills varies according to product mix and operation preference. Most of the old section mills have tandem design while new section mills are coming with continuous rolling configuration. Generally, the section rolling mill is divided into roughing, intermediate, and finishing stands (like plate mill) for throughput and dimensional tolerance reasons. Figure 2.4 depicts the layout of a typical heavy section mill with universal stands, specialised in long-span parallel flange H and I beam production [25]. It also includes an in-line cooling bank for Quenching and Self-Tempering (QST) treatment of the finish rolled section.

Blooms or cast blanks are reheated in a pusher type or walking beam furnace. A descaling machine breakdown the oxide scale on the surface of the reheated billet before it enters a roughing stand. The roughing stands are generally 2-high reversing mill with several sets of profiles used in sequence to breakdown the cast bloom. The upper roll moves vertically to reduce the roll gap between and breaks down the as-cast billets.

The product mix of section mill consists of different profile shapes and sizes from light to heavy sections, sheet piles, and equal angle channels. Figure 2.5 depicts the finishing duo-stands with grooved rolls are used in finishing mill to produce sheet piles. Similarly, Figure 2.6 shows the ‘universal’ stands with 2-horizontal and 2-vertical rolls for producing parallel flange products. A clean-cut bar end is necessary for entry into the following rolling stand. Therefore, steel mills install hot saws or cropping shears between the different sections of the mills. After finish rolling, the finished products are sectioned to cooling bed length or commercial length by saws cutters as required.

The end-user demand tight dimensional tolerances for hot rolled sections; thus, geometry control is critical in the section rolling. The dimensional control is continuously monitored using sophisticated techniques like laser beam technology and radioactive sources.

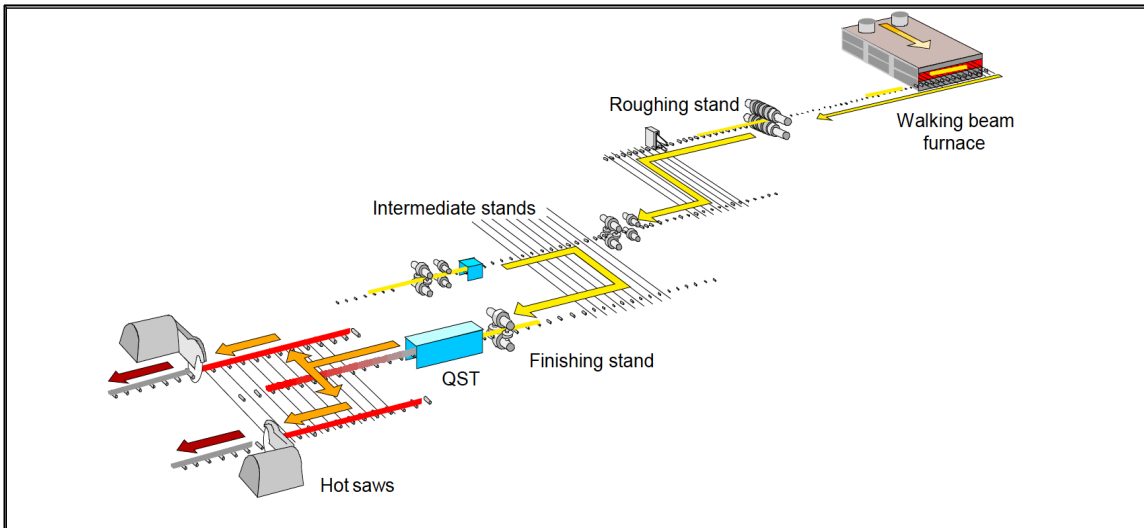


Figure 2.4 Typical layout of heavy section mill (adapted from ref [25])

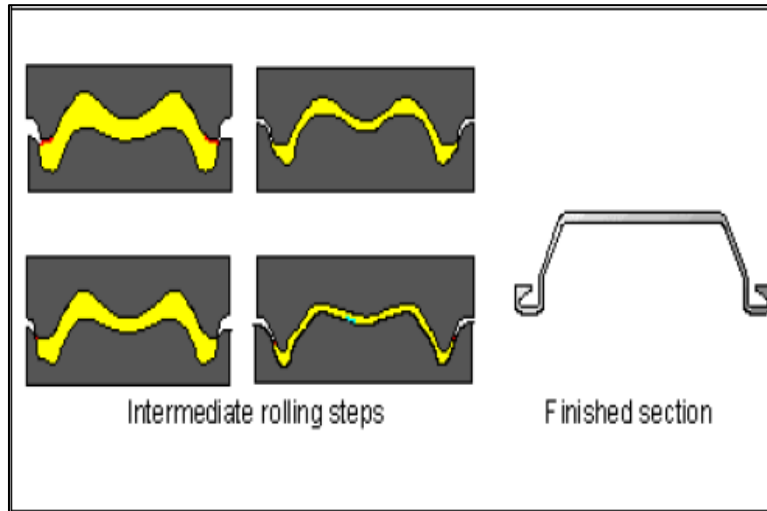


Figure 2.5 Profile roll for sheet piling sections (adapted from ref [25])

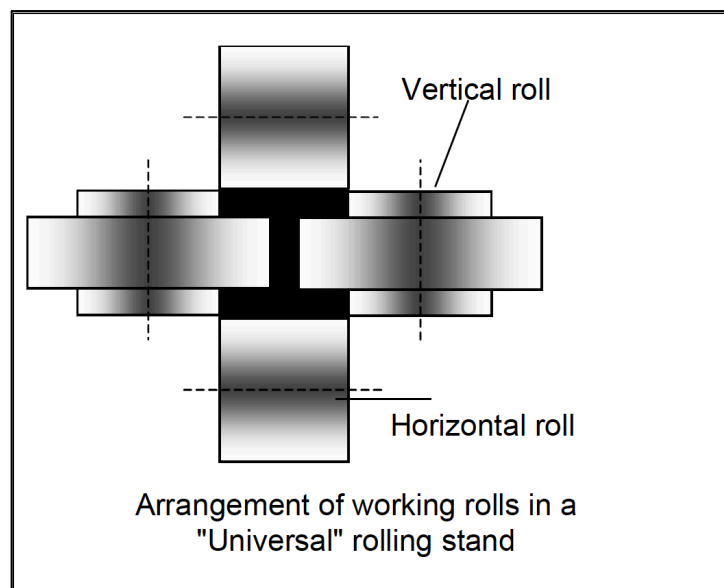


Figure 2.6 Universal stand for parallel flanged products (adapted from ref [25])

2.1.2.2 Wire Rod

Hot rolled wire rods generally have a circular cross-section with a diameter of 5-32 mm. The production of different section shapes (e.g., oval, square, hexagonal, and octagonal) is also possible through adequately shaped rollers. Hot rolled wire rods undergo further processing by cold drawing or cold heading for various applications.

Figure 2.7 shows the layout of a typical wire rod rolling mill for producing engineering steels. The pusher or walking beam furnace reheat the billet to hot rolling temperature (1100-1250°C). A descaling system breakdown the oxide scale on the reheated billet. The wire rod mills are continuous mills (like strip mill) where there is no hold or movement of rolling stock. Hence, the roughing, intermediate, and finishing rolling stands are always laid in sequence and the number of stands in mill vary depending upon a cross-section of billet. The 2-high configured roughing and intermediate sections generally consist of multi-strand (up to 4 strands), while the finishing sections are always single-stranded.

After finish rolling, the water-cooling ramps located between the final rolling stands and the coilers performs the in-line heat treatment of the wire rod. The STELMOR® cooling on conveyor belts with controlled airflow gives the wire rod the desired microstructure for further processing. The wire rod has a very high requirement for surface quality; hence the production process is always monitored round the clock to monitor for seam or lap defect on rolled wire rod. If any defect is detected in an online system, then production needs to be stopped for correcting the roll gaps profile.

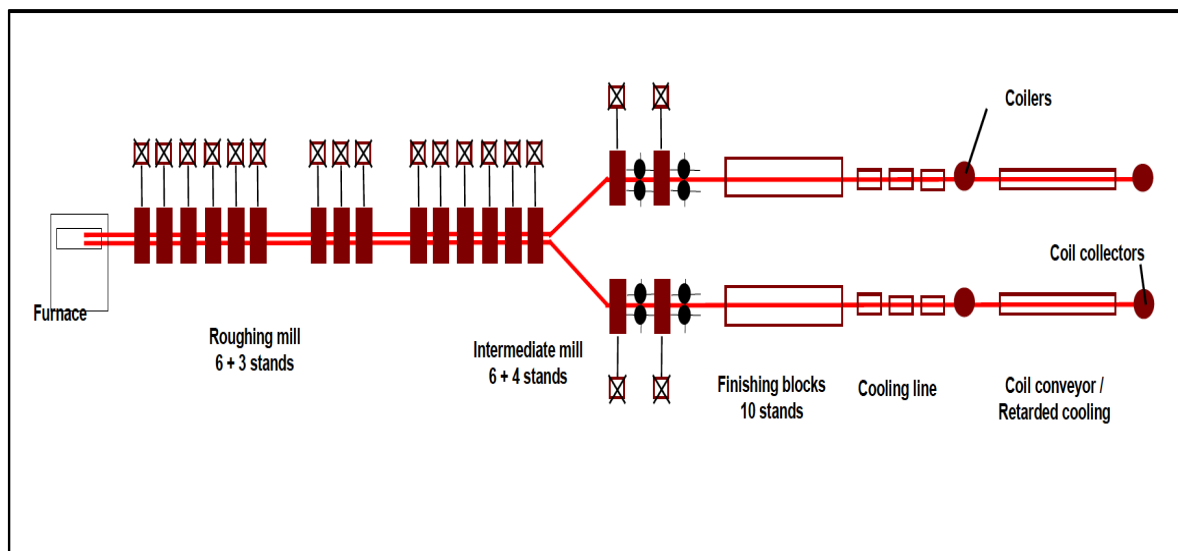


Figure 2.7 Typical layout of wire rod mill (adapted from ref [25])

2.1.2.3 Merchant and Reinforcing Bar

Hot rolled bars consist of two types of steel products, first merchant steels or engineering steels with round, square, or rectangular cross-sections. The second type consists of standard concrete reinforcing bars (rebars) with round cross-sections in diameter of 6-50 mm, mostly with ribs on their surface.

The bar rolling mills are similar in design to the wire rod mill except for the multi-strand finishing blocks. It consists of 2-high rolling mills with roughing, intermediate and finishing groups followed by shears. The new high capacity mills are all continuous type with alternating horizontal and vertical stands, while old lower capacity mills are of the ‘tandem’ type. The crop shear cut the hot rolled product to long bars, which then transferred to a cooling bed. After cooling, the bars are straightened on mechanical or hydraulic straightening machines and are cut to commercial length.

The rebar mills have a typical bar mill configuration with more focused-on throughput for cost-efficiency. The high strength rebars are produced either through the microalloying or QST route. After finish rolling, the hot rolled rebars are water-cooled intensively in a cooling box to produce the martensite layer on the surface. The residual heat from the core of rebar then tempers the martensite layer and improves the strength of rebar. In effect, rebar is a composite structure where the martensite ring on the surface gives strength and ferrite-pearlite microstructure at core gives the desired ductility. The rebars also have ribs on the surface to increase the bonding with the concrete cast. Figure 2.8 shows the typical layout of the rebar mill.

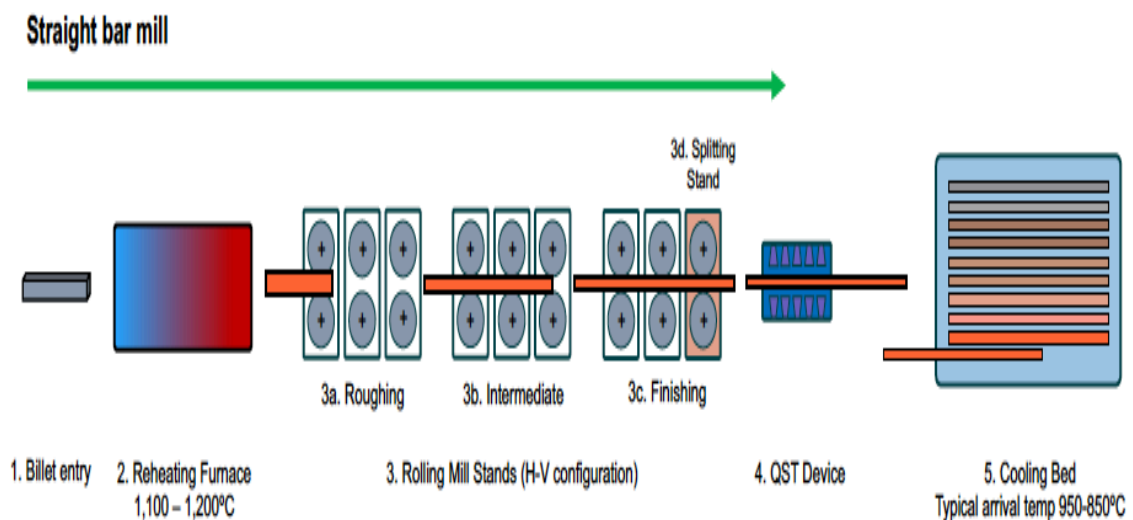


Figure 2.8 Typical layout of rebar mill (adapted from ref [26])

2.1.3 High Strength Structural Steels

High strength steels (HSS) are the type of value-added steel with yield strength equal to or higher than 355 MPa. The microalloying and TMCP technology have enabled the production of higher strength structural grades as a cost-effective construction material. The HSS is a sustainable material substitute not only for a plain C-Mn mild steel but also for the concrete. Over the last three decades, the structural engineering community has adopted grade S355 for a wide range of construction projects across the world. The HSS offers a significant cost advantage by potential weight reduction and associated handling activities. Table 2.2 summarises the specifications of current structural steel grades according to European and ASTM standards.

Table 2.2 European material specification for structural steel (reproduced from ref [27])

Standard No	Standard Name	Steel grade
EN 10025-2	Non-alloy structural steels	S275, S355 JR, J0, J2, K2
EN 10025-3	Normalised/normalised rolled weldable fine grain structural steels	S275, S355, S420, S460 N, NL
EN 10025-4	Thermomechanical rolled weldable fine grain structural steels	S275, S355, S420, S460 M, ML
EN 10025-6	Flat products of high yield strength structural steels in the quenched & tempered condition	S460, 500, 550, 620, 690, 890,960 Q, QL, QL1
EN 10210-1	Hot finished hollow structural sections of non-alloy and fine grain steel	Non-alloy: S275, S355 JRH, J0H, J2H, K2H Fine-grain: S275, 355, 420, 460 NH, NLH
The next revision of EN 10210 will include steels up to S960.		

The construction industry is facing significant challenges aftermath of financial crises and looking for cost-effective, sustainable solutions to meet modern construction requirements. The standard allows the use of weldable structural steels with a maximum yield strength of 460 MPa and good toughness, nevertheless higher strengths up to 960 MPa are also used in the quenched and tempered condition. Table 2.3 list the definition of HSS for different application sectors. The HSS is the right choice for sustainable, green and elegant design construction and would continue to grow in the near future. However, there is not widespread acceptance and demand for hot rolled weldable HSS of 460 MPa and beyond due to design code restrictions.

Table 2.3 Definition of HSS in different sectors [reproduced from ref (28)]

Sector	Product Form	Specified Minimum Yield Strength (N/mm ²)											
		235	275	300	355	400	420	460	500	550	690	890	1100+
Buildings	Profiles	L	L	M	M	H	H	H					
Foundations, quay walls	Sheet piles, piles	L	L	M	M	H	H	H					
Bridges: road (small & medium spans)	Fabricated girders/ profiles	L	L	M	M	H	H	H					
Bridges: road	Fabricated girders				L	L	M	M	H	H	H		
Bridges: rail	Fabricated girders/ profiles	L	M	M	H								
Pipelines-Onshore/Offshore trunk lines	Seam welded pipe				L	L	M	M	H	H	H		
Pipelines flow lines/risers	Seamless pipe				L	L	M	M	M	H	H		
Pipelines tubing/casing	Seamless pipe				L	L	M	M	M	M	M	H	H
Pressure vessels	Welded plate		L	L	M	M	M	H	H				
Storage tanks	Welded plate	L	M	M	H	H	H	H					
Fixed offshore rigs	Welded plate				M	M	M	M	M	H	H		
Mobile offshore rigs	Welded plate				L	L	M	M	M	H	H	H	
Bulk container ships	Welded plate	L	M	M	M	H	H						
Military ships, fast Ferries	Welded plate			L	M	M	H	H					
Wind towers	Welded plate / profiles		L	L	M	M	H	H	H	H			
Mobile cranes	Welded tubulars / profiles						L	L	M	M	H	H	H
Quarrying & mining	Wear plates					L	L	M	H	H	H		
Yellow goods	Welded plate		L	L	M	M	M	H	H	H	H		

L=Low M=Medium H=High

The steel mills have substantially relied on Nb microalloying technology to produce high strength structural steels capable of meeting the higher performance requirements. Nb microalloying addition represents less than 0.5% of the total cost of producing steel, but it adds significant value by improving strength, toughness, and weldability of the rolled product. As shown in Table 2.1, hot rolled beams and rebar constitute a significant proportion of structural steel production. For this reason, the most substantial part of the following discussion will concern with beams and rebar, but the main principles are valid for other types of products assuming an equivalent thickness.

2.1.3.1 Heavy sections

The structural engineer prefers wide flange beams and column sections for the construction of high-rise buildings, bridges, airports, and many other infrastructure activities. HSS has a higher load-bearing capacity due to its higher strength compared to equivalent mild steel grade, which allows the use of thinner cross-section instead of a normal thick one. The reduction in static weight not only offers to save in material costs but also significant savings comes from the reduction in welding, fabrication, transportation, and erection costs. The weight saving with the use of HSS depends upon the type of member and mode of loading in structure, but for many practical purposes, it might range from 10-30% [13-15].

The structural engineering community considers the development of central business districts (CBD) as a hallmark of the construction industry due to the enormous challenges it possesses. The building designs in CBD are becoming taller and taller across the major world cities, e.g., Hearst Tower in New York, Shard in London, or Emirates in Dubai. The design of high-rise buildings is a balancing act of architectural design, client aspiration, and regulatory requirement. The application of HSS in high rise design meets all the above requirements economically through substantial savings in structural weight and material costs. The structural engineers generally adopt composite/hybrid structure for high rise design to benefit from both concrete and high strength steel materials.

There is a lack of systematic studies on the reduction in carbon footprint and CO₂ emissions associated with the application of HSS. One of the studies suggests that CO₂ (cradle to gate) emission for production of 690 MPa HSS plate is 7 % higher than 350 MPa grade [13]. This looks reasonable from alloying and additional processing required for the production of the HSS. The application of HSS as a lighter structure reduces the overall steel tonnage required for the project and brings a substantial reduction in carbon footprint offsetting the initial 7% hike as reported earlier. The complete life cycle assessment of the entire structure would undoubtedly highlight the utility of the HSS as a sustainable material.

The HSS rolled, and fabricated sections are available for more than three decades but only about 5% of structural steel consumed is of grade S420 and above. Table 2.4 illustrates the distribution of the family of structural steel grades [27]. Even the production of S460 is limited up to a thickness of 50 mm due to microstructure inhomogeneity.

Table 2.4 Construction segment strength grade distribution

Commodity C-Mn S235/S275	Low Strength HSLA S345/S420	Advanced HSLA S460/S890
70%	25%	5%

There are many reasons for the slow uptake in the specification of HSS for most load-bearing structures. One of the main obstacles is the instability and serviceability design criterion in the load-bearing structure. This criterion relies upon the stiffness of steel rather than yield strength. The deflection limits restrict the use of HSS for structural members in bending as critical failure mode buckling instability [27-28]. The stiffness of a steel material directly depends upon the magnitude of the modulus of elasticity (E), which is the same for all the structural steel grades, independent of the yield strength. Therefore, the economy usage of HSS is popular and limited in structural elements where the enhanced strength is beneficial as per the design code.

The inexperience in fabrication, lack of skilled welders, and limited sources of supply are another major obstacle to the greater use of HSS. The construction industry extremely conservative with regulation codes, hence there is a general reluctance to change for HSS [27]. The development of S460 beam sections and beyond in a cost-effective manner is essential to meet the modern construction requirements.

2.1.3.2 Rebar

Steel reinforcing bar (rebar) is a primary construction material used in all types of building and infrastructure projects. In 2018, the estimated steel production of rebar was 270 million tonnes [23]. A large quantity of rebar is produced, incorporating process technologies such as Tempcore or Thermex. These technologies enabled the production of rebar at relatively low cost with adequate performance characteristics. The QST produces a metallurgical composite structure, i.e., martensite ring on the outer surface and ferrite-pearlite microstructure at the core of rebar. Most of the QST mills can produce 500MPa yield strength rebar up to 50 mm diameter and 550-600MPa up to at least 32 mm diameter.

Recently, the Peoples Republic of China issued the latest revision of GB1499.2-2018 (a national standard for steel ribbed reinforcement bars for concrete), prohibiting the use of QST technology to produce rebar [29]. In the revised standard, the tempered martensite structure is not acceptable in any grade of rebar. It recommended a predominately ferrite-pearlite structure with uniform hardness distribution. The earthquake of 2001 and 2008 in China highlighted the poor-quality control issue in QST rebars, which necessitated this revision in standard to improve the seismic performance of rebars.

Traditionally, both Nb and V microalloying additions were used to produce rebar with fine ferrite-pearlite microstructure before the invention of the QST process. Nb microalloying in rebar allows the control of reheated grain size resulting in the uniform grain size distribution after finish rolling. The amount of Nb remaining in solution precipitates in ferrite and provides necessary dispersion

strengthening to meet desired high strength requirements [26]. The recent studies have shown that Nb microalloyed rebars exhibit better fatigue performance (LCF and HCF) over the TMT rebars [30].

2.2 Microalloying and Strength

The steel industry across the globe went into the rebuilding phase immediately aftermath of World War II. During this time, some new technical developments in steel making and refining (e.g., de-oxidation with aluminium, desulphurisation) were discovered, which revolutionised both the upstream and downstream processing of steel products. There was also an evident need to develop better steel products as the specialised processing types of equipment were available. The structural steels at that time were simple C-Mn-Si type, available either in as-rolled condition or normalised condition. These steels exhibited classical ferrite-pearlite (F+P) microstructure with yield strength generally around ~ 250 MPa.

During this period, there was also a rising demand for high strength, formable, and weldable structural steels for transportation and energy-related industries. A significant requirement was from the oil & gas pipeline operators who were looking for new materials so that they could operate pipelines with higher pressure in the severe cold environment. The new materials required improved toughness and higher impact energies to avoid brittle fracture as well as higher strength for light-weighting and cost-effectiveness. The steel companies fulfilled this demand through the parallel development of microalloyed steels on the one hand and thermomechanical processing on the other [1-5].

In 1958, the Great Lakes Steel Corporation had announced the development of fine-grained high yield strength (415 MPa) hot strip products combined with excellent toughness. The addition of small, relatively low-cost addition of niobium (Nb) to an ordinary semi-killed C-Mn steel made this possible. The microstructure observations showed that a remarkable ferrite grain size refinement was present in the Nb added steel compared to the plain C-Mn steel. The investigators linked the improved strength and toughness of this newly developed steel grade to the ferrite grain size refinement. However, the addition of Nb to thicker gauge plates (>12mm) had resulted in poor toughness, and no grain refinement was noticeable. The independent investigations preceded to understand the effect of Nb under different hot working conditions for a broader range of thicknesses. The promising result of Nb treated steels attracted the attention of several other steel producers both in the US who conducted their trial based on a similar concept [2].

In the mid-1960s, the erstwhile British Iron and Steel Research Association (BISRA), Sheffield, UK carried out various laboratory and commercial rolling trials on low carbon steel plate

microalloyed with Nb. This development was initiated to investigate the poor toughness, and lack of grain refinement in a thicker product of Nb treated steels produced from Great Lake Corporation and several other similar trials. Irani *et al.* [31] discovered that the addition of Nb greatly retards the recrystallisation rate of deformed austenite during the hot rolling. The toughness of thicker plates could be improved if finish rolling was carried out at lower temperatures (e.g., 850-900°C) in the non-recrystallisation regime of austenite [31-32], termed as a controlled rolling. The new rolling procedure was a vital breakthrough in developing a new class of steel over a broader range of thickness, termed as high strength low alloy steels (HSLA).

The early commercial HSLA steels were predominately low in carbon (0.03-0.15%) and microalloyed with small quantities of carbide forming elements such as niobium, vanadium, or titanium. These steels mostly had a fine-grained ferrite microstructure with minor amounts of pearlite after the controlled rolling. The yield strength was typically in the range of 300-450 MPa, which provided a high strength-to-weight ratio over mild steels. The combination of strength, toughness, and weldability paved the way for its applications in transportation, line pipe, construction, and pressure vessel technologies.

Around the 1980s, both line pipe and automotive industry required material strength over 420 MPa in weldable low carbon steels. The air-cooled ferrite-pearlite steel could not achieve this strength level consistently even with microalloying addition. It was well established by then that increasing cooling rate shifts the austenite decomposition of HSLA steels to lower temperatures. The laboratory trials had shown that the ferrite grain refinement along with low-temperature transformation products (i.e., bainite and acicular ferrite) could provide significant strength increment.

The steelmaking companies in Japan developed accelerated cooling technology in the mid-1980s to produce non-equilibrium microstructure in an industrial environment. It was a significant development as it provided a breakthrough in transferring knowledge from laboratory trials to the practical industrial level. Thus, controlled rolling combined with accelerated cooling led to the establishment of today's TMCP technology of advanced high strength steels [5,9].

Morrison [2] found historical evidence of additions of V and Ti (up to 0.10%) to steel for improving mechanical properties even before the commercial use of Nb in the Great Lake rolling trials. The addition of V was found to be responsible for secondary hardening in heat-treated steels due to precipitation of VC in the matrix [33-34]. The addition of Ti was less widely used compared to V, although there were some published results of its grain refinement effect on forging steel [35-36]. Despite their early developments, the V and Ti addition to carbon steel was not popular due to a

lack of detailed analysis. The research on V and Ti element got momentum only when the promising results from Nb treated steels were published.

Over the years, the continuing interest of steelmakers and further research led to the development of the family of microalloyed steels that we have today. They have been applied in various industries and constitute around 10% of world steel production [37-38]. In looking forward to the future, it seems inevitable that the application of TMCP in the metal processing industry will continue to increase.

2.2.1 Role of microalloying element

Noren [39], was probably the first who introduced a term microalloying element for Nb, Ti or V since they are generally present at levels or below 0.10 wt. % (1000 grams/tonne). In the usual meaning, the amount of microalloying element required for achieving a beneficial effect was 1/10th or 1/100th of the bulk alloying elements like Mn, Si, and Ni. The microalloying elements form strong carbides, nitrides, or carbonitrides (NbCN, VCN, TiC, TiN) either in austenite and ferrite based on available supersaturation and deformation processing variables. The carbonitrides have a NaCl crystal structure and do not fit well in austenite or ferrite lattice. Table 2.5 shows the lattice mismatch for Nb and V precipitates in both austenite and ferrite. As a result of lattice mismatch, most of these microalloying precipitates nucleate on crystalline defects either in the austenite or ferrite [1].

Table 2.5 Lattice mismatch of MX precipitates (reproduced from ref [1])

Lattice parameter, a_0 nm	NbC	NbN	VC	VN
	4.4702	4.39	4.16	4.29
[100]ppt/[100] γ	25.22	22.98	16.53	20.17
[010]ppt/[010] γ	25.22	22.98	16.53	20.17
[001]ppt/[001] γ	25.22	22.98	16.53	20.17
[100]ppt/[100] α	55.95	53.15	45.13	49.67
[011]ppt/[010] α	10.26	8.28	2.61	5.81
[0-11]ppt/[001] α	10.26	8.28	2.61	5.81

Austenite: FCC, $a_0 = 0.35698$ nm; Ferrite: BCC, $a_0 = 0.2864$ nm

The development of a fine ferrite grain size in as-rolled HSLA steels requires microstructure control of austenite during rolling and ferrite during transformation. Numerous investigations [6-8, 11] have shown that microalloying elements can retard the recovery and recrystallisation of austenite both by dissolving in the austenite (solute drag) or by forming precipitates (precipitate pinning). Whether the significant portion of the retardation is due to solute drag or precipitation has been the subject of debate. However, there is ample evidence that strain-induced fine carbide particles retard recrystallisation effectively over solute drag [40-43].

Nb microalloying has received the most attention to date in this aspect, and the precise nature of its effect on austenite recrystallisation via solute drag and precipitate pinning is now known [8]. The strain-induced precipitation of Nb(CN) on subgrain boundaries retards the static recrystallisation of austenite by exerting pinning forces on moving interfaces. The unrecrystallised austenite containing intragranular effects accelerates ferrite nucleation rates during transformation, leading to essential ferrite grain refinement.

During transformation, the microalloying element remaining in solid solution forms carbonitrides in ferrite depending upon the cooling rate and transformation temperature. As shown in Table 2.5, the MX precipitates are incoherent with ferrite, considering the misfit strains of several percent. The combination of incoherency and the NaCl structure of precipitates should give dispersion hardening by restricting the movement of dislocations. This precipitation strengthening contribution is given by Ashby-Orowan mechanism [10] and can be quantified using the following equation

$$\Delta\sigma_p (MPa) = \frac{10.8f^{\frac{1}{2}}}{X} \ln \frac{X}{6.125 \times 10^{-4}} \quad (2.1)$$

where X is the mean diameter of precipitate in μm , and f is the volume fraction of precipitate. As shown in equation (2.1), the precipitation strengthening depends upon particle size and volume fraction of precipitate. Hence it is essential to tailor composition and processing conditions of microalloyed steels for the high-volume fraction of fine size precipitation. Figure 2.9 shows the dependence of precipitation strengthening on particle size, X , and volume fraction, f_v , according to the Ashby-Orowan model.

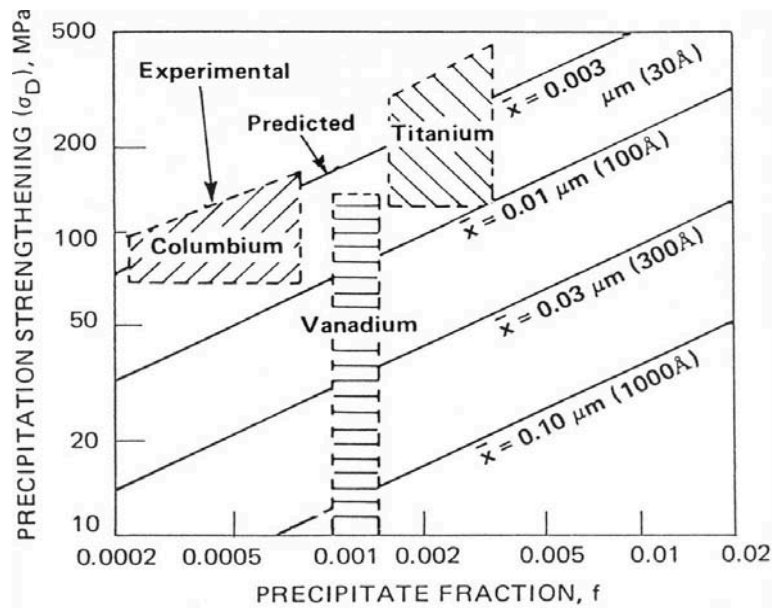


Figure 2.9 Influence of precipitate size (X) and a fraction (f) on precipitation strengthening according to the Ashby-Orowan Model. The experimental observations for given microalloying additions are given for comparisons with a theoretical prediction (adapted from Ref [3,10]).

2.2.2 Structure-property relationship

The microstructure-properties relationship has received considerable attention, and its comprehensive reviews are available [1-3,10]. The development of designer steel philosophy in the 1960s and the introduction of microalloyed steel had advanced the research interest in this field [2]. There is a form of empiricism connected with some of these equations with a range of variables and exponents. However, they are in line with the fundamental theory of the effect of microstructure on mechanical properties. The expanded Hall-Petch relationship states yield strength of ferrite-pearlite microalloyed steel as [1-3]:

$$\sigma = \sigma_0 + \Delta\sigma_S + \Delta\sigma_T + \Delta\sigma_P + \Delta\sigma_D + k_y d_f^{-\frac{1}{2}} \quad (2.2)$$

where σ is the observed yield strength, σ_0 is lattice friction stress, and $\Delta\sigma_S$, $\Delta\sigma_T$, $\Delta\sigma_P$ and $\Delta\sigma_D$ are the strengthening increments from solid solution, texture, precipitation, and dislocation effects, respectively. The last term $k_y d_f^{-\frac{1}{2}}$ is strengthening contribution from ferrite grain size refinements.

Figure 2.10 illustrates possible strengthening mechanism operative in hot rolled mild steel, and the controlled rolled HSLA steels [44]. These two grades of steels differed in grain size and presence of a precipitation hardening increment ΔY ($\Delta\sigma_P$ in Equation 2.1) in the HSLA steel. A decrease of ferrite grain size from ASTM 6-8 (typical of hot rolled mild steels) to ASTM 12-13 (typical of HSLA steels) resulted in yield strength increment of about 210 MPa (based on Hall-Petch relationship, $k_y d_f^{-\frac{1}{2}}$). The precipitation strengthening ΔY of 100 MPa is due to the formation of fine carbides or carbonitrides either in the austenite and ferrite. The combination of the ferrite grain size refinement and precipitation strengthening in HSLA steel makes it twice as strong as the hot rolled mild steel.

The fundamental research in microstructure-property relations in ferrite-pearlite steels gave a different view regarding the origin of strength and toughness. As now, we understand that the strength of steel can be increased simply by the addition of either precipitation hardening or solute strengthening elements. On the other hand, the resistance to brittle fracture is governed only by the control of the final microstructure, not by the addition of alloying elements. Figure 2.11 illustrates that the reduction of ferrite grain size and a cementite free microstructure (e.g., no pearlite or upper bainite) are the only mechanism which increases the toughness and lowers the ductile to the brittle transition temperature of microalloyed steels [45].

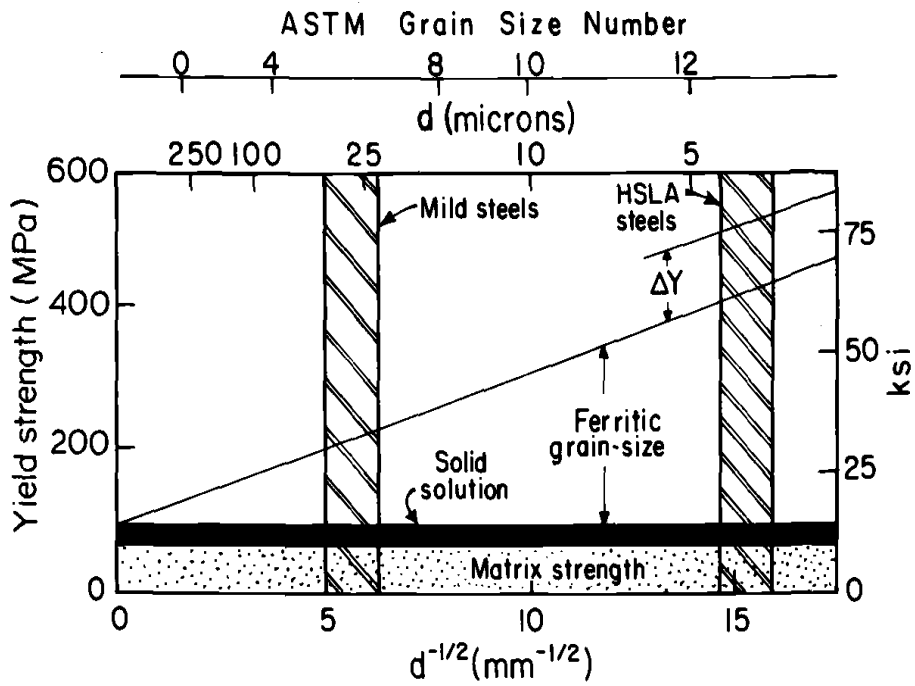


Figure 2.10 Illustration of possible strengthening mechanisms operative in low-carbon steels (adapted from ref [44])

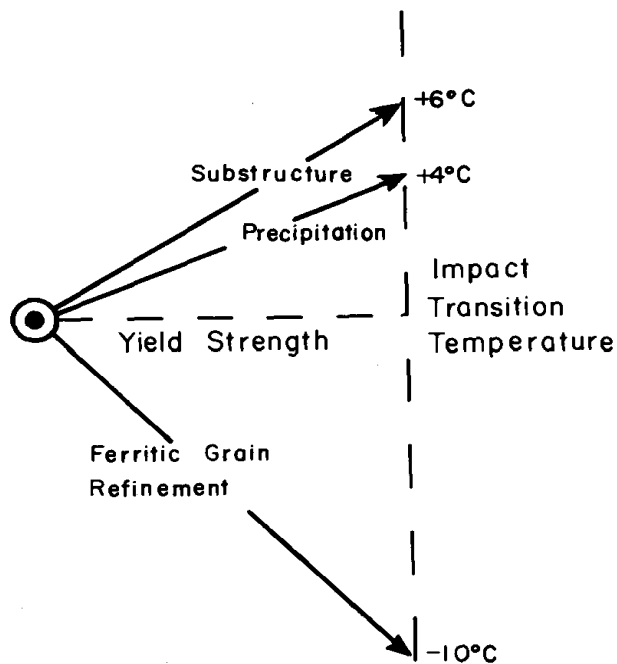


Figure 2.11 The influence of metallurgical structure /factors on yield strength and impact transition temperature. Numbers indicate the change in transition temperature per 15 MPa increase in yield strength (adapted from ref [45]).

2.2.3 Applications

The main properties of HSLA steels (i.e., strength, toughness, weldability, and cost-effectiveness) make them suitable for a wide variety of applications. The HSLA allows the more efficient design of the product with improved performance due to its superior mechanical properties over plain C-Mn steel. Furthermore, they allow taking relative strength–section cost advantage and associated weight reduction.

Energy - Oil & Gas

Figure 2.12 illustrates the improvement in HSLA steel quality within the framework of the development of new pipeline steels in recent decades [1]. The application of high strength line pipe steels made exploration and transportation of oil and gas very economical from steep terrain of the world. The new material development had a dramatic effect on the oil and gas industry across the world.

Automotive

Every passenger and the commercial vehicle that we drive and see on roads every day has a significant portion of HSLA steels in it. The application of HSLA in body-in-white (BIW) and structural components allows substantial weight reduction, improving fuel efficiency, and reducing the carbon footprint. The superior crash performance of advanced high strength steels has significantly improved vehicle safety.

Structural

The HSLA steels have a high load-bearing capacity in comparison to mild steel, which allows the weight reduction of structural members. The overall cost reduction of 10-30% is possible with saving in fabrication, transportation, and erection cost of structures in most of the projects. The use of HSLA steels reduces the overall carbon footprint of the project, making it green and sustainable construction. Figure 2.13 illustrates various applications of HSLA steels.

In summary, the parallel development microalloying technology and TMCP led to the successful development of today's high strength and tough steels. What follows is a review of various aspects of TMCP, underlying physical metallurgy, and recrystallisation kinetics simulation of microalloyed steels.

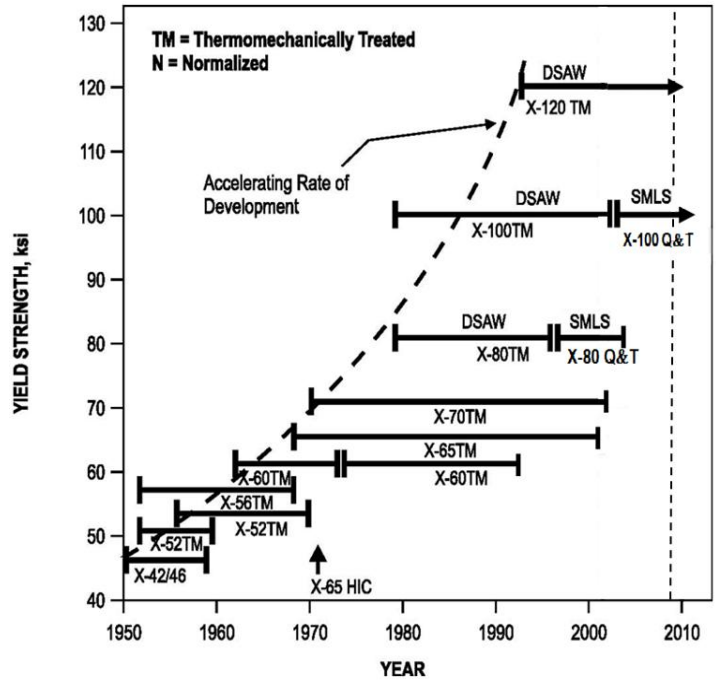


Figure 2.12 Development of line pipe steel as an example of HSLA steel research [adapted from ref [1])

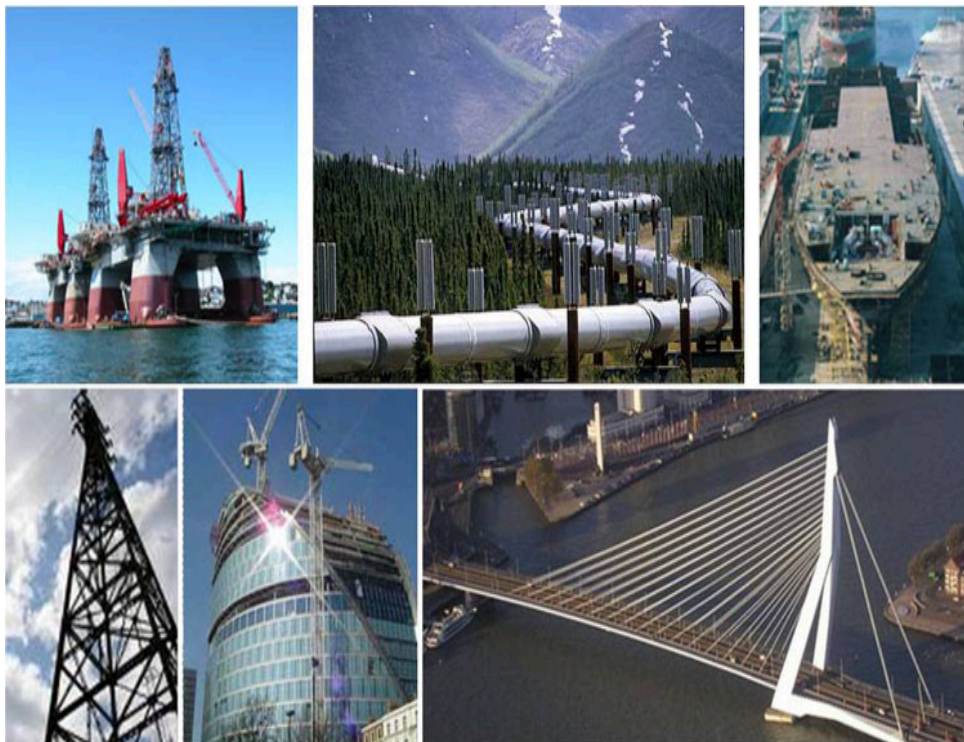


Figure 2.13 Various applications of HSLA steels (adapted from ref [4])

2.3 Thermomechanical Processing

The traditional deformation processing such as rolling and forging are primarily concerned with the production of a particular size and shape via a reduction in thickness at high temperatures. Thermomechanical processing (TMP) differs from traditional processing in this particular aspect and adds value beyond thickness reduction. TMP is mainly concerned with the production of specific microstructure, which in turn controls particular mechanical and physical properties. It involves the control and interaction of following fundamental mechanisms (among others):

- Dislocation glide and climb
- Recovery
- Recrystallisation
- Grain Growth
- Phase Transformation
- Precipitation
- Particle coarsening
- Particle Pinning
- Solute Drag

All of the above underlying mechanisms have been subjected to a good deal of analysis so that fundamental law governing their operation are now widely known. By contrast, TMP is concerned with the synthesis of these essential building blocks and, in particular, with their interactions under industrial processing conditions.

2.3.1 Microstructure Control and Significance of S_v

HSLA steel requires microstructure control of austenite during rolling and of the ferrite during transformation to the achieve desired fine ferrite grain size in the rolled product. Figure 2.14 illustrates the influence of various process and compositional variables on the microstructure control during the hot rolling process of HSLA steels [46]. The microstructure and properties of the finished product do not only depend upon austenite morphology before the transformation but also on the austenite-to-ferrite transformation characteristics.

The static recrystallisation and grain growth of austenite during interpass times govern the austenite morphology before the transformation. The deformation processing variables (i.e., temperature, strain, strain rate, and precipitation) have a direct influence on both of these static events. Cohen *et al.* [46] have reviewed the hot rolling of HSLA steels and divided it into four-stages from the standpoint of austenite recrystallisation and grain growth.

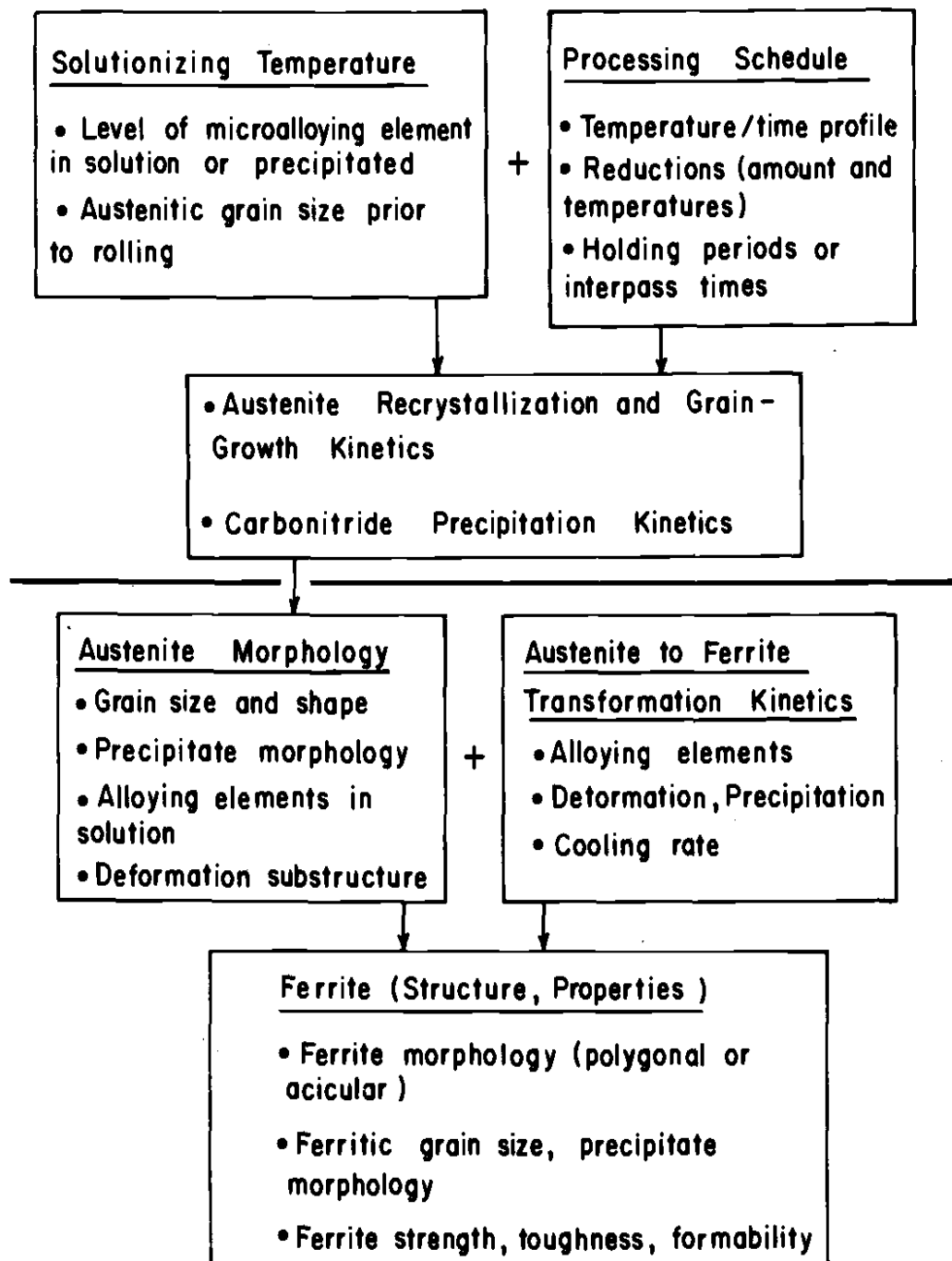


Figure 2.14 Interactions between process & compositional variables during hot rolling of HSLA steel (adapted from ref [46])

Figure 2.15 depicts the microstructural changes associated with each stage of rolling. The thermomechanical processing of austenite produces a variety of austenite morphologies at a different range of temperatures. It is essential to understand this microstructural evaluation since it has a significant effect on subsequent transformation. The temperature ranges over these structural changes (stage I to IV) occur vary with steel compositions and in particular, microalloying addition

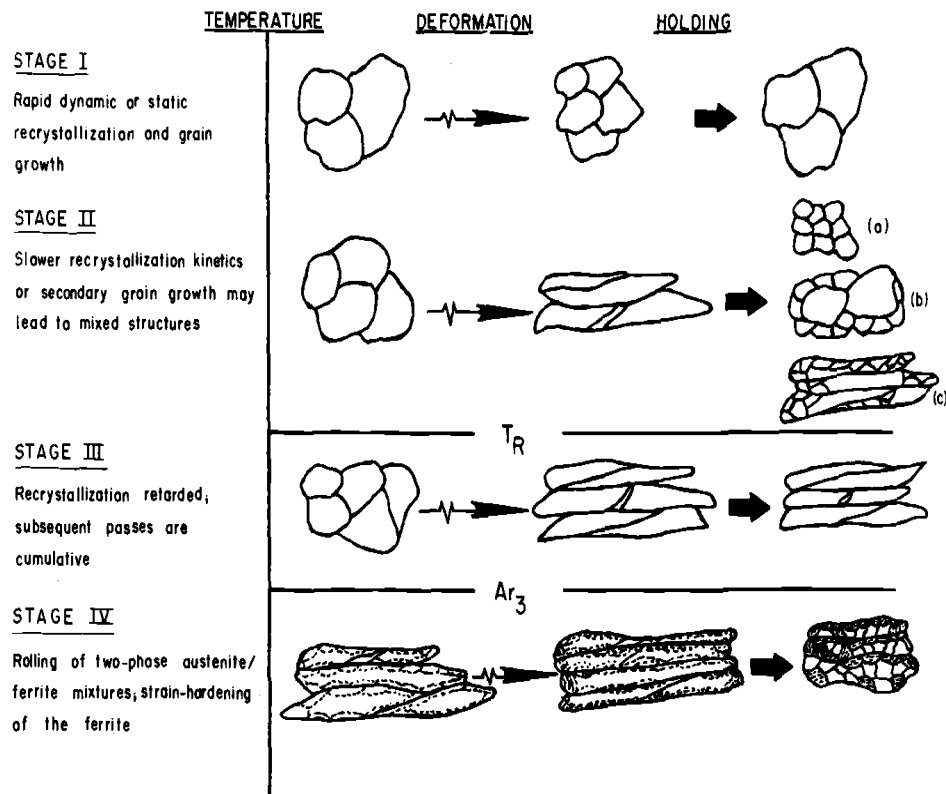


Figure 2.15 Four stages of hot rolling in the thermomechanical processing of HSLA steel. T_R is the rolling temperature below in which a critical degree of carbonitride supersaturation is reached for carbonitride precipitation to inhibit austenite recrystallisation (adapted from ref [46]).

The austenite-ferrite transformation characteristics and, in turn, the ferritic grain size depends upon the ferrite nucleation and growth rates. The prior austenite grain boundaries, alloying elements, and processing variables like cooling rate and coiling temperature significantly influence the nucleation rates. Their nucleation rates increase with an increase in the number of potential nucleation sites and nucleation rates per site [1,8-9]. Several researchers attempted to quantify the number of strain-induced heterogeneities introduced into austenite, which act as a site for ferrite nucleation. This quantification was a critical factor in understanding the link between microalloying and hot rolling of austenite with ferrite grain refinement.

Underwood [47] had defined the stereological parameter, effective interfacial area per unit volume (S_v), to describe all the near crystalline defects in a polycrystalline aggregate using quantitative metallography. The parameter S_v had the units of mm^2/mm^3 or mm^{-1} . Kozasu [48] adopted this parameter to describe the austenite structure and defined it as the total effective interfacial area of austenite per unit volume. The parameter S_v is a parameter like grain size, which magnitude indicates the degree of austenite conditioning. The higher the S_v , the more grain boundaries and deformation bands per unit volume; hence, the more effective the austenite would be in nucleating ferrite and also in stopping the growth of cleavage cracks [1,8, 49].

Figure 2.16 shows the influence of S_v on ferrite grain size in Nb-microalloyed steel deformed in both non-recrystallisation and recrystallisation region [49]. For a fixed value of S_v , the unrecrystallised austenite grain results in fine ferrite grain size over recrystallised grain. There are three entirely different approaches to achieve high S_v through the combination of alloy design and thermomechanical processing. The interaction between recrystallisation and precipitation is the important metallurgical mechanism and of particular interest in TMP of steel, both flat and long products.

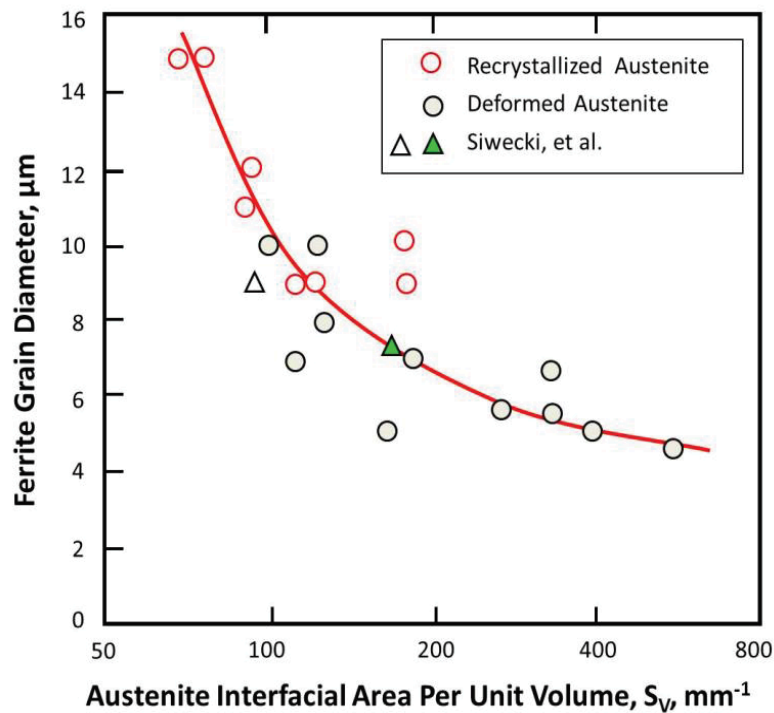


Figure 2.16 Relationship between Ferrite grain sizes and S_v values for recrystallised and unrecrystallised austenite (adapted from ref [49]).

2.3.2 Recrystallisation Controlled Rolling

Heavy plates, forgings, and jumbo sections require higher finishing temperatures ($>950^{\circ}\text{C}$) due to excessive rolling load, especially with underpowered rolling mills. In such cases, it is possible to produce a fine ferrite microstructure by carefully controlling the static recrystallisation of austenite in each pass. Sekin and coworker [50] originally proposed this hot rolling process and termed it as recrystallised controlled rolling (RCR).

The initially reheated austenite grains undergo repeated recrystallisation in multi-pass high-temperature deformation. The recrystallized austenite grain exhibits high S_v due to its fine size. The hot deformation would take place at a temperature above $T_{95\%}$ ($> 950^{\circ}\text{C}$) and below the reheating temperature ($> 1200^{\circ}\text{C}$). The lower the $T_{95\%}$, the larger will be the processing window for hot deformation of austenite. In RCR practice, the total S_v is expressed as

$$S_v = S_v^{GB} = \frac{3}{D_\gamma} \quad (2.3)$$

where D_γ is recrystallised austenite grain size prior to transformation, lower the D_γ higher the S_v .

There are two requirements for the operation of this process to be successful, i.e., achieving and maintaining a fine austenite grain size. The first requirement is that the recrystallisation should not be too sluggish, so that time required should not be too long [51]. The second requirement is the prevention of grain growth after each cycle of recrystallisation, which requires suitable inhibition mechanisms to suppress grain coarsening. The fine austenite grain has a strong tendency to coarsen with interpass time. The grain coarsening can negate the refining effect of recrystallisation, particularly at lower temperatures. Siwecki *et al.* [52] recommended the dispersion of second phase particles with the appropriate size and distribution to prevent the grain growth of austenite after each cycle of recrystallisation [51].

Cohen *et al.* [46] simulated the RCR of 0.10C-1.4Mn-0.05Nb HSLA steel plates in a laboratory as a function of temperature and initial grain size. Figure 2.17 shows that the austenite grain size decreases progressively with temperature and approaches a limiting grain size of $20\ \mu\text{m}$ after hot deformation. As shown in Figure 2.18, even the variation in the initial grain size of austenite led to a similar limiting grain size trend. As a result, there will also be a limiting ferrite grain size since ferrite preferentially nucleates on recrystallised austenite grain boundaries.

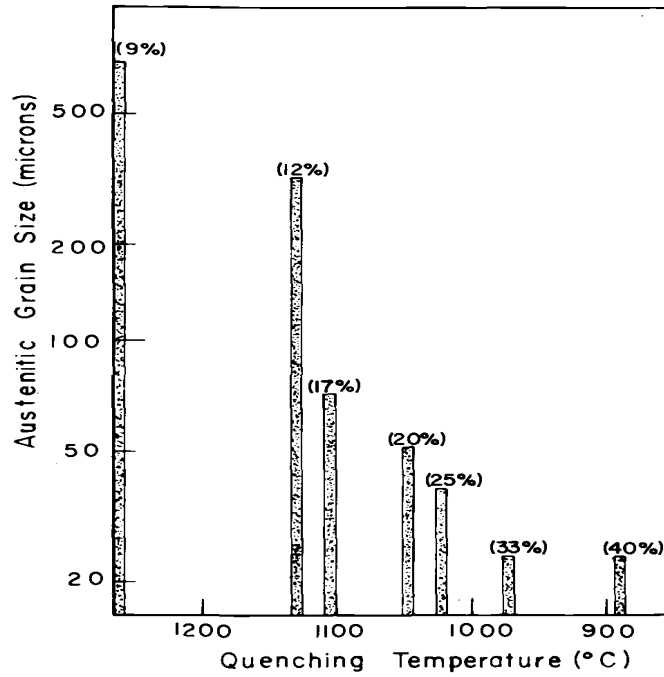


Figure 2.17 Progressive austenitic grain refinement via recrystallisation during simulated plate rolling. The austenite was reduced at the indicated temperature by the amount shown in parentheses and quenched in 7 secs after deformation (adapted from ref [46])

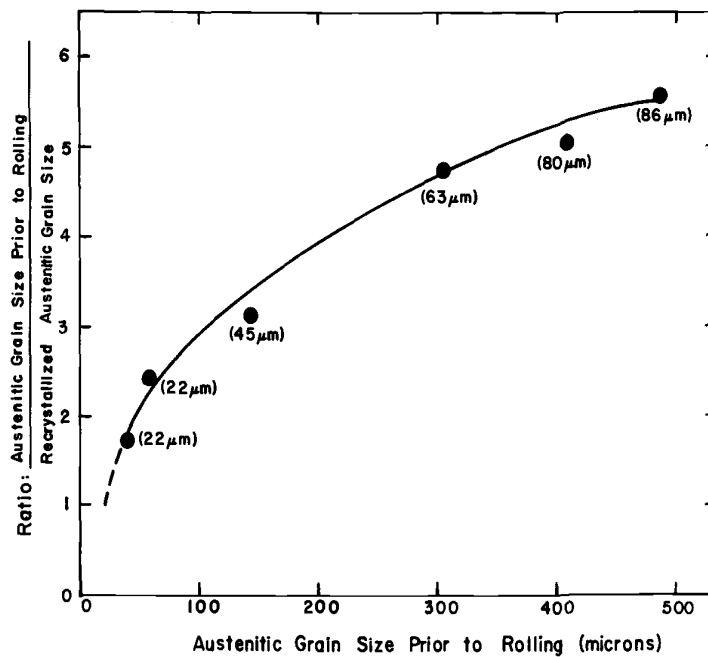


Figure 2.18 Degree of austenitic grain refinement achieved via recrystallisation after a 50% reduction, as a function of the initial austenitic grain size. As-recrystallised grain sizes, in parentheses (adapted from ref [46])

The limiting ferrite grain size can be estimated assuming the saturation of ferrite nucleation sites at prior austenite grain boundaries. The ferrite grain size would be then equal to average ferritic growth distance, which is about one half of the prior austenite grain diameter. The recrystallised austenite of grain size about 20 μm (ASTM 8) will transform into a ferrite of 10 μm (ASTM 10) grain size. The ferritic grain refinement in RCR is useful but not exceptional compared to CCR practice.

Siwecki *et al.* [52] published the results of the low carbon microalloyed steels (0.15C-0.01Ti-0.08V-0.013N) rolled to 25 mm plates using the RCR practice with and without application of accelerated cooling. They performed the industrial-scale trials with deformation parameters gathered from extensive laboratory simulations in earlier research [52]. Some of the slabs rolled into a 20 mm plate with CCR practice (i.e., low finishing temperature) followed by air cooling for comparison purposes. Table 2.6 gives the relevant processing parameters of industrial scale rolling trials.

Table 2.6 Process Parameters for full-scale production

Process	Thickness mm	Time min	RHT °C	FRT °C	FCT °C	No of passes	CR °C/s
RCR	25	3	1250	1050	-	10	0.4
RCR+ACC	25	3	1250	1050	600	10	7
CCR	20	8	1250	825	-	13	0.5

Figure 2.19 compares the measured rolling load of two types of rolling processes [53]. The rolling loads for the CCR process are 25% higher than the RCR process due to low finishing temperature and accumulated deformation below $T_{5\%}$ temperature. Also, the longer time in the CCR process is mainly due to the delay in cooling the transfer bar (40 mm thickness) from 1100 to 920°C. There were also three additional finishing passes in case of CCR rolling.

Figure 2.20 shows the summary of the mechanical properties of as-rolled plates. The accelerated cooling in the case of RCR practice resulted in ferrite grain size refinement (e.g., 7-10 μm in diameter) and elimination of pearlite banding. The apparent yield strength improvement of 100 MPa in RCR+ACC rolling was a result of grain refinement. The CCR practice exhibited the finest ferrite grain size even though it was air-cooled after the deformation. It exhibited similar mechanical properties of RCR+ACC practice. The further grain refinement and improvement in mechanical properties of CCR practice would have been possible with the application of accelerated cooling. This finding suggests that the recrystallisation of austenite must be avoided to obtain finer ferrite grain size, which is the basic principle of CCR practice.

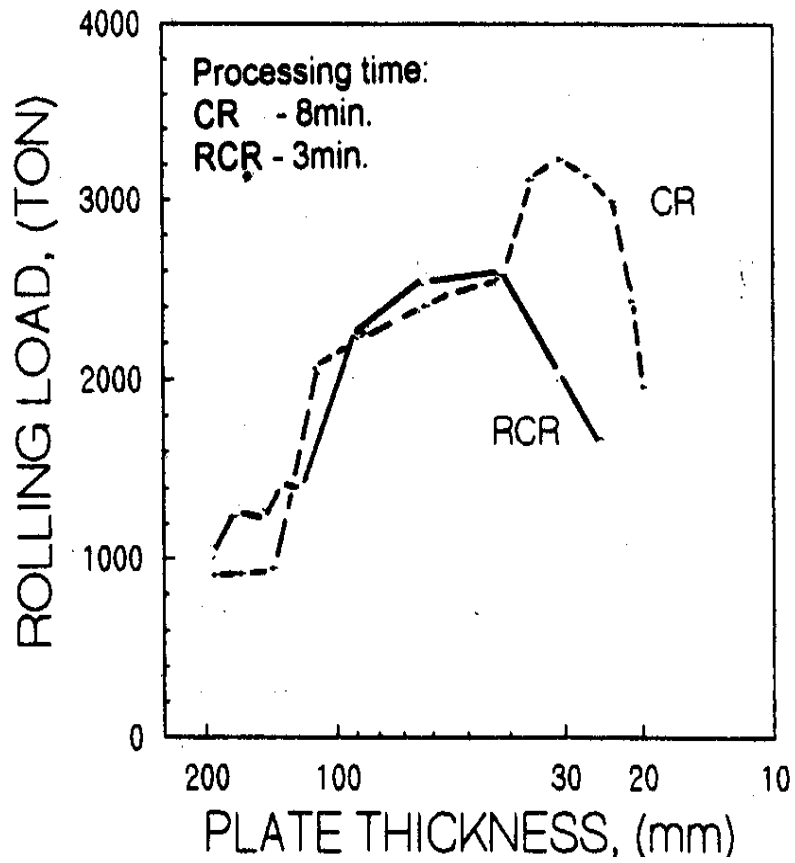


Figure 2.19 Comparison of measured rolling loads during RCR and CCR rolling (adapted from ref [53])

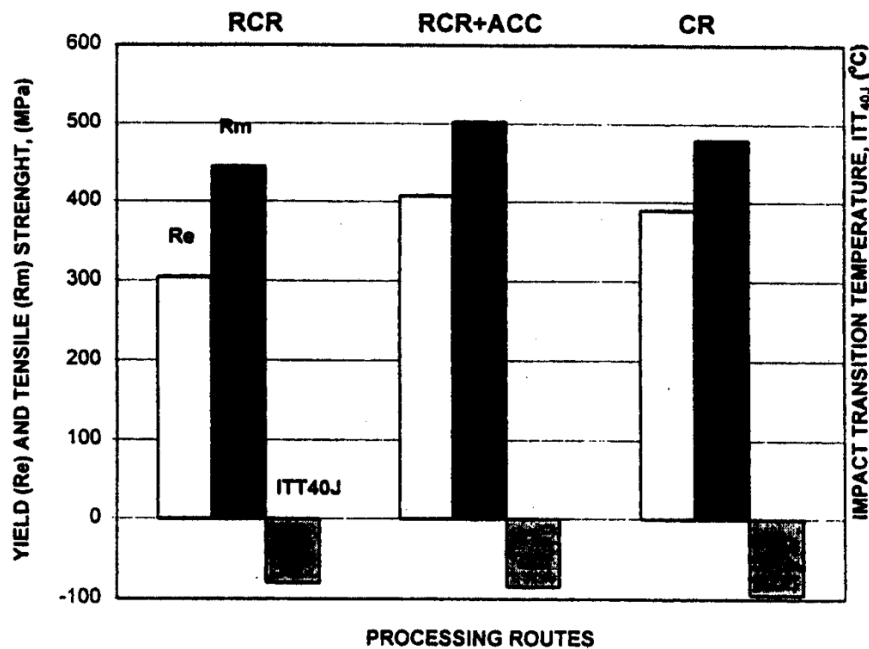


Figure 2.20 Mechanical properties of commercially processed 0.15C-0.01Ti-0.08V-0.013N steel plates produced from different processing routes (adapted from ref [52]).

2.3.3 Conventional Controlled Rolling

Conventional Controlled rolling (CCR) is a technique or rolling practice in which the austenite undergoes heavy deformation in a temperature range where there are minimal recovery and no recrystallisation in between interpass time [9, 54]. In steel shop terminology, it is rolling to control the microstructure of austenite, from equiaxed to pancaked consisting of intra-granular defects. The higher the $T_{5\%}$, the larger the number of passes can be used for flattening the austenite grains and more productive is rolling the practice. Hence, the steel designed for the CCR process must have a high recrystallisation-stop temperature ($T_{5\%}$).

The static and dynamic recrystallisation of austenite is strongly retarded with a small addition of Nb microalloying addition through solute drag and pinning effect of Nb(CN) precipitation. Numerous investigations [11, 40-42, 48] have reported the typical Nb(CN) precipitation start time (P_s) as short as 1-2 sec and as long as 50 sec. An important distinction can be drawn between various kinds of the rolling process in terms of propensity of Nb(CN) precipitation for an average P_s time of 10 sec.

Thus, reversing mills such as plate, steckel, and section mill allows plenty of time for precipitation to take place between rolling passes. The presence of abundant amounts of precipitation gives required strain accumulation, and austenite pancaking for CCR rolling. While tandem mills such as rod and hot strip involve such short process times (1-2 sec) that there is little or no precipitation during the pass sequence. The solute retardation of static recrystallisation becomes an essential factor in the case of tandem mills.

Figure 2.21 depicts austenite microstructure changes accompanying the hot deformation in three stages of CCR practice. Baird and Preston [44] originally proposed this three-temperature rolling schedule for C-Mn-Nb steel plates in the year 1972. The initial (rough) rolling is carried out in temperature range in between 1050-1250 °C at which Nb remains in solution. The rough rolling in this temperature range results in rapid static recrystallisation of austenite (γ). After rough rolling, the intermediate transfer bar is held on the run-out table to reduce the temperature from 1050°C to recrystallisation-stop temperature ($T_{nr} / T_{5\%}$). This process is called a delay (Hold Period) and generally lasts for 5-10 minutes. If any rolling is carried out above $T_{5\%}$, the partial recrystallisation occurs, thereby leading to the formation of a mixed grain structure and correspondingly poor toughness.

The final (finish) rolling is carried out in the non-recrystallisation region with a substantial reduction (3.5:1), which forms a highly deformed and elongated austenite microstructure. The rolling loads and mean flow stress increases with decreasing temperature because of the highest accumulated

density of dislocations in austenite. Interestingly, these three temperature ranges remain the core block of today's TMCP schedule after a gap of more than 50 years.

During finish rolling of austenite below the $T_{5\%}$, the work hardening is retained from pass to pass with no static or dynamic softening even at a sufficiently large strain. The austenite grains become highly elongated with the buildup of intra-granular defects such as deformation bands or twin boundaries. The pancaked austenite exhibits high S_v and consists of two components. The first one represents the grain boundary surface area per unit volume (S_v^{GB}) and second, corresponds to the surface area of the deformation bands and twist boundaries.

$$S_v = S_v^{GB} + S_v^{DB} \text{ mm}^{-1} \quad (2.4)$$

$$S_v = S_v^{GB} + S_v^{DB}$$

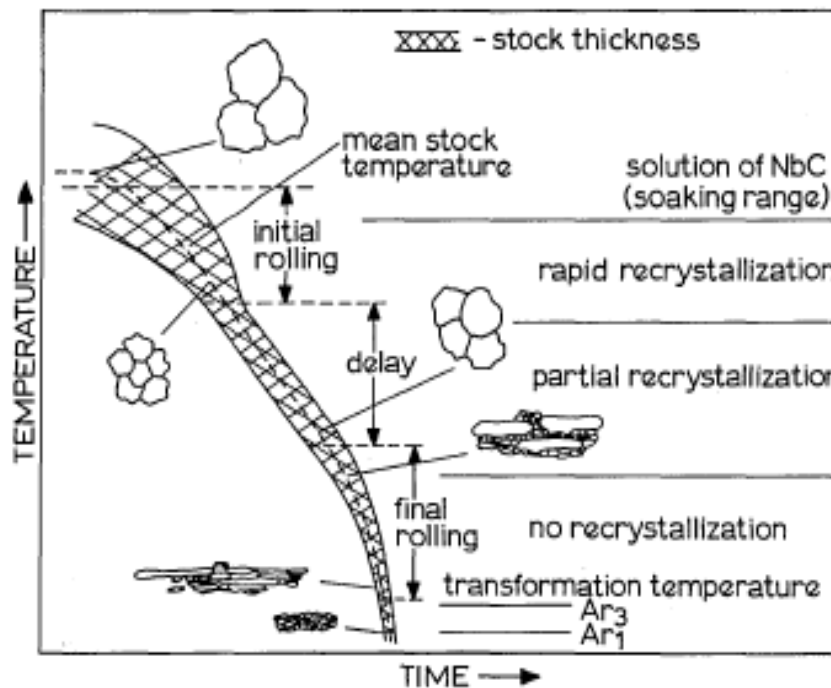
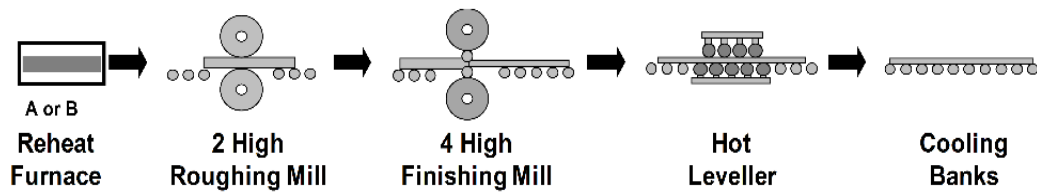


Figure 2.21 TMCP Rolling Practice for C-Mn-Nb steel three stages of rolling (adapted from ref [44])

Speich *et al.* [55] calculated the variation in S_v^{GB} for a hypothetical array of cube grains of variable sizes. The grains were subjected to plane strain deformation to simulate the behaviour of grains under the controlled rolling. The contribution of S_v^{GB} to the total S_v will vary with rolling reduction ratio as follows:

$$S_v^{GB} = \frac{1}{D} \left(1 + \frac{1}{R} + R \right) mm^{-1} \quad (2.5)$$

The deformation bands generally look like a close-packed pair of parallel lines terminating within grains, creating a twin-like pattern in heterogeneous distribution. Figure 2.22 shows an elongated austenite structure produced by deformation in the non-recrystallisation region (Figure 2.21a) and partially transformed grain structure (Figure 2.21b). The ferrite (α) grains were nucleated in deformation bands as well as on prior austenite (γ) grain boundaries upon cooling. The ferrite α -grains were also nucleated within the austenite grains which possibly could be on precipitates or inclusion sites.

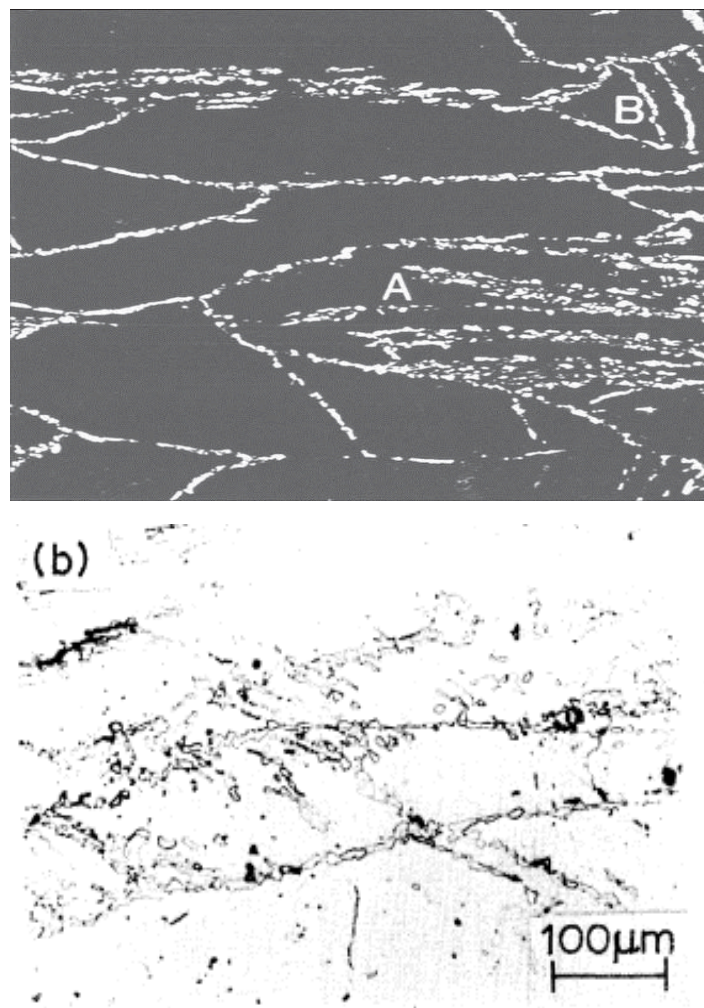


Figure 2.22 (a) Pancaked austenite grains with deformation bands after heavy deformation (b) proeutectoid ferrite formation on deformation band and grain boundaries upon cooling (adapted from ref [54])

Ouchi *et al.* [56] reviewed numerous studies on deformation bands below $T_{5\%}$ and concluded that deformation bands form only when a rolling reduction goes above 30%. He proposed that the deformation band density increases linearly with an increasing reduction and approaches a practical limit beyond 65% reduction, as shown in Figure 2.23. The change of temperature within the non-recrystallised region did not affect the band density. However, the band density decreased rapidly for deformation in recrystallisation region, generally at 1000°C and above. The deformation band and twin boundaries contribute to S_v as follows:

$$S_v^{DB} = 0.63 (\%Reduction - 30) \text{ mm}^{-1} \quad (2.6)$$

The subsequent accelerated cooling of deformed austenite nucleates low-temperature transformation products (i.e., ferrite and bainite) on the grain boundaries and inter-granular defects. A homogeneous microstructure consisting of fine polygonal ferrite plus pearlite forms if slow air cooling follows deformation. Figure 2.24 shows the typical transformation sequence in an unrecrystallised austenite on continuous cooling (0.2°C/s). The considerable transformation had taken place by 700°C, as intergranular nucleation of ferrite covered most of the prior austenite grain boundaries. At 650°C, ferrite formation was almost complete while on further cooling, and the remaining austenite transforms into the pearlite.

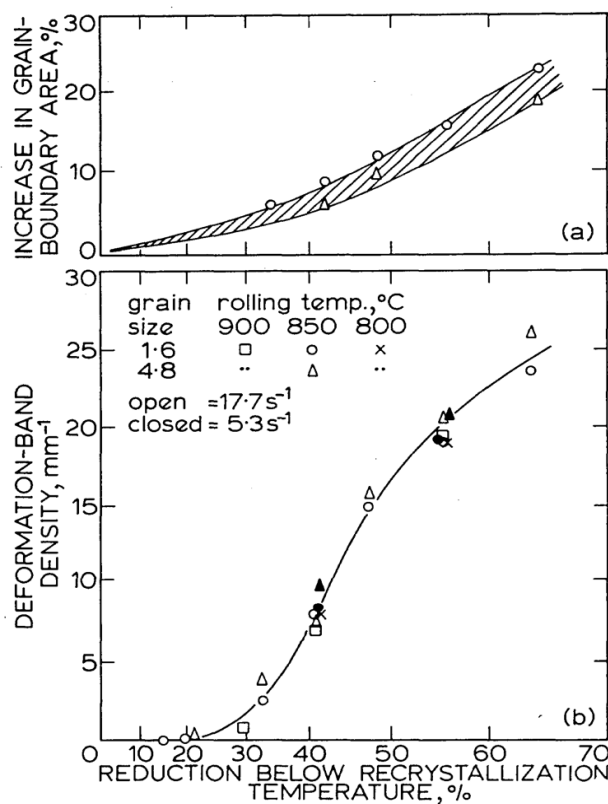


Figure 2.23 Variation in S_v with the introduction of deformation bands for 0.03%Nb steel after reduction in the non-recrystallisation region. The initial grain size was varied by rolling in two passes at higher temperatures after reheating to 1250°C (adapted from ref [48]).

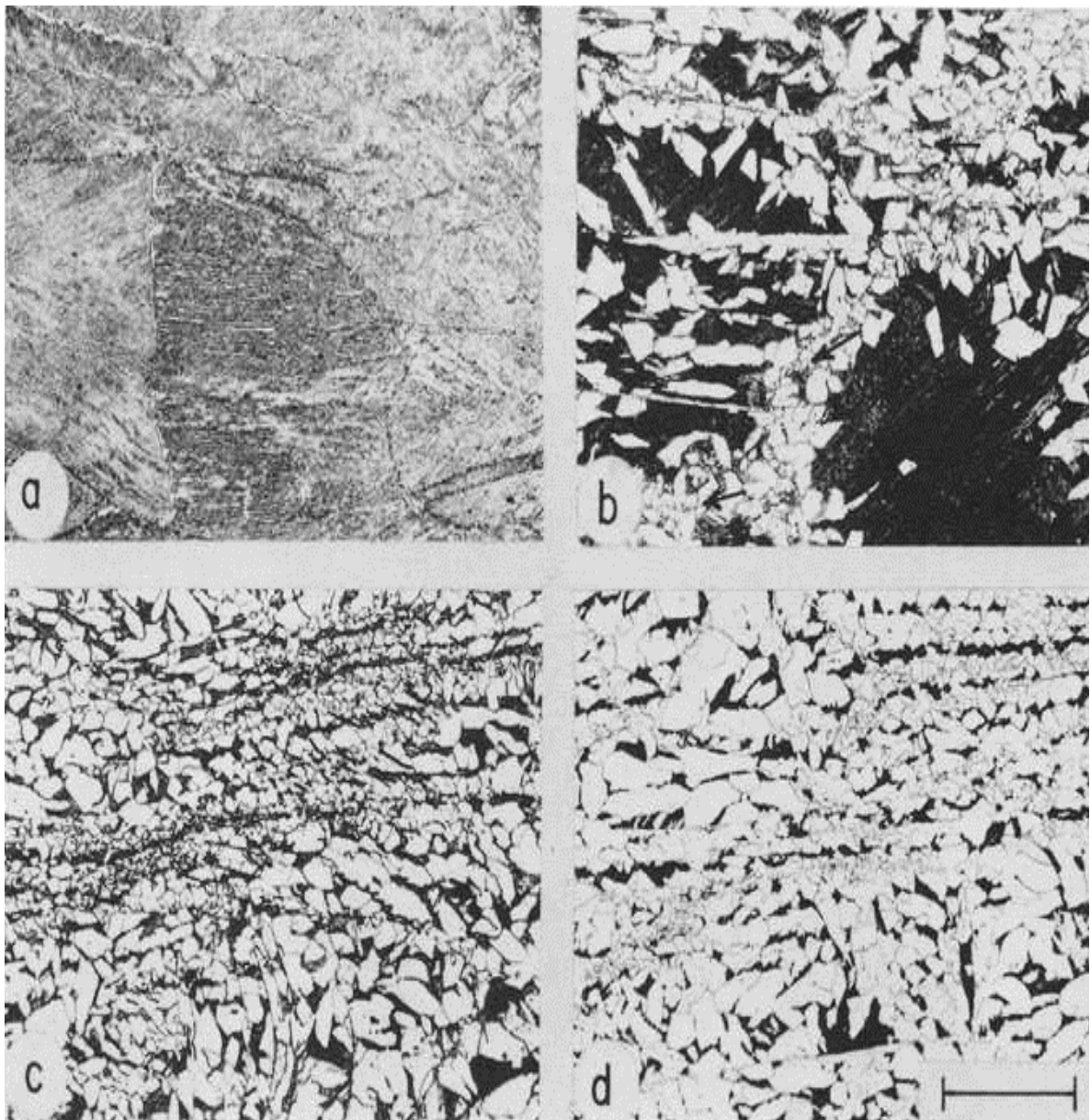


Figure 2.24 Stages of the transformation of a 0.1C-1.3Mn-0.03Nb unrecrystallised austenite on cooling at 0.2 °C/s. The samples were homogenized (1250°C for one hour), deformed 50% at 950°C and then cooled continuously, being quenched from the indicated temperatures: (a) 750°C, (h) 700°C. (c) 650°C, and (d) 550°C. Scale mark indicates 200 μm (adapted from ref [46]).

The finer ferrite grain is expected from unrecrystallised austenite than from recrystallised austenite due to the high nucleation rate of ferrite. If the austenite grain size before finish rolling is 25 μm (ASTM 8), then the rolling reduction of 80% below $T_{5\%}$ should produce severely pancaked austenite. A ferrite grain size smaller than 2 μm (ASTM 14-15) might obtain after transformation. This degree of grain refinement will give a strengthening increment of 250 MPa over a ferritic grain size obtainable from recrystallised austenite in RCR practice. Thus, the CCR plus accelerated cooling is the preferable route to achieve high yield strength and toughness in finished steel products.

2.3.4 Dynamic Recrystallisation Controlled Rolling (DRCR)

In the case of the tandem mill rolling process, e.g., bar, wire rod, and hot strip, there is insufficient time for the progress of classical static recrystallisation due to the short interpass time (15 ms). Similarly, the amount of Nb(CN) precipitation during the pass sequence is also severely limited. As a result, austenite undergoes an alternative form of recrystallisation, known as dynamic recrystallisation (DRX), which involves the nucleation and growth of new grains during the deformation [56-59]. The accumulation of appreciable strains ($\epsilon \geq 0.80$) or more is necessary to initiate dynamic recrystallisation in microstructure inherited from roughening passes.

Pussegoda *et al.* [58] simulated a seamless tube mill piercing rolling schedule in a laboratory using torsion testing for a composition 0.10C-0.03Nb-0.04V. Figure 2.25 shows the mean flow stress (MFS) values obtained during the laboratory simulation of stretch reducing mill (SRM) of the Nb-V steel. The simulation was carried out at three entry temperatures of 1000°C, 960°C and 940°C to understand the influence of precipitation on recrystallisation kinetics.

The conventional SRM schedule (open square) simulation for entry temperature of 1000°C shows that the strain was accumulated up to pass seven (like the pancaking slope) and the accumulation rate decreased with the progress of subsequent passes due to nucleation of dynamic recrystallisation. The critical strain for dynamic recrystallisation was reached well before the initiation of any strain-induced precipitation (ideal DRCR schedule).

In the case of an entry temperature of 940°C, the strain-induced precipitation was nucleated well before the critical strain for dynamic recrystallisation was attained. As a result, the pancaked austenite like controlled rolling was observed at the end of the rolling. For entry temperature of 960°C, the concurrence nucleation of precipitation and dynamic recrystallisation produced partially recrystallised microstructure. Hence, the SRM entry greater than $T_{5\%}$ was recommended for DRCR practice to avoid interaction with precipitation and partially recrystallised microstructure.

As shown in Figure 2.16, the ferrite grain size refinement depends upon austenite morphology before the transformation, a high S_v . Both RCR and CCR methods have the same objective of attaining structural refinement in the plate, strips, or forged product by achieving higher S_v values through austenite conditioning. The increase in S_v for RCR practice comes from the decrease in the average austenite grain volume while for CCR practice results from the increase in grain boundary area per unit volume from a change in grain shape and through the addition of the transgranular twins and deformation bands.

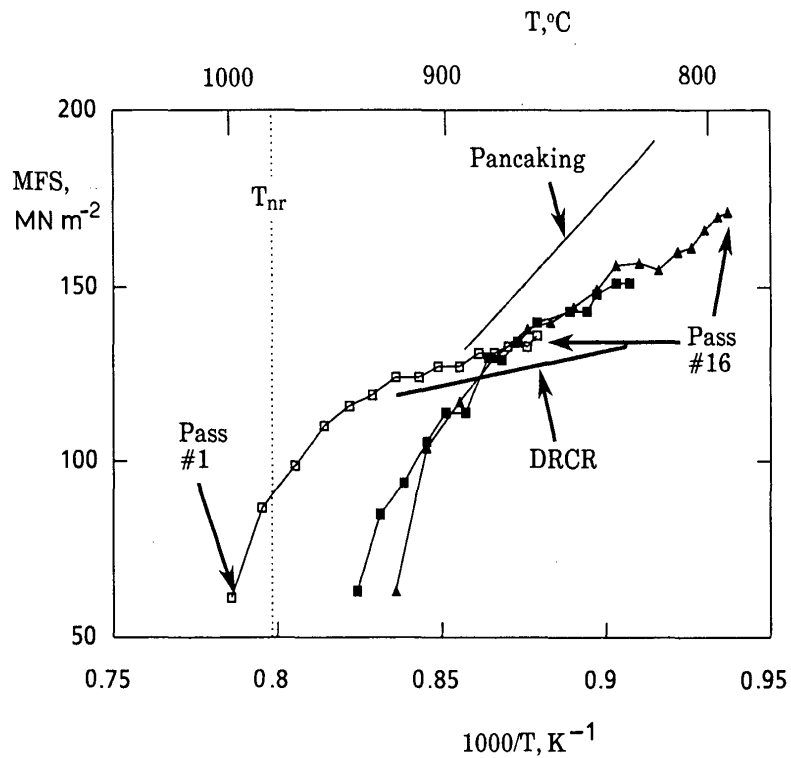


Figure 2.25 Laboratory simulation of stretch reducing mill (SRM) to achieve typical DRCR practice (adapted from ref [58])

In summary, when static recrystallisation occurs before precipitation, the conditions are appropriate to RCR rolling. Alternatively, when precipitation occurs precedes static or dynamic recrystallisation, the requirements of CCR rolling are satisfied. Finally, when dynamic recrystallisation precedes to precipitation, the process parameters are suitable for DRCR rolling. Table 2.7 compares the three types of rolling processes and sets of conditions relevant to them.

Table 2.7 Relations between recrystallisation and precipitation for three types of the rolling process

Type of process	T range with respect to T_{nr}	Role of strain-induced precipitation	Relation between strain-induced precipitation and recrystallisation
RCR	Above	Absence required	Static recrystallisation before precipitation
CCR	Below	Presence required	Precipitation before static or dynamic recrystallisation
DRCR	Below	Absence required	No static recrystallisation Dynamic recrystallisation before precipitation

2.4 Austenite Recrystallisation and Grain Growth

The austenite undergoes a significant amount of plastic deformation, i.e., work hardening during a hot working operation at the strain rate and temperature of interest. As the deformation progresses during the hot rolling, only a small fraction of the deformation energy is stored within the austenite, while the majority of the remaining energy is dissipated as the deformation heating. The stored energy of deformation is strain energy associated with various lattice defects (e.g., dislocations) and is of the order of 10-200 Jmol⁻¹ [60].

The austenite relieves the internal stresses through several competing softening (restoration) processes to undergo further plastic deformation in multiple hot rolling passes. The stored energy discussed above acts as the driving force for any restoration or softening process to occur. The competing restoration process that may occur in the austenite is the static and dynamic recovery [61] and recrystallisation [62-63]. The restoration leads to lowering down the stored energy of work-hardened austenite to energetically stable condition through a process of polygonisation or nucleation of new strain-free grains.

Several factors influence the type and kinetics of the softening process of austenite in hot rolling operation [63]. The material factors include the stacking fault energy (SFE), chemical composition, initial grain size, texture, and presence of second phase particles. The processing factors include the mode of deformation, strain, strain rate, temperature, and interpass time. The overall evolution of austenite microstructure during hot rolling depends upon the complex interactions between several of these factors.

2.4.1 Dynamic Microstructural Changes

Several authors [64-68] have described the mechanism of dynamic restoration events in metal. The following section deals only with its occurrence in the hot rolling of C-Mn steel and associated condition.

2.4.1.1 General Flow Behavior

Dynamic recovery and recrystallisation are thermally activated processes and exhibit higher softening at low strain rate ($\dot{\epsilon}$) and high temperature (T). The Zener Hollomon (Z) parameter describes the mutual effect of temperature and strain rate on softening and microstructure:

$$Z = \dot{\epsilon} \exp\left(\frac{Q_{\text{def}}}{RT_{\text{def}}}\right) \quad (2.7)$$

where Q_{def} is the activation energy for deformation (J/mol), $\dot{\epsilon}$ is the strain rate of deformation, R is the ideal gas constant (J/mol K), and T_{def} is the absolute temperature at which deformation occurs.

Figure 2.26 illustrates general hot flow behaviour and microstructure evolution of single-phase austenite during hot deformation [69]. It shows the three distinct forms of flow curve depending upon the restoration mechanism operating under the given conditions of Z .

Curve 1 (work hardening): curve 1 is characteristic of high Z condition (low T_{def} & high $\dot{\epsilon}$) representing the work hardening of austenite. The austenite grains will be highly elongated, and very little softening occurs, making further deformation more difficult. The deformed structure retains highly unstable dislocations substructures, which will be modified by static recovery and recrystallisation events after the pass.

Curve 2 and 3 are characteristic of low Z (high T_{def} & low $\dot{\epsilon}$) deformation conditions representing the dynamic softening of austenite. The flow behaviour under these conditions is described with parameters of critical strain for onset of dynamic recovery (ϵ_c^{r}) and recrystallisation (ϵ_c^{R}), respectively, and finally, strain (ϵ_p) to peak stress.

Curve 2 (DRV): The flow stress steadily increases with an increase in strain due to dislocation multiplication and vacancy formation for any strain below ϵ_c^{r} . However, when the strain exceeds ϵ_c^{r} but less than ϵ_c^{R} , the structure becomes unstable, and the rearrangement of lattice defect occurs. As dislocation density increase further, the dynamic recovery occurs through the annihilation of dislocation and formation of subgrain boundaries. In this condition, the balance between work hardening and softening process give rise to steady-state conditions.

Curve 3 (DRX): The dynamic recovery process is relatively slow in the austenite due to its low stacking fault energy and having difficulty in crossing slip. On the continuation of straining beyond ϵ_c^{r} , sufficient deformation energy is stored to nucleate dynamic recrystallisation. The new grain preferentially forms at grain boundaries, and deformation bands as soon as applied strains exceed critical strain for recrystallisation, ϵ_c^{R} . The formation of new grains consumes most of the stored energy of work-hardened austenite, and dislocation density decreases.

The additional softening produced by dynamic recrystallisation causes flow stress to pass through a maximum at ϵ_p before falling to steady-state values at ϵ_s . A mixture of elongated grains and dynamically recrystallised grain exists between the ϵ_c^{R} and steady-state, ϵ_s . In the steady-state region, deformation (which creates lattice defects) and recrystallisation process, (which removes lattice defect) reach a balanced state. The steel strained in this region exhibits fine equiaxed grains compared to the initial coarse microstructure before deformation. It is to note that the dynamic recrystallisation happens only when applied strain exceeds the corresponding critical strain ϵ_c , just below the peak strain ϵ_p [69].

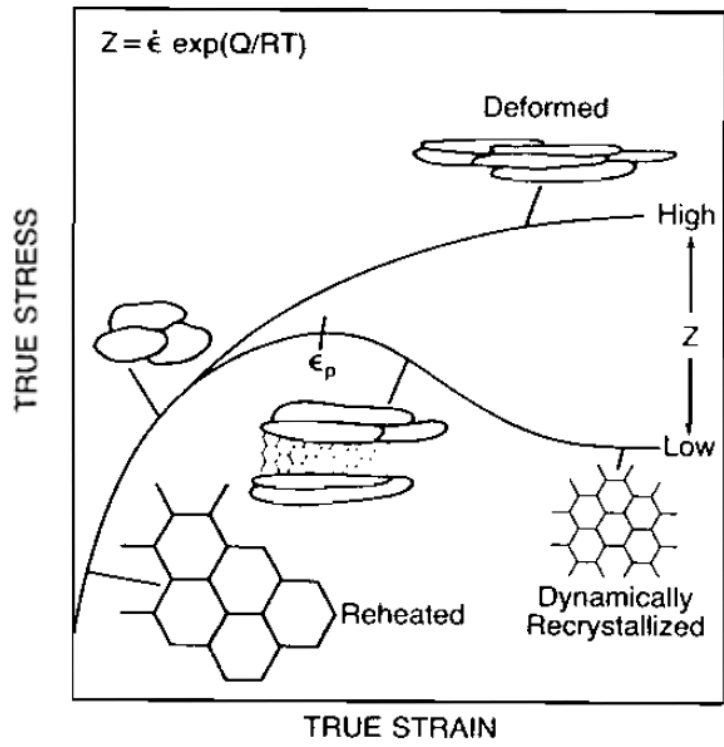
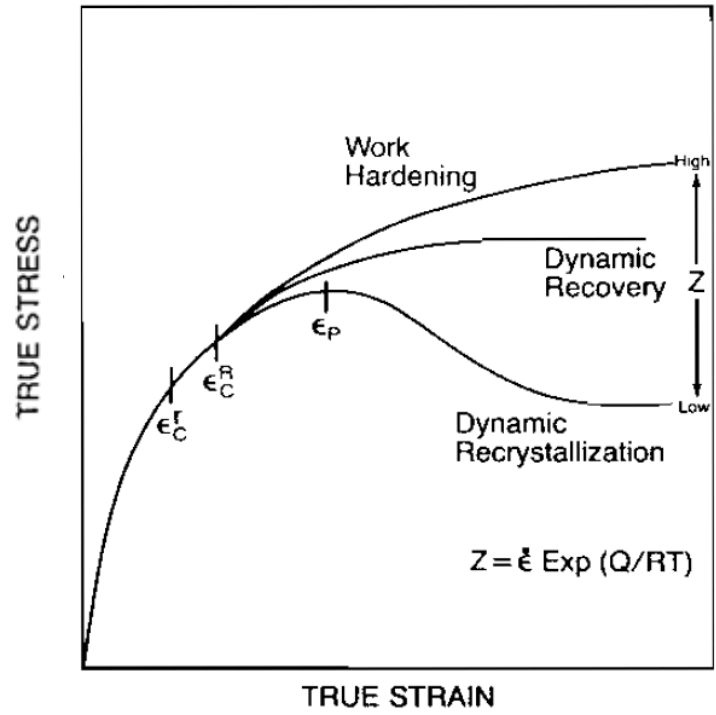


Figure 2.26 Stress-strain curve representing dynamic microstructural change (adapted from ref [69])

2.4.1.2 Relationship between ϵ_c and ϵ_p

The peak strain, ϵ_p increases with increasing initial grain size (d_0) and Zener-Hollomon parameter (Z). The analysis of experimental data on the C-Mn steels resulted in an equation of the following form for deformation at the strain rate and temperature of interest in hot working:

$$\epsilon_p = d_0^m Z^n \quad (2.8)$$

where the exponents m and n have mean values of 0.5 and 0.15 respectively for the C-Mn steels, although there are considerable variations in the individual sets of data [70-71]. Even though the form of the equation is empirical, it covers the physical principles governing the process. The grain size influence on ϵ_p is reasonable as the DRX nucleates preferentially on grain boundaries. An increase in ϵ_p reflects a need for the increased driving force for the recrystallisation to take place.

The critical strain, ϵ_c is much more challenging to measure and is usually deducted from the observation of ϵ_p . The relationship between the two strains is not simple, but a comparative analysis gives the following form:

$$\frac{\epsilon_c}{\epsilon_p} = 1 - a \left(\frac{\epsilon_x}{\epsilon_p} \right)^x \quad (2.9)$$

where ϵ_x is the strain interval for 95% dynamic recrystallisation to occur. The ϵ_x/ϵ_p ratio changes very slowly only with Z for a given material and grain size. As a result, experimental observations have suggested an approximately constant ratio of ϵ_c/ϵ_p for a given condition. However, the ratio observed vary quite widely for C-Mn steel e.g. values of 0.83 [72], 0.86 [73] and 0.67 [74]. The grain dependence of ϵ_c is expected to be smaller than that of ϵ_p because ϵ_x depends strongly on the grain size [66,75]. However, real dependence may arise from the influence of grain size on work hardening [76].

Figure 2.27 shows the dependence of ϵ_p (strain to peak flow stress) and ϵ_s (strain to the onset of steady-state) as a function of Z for low C-Mn steel. Whiteman *et al.* [77] generated this experimental data from the series of laboratory torsion tests on C-Mn steels. The plate mill rolling reduction and scales of equivalent temperatures were superimposed in the figure for comparison purposes. Both ϵ_p and ϵ_s increases with increasing Z and significantly increased by reheating to 1280°C. The increased grain size significantly affected the onset and rate of DRX.

A single rolling pass (less than 20% reduction) did not result in DRX except at high temperatures. The SRX was also very rapid at a higher temperature, which eliminated any DRX structure in between the passes, even if it occurred. At low temperatures, ϵ_p was sufficiently high for the dynamic recrystallisation; hence, the strains of more than one passes were accumulated. Therefore, it is reasonable to neglect the occurrence of dynamic recrystallisation in a section or plate rolling.

The reduction per passes are higher in strip or wire rod rolling; hence, the dynamic recrystallisation would be a primary restoration process for such conditions.

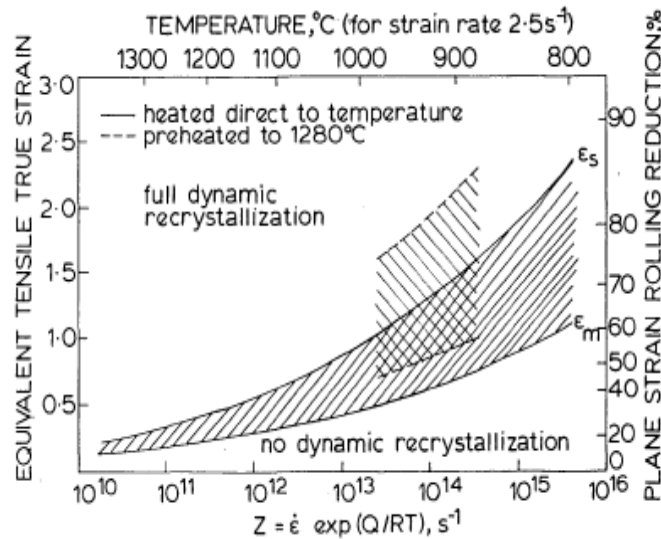


Figure 2.27 Dependence of ϵ_p (strain to peak flow stress) and ϵ_s (strain to the onset of steady-state) on strain rate and temperature for low C-Mn steel (adapted from ref [77]).

2.4.1.3 Dynamically recrystallised grain size

The dynamically recrystallised grains are much smaller than the original grains at a high strain rate typical of hot working conditions in the industry. Figure 2.28 is a schematic illustration of the progress of DRX by the process of repeated nucleation and limited growth [78]. Profuse nucleation initially occurs at the grain boundaries to give a necklace structure, Figure 2.28(b). For recrystallisation to proceed, new grains must nucleate and grow to appropriate size. This nucleation occurs preferentially at the interface between the necklace and the remaining part of the original grains, leading to a cascade of nucleation and limited growth events, Figure 2.28(c). Some nucleation and limited growth may also occur from deformation bands to generate new “cascades” of grain. The first formed necklace grains may have reached their critical strains and recrystallizes again before recrystallisation is complete in original grain, Figure 2.28 (e). The 4th stage of cascade includes new grains at the original grain boundaries

The deformation conditions determine the size of dynamically recrystallised grains. It is independent of the original grain size and is related to steady-state flow stress as below:

$$\sigma_s = \sigma_0 + k_5 d_{rex}^{-n} \quad (2.10)$$

where σ_0 is assumed to be about zero, $n = 3/4$, and k_5 is a material constant [79]. Figure 2.28 illustrates this relationship for C-Mn steel.

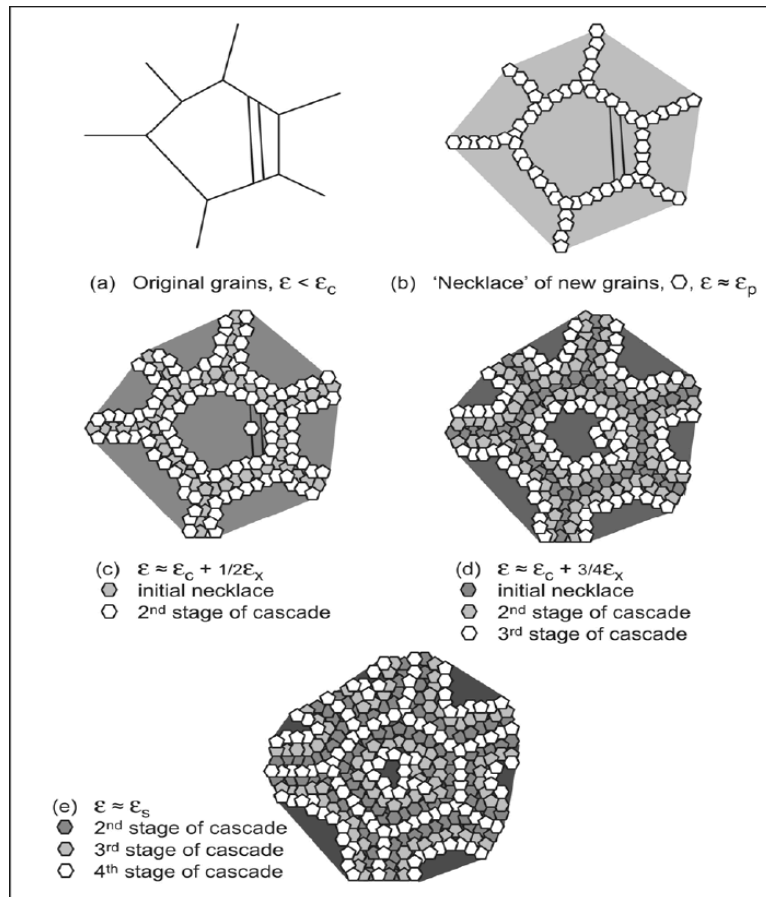


Figure 2.28 Progress of dynamic recrystallisation at high values of Z when the recrystallised grain size is much smaller than the original grain size. Shading of grains darkens with dislocation density (adapted from ref [78])

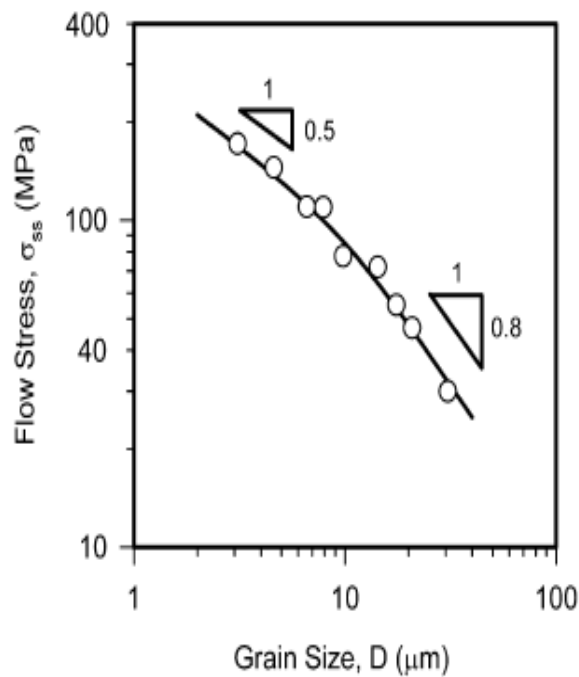


Figure 2.29 Relationship between dynamically recrystallised grain size and steady-state flow stress (adapted from ref [79])

2.4.2 Static Microstructural Changes

The hot deformation during industrial working processes (such as rolling and forging) takes place in a series of “passes” separated by an interval of time. The austenite microstructure is modified during this time interval via static recovery and recrystallisation, and grain growth at elevated temperatures.

2.4.2.1 Static Recovery

Static recovery takes place immediately after the deformation is halted and proceeds at a decreasing rate with time. The recovery process involves the annihilation of dislocation and typically causes minor fine-scale changes in the deformed austenite microstructure. The initial flow stress decreases if the material is re-deformed, but the flow stress rapidly approaches the level expected without static recovery as strain increases [80].

At low strains, the stored energy is insufficient to cause static recrystallisation, and limited softening takes place via static recovery event. The critical strain for static recrystallisation for C-Mn steel after deformation at higher strain rates appears to be 0.05-0.10 depending upon deformation conditions. Morrison [81] reported the static recrystallisation after strains of $\epsilon = 0.07$ or less over the temperature range of 900-1000°C ($Z: 2 \times 10^{11} - 2 \times 10^{14} \text{ s}^{-1}$). Therefore, static recovery will be followed by classic static recrystallisation after most pass strains of interest in plate and section rolling of low carbon steels.

2.4.2.2 Static Recrystallisation

Static recrystallisation is the dominant restoration process in hot deformed austenite. It causes significant microstructural changes, and the total softening of the material occurs in between the interpass time. During multipass deformation in an industrial rolling, the static recrystallisation is initiated first during hold time provided pass strain less than critical strain for dynamic recrystallisation. If not, the dynamic recrystallisation is initiated before static recrystallisation.

The kinetics of static recrystallisation can be quantified using the classical nucleation and growth theory of phase transformations embodied in the form of JMAK equation which relates the fraction recrystallised (X_v) to hold time (t) as follow

$$X = 1 - \exp \left[-0.693 \left(\frac{t}{t_{0.5X}} \right)^k \right] \quad (2.11)$$

which provides a satisfactory explanation of recrystallisation curves in terms of two parameters. The exponent k , typically has a value from 1 to 2, is not sensitive to deformation parameters whereas the time to 50 % recrystallisation ($t_{0.5X}$) changes by order of magnitude over the range of conditions

encountered during hot rolling. It is therefore essential to have quantitative description of $t_{0.50X}$ in terms of the process variables. From basic physical metallurgy, it is known that kinetics of recrystallisation depend upon the density of nucleation sites, the driving force for growth and the mobility of grain boundaries. However, apart from the temperature dependencies arising from thermally activated process, theory does not yet define the form of dependence on the other processing variables. Therefore, physically reasonable empirical equations have therefore been adopted to describe experimental observations. Numerous investigations [82-85] have studied the impact of deformation processing variables on recrystallisation kinetics of hot deformed austenite. The following general power law relationship has been proposed for $t_{0.50X}$:

$$t_X = A Z^{-m} d_0^n \varepsilon^{-r} \exp\left(\frac{Q_{rex}}{RT}\right) \quad (2.12)$$

where A and the exponents (m, n, r) depend upon the composition and conditions of the deformation, Z is the Zener-Hollomon parameter, d_0 is the initial grain size, ε is the strain, Q_{rex} the activation energy for recrystallisation, R is the universal gas constant and T is the deformation temperature in kelvin.

Sellars [86] proposed the equation to describe the time for the onset of static recrystallisation, $t_{0.05X}$ when the Nb is in solid solution:

$$t_{0.05X} = 6.75 \times 10^{-20} d_0^2 \varepsilon^{-4} \exp\left(\frac{300000}{RT}\right) \exp\left\{\left(\frac{275000}{T} - 185\right) [Nb]\right\} \quad (2.13)$$

where niobium content [Nb] in wt pct. This equation applies to the range of strains ($\varepsilon < 0.8 \varepsilon_p$) before the onset of dynamic recrystallisation and is compatible in a form to equation previously adopted for plain C-Mn steel [70].

This type of equation indicates that $t_{0.05X}$ values increase with increased initial grain size, and decrease with increased strain, strain rate, or temperature. The effect of grain size (d_0) on the recrystallisation kinetics arises directly from its effect on the density of nuclei, because grain boundaries provides preferential sites for nucleation. Barraclough *et al.* [80] observed the accelerated recrystallisation kinetics in fine-grained austenite over the coarse-grained structure. A dependence on ε^{-4} in equation (2.13) from the effect of strain on density of nuclei for which there is no simple physical model. The real situation is clearly more complex than this, but the above arguments serve to show that what is mean by physically reasonable empirical equations. The physical reasonableness is essential if modelling is to have predictive capability before there is complete basic theory for the mechanism involved.

In view of the empirical nature of equations (2.11) and (2.12), it is not surprising that different research groups have arrived at somewhat different formulations from analysis of different set of

data on equivalent steels [70, 87-92]. Table 2.8 presents the exponent's values reported in the literature for the estimation of $t_{0.05X} / t_{0.5X}$ in various low carbon microalloyed steels. All agree on the important effects of strain, grain size and temperature of holding. They differ somewhat in including effects of strain rate and temperature of deformation (or Zener-Hollomon parameter), which would be expected to appear in the relationship because of their effect on the dislocation density. Sellars [86] observed that Z has very small or negligible effect on $t_{0.05X} / t_{0.5X}$ in low carbon steels. The reasons for it have been discussed elsewhere. The one important difference between different formulation is in defining the strain limits over which the equations apply.

The physical significance of Q_{rex} is not completely understood for hot deformation and cannot be related to one single process. The modern recrystallisation theory indicates that the Q_{rex} doesn't remain constant throughout the recrystallisation process. It changes continuously during the recrystallisation as the driving force for recrystallisation (the stored energy) is depleted with time [61]. For simplicity, Q_{rex} is considered as an empirical constant and derived from the experimental data. According to equation (2.11), Q_{rex} was measured taking $\ln(t_{0.50X})$ as a function of $1/T$, the slope being equal to Q_{rex} / R .

Previous studies [144] have shown that activation energy (Q_{rex}) is sensitive to changes in the chemical composition. The Q_{rex} of relatively pure iron is about 280 kJ/mol, whereas that of low carbon steel is approximately 300 kJ/mole as a result of solute strengthening by Mn or Si. The Q_{rex} of HSLA steels are generally much higher (330 - 450 kJ/mol) than those of C-Mn steels because of both solute and formation of microalloying carbonitrides at temperatures between 800-1000°C [68]. However, the Q_{rex} is similar for plain C-Mn and HSLA steel at high temperature 1000-1300°C based on limited available experimental data.

The initial grain size and pass strain directly affect the recrystallised grain size along with the temperature of holding. Sellars [70] proposed the following relationship for the static recrystallised grain size:

$$d_{rex} = 0.9d_0^{0.67} \varepsilon^{-0.67} \quad (2.14)$$

It is essential to distinguish between the two independent roles that temperature plays in influencing the recrystallisation after deformation at a constant strain rate. The rate of recrystallisation decreases with decreasing the holding temperature. However, decreasing the deformation temperatures increases the stored energy at a given strain and tends to increase the recrystallisation rate. It means that recrystallisation occurs more rapidly when the temperature at which deformation occurred is well below the temperature of holding.

Table 2.8 Exponents value for estimation of $t_{0.05X}$ in Nb-microalloyed steels (reproduced from [92])

Author	Steel Chemistry			Value of Exponents and Constants					Notes
	C wt%	Nb wt%	N ppm	d_0 μm	ϵ	$\dot{\epsilon}$ s^{-1}	Q_{rex} KJ/mol	constant	
Sellars [70]	0.16	< 0.04	80	2	-4	0	325 780 130	2.52×10^{-19} 5.94×10^{-38} 9.24×10^{-9}	T > 1005°C 891<T<1005°C T<891°C
Jonas <i>et al</i> [87]	0.08	0.055		0	-3.81	-0.36		1.27×10^{-18}	T > SIP
Medina <i>et al</i> [88]	0.11 0.11	0.041 0.093	112 119	1	-1.96	-0.44	262 272	3.94×10^{-13}	T > 1030°C T > 1060°C
Karjalainen [89]	0.07	0.046	72	2	-3.3	-0.25	330	6.5×10^{-19}	T < 1000°C
Hodgson and Gibs [90]	-	< 0.03	-	2	-4+77[Nb]	0	330	$(-5.24 + 550[\text{Nb}]) \times 10^{-18}$	
Cho <i>et al</i> [91]	-	-	-	2	-2.28	-0.41	324	1.9×10^{-18}	
Fernandez <i>et al</i> [92]	0.10 0.07	0.035 0.034	53 43	1	$-5.6D^{-0.15}$	-0.53	180	9.92×10^{-11}	T > 1100°C

2.4.2.3 Driving Force for Static Recrystallisation

Static recrystallisation preferentially nucleates on preexisting grains boundaries, phase interfaces, twin boundaries, and deformation bands [93-95]. The various nucleation mechanism such as particle stimulated nucleation, nucleation due to sub-grain coarsening, and strain-induced boundary migration (SIBM) are mentioned in the literature. The model of SIBM is a widely accepted mechanism among all models for the nucleation of the static recrystallisation [96-101]. Beck and Sperry [97-99] originally put forward this model for aluminum alloys. Bailey and Hirsch [100] subsequently proposed the modification through their work on polycrystalline metals.

SIBM model is based on the principle that the driving force for recrystallisation comes from the difference in volume strain energy between the adjacent austenite subgrain [94]. The austenite grains of low dislocation density (i.e., low energy) will “bulge” into grains of high dislocation density (i.e., high energy) [97]. Figure 2.30 schematically illustrates subgrain coarsening and boundary bulging associated with recrystallisation nucleation [102].

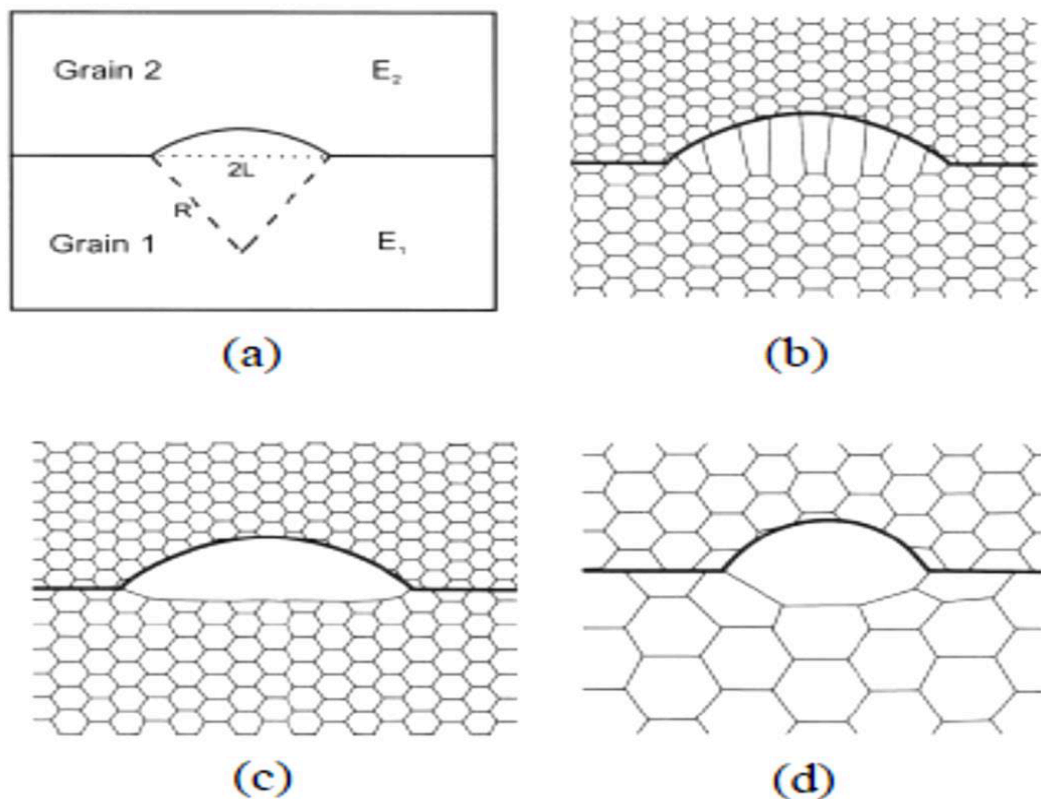


Figure 2.30 (a) SIBM of a boundary separating a grain of low stored energy (E_1) from the higher energy one (E_2), (b) dragging of the dislocation structure behind the migrating boundary, (c) the migrating boundary is free from the dislocation structure (d) SIBM originating at a single large subgrain (adapted from ref [102]).

The driving force for recrystallisation (F_{RXN}) can be expressed quantitatively [97-100] as:

$$F_{RXN} = \frac{\mu b^2 \Delta\rho}{2} \quad (2.15)$$

where μ is the shear modulus of austenite, b is the Burgers vector, and $\Delta\rho$ is a change in dislocation density associated with migration of the recrystallisation front into the deformed region. The shear modulus of austenite has been measured to be 4×10^4 MPa [40], and the average burger vector calculated to be 2.5×10^{-10} m [61].

The recrystallisation is a thermally activated process; hence equation (2.15) should certainly display temperature dependence. The dislocation density, $\Delta\rho$ term, is directly influenced by the deformation temperature. The $\Delta\rho$ becomes smaller with an increase in temperature due to the increasing number of operative slip systems [103-104]. In theory, F_{RXN} should decrease with increasing deformation temperature as a function of $\Delta\rho$ term.

The direct measurement of dislocation density in hot deformed austenite is difficult as austenite transforms into the ferrite or martensite upon cooling to room temperature. The average $\Delta\rho$ for the hot deformed austenite was measured by TEM and reported in the order of 10^{14} - 10^{16} dislocation lines/m² [105]. However, the deviation ranges of the evaluated $\Delta\rho$ are about 60% from the average values because of its temperature dependence (low and high Z conditions).

Due to this lack of reliable measurement technique, the $\Delta\rho$ is generally estimated from empirical equations by linking the flow stress in material to the $\Delta\rho$. Keh [106] proposed the following equation to relate the rise in flow stress, $\Delta\sigma$, during work hardening with the increase in the dislocation density, $\Delta\rho$, as follows:

$$\Delta\sigma = 0.2\mu b \Delta\rho^{1/2} \quad (2.16)$$

The value of $\Delta\sigma$ is obtained from subtracting the initial flow stress from the maximum flow stress reached in the σ - ϵ curve of the hot deformation pass. Cuddy [5] adopted this work and estimated the $\Delta\rho$ from the above equation as:

$$\Delta\rho = \frac{25 \Delta\sigma^2}{\mu^2 \cdot b^2} \quad (2.17)$$

It is to note that Keh's original work deals with alpha-iron, i.e., ferrite. Hence, the relationship between flow stress and dislocation density must be different for gamma-iron, i.e., austenite. To overcome this issue, Dutta *et al.* [107] have used the Taylor formula to establish the relationship between $\Delta\sigma$ and $\Delta\rho$ as follows:

$$\Delta\sigma = \bar{M} \alpha \mu b \Delta\rho^{1/2} \quad (2.18)$$

where M is the Taylor factor of the studied material, and alpha is a constant taken to be 0.15. The Taylor factor for gamma iron, i.e., austenite, is found to be 3.1 being the FCC structure. The $\Delta\rho$ is estimated from the following equation if $\Delta\sigma$ is known:

$$\Delta\rho = \frac{4.63 \Delta\sigma^2}{\mu^2 \cdot b^2} \quad (2.19)$$

Gomez *et al.* [108] investigated the static recrystallisation behaviour of Nb microalloyed steel in multi-pass torsion tests. He found considerable variations in F_{RXN} depending upon the $\Delta\rho$ estimation methods applied. Keh's equation was recommended to estimate the increase in dislocation density $\Delta\rho$, equating the flow stress $\Delta\sigma$ to the applied or maximum stress or MFS.

Table 2.9 presents the values of F_{RXN} reported in the literature for various hot deformation studies. There is a wider scatter in data even though most of them were based on experimentally measured $\Delta\sigma$ values. However, the uncertainties arising from the estimation of $\Delta\rho$ by different methods.

Table 2.9 F_{RXN} calculations made in the literature

Author	Composition	Temperature °C	Strain	F_{RXN} (MPa)	Notes
Hansen et al. [40]	0.11C-0.031Nb-0.010N	800 1200	0.35	14	Keh's Equation
Kwon et al. [42]	0.10C-0.04Nb-0.008N	900 1100	0.30 0.45	9	Keh's Equation
Palmiere et al. [154]	0.08-0.02Nb-0.008N	900 1100	0.30	22-30	Area Under Curve
Gomez et al. [108]	0.02-0.007Nb-0.006N	800 925	0.35	1.5 – 3.0	Taylor Equation
Dutta et al. [178]	0.08C-0.03Nb-0.007N	850-1050	0.10-0.40	2	Taylor Equation

2.4.3 Grain Growth

When recrystallisation is complete, further grain growth takes place at sufficiently rapid rates to reduce the grain boundary area per unit volume. There appears to be little data on grain growth of C-Mn steel during the relatively short time of interest between passes in hot rolling. The time (t) and temperature (T) dependence of grain size after complete recrystallisation can be represented as

$$d^n = d_{rex}^n + At \exp\left(\frac{-Q_{gg}}{RT}\right) \quad (2.20)$$

where A is the material constant, and Q_{gg} is the activation energy for growth. The exponent of d (n=10) in equation (2.20) very much higher than expected theoretically (n=2). Sellars [70] proposed this exponent value from the observation on several C-Mn steels and low alloy steel [109]. Figure 2.31 illustrates how an exponent, n=10 best fits the data for times up to 100 sec. The exponent value would decrease towards expected theoretical value at longer times. Furthermore, Q_{gg} may be much higher than expected for diffusion-controlled boundary migration.

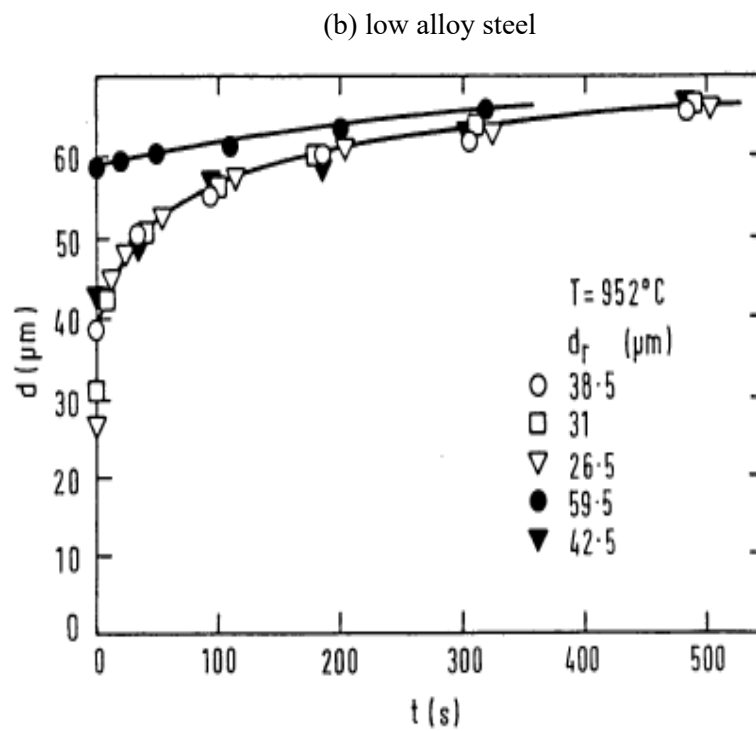
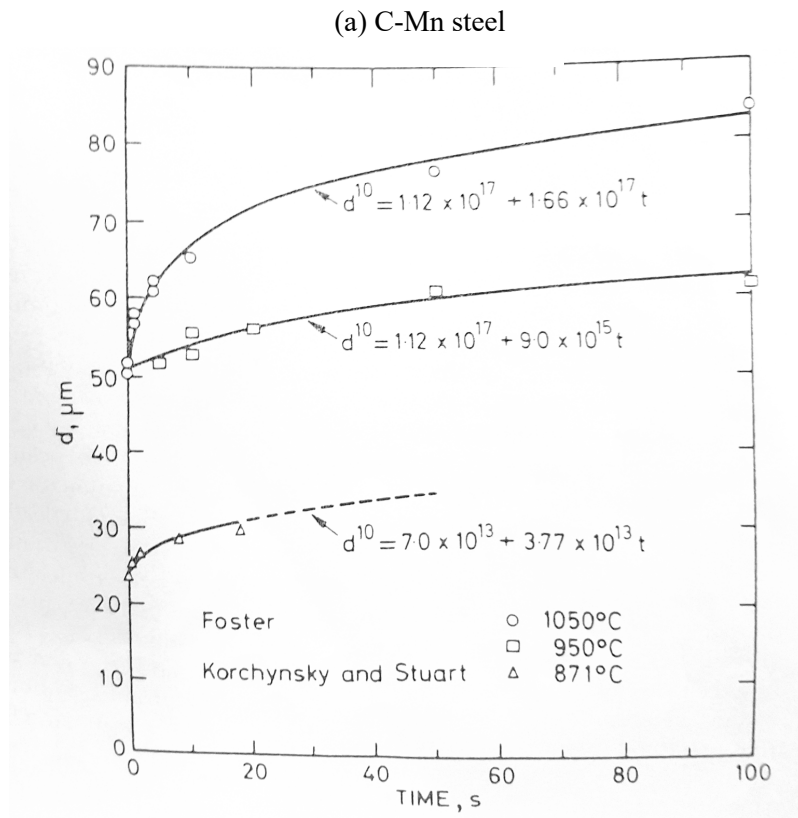


Figure 2.31. Grain growth as a function of time after complete static recrystallisation in (a) C-Mn and (b) low alloy Steels (adapted from ref [70, 109])

2.5 Fundamentals of Nb Microalloying

It is now well known that Nb microalloying plays a vital role in the restoration process of HSLA steel. The retarding effect of Nb on recovery and recrystallisation has been the subject of numerous investigations through different testing methods. It has been attributed to either solute drag effect, strain-induced precipitation of Nb(CN), or the combined effects in most of the situation. Solute drag [6-8,57] and particle pinning [40-42, 73-75] are two major retarding forces that resist microstructure restoration of austenite during hot deformation.

2.5.1 Solute Drag

Solute drag has been extensively studied for ferrous and non-ferrous alloys systems as early as 1957's. The theoretical treatment of the effect of solute atoms on grain boundary migration has been developed and extensively debated [110-114]. When a grain boundary moves, the original symmetric distribution of solute atoms on both sides of the grain boundary breaks down. The asymmetric distribution of solute atoms will then exert a dragging force attracting the boundary to redistribute the solute atoms.

The effect of solute addition on recrystallisation behaviour depends primarily on the difference in atomic size and outer shell electron between the solute and solvent atoms. Hence, it is related to the nature of solutes and their concentration in the solution. Among the microalloying element, Nb has a strong solute drag effect in retarding the austenite recrystallisation compared to V and Ti. The main reason being the atomic size of the Nb atom, which is 15 % higher compared to γ iron. This justification is a qualitative argument for a long time. The quantitative relationship between recrystallisation kinetics and solute drag is still lacking.

In the early 1980s, Akben *et al.* [115] investigated the effects of microalloying additions on recovery and recrystallisation in austenite for low carbon base composition. She had defined a solute retarding parameter (SRP) for static recrystallisation of austenite:

$$SRP = \log \left(\frac{t_x}{t_{ref}} \right) \times \frac{0.1}{at \% X} \times 100 \quad (2.21)$$

where t_x and t_{ref} are the times to initiate static recrystallisation in the steel containing the solute element X and a reference C-steel, respectively. Among the all substitutional elements, the SRP for Nb addition was high because of the solute Nb influence on the static recrystallisation. The high grain boundary dragging pressure associated with Nb addition could not be quantified. However, the equation (2.20) provided an easy and straightforward way to compare the influence of microalloying elements in solution on static recrystallisation retardation.

Suehiro [116] compared the potency of the solute drag against precipitate pinning in retarding static recrystallisation. He noticed a significant retarding effect on grain boundary velocity above a critical Nb concentration level in ultra-low carbon steel. The quantitative assessment revealed that the reduction in mobility was mainly due to the solute drag effect of Nb atoms. However, cold working and annealing work involved than the more usual hot working simulation has put the question marks over his results. The grain boundary driving forces are low in dynamic recovery, which makes the precipitation pinning more feasible and potent in retarding recrystallisation in the hot working process.

2.5.2 Nb(CN) Precipitation

The precipitation potential depends upon the two factors, the supersaturation of the microalloying element in the austenite and the kinetics of carbide formation. The supersaturation is a function of the composition of steel (mainly C and N content) and reheating temperature. The kinetics of carbide formation is strongly influenced by hot working process variables like deformation temperature, strain, strain rate, and interpass time [117]. In the following sections, the precipitation behaviour of Nb(CN) in the austenite is briefly reviewed.

2.5.2.1 Nb(CN) Solubility Products

The solubility of Nb(CN) in austenite has been studied extensively with the aid of experimental measurements as well as thermodynamic predictions. Many of the data have been analyzed in the form of solubility equations and assuming NbC is stoichiometric in composition. For simplicity, consider the dissolution of a stoichiometric compound of NbC in austenite at a given temperature. The following reaction is given:



$$\Delta G^0 = -RT \ln K = -RT \ln (a_{NbC} | a_{Nb} a_C) \quad (2.23)$$

where ΔG^0 is the standard free energy change for the formation or dissolution of NbC, K is the equilibrium reaction constant and a_{NbC} , a_{Nb} and a_C are the activities of NbC, Nb, and C in the austenite, respectively.

Two assumptions are made for the calculation of equilibrium constant (K), also referred to as the solubility product. The first assumption is that Nb is dilute solute in austenite; hence, the activities of Nb and C can be represented by their weight per cents. Second, the interaction between solutes in the system is neglected for simplicity.

The ΔG^0 is given by $\Delta H^0 - T\Delta S^0$ where ΔH^0 and ΔS^0 are the standard enthalpy and entropy changes, respectively, for the formation of the NbC. Assuming ΔG^0 is linearly related to the temperature, the equation (2.23) can be rewritten for calculation of equilibrium constant (K)

$$\log[\%Nb][\%C] = \frac{\Delta S^0}{2.303R_g} - \frac{\Delta H^0}{2.303R_g T} \quad (2.24)$$

The solubility product can be simplified and represented as following

$$\log[\%Nb][\%C] = A - \frac{B}{T} \quad (2.25)$$

where $[\%Nb]$ and $[\%C]$ is the weight percent of Nb and C dissolved in austenite respectively, T is reheating temperature in Kelvin, A and B are approximate constants related to the enthalpy and entropy of carbide formation respectively.

The solubility product changes significantly depending upon the composition of Nb(CN). Figure 2.32 depicts the solubility product (k_s) for various Nb precipitates in austenite versus the temperature [118]. The solubility product NbCN precipitate decrease as the compound is enriched with nitrogen approaching towards pure NbN compound. It means high N precipitate will be more thermally stable and difficult to dissolve. Second, the solubility of the precipitating compound decreases as the temperature decreases. The vacancy content becomes smaller which restricts the solubility in austenite.

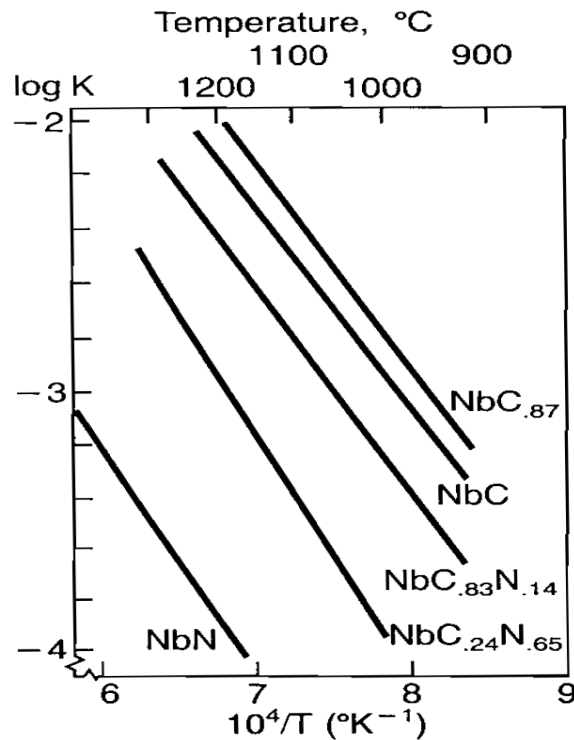


Figure 2.32 Solubility Product of various Nb precipitates in austenite (adapted from ref [118])

Table 2.10 lists the solubility equations proposed and expressed in terms of A and B values from various investigations up to the 1980s on NbC, NbN, and Nb(CN) precipitation system [118-130]. The agreement among the reported solubility products to be weak, and the method of interpretations also vary. These discrepancies are attributed mainly to the different experimental techniques, inaccuracy of the thermodynamic data and assumption made in deriving the relationship. The details comparison between solubility products is reviewed elsewhere [8, 130-131].

Figure 2.33 shows the comparison between solubility products for stoichiometric NbC and NbC_xN_y precipitates as a function of deformation temperature. The composition used for analysis is 0.20C-1.0Mn-0.021Nb-0.0070N. The solubility of Nb in austenite substantially decreases as the temperature decreases.

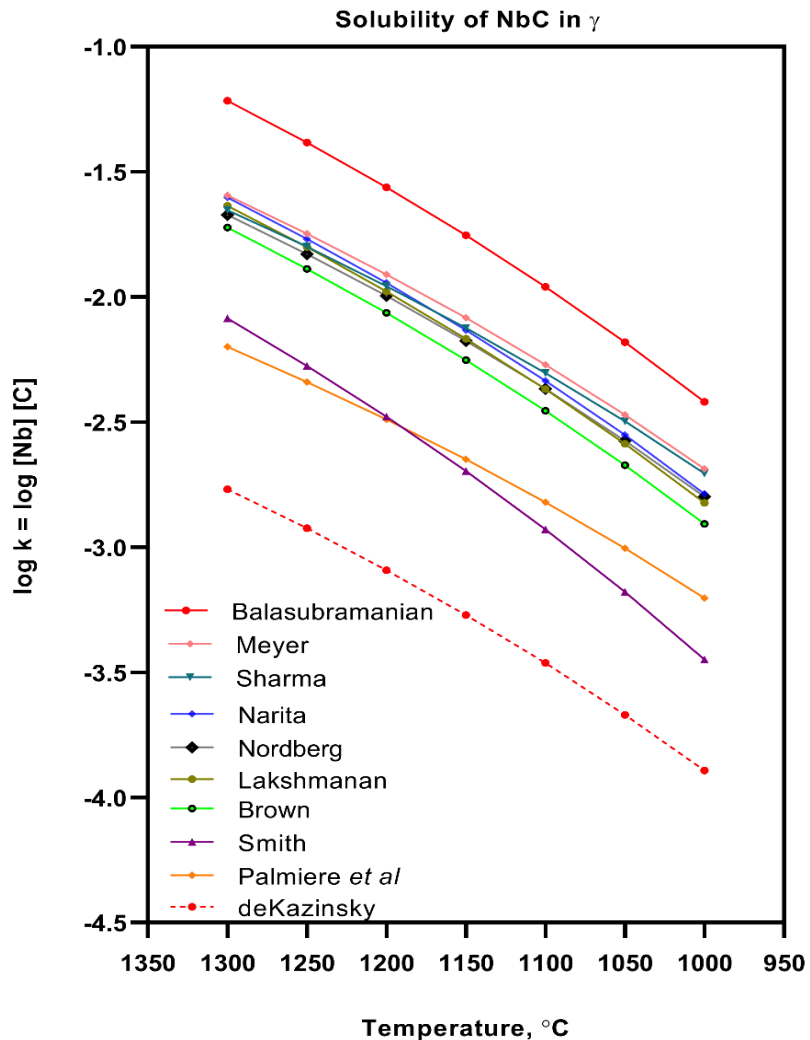


Figure 2.33 Solubility product of NbC as a function of deformation temperature

Table 2.10 Solubility Products for Nb-C, Nb-N and Nb-C-N Systems in austenite

Product	Method	Reference
<u>NbC System</u>		
$\text{Log [Nb][C]} = 2.90 - 7500/T$	D	[118]
$\text{Log [Nb][C]} = 3.04 - 7290/T$	B	[118]
$\text{Log [Nb][C]} = 3.70 - 9100/T$	C	[119]
$\text{Log [Nb][C]} = 3.42 - 7900/T$	B	[120]
$\text{Log [Nb][C]} = 4.37 - 9290/T$	C	[121]
$\text{Log [Nb][C]}^{0.87} = 3.18 - 7700/T$	B	[122]
$\text{Log [Nb][C]}^{0.87} = 3.11 - 7520/T$	E	[118]
$\text{Log [Nb][C]} = 2.96 - 5100/T$	E	[118]
$\text{Log [Nb][C]}^{0.87} = 3.40 - 7200/T$	A	[118]
$\text{Log [Nb][C]}^{0.87} = 2.81 - 7019.5/T$	A	[123]
$\text{Log [Nb][C]} = 3.89 - 8030/T$	-	[124]
$\text{Log [Nb][C]} = 2.06 - 6700/T$	-	[130]
<u>NbN System</u>		
$\text{Log [Nb][N]} = 4.04 - 10230/T$	C	[125]
$\text{Log [Nb][N]} = 3.79 - 10150/T$	B	[122]
$\text{Log [Nb][N]} = 2.80 - 8500/T$	B	[120]
$\text{Log [Nb][N]} = 3.70 - 10800/T$	B	[128]
$\text{Log [Nb][N]}^{0.87} = 2.86 - 7927/T$	A	[123]
$\text{Log [Nb][N]} = 4.2 - 10000/T$	-	[124]
<u>NbCN System</u>		
$\text{Log [Nb][C]}^{0.24}[\text{N}]^{0.65} = 4.09 - 10500/T$	B	[118]
$\text{Log [Nb][C+12/14N]} = 3.97 - 8800/T$	C	[126]
$\text{Log [Nb][C+N]} = 1.54 - 5860/T$	B	[118]
$\text{Log [Nb][C]}^{0.83}[\text{N}]^{0.14} = 4.46 - 9800/T$	B	[118]
$\text{Log [Nb][C+12/14N]} = 2.26 - 6770/T$	C	[127]

A: thermodynamic calculation; B: chemical separation and isolation of precipitate; C: carbon content analysis on Nb steels equilibrated with H₂-CH₄ atmosphere at different temperatures; D: hardness measurements; E: statistical treatment of previous solubility products.

Meyer [129] and Mori *et al.* [122] have shown that the Nb(CN) precipitation is favorable at a C/N ≤ 5 over NbC precipitation. Irvine *et al.* [127] proposed that we can use (C+12/14N) to determine the solubility of Nb(CN) in a steel composition having C/N ≥ 10 . Irvine *et al.* [127] solubility equation is most commonly used in the industry for the Nb(CN) precipitation system. This solubility product was experimentally determined from chemical separation and isolation of precipitates in a laboratory cast steel (0.16C-1.0Mn):

$$\log[\%Nb] \left[\%C + \frac{12}{14} \%N \right] = 2.26 - \frac{6770}{T} \quad (2.26)$$

Palmiere *et al.* [130] proposed a solubility product for NbC precipitating systems from experimental data measured using an atom probe tomography (APT) technique. The steel (0.08C-1.5Mn-0.025Nb-0.008N) specimens were reheated to different temperature and quenched to quantify the amount of Nb in solution as a function of temperature. The solubility equation is given as:

$$\log[\%Nb] [\%C] = 2.06 - \frac{6700}{T} \quad (2.27)$$

Palmiere *et al.* [130] solubility product proposed the higher thermal stability of precipitates as a consequence the higher dissolution temperature is recommended compared to most of the earlier solubility equation. This solubility equation is now most commonly used for determining the dissolution temperature of NbC precipitates as well as the equilibrium amount of Nb in austenite at any reheating temperature, given the quantities of the other elements in the precipitating system are known, as an example:

$$[\%Nb]_{eqm} = \frac{10^{2.26 - \frac{6770}{T}}}{\left[\%C + \frac{12}{14} \%N \right]} \quad (2.28)$$

Solubility product can also be used, conversely, to calculate the excess of soluble Nb more than what is thermodynamically possible at equilibrium. This is expressed as the supersaturation ratio, k_s as given below:

$$k_s = \frac{[\%Nb] \left[\%C + \frac{12}{14} \%N \right]}{2.26 - \frac{6770}{T}} \quad (2.29)$$

The higher supersaturation ratios should inevitably lead to higher precipitation potential for any Nb-microalloyed steels. However, the ratio of the wt.% Nb and C content is also a critical deciding factor. The precipitation potential is the highest for the stoichiometric ratio of 7.8 [132]. As shown in Figure 2.34, the precipitation potential continually decreases as the deviation from the stoichiometry ratio (hyper or hypo) occurs during cooling.

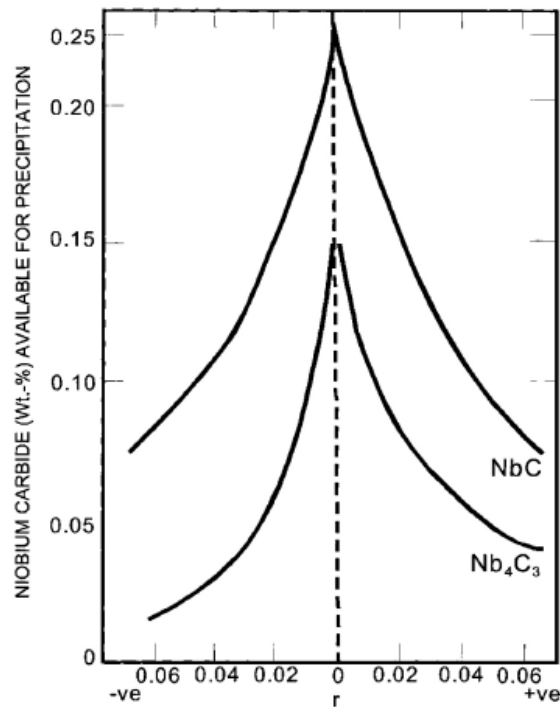


Figure 2.34 Amount of niobium carbide available for precipitation at 650°C as a function of the degree of deviation from stoichiometry r : positive values of r indicate C rich compositions while negative values indicate Nb rich (adapted from ref [132]).

The above study was focused on NbC precipitation in ferrite during or after phase transformation. The strain-induced precipitation of Nb(CN) in austenite during hot working mainly depends upon deformation processing variables along with supersaturation. The next section highlights the relationship between processing variables and precipitation kinetics.

2.5.2.2 Kinetics of strain-induced precipitation

A large number of researchers have studied the precipitation kinetics of the Nb microalloying element and their effect on the austenite microstructure [40-42, 73-75, 87-92]. The findings from these studies have been debated over discrepancies and common ground in results. These studies had a number of processing variables such as deformation temperature, strain, strain rate, initial grain size, and type of deformation along with material factor-like alloy design. It is difficult to make a direct comparison of all the experimental results as these studies also employed a variety of techniques for the detection of precipitate size and volume fraction (e.g., chemical analysis, flow curves, dilatometry, hardness testing, and quantitative electron microscopy).

The result of these studies conclusively shows that the strain-induced precipitation behaviour appears to follow the C-curve kinetics with the nose of the curve located between 900-950°C [40, 74, 86]. Also, the kinetics of precipitation, i.e., precipitation times in this temperature ranges varies depending upon the amount of prior deformation [40-42]. The effect of time and temperature on

the precipitation kinetics is traditionally shown in the form of precipitation-time-temperature (PTT) plots. Such plot generally shows a precipitation start time (P_s) where, typically, 5% of the available precipitation has occurred ($P_{0.05}$), and often show a precipitation finish time (P_f) where 95% of the precipitation event is complete [40, 86]. Table 2.11 shows the experimentally measured $P_{0.05}$ reported in the literature for Nb-microalloyed steels [133-145].

Dutta and Sellars [86] proposed the Nb(CN) precipitation model based on the thermodynamics of the system and diffusing controlled nucleation theory for isothermal deformation. The model derives the precipitate-time-temperature relationship as a function of strain for a given Nb composition. The time for 5% precipitation ($t_{0.05P}$) is calculated using the following equation:

$$t_{0.05P} = A [Nb]^{-1} \varepsilon^{-1} Z^{-0.5} \exp\left(\frac{270000}{RT}\right) \exp\left(\frac{B}{T^3 (\ln k_s)^2}\right) \quad (2.30)$$

where [Nb] is the amount of Nb in solution in austenite in wt. %, ε is the strain, Z is the Zener-Hollomon parameter, R is universal gas constant, T is the deformation temperature in Kelvin and k_s represents the Nb supersaturation ratio at temperature T . The constant A (3×10^{-6}) and B (2.5×10^{10}) were calculated to fit the published experimental data of Nb bearing steels with proposed equation. The derived model is simple and shows good agreement with many of the experimental data. Many other research groups developed a similar form of empirical relationship following Dutta's work [86] and suggested similar precipitation start time relations.

Dutta *et al.* [146] re-examined the earlier precipitation work and proposed that precipitate coarsening starts simultaneously with nucleation due to pipe diffusion on dislocation cores. Building on earlier work, Dutta *et al.* (107) analyzed the earlier work and put forward a comprehensive model of strain-induced precipitation kinetics in Nb microalloyed steels. The precipitate radius and number density evaluation as a function of time was determined based on the thermodynamic model complemented by experimental data. The model assumed heterogeneous precipitation upon dislocation nodes with enhanced coarsening via pipe diffusion.

Figure 2.35 shows one example of C-curve precipitation kinetics in austenite with and without prestrain applied for Nb-microalloyed steels. The precipitation kinetics are slow at high temperature, due to low Nb the supersaturation. At intermediate temperatures, the plot shows a nose, where the fastest precipitation occurs hence sometimes referred to as C-curve for nucleation. The kinetics becomes slow again at low temperatures because of slow diffusion rates. The rate of strain-induced precipitation which occurs after the deformation was much faster than the precipitation without deformation. Early work has shown that dislocation structure in deformed austenite provides the preferential nucleation sites for Nb(CN) precipitation and in turn, accelerates the overall precipitation kinetics [86].

Table 2.11 Experimentally measured precipitation starts times (P_s) from the literature

Author	Steel Chemistry			Deformation conditions			Nose Temp °C	Ps / $t_{0.05P}$ sec	Detection Method	Ref
	C wt %	Nb wt %	N ppm	d_0 µm	ϵ	$\dot{\epsilon}$ s ⁻¹				
LeBon et al. (1975)	0.17	0.04	90	900	0.75	0.25	950	10	Microhardness testing	74
Davenport et al. (1977)	0.080	0.09	200	870 1200	0.22 0.92	-	870	Within 4 sec	Chemical extraction / XRD peak broadening/thin foil TEM	133
Watanabe et al. (1977)	0.063	0.084	58	980	0.36	-	925	10	Electrolytic extraction	134
Hoogendorn et al (1977)	0.10	0.040	90	-	0.80	-	?	?	Electrolytic extraction	135
Simoneau et al. (1978)	0.07 0.19	0.040 0.058	103 72	?	-	-	900 900	2000 700	Electrical Resistivity	136
Ouchi et al. (1977)	0.16	0.031	54	-	0.69	-	880	10	Hardness Drop	137
Hansen et al. (1980)	0.10	0.095	100	900 950	0.70	2.6	950 950	2-3 10	TEM Extraction Replica	41
Janampa (1982)	0.081	0.12	141	800 1000	0.29	4.2	1000 900 850	0.2 0.2 0.7	Electrolytic extraction and TEM	138
Yamamoto et al. (1982)	0.02	0.095	28		0.69	10	950	10	TEM Extraction Replica	139
Fitzsimmons et al. (1984)	0.08	0.07	200	800 925	0.60 0.90	2	850	0.4	Thin Foil TEM	140
Park et al. (1992)	0.067	0.04	60	900	0.05	0.10	900	12	Dilatometer	141
Herman et al. (1992)	0.10	0.08	33	900	0.44	0.10	900	10	-	142
Silveira & Barbosa (1993)	0.026	0.11	10	850 1050	0.10	0.10	950	20	Stress Relaxation	143
Medina & Quispe (1996)	0.10	0.093	119	1000	0.35	3.63	1000	25	Mechanical Testing	144
Kang et al. (1997)	0.076	0.03	61	900	0.30	10	950	3	Mechanical Testing	145

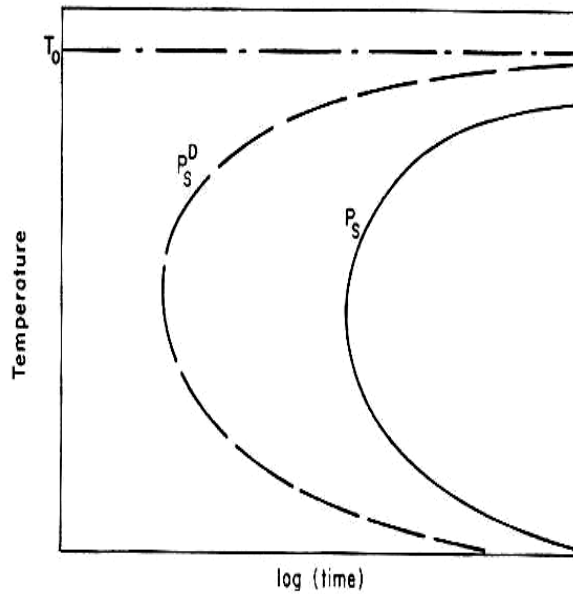


Figure 2.35 Typical precipitation-time-temperature (PTT) curves showing precipitation kinetics in a microalloyed steel as a function of deformation. Precipitation start times with (P_s^D) and in the absence of (P_s) deformation are marked. (adapted from ref [41]).

Most of the research work on precipitation kinetics is based on deformation under isothermal conditions. Some researchers [141, 145-146] have considered precipitation during continuous cooling, which is generally observed in industrial rolling. Park *et al.* [141] found that precipitation kinetics are slower during continuous cooling testing compared to isothermal deformation. Sun *et al.* [147] studied the particle size and number density as a function of interpass time during continuous cooling via hot torsion experiments. Figure 2.36 shows the evaluation of mean particle size and density with interpass time for a multipass rolling.

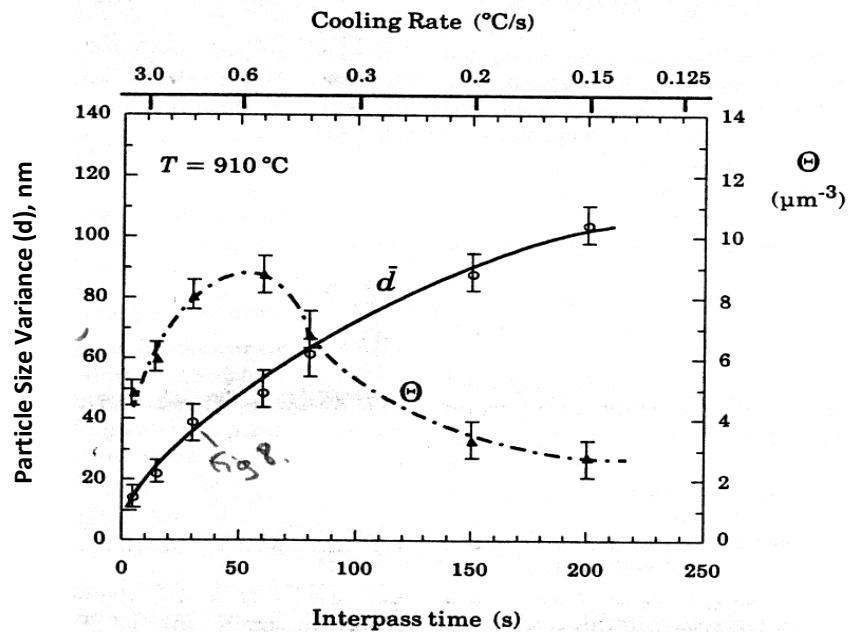


Figure 2.36 Particle size variance (d) and precipitate density (Θ) as a function of isothermal hold time during a rolling simulation under continuous cooling conditions (adapted from ref [147]).

2.5.3 Nb(CN) Pinning Force Models

The particle pinning has been subjected to more quantitative treatment compared to precipitation kinetics. It is now well known that the strain-induced precipitation of fine Nb(CN) on austenite grain and subgrain boundaries retards the recrystallisation of austenite during hot deformation within a specific temperature window.

Zener [149] was the first to treat the retarding effect of second phase particles on migrating grain boundary. He indicated that the effective energy of grain boundary would be lowered when the particles are present in the vicinity of the grain boundary. The movement of grain boundary away from particles will require work as an effective grain boundary area is increased [150]. Gladman [151] subsequently modified the original theory of Zener and quantified the pinning forces, f_p , for each particle assuming a rigid motion of the grain boundaries through an array of particles. He gave the pinning force, f_p , required to separate the boundary from particles as

$$f_p = 4r\gamma \quad (2.31)$$

where r is the radius of the particle, and γ is the interfacial energy per unit area of the grain boundary. Gladman had derived the expression for the critical particle size, r_c , below which the grain boundary is pinned as

$$r_c = \frac{6R_0 f_v}{\pi} \left(\frac{3}{2} - \frac{2}{z} \right)^{-1} \quad (2.32)$$

where R_0 is the mean radius of matrix grain, f_v is the volume fraction of second phase particles, and z is the ratio the radii of growing grain to matrix grains. The relationship in equation (2.31) was obtained by equating the rates of the grain boundary energy increase and the pinning force during the grain growth.

Equation (2.30) can be expanded to calculate total pinning force, F_{PIN} , exerted on the grain boundary for a number of particles per unit area, N_s . The total F_{PIN} is expressed as

$$F_{PIN} = f_p N_s = 4r\gamma N_s \quad (2.33)$$

Three different models have been postulated in explain how microalloying precipitate influence the retardation of recrystallisation in austenite. All of these models are based on the general form of equation (2.33) but differ in the manner how N_s is calculated.

The first of these models was an extension of Gladman's [151] work on the particle pinning. This model is often referred to as a rigid boundary model (RBM) because it assumes the motion of a rigid grain boundary that interacts with particle lying within $\pm r$ of the boundary plane [149-151]. Under this set of conditions, the N_s is defined as

$$N_s = 2rN_v \quad (2.34)$$

where N_v is the number of particles per unit volume. For spherical particles having a radius, r , and volume fraction, f_v , the N_v can be expressed as follow

$$N_v = \frac{3f_v}{4\pi r^3} \quad (2.35)$$

Combining the equation (2.34) and (2.35) yields

$$N_s^R = \frac{3f_v}{2\pi r^2} \quad (2.36)$$

Cuddy [5,152] proposed a second model, which was at the opposite extreme of the rigid boundary model. This model was termed as a flexible boundary model (FBM). It assumed that an infinite flexible boundary was capable of interacting with every particle in a three-dimensional array until the grain boundary is fully pinned. This led to the following relationship

$$N_s = r f_v^{-\frac{1}{3}} N_v \quad (2.37)$$

Combining the equation (2.36) and (2.34) yields

$$N_s^F = \frac{3f_v^{\frac{2}{3}}}{4\pi r^2} \quad (2.38)$$

The more realistic model for hot worked austenite structure is the subgrain boundary model (SBM). The electron microscopy investigations have shown that Nb(CN) nucleates in localised manner, preferentially on grain boundaries and subgrain boundaries. Hutchinson and Duggan (1978) suggested a model for subgrain boundary pinning by particles that lie inhomogeneously on boundaries. Hansen *et al.* [40] adopted this model for microalloyed steels considering profuse nucleation of precipitates on subgrain boundary in his investigation. Assuming the average intercept distance between the subgrain is l , the surface area per unit volume for such subgrain boundaries would be $2/l$ which will give N_s as

$$N_s = \frac{lN_v}{2} \quad (2.39)$$

As before, combining equation (2.35) and (2.39) gives

$$N_s^S = \frac{3f_v l}{4\pi r^3} \quad (2.40)$$

Substitution of the expression for N_s^R , N_s^F and N_s^S into equation (2.33) gives the respective total pinning force, F_{PIN} , for each model.

$$F_{PIN}^R = \frac{6\sigma f_v}{\pi r} \quad (2.41)$$

$$F_{PIN}^F = \frac{3\sigma f_v^{\frac{2}{3}}}{\pi r} \quad (2.42)$$

$$F_{PIN}^S = \frac{3\sigma f_v l}{2\pi r^2} \quad (2.43)$$

2.6 Hot Deformation of Microalloyed Austenite

It has been long recognized that the recovery and recrystallisation of austenite are significantly retarded by the addition of microalloying elements such as Nb, V, and Ti. The retardation of recrystallisation is primarily attributed to the formation of SIP during hot working. A large number of researchers have studied recrystallisation kinetics of low carbon microalloyed steels and their subsequent effect on the microstructure using different deformation techniques. It is tough to make a comparison between these data since the deformation schedule, equipment, and evaluation procedure all influence the derived recrystallisation kinetics.

2.6.1 Recrystallisation Stop Temperature ($T_{RXN} / T_{5\%}$)

In the early 1980s, a series of investigations were performed in low carbon microalloyed steels to understand the influence of microalloying element on the $T_{RXN} / T_{5\%}$ of austenite. The steels were subjected to plane strain rolling deformation at various temperatures. The T_{RXN} was determined using the optical metallography technique at each deformation temperatures. Figure 2.37 shows result from one of those studies which relate the T_{RXN} to the initial solute content of microalloying elements (Nb, Ti, Al, and V) in austenite. The initial levels were predicted using the published solubility equations for Nb(CN), TiN, AlN, and VN systems at various reheating temperatures. Any precipitation of upon cooling to the respective deformation temperature was neglected.

Figure 2.37 shows two essential features of microalloying additions concerning the recrystallisation retardation. The first is that the T_{RXN} was increased with a corresponding increase in the amount of microalloying additions. Assuming identical reheating and deformation temperatures, an increase in microalloying addition will give rise to more stable precipitating species. A higher solute supersaturation and consequent large driving force for precipitation translated into a higher volume fraction of the second phase particle. These precipitates then retard austenite recrystallisation, which in turn yields a higher T_{RXN} .

The second exciting feature has the most industrial significance and concerned with the effectiveness of each microalloying element in increasing the T_{RXN} . For any given solute level, Nb has the highest effect in increasing the T_{RXN} of investigated steel under the given deformation condition. Cuddy *et al.* [5] assigned a constant parameter for each microalloying element based on the power-law fit of the data. This parameter was interpreted as the measure of each solute's ability to increase the T_{RXN} . Niobium displayed the highest value (1340), followed by Ti (400).

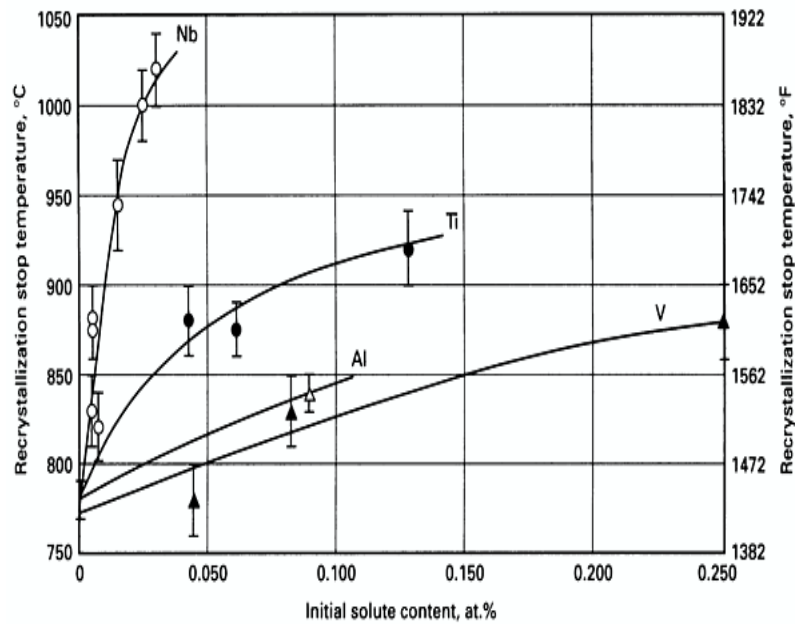


Figure 2.37 The increase in recrystallisation stop temperature with an increase in the level of microalloying solutes in 0.07% C-1.4% Mn-0.25% Si steel and deformation per pass 10-15% (adapted from ref [5])

DeArdo [35] further explained why the one microalloying element is effective than another in controlling the T_{RXN} in reference to the Cuddy diagram. Figure 2.38 shows the supersaturation as a percent of the total microalloying element (measured using the solubility relations) against the deformation temperature. The four different precipitating systems are highlighted with representative composition used in commercial alloys. The range of deformation temperature, T_ϵ used in rolling and forging operation is superimposed in Figure 2.38.

The intersection of each curve with 0% supersaturation corresponds to the dissolution temperature of that precipitate system. The Ti-N system exhibit higher supersaturation at a temperature greater than the T_ϵ while the V-based system exhibit high supersaturation at a temperature lower than T_ϵ . Of all the precipitating systems, Nb exhibits high supersaturation over a large portion of the typical hot rolling temperature range in industrial practice.

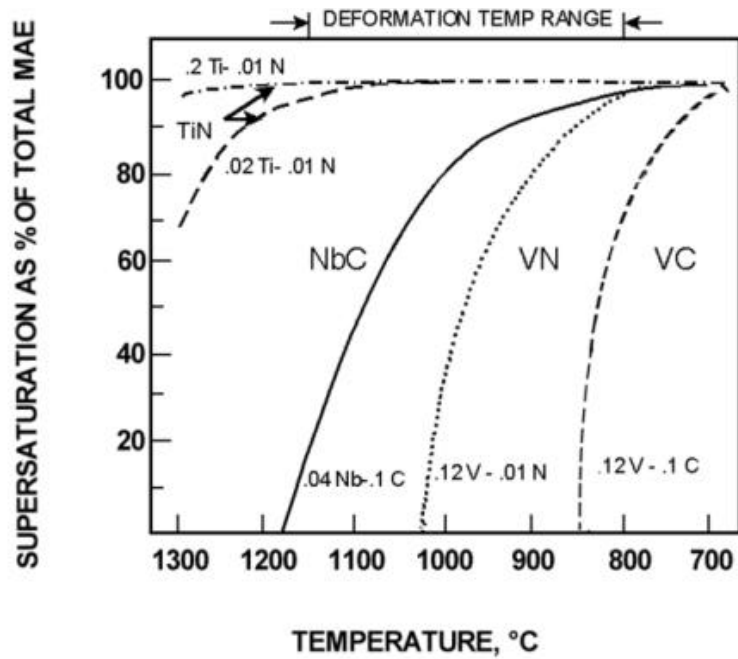


Figure 2.38 Precipitation potential of four commonly used microalloying systems (adapted from ref [35])

Yomamoto *et al.* [139] also investigated the effect of microalloying elements on recovery and recrystallisation of deformed austenite through torsion deformation. He ranked the microalloying element in the following descending order $Nb > Ti > Mo > V > Mn > Cr > Ni$ based on solute drag and precipitation efficiency. Figure 2.39 shows the comparison of the solute retarding effect of three microalloying elements (Nb, Ti, and V) in 0.002C steels. The V has the weakest retarding effect, with Ti intermediate, and Nb has the strongest. The behaviour exhibited in Figure 2.39 is in good correspondence with the work of the Cuddy diagram.

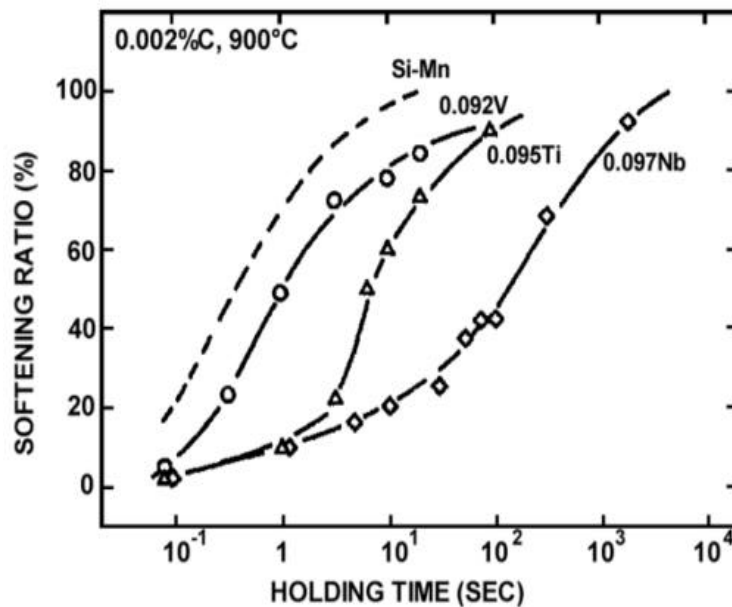


Figure 2.39 The comparison of Nb, V, and Ti effect on the softening behaviour in 0.002C steels (adapted from ref [139])

The implication of this is that Ti can be used for control of grain growth at high temperature, T_{GC} during reheating. The Nb-system can be used for intermediate temperature operation (T_{RXN}) during hot rolling. A large portion of V can be held in austenite solution for eventual precipitation hardening in the low-temperature transformation product.

Yomamoto *et al.* [139] suggested that the retarding effect of Nb / Ti / V is stronger on the progress of recrystallisation via precipitate interaction. The Nb microalloying element delayed the onset of recrystallisation when it was in solution, but the magnitude was much smaller compared to precipitation. Figure 2.40 presents a comparison of the relative retarding effects of Nb as a solute and as a precipitate. The Nb in the steel with 0.002%C was in solution, whereas the Nb in the steel with 0.019C was present as a precipitate. The NbC precipitation had caused an order of magnitude longer delay for the onset of recrystallisation and even much larger retardation in the progress of recrystallisation.

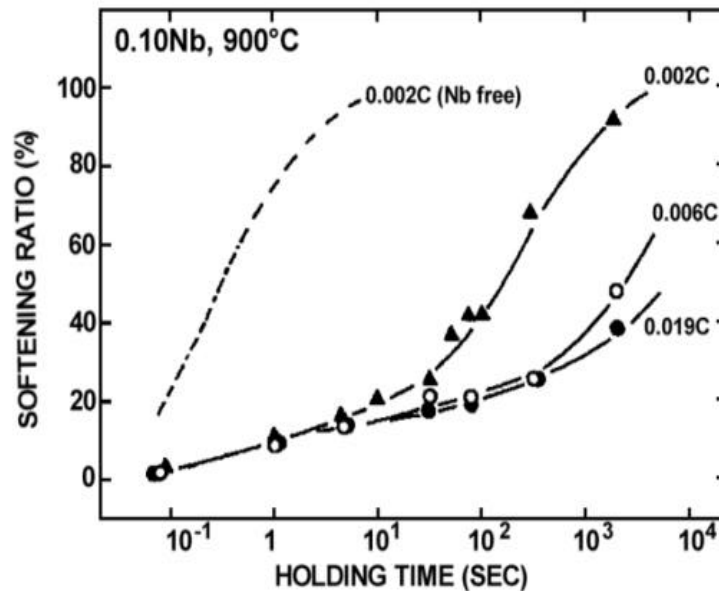


Figure 2.40 The effect of C content on the softening behaviour in 0.10%Nb steels at 900°C (adapted from ref [139])

Bai *et al.* [147] examined the effect of strain, strain rate, interpass time, and steel composition on recrystallisation behaviour of low carbon microalloyed steel with 0.05-0.09 % Nb under continuous cooling conditions. Their study was closer to practical situations faced in the rolling industry, and they proposed empirical relations correlating the $T_{5\%}$ with strain. They found that solute drag controls the recrystallisation behaviour when interpass times are short (< 12 secs), whereas strain-induced precipitation is controlling mode when interpass times are long ($12 < t < 50$ secs). The interpass time during industrial plate rolling is generally about 10–20 secs; hence, it was difficult to separate the individual effect of retarding force in their experiments.

2.6.2 RPTT Diagram

The recrystallisation is a thermally activated process; hence, its kinetics decreases as the deformation temperature is lowered. The precipitation follows C-curve kinetics, where the nucleation and growth/diffusion process respectively control the nucleation rate for a temperature above and below the nose.

In the early 1980s, Akben *et al.* [115] investigated the effect of Nb and V on static recovery and recrystallisation of austenite in low carbon microalloyed steels with high and low levels of Mn. They noted that the start of recrystallisation in microalloyed austenite would occur between 0.1-0.5 secs, whereas the precipitation start time may range from 10-100 secs for temperature interval of 900-1000°C. As illustrated in Figure 2.41, Nb addition shifts the recrystallisation-temperature-time (RTT) diagram to considerably on the right side to plain carbon steel. They attributed this effect entirely to Nb in solution when there was no precipitation involved before the start of recrystallisation.

When recrystallisation start curve of microalloyed steel intersected precipitation-start C nose, the whole RTT curve was further shifted to the right-hand side. They concluded that the precipitation could not act rapidly enough to prevent recrystallisation and the solute drag is the dominant retarding mechanism. However, they acknowledged the actual precipitation start time might be shorter than reported values in their studies.

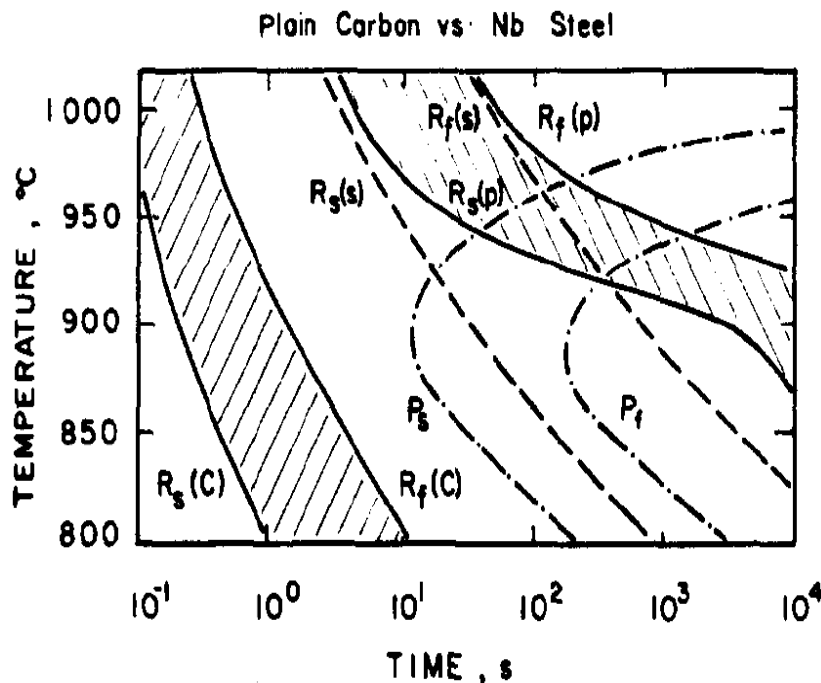


Figure 2.41 PTT diagram for the 0.035Nb-1.25Mn steel shown concerning RTT diagram for the typical plain C and Nb steels (adapted from ref [115])

Hansen *et al.* [40, 41] analyzed the complex interaction between static recrystallisation and precipitation by overlapping both kinetics curves together, termed as recrystallisation-precipitation-time-temperature (RPTT) diagram. Figure 2.42 shows the three-stage interaction between recrystallisation and precipitation based on the experimental results of their study.

In stage I ($T_{\text{def}} \geq T_{95\%}$), the recrystallisation is completed (R_f) before the actual start of precipitation (P_s) therefore recrystallisation is not expected to be influenced by precipitation. In this high-temperature range, the start of recrystallisation is controlled by the type and amount of solute element present in austenite. Since the precipitation occurs after completion of recrystallisation, the start of precipitation (P_s) is accelerated gradually shifting the left from the P'' curve, which corresponds to the start of precipitation in the undeformed coarse austenite structure.

In stage II ($T_{95\%} \leq T_{\text{def}} \leq T_{5\%}$), the precipitation takes place after the partial recrystallisation (i.e., during the time interval between the R_s and R_f). The precipitation kinetics are accelerated in this temperature region because of the presence of deformation defects in the partially recrystallised austenite. The progress of recrystallisation is delayed, and the recrystallisation finish curve is shifted to the right due to the pinning effect of Nb(CN).

In stage III ($T_{\text{def}} \leq T_{5\%}$), the precipitation is initiated before recrystallisation through accelerated kinetics as more sites for nucleation are available in the deformed austenite. Consequently, the initiation of recrystallisation is delayed by the pinning effect of precipitates at those nucleation sites, and complete non-recrystallised austenite microstructure is obtained at the end of hold /interpass time.

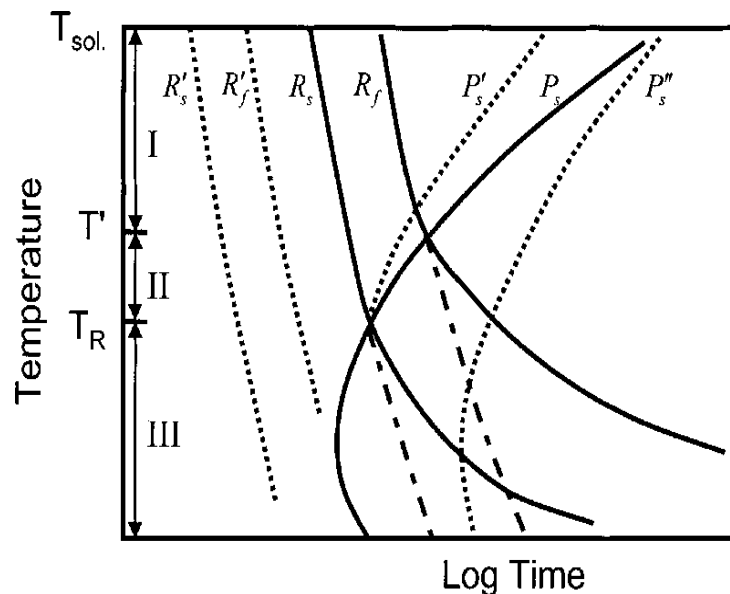


Figure 2.42 RPTT Diagram showing the interaction between recrystallisation and precipitation (adapted from ref [40])

Hansen and coworkers [40, 41] reported two stages for the strain-induced precipitation of Nb(CN) in deformed austenite. In the first stage, precipitation forms on grain boundaries and deformation band while in the second stage, precipitation takes place in unrecrystallised austenite. The kinetic of precipitation in the second stage is accelerated or slow down depending upon whether recrystallisation precedes Nb(CN) precipitation. This observation invalidates the uniform precipitate distribution theory and highlights the challenges of predicting the correct volume fraction of precipitates.

Kwon *et al.* [42] have examined the strain-induced precipitation in Nb microalloyed steels under interrupted PSC deformation. In their investigation, the precipitation occurred in areas of high dislocation density, such as prior austenite grain boundaries, deformation bands, and austenite sub-grain boundaries. Palmiere *et al.* [154] also reported the localised precipitation on austenite grain boundaries, which provided necessary pinning forces to retard the progress of static recrystallisation.

Figure 2.43 schematically depicts the localised precipitation of Nb(CN) after the deformation. It has been postulated that there may be segregation of Nb and C towards microstructure inhomogeneities. Upon precipitation, a high localised volume fraction of Nb(CN) will yield a higher pinning force.

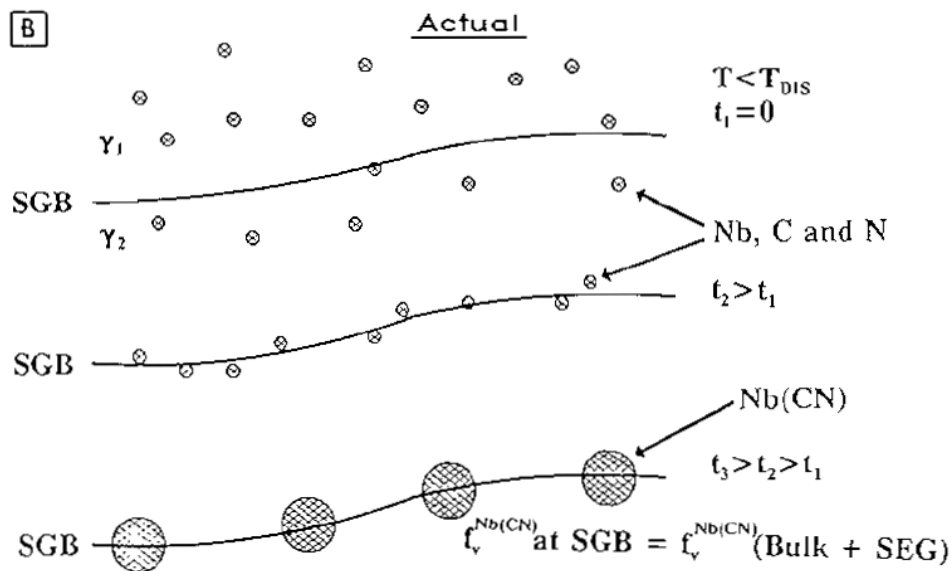


Figure 2.43 Schematic representation of the localised distribution of Nb(CN) along the austenite subgrain boundaries (adapted from ref [154])

2.6.3 F_{RXN} vs. F_{PIN}

The microstructure condition of austenite at the transformation temperature is dependent on the complex interplay between stored energy of deformation, on the one hand, i.e., the driving force (F_{RXN}) for softening and retarding forces (F_{PIN}) on others. If $F_{PIN} > F_{RXN}$, then softening will not occur, and deformation conditions will remain as it. The importance of F_{PIN} is significant in controlled rolling because higher S_v value will only be obtained if recrystallisation of austenite (γ) is retarded during hot deformation.

Palmiere *et al.* [154] studied the effect of Nb on recrystallisation-stop temperature, $T_{5\%}$ in two low carbon steel grades with varied Nb addition, steel E3 (0.02%Nb) and steel E4 (0.09 wt% Nb) respectively. The volume fraction and size of Nb(CN) precipitation were measured through TEM studies at austenite grain boundaries and the grain interiors. The F_{PIN} was calculated using equation (2.43) for both steel grades based on TEM precipitation data and compared with F_{RXN} . Figure 2.44 summaries the calculated F_{PIN} values for both steel grades E3 and E4.

For steel E4, the F_{PIN} at γ grain boundaries were approximately 19 MPa higher than the F_{RXN} ; on the other hand, the calculated F_{PIN} from grain interiors was about 1 MPa less than the F_{RXN} . Whenever the $F_{PIN} > F_{RXN}$, it resulted in complete retardation of recrystallisation (the data to the right-hand side of the curve), when $F_{PIN} < F_{RXN}$, it resulted in a partially or fully recrystallised austenite microstructure (data to the left-hand side of the curve).

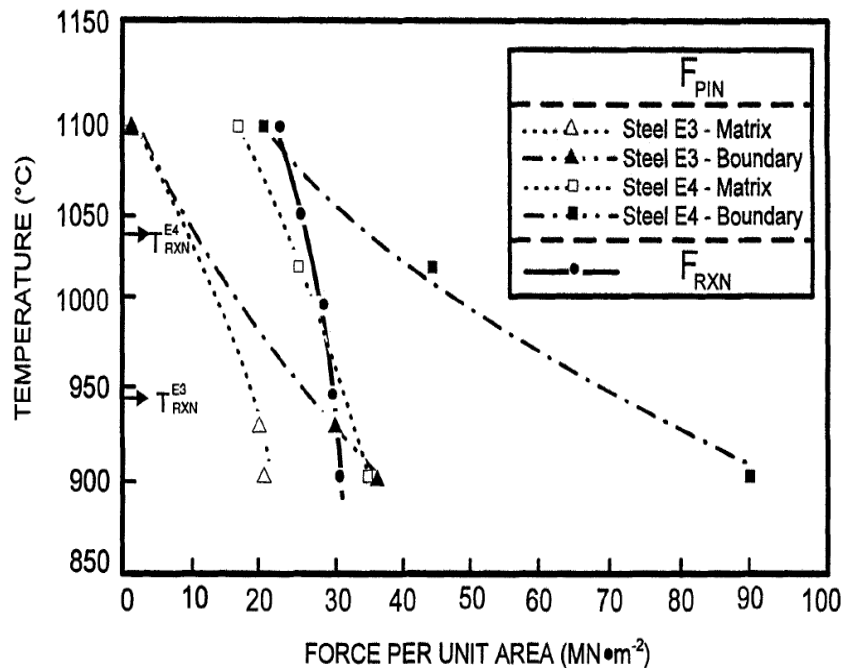


Figure 2.44 Comparison between F_{PIN} & F_{RXN} at different deformation temperature for grain boundary and matrix precipitation (adapted from ref [154]).

2.7. Laboratory Simulation

During TMCP processing, austenite is subjected to complex temperature-time-strain-strain rate histories at each stage of the hot working process. It is challenging to investigate the effect of all possible variables on the microstructure and properties of a product by industrial trials, which could be prohibitively expensive and difficult to monitor. It could also be limited in the range of change of variables that can be applied and in the stages at which the microstructure can be examined. The industry and academia require accurate material flow stress data for designing deformation strategies, modelling hot rolling process, and correlating it to microstructure evolution of HSLA steels.

This necessitated the development of the laboratory tests which are capable of simulating the influence of crucial processing variables, i.e., strain, strain rate, interpass time, the temperature of real industrial processing conditions on the recrystallisation kinetics of austenite. This need could be filled by performing a series of DHT or multipass tests at constant strain rates under constraints and conditions similar to that of plate and strip rolling on modified compression testing machines.

2.7.1 Mechanical Testing Methods

The laboratory-based mechanical testing methods consist of like a pilot rolling mill, axisymmetric compression, tension, plane strain compression (PSC), and torsion testing. The multipass torsion testing was first developed at IRSID and University of Sheffield in the 1960s, which coincided with the emergence of microalloying technology [70]. Both PSC and torsion methods are quite popular with researchers because of their useful strain range up to ~ 5 for full simulation of multipass industrial processing conditions. Both techniques have their merits and limitations as laboratory simulation test methods. It should be noted that there is no ideal simulation test, whether torsion or PSC is preferred depends on which aspects of recrystallisation simulation are considered to be most important for specific research problems.

The laboratory mechanical testing methods further can be divided into two main groups, i.e., multi-deformation tests (continuous cooling) and isothermal deformation tests (constant temperature). The first group consists of multideformation tests carried out under continuous cooling conditions for simulating the industrial rolling reduction schedule of plate and strip products, which are mainly focused on the determination of the $T_{5\%}$. These tests are generally performed on hot torsion machines as $\epsilon \geq 3$ can be achieved. In torsion, the maximum strain achieved is limited only by intrinsic ductility of the material, which is mainly under the shear conditions for many materials. However, multi-deformation tests fail to provide any information on static recrystallisation behaviour of microalloyed steels in between two deformation passes.

Isothermal deformation tests represent the second group of experiments that are carried out at isothermal temperature conditions. It involves simulating the static recrystallisation of microalloyed austenite as a function of temperature and interpass time. The extent of recrystallisation in the form of fractional softening is determined as a function of interpass time in between two deformation passes at a constant temperature. The best-known techniques in this group are a double hit test (DHT) and a stress relaxation test (SRT). These tests can be performed with a wide variety of deformation modes on different types of equipment, such as plane strain compression on TMTS simulator or Gleeble, the torsion on hot torsion machine, and uniaxial compression on deformation dilatometer or high-speed press.

2.7.2 PSC + Double-Hit Tests

PSC testing was first proposed by Orowan [155] as a modified compression test which could simulate material flow behaviour expressed during rolling. The industry and academia require accurate material flow stress data for designing deformation strategies, modelling hot rolling process and correlating it to microstructure evolution of HSLA steels. This need could be filled by performing a series of DHT or multipass tests at constant true strain rates on modified compression testing machines under constraints and conditions like that of plate and strip rolling.

The University of Sheffield built-up the first computer-controlled servo-hydraulic thermomechanical treatment simulator (TMTS) in the year 1980 to simulate hot forming behaviour of metal alloys. This successful development was achieved in close collaboration with a local company called Servotest, UK. The current TMTS simulator (3rd generation) was commissioned in 2003 with a robust control system and advanced software for data analysis. The test machine is capable of simulating a wide range of industrial thermomechanical processes in a temperature range of 0-1250°C. The servo-hydraulically control offers high-speed compression testing at constant strain rates, as high as 100 s⁻¹. The typical strain rates for practical plates and strip rolling are in the range of 2-50 s⁻¹.

The static recrystallisation studies are generally carried out using an interrupted PSC test for isothermal deformation under constant strain rate conditions. Palmiere et al. [154] trace the origin of this technique to the initial work of Wilbur et al. [158], who studied the static softening of AISI 1010 steel under high-temperature tension. Various research groups widely adopted his technique for hot compression studies of austenite [159-163]. Today, this technique is popularly known as a double-hit test (DHT) for recrystallisation and precipitation simulation under isothermal deformation conditions. The specimens deformed on TMTS are large (10-15 x 30 x 60 mm) which gives a large metallography area for post analysis and gives macroscopic flow behaviour similar to industrial conditions.

Very recently, Lopez et al. [159] made a systematic comparison of the double hit simulation test on torsion and PSC for the similar Nb microalloyed steel. They found that the PSC produces shorter recrystallisation times compared to torsion testing. The times for 50% softening obtained from PSC was about 3.5 sec, while the corresponding time from torsion tests was 10.8 sec. The discrepancy was attributed to strain inhomogeneities and associated slip line fields in both torsion and PSC tests. The strain inhomogeneity in the PSC test varies from +/- 10 % to nominal applied strain. However, there is larger strain gradient and inhomogeneities in the torsion test which in effect gives slower recrystallisation kinetics. The fraction softening calculations in this study were performed from torsion curves at $r = 0.76R$ which is close to an effective radius.

2.7.3 Fraction Softening Analysis

In literature, different workers have employed different analyzing methods to calculate the fraction softening from the equivalent stress-strain curves resulting from a double deformation test. Moreover, different simulation equipment, i.e., hot torsion, compression, and tension, have been used in softening studies, which makes it very difficult to compare between different analyzing methods.

The hot compression test conducted with the mechanical-powered hard machine (having low machine compliance) can give an accurate prediction of yield strength to allow differentiation between elastic and plastic behaviour. As a result, most of the early recrystallisation kinetic studies were performed with a torsion machine powered by electric motors. The popular fraction softening estimation methods 0.2% offset, 2 % offset, the 5 % true strain are principally based on this particular characteristic of the torsion test.

The TMTS provides poor accuracy in the determination of yield strength since it is a servo-hydraulically powered elastically soft machine with higher machine compliance. The most frequently used analyzing methods would give uncertainties in fractional softening results. Kwon *et al.*, proposed the fractional softening parameter, X_A , for the evaluation of softening kinetics [42] on the servo-hydraulically power machine.

The softening parameter, X_A , is based on the measurement of area under the flow curves, as shown in Figure 2.45. The expression of this fractional softening parameter is given below:

$$X_A = \frac{A_3 - A_2}{A_3 - A_1} \quad (2.44)$$

where A_1 is the common area under the flow stress between the first deformation in an interrupted test and the part in the monotonic test to the same prestrain level. A_2 is the area under the flow curve of the second deformation in the interrupted compression test, while A_3 is the area under the flow

curve in the monotonic test over the strained region equivalent to the second deformation in the interrupted tests.

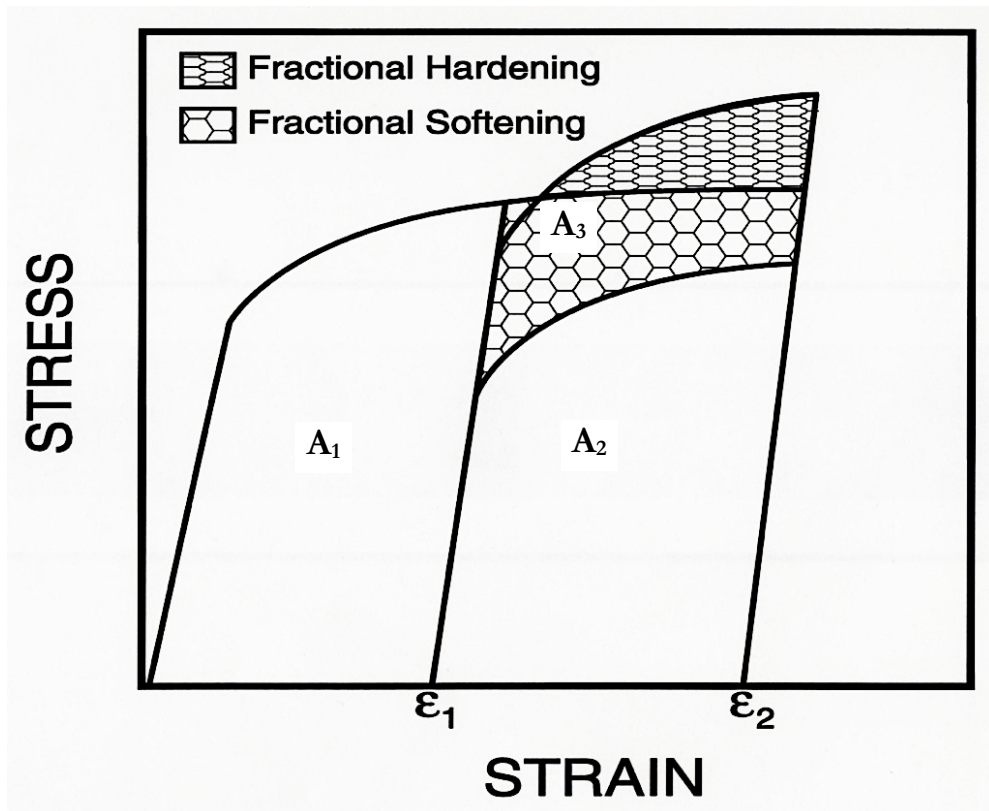


Figure 2.45 Schematic illustration of fraction softening calculations by MFA method

Lopez et al. [159] also made a comparison between different fraction softening analysis methods for torsion tests i.e. 0.2% offset, 2 % offset and 5% plastic strain etc. They found that a 2 % offset method at strain and strain rate at $r = 0.76R$ gives the best estimation for fraction softening kinetics. The offset removes any effect static recovery so that fraction softening coincides with a fraction of recrystallisation. As discussed above, the fraction softening analysis based on yield strength is not suitable for the servo-hydraulic machine. However, a good correspondence between 5% PS and mean flow area method is observed for PSC tests.

2.8. Knowledge Gap

The construction industry is also facing some operation and economic challenges like the manufacturing and service industry sector aftermath of the recent financial crises. There is a need to develop smart materials and technology for safe and sustainable construction, which will help us to save vital resources like energy, materials, and workforce.

Research in the development of new high strength steel (HSS) grades, better building components, and composite structures is necessary to solve some of the problems and challenges faced by the construction industry. Nb microalloying technology has the potential to develop high strength structural steels capable of meeting higher performance requirements. Application of Nb bearing structural steels can reduce the overall material and construction costs fulfilling the challenges of safe, healthy, and sustainable construction.

Most researchers agree to the following facts with regard to microalloying technology in flat product: (1) Nb in a solution can retard the recrystallisation to some extent until strain-induced precipitation could begin; (2) the retardation or pinning effect from strain-induced fine Nb(CN) (< 25 nm in diameter) precipitation is stronger and is an order of 1 or 2 magnitudes in times compared to solute drag, and; (3) Nb should be in solution prior to deformation, pinning effect increases with Nb supersaturation in austenite [40, 146, 178].

However, there are still known unknowns for the application of Nb microalloying technology to hot rolled long products. The limited solubility of Nb in structural steels (0.20-0.30%C) along with processing constraint has limited the use of Nb for such products. The existing solubility equations have a limitation in predicting Nb dissolution temperature as most of them were derived from the data on low carbon steels. As a result, there are no systematic studies concerning the effect of Nb supersaturation on recrystallisation process in structural steels. The rolling processing parameters (high strain rates and temperature) are also not conducive to thermomechanical processing.

Because of the above, there is an imminent need to study the effect of dilute concentration ranging from 50-200 ppm to gain better control of microstructure evaluation. There are very few scientific studies concerning the precipitation kinetics in structural steels. A better understanding of the physical metallurgy principle will significantly benefit the metallurgical community across the world. The development of value-added structural steels represents an essential area for cost efficiencies and will continue to remain in the near future.

2.9. Summary of Literature Review

The following summarises the critical points from the literature review and challenges for present work:

1. The principle goal of TMCP practice is to achieve finer ferrite grain size and the minimum amount of lower temperature transformation product containing cementite (i.e., pearlite and upper bainite). The ferrite grain refinement is the only strengthening mechanism which increases the toughness and lowers the ductile to the brittle transition temperature of low carbon microalloyed steel.
2. The ferrite grain refinement is a function of grain parameter, S_v , total effective area per unit volume. The austenite conditioning in the non-recrystallisation region generates intragranular defects in deformed grains, resulting in higher S_v , which in turn leads to finer ferrite grain size upon phase transformation.
3. Nb microalloying element has the most potent retarding effect on the recovery and recrystallisation of austenite. The atomic size of Nb, which is 15 % larger than the Fe atom, generates a strong solute drag effect along with the effect of outer shell electrons. The strain-induced precipitates of Nb(CN) have a retarding effect on recrystallisation, which is 1 or 2 times stronger than solute drag.
4. Nb supersaturation in austenite controls the precipitation potential of Nb(CN) during the hot deformation of austenite. With higher Nb supersaturation in austenite, profuse precipitation takes place on austenite subgrain boundaries which lock the substructure and retards the recrystallisation. The strain-induced precipitation is localised in nature and nucleates preferentially on microstructure heterogeneities.
5. The recrystallisation and precipitation are competing process; hence the kinetics of these processes depends upon which process occurs first. If the precipitation nucleates before recrystallisation then recrystallisation is significantly delayed through substructure locking. If recrystallisation occurs before precipitation, then the recrystallisation will be sluggish depending upon precipitation intensity.
6. The interaction between precipitation and recrystallisation dictates the three different types of rolling processes (CCR, RCR and DR CR) for achieving desired ferrite grain refinement. The RCR and DR CR rolling have a limiting austenite grain size as a function of deformation

processing, which means there is limiting ferrite grain size beyond which no refinement is possible. The CCR process produces deformed austenite accelerating ferrite nucleation and achieves significant grain refinement.

7. The recrystallisation and precipitation kinetics simulation are possible with various laboratory mechanical testing techniques. The PSC test is the most suited method to simulate the hot rolling process under isothermal (and continuous) deformation conditions.
8. There are still known unknowns for the application of Nb to hot rolled long products even though the microalloying technology is very well established for flat products. The effect of dilute Nb concentration (50-200 ppm) in structural steel with 0.20-0.30%C has not been studied systematically even it is in use for 460MPa products from the last three decades.
9. The limited solubility of austenite with typical carbon levels has restricted the use of Nb in such steel products. Additionally, the structural steel products are generally finished at a higher temperature where the precipitation kinetics are slow to control any microstructure evaluation. Also, the processing conditions are not conducive to controlled rolling practice.
10. Even with limited solubility, the dilute Nb has improved the mechanical properties under some industrial rolling conditions. The strain-induced precipitation at low temperatures has allowed ferrite grain refinement in some industrial trials. Numerous investigations proposed the random precipitation in ferrite enhanced the strength up to 30-50 MPa.
11. The dilute Nb additions have the potential to improve the mechanical properties of structural steel products at the lowest cost addition. The application of Nb microalloyed HSS can accomplish the goal of sustainable and green construction in a wide range of applications.

This page is internationally left blank

Chapter 3

Aims and Objectives

3.1 Project Aim

This project aims to understand the influence of dilute niobium concentration (50-200 ppm) on microstructural evolution in structural steels. It is envisaged that control of microstructure changes occurring during hot deformation would improve the mechanical properties of existing low value-added products.

3.2 Project Objectives

In addressing the identified targets, the experimental research program was set based upon an isothermal PSC testing, with the following objectives:

- To determine the effect of deformation processing variables (strain, strain rate, temperature and interpass time) on precipitation kinetics of Nb(CN) and static recrystallization of austenite
- To determine $T_{5\%}$ (recrystallisation-stop) and $T_{95\%}$ (recrystallisation-limit) temperatures as a function of strain and interpass time for designing a viable thermomechanical processing schedule for structural sections and rebars
- To quantify the role of Nb supersaturation in austenite on retardation of static recrystallisation for a range of processing variables and applicable rolling practices
- To evaluate the effect of Nb concentrations on grain coarsening and transformation behaviour of austenite during reheating and phase transformation, respectively.
- To evaluate the current empirical models to predict the microstructure evolution in structural steels and understanding the constraints regarding chemical composition

This page is internationally left blank

Chapter 4

Experimental Procedure



4.1. Material Alloy Design and Processing

The material used in this research involves a series of low carbon (0.20C), silicon killed laboratory steels. The steel melts were made through vacuum induction melting followed by ingot casting in a laboratory unit of the Tata Steel, UK (former Swindon Technology Center). Table 4.1 gives the detail the chemical composition of these experimental heats. The use of Si as a deoxidizer over aluminum was to avoid any confounding effects of the AlN precipitation, particularly for the grain coarsening studies. We kept the phosphorous level intentionally high to assist in the metallographic technique associated with revealing prior-austenite grain boundaries [126, 130]. The amount of C-Mn-Si in these steels was chosen to represent typical levels in structural steel grades for beams, sections, and rebar applications.

Three different grades of steels (B1-B3) microalloyed with dilute Nb additions were developed from the base steel B0, respectively. The microalloyed grades have similar nitrogen levels with varying dilute Nb concentrations. These steels should display three different forms of Nb in the solid solution of austenite if similar reheating and deformation conditions are applied regardless of which solubility equation employed from the literature.

Table 4.1 Chemical composition of the experimental heats in wt. %

Element	Composition in wt. %			
	B0/Base	B1	B2	B3
C	0.20	0.20	0.20	0.20
Mn	1.03	1.03	1.01	1.01
Si	0.20	0.19	0.19	0.19
P	0.018	0.018	0.015	0.015
S	0.008	0.008	0.007	0.007
Nb	0.0000	0.0066	0.0121	0.0214
N	0.0058	0.0056	0.0074	0.0070

As highlighted in section 2.5, the static recrystallisation of austenite in Nb microalloyed steel is suppressed by solute drag and precipitate pinning mechanism. The driving force for SIP of Nb(CN) is directly related to Nb supersaturation in austenite [40]. Hence, these lab heats should give us quantifiable evidence on the role of Nb supersaturation and precipitate in the suppression of the austenite recrystallisation for a given 0.20%C level.

The as-cast ingots were further processed to refine the as-cast microstructure and to produce material of suitable gauge for subsequent machining of PSC test specimens. The ingots were reheated to 1250°C and hot rolled down to plates of 25 mm (T) x 105 mm (W) x 1500 mm size in multiple passes. The fully instrumented 2-high reversible Hille rolling mill of 50 tons load capacity was used for this purpose. The plates were cooled to room temperature from the finish rolling temperature of 1100°C under natural air conditions similar to normalized rolling practice. This material condition will be referred to as the starting condition in the following chapters.

4.2. Grain Coarsening Studies

The isothermal grain coarsening studies were performed to ascertain the austenite grain size and amount of soluble Nb as a function of reheating temperature. The cubes specimens (10x10x10 mm³) were machined from the as-rolled plates for all the steel grades. The six different temperature spanning the austenite field are selected for the reheating studies. The highest test temperature was 1250°C, while the lowest temperature was 1000°C. The other four temperatures were at 50°C increments within this range.

A programmable quartz tube furnace was employed for the grain coarsening studies. The furnace was calibrated with the dummy samples embedded with a K-type thermocouple for better temperature control. The furnace was sealed from both ends, and dry argon gas was circulated to prevent oxidation of specimens. The samples were soaked for 30 minutes following equilibrium of furnace at respective reheat temperature. The samples were immediately quenched in water after the soak time to freeze the austenite microstructure.

The specimens from the grain coarsening studies were sectioned in half along the rolling-normal direction (RD-ND). One half of the specimen was used for measuring the prior austenite grain boundaries, while the second half was later analyzed using TEM to determine Nb in solution. The prior austenite grain was measured with a linear intercept method in RD-ND directions.

4.3. Static Softening Studies

The static recrystallisation studies are carried out using an interrupted plane strain compression test for isothermal deformation under constant strain rate conditions. Palmiere *et al.* [154] traced the origin of this technique to the initial work of Wilbur *et al.* [158], who studied the static softening of AISI 1010 steel under high-temperature tension. Today, this technique is popularly known as a double-hit test (DHT) for recrystallisation simulation

4.3.1 PSC Specimen

The PSC specimens were machined from the as-rolled plates to dimension 10 (H) x 30 (W) x 60 (L) mm. The rolling direction of as-rolled plates was perpendicular to the axis of compression. The rectangular geometry of the test piece was chosen to have uniformity in temperature and deformation within the machine load capacity. It also gives large enough post deformation areas for microstructure characterization compared to other simulation techniques. A hole of $\varnothing 1.1$ (D) x 15 (L) mm for thermocouple was drilled at the center width of the PSC specimen to monitor the temperature during the hot compression testing. Figure 4.1 shows the geometry and section view of the standard PSC test specimen.

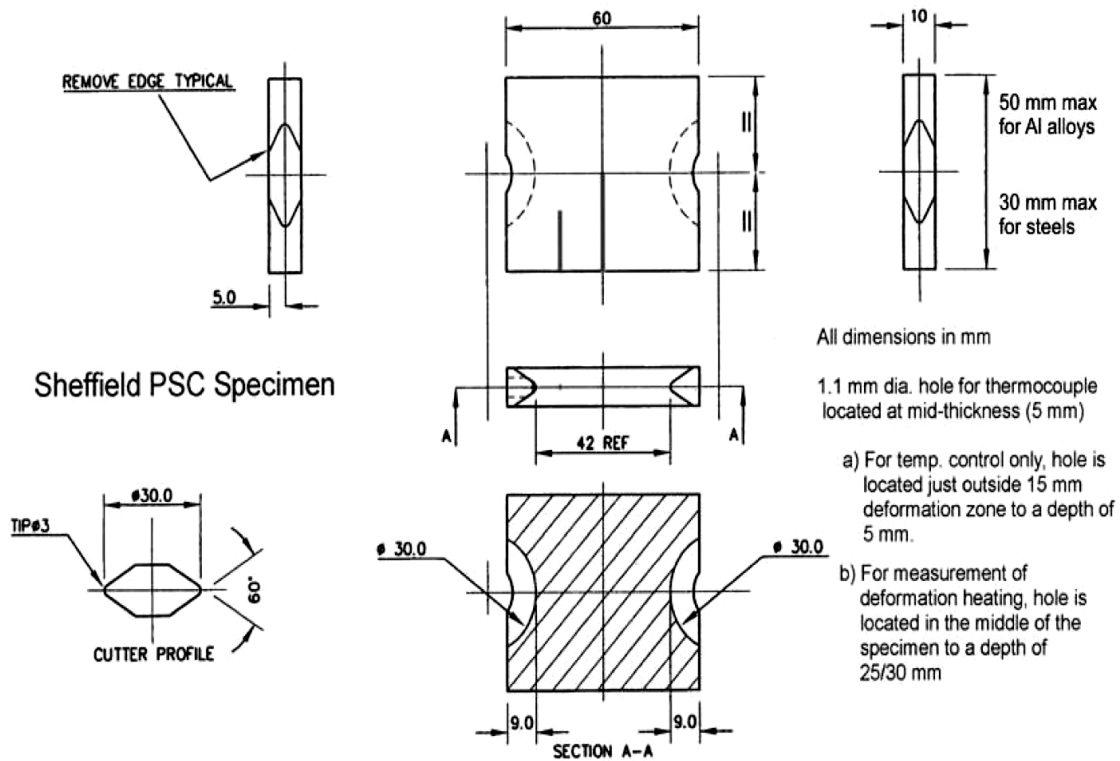


Figure 4.1 Geometry and dimension of standard PSC test piece,

4.3.2 Test Plan

Figure 4.2 illustrates the temperature-time experiment schedule designed to measure the overall softening of austenite under a prescribed delay time of $t_D = 5$ and 20 sec. The present test program is unique as the overall static softening behaviour of austenite is measured as a function of deformation temperature under a constant delay time.

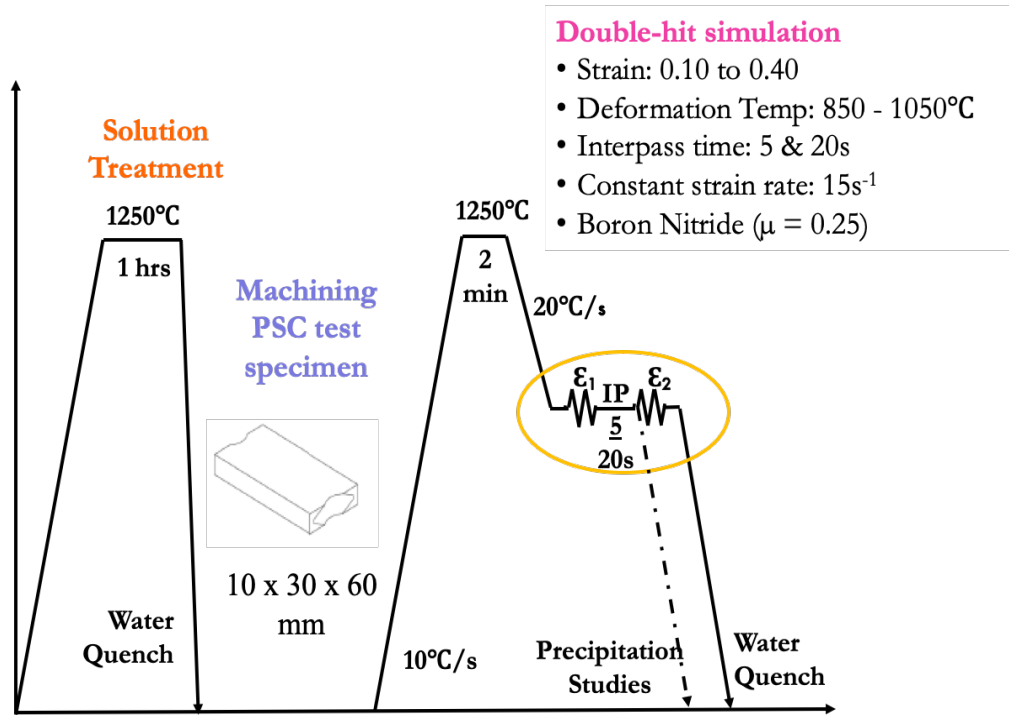


Figure 4.2 Time-Temperature schedule designed to measure static softening

It is essential to dissolve the precipitates of Nb(CN) back into solid solution and restore a fully equiaxed microstructure before the hot deformation studies. Table 4.2 shows the solution temperature to bring complete Nb in austenite solution for a given carbon and nitrogen content in steel B1-B3. Palmiere *et al.* [130] solubility equation gave the most conservative estimate of the solution temperature, i.e., 1245°C for steel B3 (0.021%Nb). We selected the critical reheating temperature of 1250°C from predicted results in Table 4.2. The reheating temperature not only dictates the amount of Nb in solution but also determines austenite grain size before deformation.

We applied a two-stage reheating cycle involving both a box furnace and an FTTU unit of TMTS. The logic behind the two-stage reheating step was to perform the majority of reheating in a box furnace, thus extending the life of test furnace in TMTS (radiation heating). In the first stage, the specimens were austenitized at 1250°C for 1 hour in a box furnace filled with an N₂ atmosphere. Immediately following a soak time, specimens were quenched in a tank filled with ice water so that the composition of austenite at 1250°C could be retained.

Table 4.2 Nb(CN) dissolution temperature of steel for steel B1-B3, calculated from published solubility equations

Author	Solubility Equations	Sol. Temp °C			Ref
		B1	B2	B3	
Irvine	$\log(\text{Nb})(\text{C}+12/14\text{N}) = 2.26-6770/T$	1047	1118	1194	[127]
Smith	$\log(\text{Nb})(\text{C}) = 3.7-9100/T$	1112	1170	1230	[125]
Meyer	$\log(\text{Nb})(\text{C}+12/14\text{N}) = 1.54-5860/T$	1056	1140	1231	[129]
Palmiere	$\log(\text{Nb})(\text{C}) = 2.06-6700/T$	1086	1163	1245	[130]

Prior to the second stage reheating in the FTTU, the as-quenched specimen was uniformly coated with the lubricant of Boron Nitride (BN). The BN coating minimizes the friction between the PSC specimen and tool dies, avoiding in-homogeneous deformation conditions. After the coating, the specimens were loaded into the manipulator's arm and were placed within an inductive heating system of FTTU. PSC specimen was reheated to 1250°C, held for 2 minutes to allow for equilibrium within the specimen. Following the hold time, the reheated specimen was forced air-cooled at a rate of 20°C/s to one of the five deformation temperatures and immediately transferred to test furnace for hot deformation.

The hot deformation was undertaken in a double pass of the equal magnitude of a true strain from $\varepsilon_1 = \varepsilon_2 = 0.10 - 0.40$ with a hold time of 5 or 20 sec in-between two passes (Figure 4.2). The deformed specimen was immediately water quenched to room temperature (quench time 1.0-1.5s) after the second deformation pass (ε_2). A constant strain rate of 15s^{-1} was applied during the deformation passes. An uninterrupted deformation was also carried out for total strain $\varepsilon = \varepsilon_1 + \varepsilon_2$ without any intermediate holding time for each test condition.

The five deformation temperatures (1050, 1000, 950, 900, and 850°C) selected in this study represent the typical finish rolling processing window for long products. The typical finish rolling start and end temperature for most structural steel long products are between the selected temperature range. The holding time of 5 and 20 sec between two passes also represents typical industrial rolling interpass time for beam, small sections, and long rails.

The Nb(CN) SIP analysis was crucial to understanding the interaction between precipitation and the static restoration process as a function of deformation processing variables (temperature, strain, and time). The PSC specimens were deformed to initial true strain, $\varepsilon_1 = 0.40$, isothermally held for the 20 sec, followed by immediate water quenching. The temperature of 850-1000°C with an increment of 50°C was selected to verify the findings from DHT softening studies. Additionally, some specific test conditions were selected for steel B1 and B2 based on the analysis of softening studies. The extensive TEM characterization was performed only on the isothermal hold samples.

4.3.3 Fraction Softening Analysis

The raw load-displacement was converted into equivalent stress-strain flow curves using an excel template. The excel utility is based on NPL standard practice for evaluating the hot flow stress in PSC testing [157]. Appendix A covers the step by step procedure for measuring the hot flow stress in the PSC test.

The TMTS used in this investigation provides poor accuracy in the determination of yield strength since it is a servo-hydraulically powered elastically soft machine with higher machine compliance. The most frequently used fraction softening analysis methods (i.e., 0.2 % and 2 % yield offset, 5 % true strain, and the back-extrapolation) would give uncertainties in softening results for TMTS. As a result, the fractional softening parameter, X_A , first used by Kwon *et al.* [42], has been adopted in this present study for evaluation of fraction softening of austenite for each deformation condition. The details of this technique and the method of calculation are described elsewhere [161].

The X_A is based on the measurement of area under mean flow stress curves. The amount of softening X_A is calculated from the area under the flow curves areas A_1 , A_2 , and A_3 as below:

$$X_A = \frac{A_3 - A_2}{A_3 - A_1} \quad (4.1)$$

where A_1 is the area under the flow curve during the first deformation pass, A_2 is the area under the flow curve of the second pass after holding time; and A_3 is the area under the flow curve in the monotonic test over the strained region equivalent to the second deformation pass in the interrupted tests.

4.4. Transformation Behaviour Studies

The aim of the phase transformation studies was to evaluate the effect of continuous cooling conditions on the microstructure and mechanical properties of investigated steels. The chemical composition of steel grades allows us to study the effect of solute Nb on phase transformation behaviour simultaneously along with the cooling rate. The phase transformation behaviour was studied using the purpose-built Advanced Thermal Treatment Simulator (ATTS).

The ATTS unit was designed and manufactured by Inductlec Ltd, Sheffield UK, in close collaboration with the University of Sheffield. It consists of a 30-kW induction coil to simulate the thermal treatment as per user specified pre-written PLC programming, which is operated through a controlled box. The control of the thermal profile is achieved with the PID control feedback system according to user-defined temperature set points for a given heating/cooling rate. The control

system toggles ON/OFF power inputs when the specimen temperature is below or above the setpoints specified by the user-defined thermal program.

The cylindrical specimens of 12 (D) x 155 (L) mm were machined in a longitudinal direction from the as-rolled plates. The machined specimens were solution treated at 1250°C for 45 mins, followed by immediate oil quench. Again, the solution treatment aimed to dissolve all Nb(CN) into austenite solution. After the solution heat treatment, the specimen was vertically mounted within the induction coils in between a non-conductive fixed pin and a free moving mono-directional push rod. A K-type thermocouple was spot welded the surface of each specimen, halfway along the gauge length. The dilations during an applied thermal program are transferred through a push rod and measured by a transducer at another end.

The critical temperatures Ac_1 and Ac_3 during heating were determined experimentally, and comparison was made with estimation obtained from the empirical formula. The thermal cycle consisted of heating the test specimen to 700° at a constant rate of 10°C/s. The heating was continued further at a nominal rate of 0.05°C/s until the Ac_1 and Ac_3 temperatures were identified. These critical temperatures were determined from the change in the slope of strain vs. temperature plot as per ASTM specification A1033-10 [164].

Each continuous cooling transformation cycle consisted of heating a test specimen to an austenitizing temperature of 1250° at a constant rate of 10°C/s and soaking for 2 minutes. The test specimen was then cooled to a correct soaking temperature of $Ac_3 + 50^\circ C$ at a cooling rate of 20°C/s. The test specimen was held at a soaking temperature for 5 minutes and then cooled to room temperature at a nominal cooling rate of 0.05 and 5°C/s. A separate test specimen was used for each thermal cycle. Figure 4.3 shows the schematic of the time-temperature schedule applied for continuous cooling experiments.

4.5. Microstructural Studies

Light microscopy is the most popular technique to quantify grain structure characteristics, i.e., grain size, aspect ratio, and volume fraction. Since 1950's various research groups have used the CTEM to characterise the Nb(CN) precipitation in austenite and ferrite with the help of extraction replica or thin foil technique. This approach is still relevant today and has been summarised well in various books and articles [166,170].

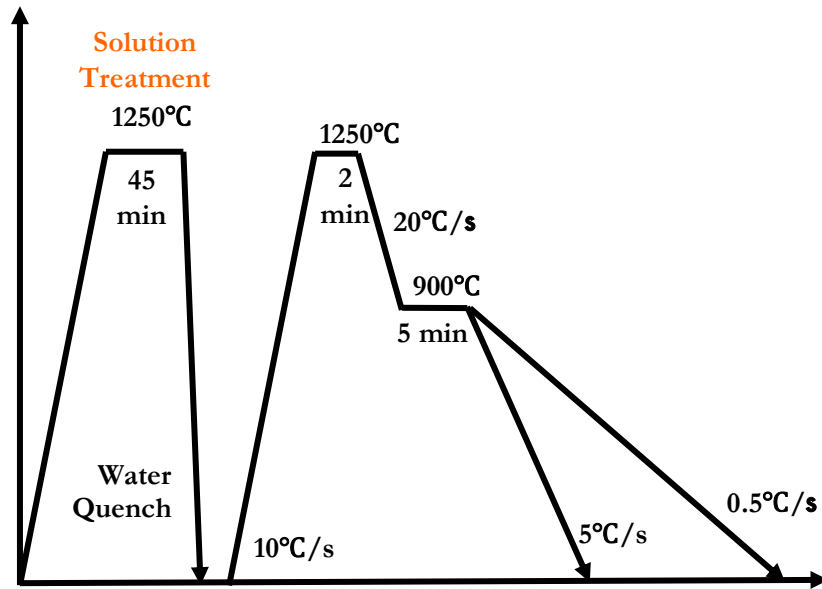


Figure 4.3 Time-Temperature Schedule for phase transformation studies

4.5.1 Metallography Preparation

The deformed specimens from the static softening studies were analyzed along the rolling-normal direction (RD-ND). Mirza *et al.* [165] studied the strain distribution in the deformed specimen under both homogeneous and inhomogeneous conditions with FEM simulations. As shown in Figure 4.4, the central area represents the homogeneous deformation condition and represents applied equivalent strain. Hence, we confined the microstructure analysis to only the central region of each deformed specimen.

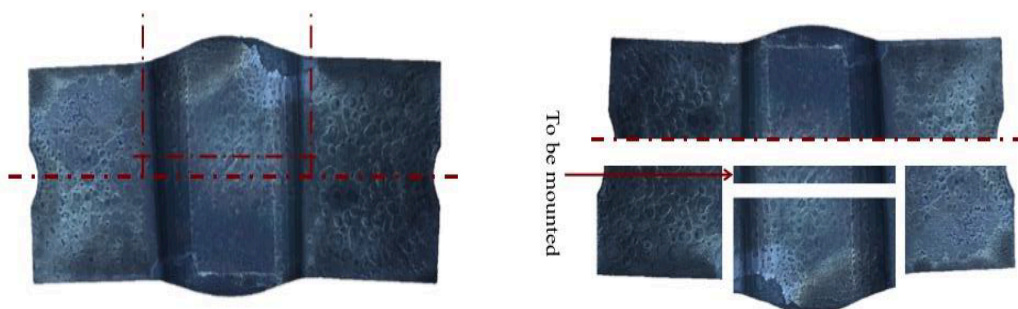


Figure 4.4 Illustration of Sectioned Deformed PSC Specimen for LM Analysis (a) deformed specimen (b) central area section plan

The initial sectioning was gently made with the Buhler AbrasiMet machine using a water-cooled 10'' silicon carbide abrasive cut-off the blade. The water cooling and slow speed were primarily maintained to minimize any deformation damage induced during cutting. The final slices were sectioned on Struers Secotom-50 with 8'' aluminium oxide coated blades for a precise cut and to

minimize the cutting damage. The metallographic preparation was carried out using a standard grinding and polishing technique, as shown in Table 4.3.

Table 4.3 Metallography Sample Preparation Method

Surface	Lubricant	Abrasive Type/ size	Time	Force	Platen Speed	Head Speed	Rotation
Planar Grinding							
SiC paper	water	P120 – P400	3 min	25	241	60	comp
Fine Grinding							
SiC paper	water	P800 – P2500	3 min	25	241	60	comp
Final Polishing							
SiC Paper	water	P4000	3 min	15	141	60	comp
Nap cloth	-	1 μ m diamond	5 min	15	141	60	contra
Synthetic suede	drips	0.05 μ m CS	5 min	15	141	60	contra

The heat-treated specimens from the phase transformation studies were analyzed for metallography to understand the effect of cooling rate on transformation products. The specimens were sectioned along the RD-ND direction and prepared for microstructure analysis.

4.5.2 Chemical Etching

The prior austenite grain boundaries were revealed using a solution of saturated picric acid at elevated temperature. The saturated solution consisted of 100 ml of distilled water, 4 grams of picric acid, and 0.5 ml of HCl. The picric acid crystals were first added to a 100 gm distilled water solution. This solution was kept on the hot plate and stirred gently until the complete dissolution of picric acid crystals. The temperature was kept constant at 85-90°C. One gram of a wetting agent (Sodium dodecyl sulphate) was added to the solution to improve the performance of the etching solution. Finally, five drops of HCl were slowly added into the solution to delineate grain boundaries.

The prepared solution was concentrated and acidic; hence the etching could not be commenced straight away. The four dummy steel specimens were sequentially immersed in the solution for 5 min each to reduce the acidic nature of the solution. This process can be termed as a maturing process. Figure 4.5 shows the color difference between the freshly made and matured solution. The release of iron ion from dummy specimens helps to enhance the etching performance. In the literature, various research groups have tried a large number of wetting agents (surfactants) from different sources. In this study, we found that the Sodium dodecyl sulphate gives the best etching performance for carbon steel up to 0.60% C.

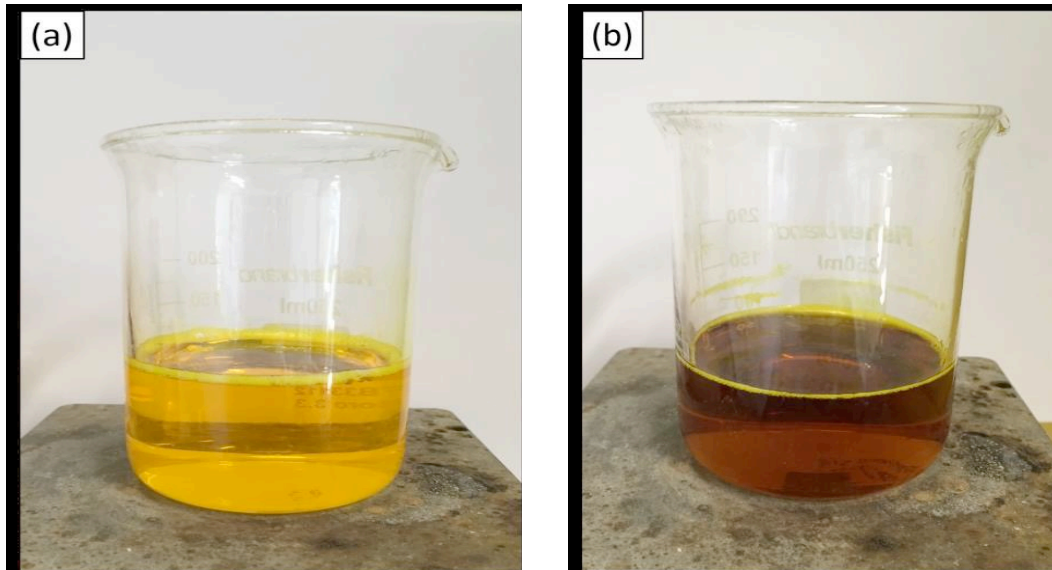


Figure 4.5 Colour difference between freshly made and matured saturated picric acid solution.
Adapted from [19]

The mounted specimen was immersed in a mature solution with polished face-up and etched for 2-4 minutes without any stirring. The specimen was removed, and black film on the etched surface was cleaned with wet cotton soaked in detergent soap. It was further washed under running water followed by isopropanol to clean any traces of picric acid and then finally dried with hot blower. A Nikon Eclipse LV150 optical microscope and Omnimet image analysis program was used to capture the microstructure images at different magnification.

The polished samples from dilatometer experiments were first etched with a 2% Nital solution, followed by a 4% Picral solution to reveal both ferrite and pearlite morphologies. The microstructure images were taken at different locations and magnification to quantify the microstructure constituents.

4.5.3 TEM Characterisation

The electron microscopy was used to characterise the strain-induced precipitation of Nb(CN) in deformed austenite. The samples were prepared with standard carbon extraction replica and thin foils technique. Appendix B describes the five stages of the sample preparation technique.

4.5.3.1 Microscope Features

The EM420 is equipped with a Tungsten element and has a maximum electron accelerating voltage of 120kV. This microscope is perfect for conventional TEM imaging due to its excellent optics and classical design. However, the diffraction pattern and high magnification images are of less resolution because of low electron accelerating voltage. For these purposes, the FEI Tecnai 20 analytical electron microscope was principally used along with EM420. The Tecnai T20 operates

at 200kV electron accelerating voltage and is equipped with a Lanthanum hexaboride (LaB6) element. It is suitable for high-resolution convention TEM imaging (BF-DF) combined with the EDS system for advanced chemical imaging and analysis. Table 4.4 gives the detail characteristics of the T20 electron microscope.

Table 4.4 Characteristics of FEI Tecnai T20 Microscope

Tension	200kV
Emission mode	Field emission (Schottky)
Point resolution (nm)	0.194
Information limit (nm)	0.12
Probe minimum size	~0.4 - 0.2
Spherical Aberration Coeff., Cs (mm)	1.2
Cc (mm)	1
Object Slides	Simple tilt $\pm 35^\circ$, Double tilt ($\pm 25^\circ$ - $\pm 25^\circ$)
Analysis Accessories	EDX Oxford (Ultrathin window UTW) Digi-PEELS Gatan

4.5.3.2 Imaging Mode

The conventional TEM imaging is typically carried out in either bright field (BF) or dark field (DF) mode. The BF image is formed through a transmitted beam, while the DF image is formed with a diffracted beam. In thin foils, it is possible to see the exact location of precipitates and study the orientation relationships between them and the matrix. The specimen holder needs to be tilted along an adequate zone axis to see all the precipitates sharing the same orientation relationship with the iron matrix phase. The DF imaging requires more skill compared to BF to get the correct quantifiable data. The BF imaging of extraction replica allows the determination of particle diameter and distribution with more accuracy compared to thin foils. Figure 4.6 shows an example of a bright and dark field imaging technique used in TEM for SiO₂ samples.

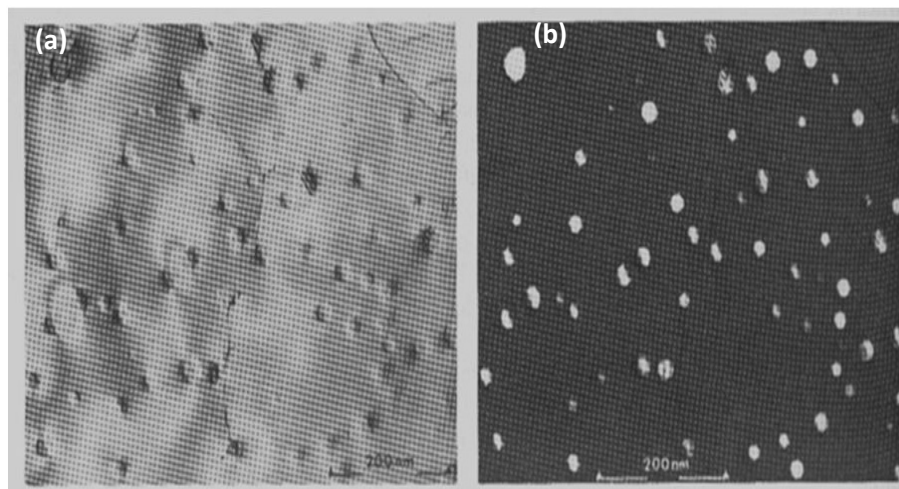


Figure 4.6 TEM images of the same area through (a) BF and (b) DF technique (adapted from ref [167])

4.5.3.3 Analytical electron microscopy

The principles of analytical electron microscopy are covered and detailed in the various textbook of electron microscopy like Williams and Carter [170]. The goal of AEM is to characterize the chemical composition at the site of interest with atomic resolution. The EDAX and EELS spectroscopy was performed on nanometre size Nb(CN) precipitates to get information about their chemistry at a spot along a line or in a particular area.

The EDAX analysis was performed using a silicon drift detector (Oxford Instruments) fitted on the FEI-Tecnai T20 microscope. INCA software associated with the EDS system was used to perform calibration and various corrections. The quantitative analysis is done using a simple atomic ratio technique first developed by the Cliff and Lorimer in the early 1970s [171]. The peak intensities are proportional to concentration and specimen thickness. They introduced the “K-factor” to relate the intensity ratio to concentration ratio:

$$\frac{C_A}{C_B} = K_{AB} \frac{I_A}{I_B} \quad (4.2)$$

where I_A and I_B is the peak intensity for element A and B, respectively, C_A and C_B is the concentration in weight % for element A and B, respectively. The quantitative analysis of light elements, C and N in EDAX is troublesome due to partial absorption of photons, either by the sample atoms or by the detector protection window. As the detection efficiency of light elements is less than unity, it is necessary to use EELS for accurate determination of C and N in the precipitate compound. The EELS analysis was performed on the JEOL 2010F analytical microscope fitted with silicon drift detector

4.6. Quantitative Metallography

The deformation processing variables (i.e., strain, strain rate, and initial grain size) has a significant influence on the austenite morphology during hot rolling. Its control plays a crucial role in ferrite grain refinement; hence, it is essential to quantify the austenite grain size and recrystallisation evaluation during compression testing.

4.6.1. Grain Size: Linear Intercept Method

The PAGS of both solutions treated and deformed conditions were measured using the linear intercept method, according to ASTM E112 [172]. It is the most popular method to determine the grain size of materials in a planar section. The method consists of measuring the average distance between the grain boundaries along the line placed at random on the polish plane.

The conventional notation for defining the principal directions is used, i.e., 1 for the maximum principal strain (RD), 2 for the intermediate principal strain (STD) in which the strain is zero for plane strain rolling (the width direction) and 3 for the minimum principal strain (ND) in which the strain is negative [173]. Figure 4.7 shows a deformed austenite microstructure image on which parallel spaced grid lines were superimposed on the RD and ND directions.

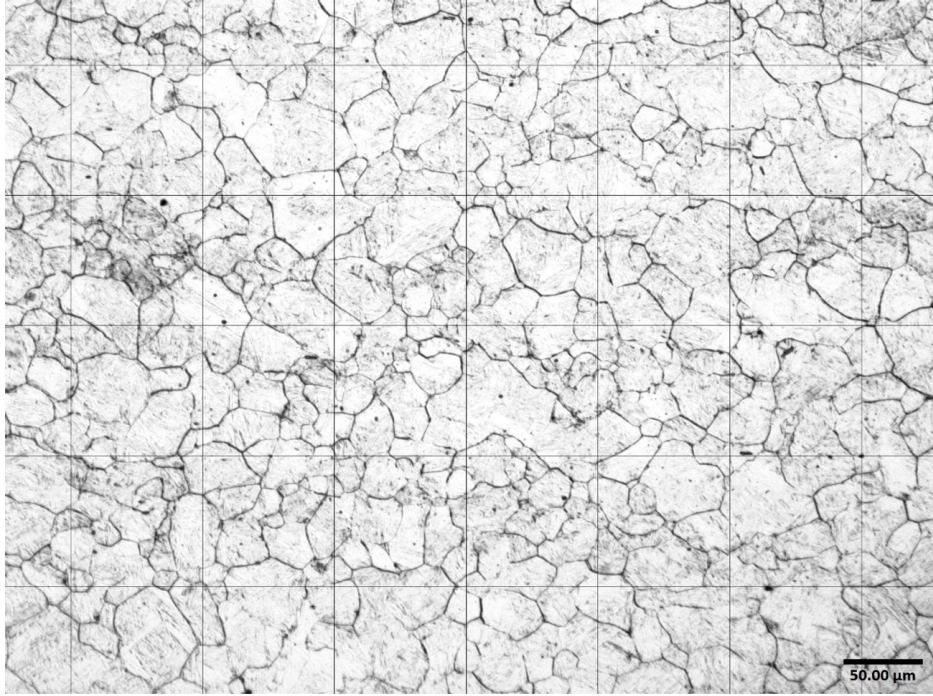


Figure 4.7 Example of measuring linear intercept grain size on microstructure image

For each line i , the prior austenite grain size, L_i was calculated by dividing the total length of the line by the total number of PAGB crossed (\overline{N}_L). The measurements of PAGS on an individual line basis was summed up and divided by the total number of lines to calculate mean linear intercept in each direction \overline{L}_1 or \overline{L}_3 .

$$\overline{L}_1 = \frac{1}{\overline{N}_L} \quad (4.3)$$

The standard deviation of measurement in each direction was calculated using the formula:

$$s^2 = \frac{\sum(L_i - \overline{L})^2}{n-1} \quad (4.5)$$

where s is the standard deviation of measurement, L_i is the PAGS of line i , \overline{L} is the average PAGS intercept, and n is the number of lines. The standard error was calculated from the standard deviation as follows:

$$S(\overline{L}_1) = \frac{s}{\sqrt{n}} \quad (4.6)$$

The mean grain linear intercept (\overline{L}) is calculated from intercept measurement in both the directions \overline{L}_1 and \overline{L}_3 as follows:

$$\bar{L} = (\bar{L}_1 \bar{L}_3)^{\frac{1}{2}} \quad (4.4)$$

The standard error for \bar{L} was calculated by applying the method of propagation of errors as:

$$S(\bar{L}) = S(\bar{L}_1)^2 \frac{1}{4} \cdot \frac{\bar{L}_3}{\bar{L}_1} + S(\bar{L}_3)^2 \frac{1}{4} \cdot \frac{\bar{L}_1}{\bar{L}_3} \quad (4.7)$$

Finally, the mean linear intercept grain size of measurement is expressed as:

$$\bar{L} \pm (t_{95n-1}) S(\bar{L}) \mu\text{m} \quad (4.8)$$

Table 4.5 shows the value of t as a function of the number of degrees of freedom. The 95% confidence limit for \bar{L} was calculated using a relevant t-value from the statistical table.

Table 4.5. Value of t for 95% confidence limits as a function of the number of degrees of freedom, $v = n-1$

v	(t_{95n-1})
20	2.086
25	2.060
30	2.042
40	2.021
60	2.000
120	1.98
∞	1.96

4.6.2. Mean Aspect Ratio

The hot deformation of austenite at a temperature of less than $T_{5\%}$ results in the elongation of grains in the rolling direction. It is essential to measure the degree of elongation of the austenite as this has a significant effect on the kinetics of ferrite transformation. The aspect ratio can be defined as the ratio between the largest and the smallest grains size when it is measured along with the three orthogonal directions. In the case of plane strain deformation, the mean aspect ratio of grain structure can be found by the ratio of linear intercepts measurements in the RD and ND direction.

$$\bar{r} = \frac{\bar{L}_1}{\bar{L}_3} \quad (4.9)$$

4.6.3. Surface Area per Unit Volume

The stereological parameter S_v , the grain boundaries area per unit volume, is directly related to the number of grain boundary intercepts per unit length, N_L . The relationship for equiaxed grain structure is given as:

$$S_v = 2N_L = \frac{2}{\bar{L}} \quad (4.10)$$

In the case of elongated austenite structure after hot deformation in an unrecrystallised region, S_v can be calculated from the weighted average of the values of N_L in each of the three principal directions [173]. The relationship for deformed austenite is given below:

$$S_v = 0.429N_{L1} + 0.571N_{L2} + N_{L3} \quad (4.11)$$

4.6.4. Recrystallised volume fraction

The volume fraction of recrystallisation austenite in partially recrystallised microstructure was determined using the point-counting method as per ASTM E562 [174]. The parallel spaced grid lines like grain size measurements were superimposed in the RD and ND directions on the microstructure image. The intersection of grid lines falling inside a recrystallised grain was counted as one unit, whereas points at the boundary of the feature were counted as one –half unit. The point fraction of recrystallised grains (P_r) or volume fraction of recrystallised grains (V_r) was calculated from the following formula:

$$P_r = \frac{\Sigma P_r}{P_T} = \frac{\Sigma P_r}{nP_0} = V_r \quad (4.12)$$

where P_r is the number of test points inside a recrystallised grain, P_T is the number of grid points. The standard deviation and confidence limits of measurements were calculated from the formula described in the grain size section.

4.6.5. Determination of Precipitate Radius

Several stereological techniques have been established for analyzing the precipitate size and distribution from both planners and projected TEM images over the years. It is usual to assume that the precipitates are spheroidal in volume so that they can be considered in terms of equivalent sphere diameter or circle diameter.

ImageJ is a free versatile program package for image processing and manipulations which runs under Java [175]. The TEM images need to be a threshold in such a way that the particles appear as a dark spot in the black and white mode. The in-built function ‘‘Analyze Particles’’ then allows automatic determination of particle size and their distribution. The area of the particle in an image was measured in terms of pixels and converted into an equivalent circle diameter. Figure 4.8 depicts the process of measuring the particle diameter with the help of Image Analyzer. The histogram of particle size distribution was then plotted based on measurements of at least six images representing enough random areas in a specimen. The mean diameter of precipitates and the standard deviation was calculated from the statistical formula.

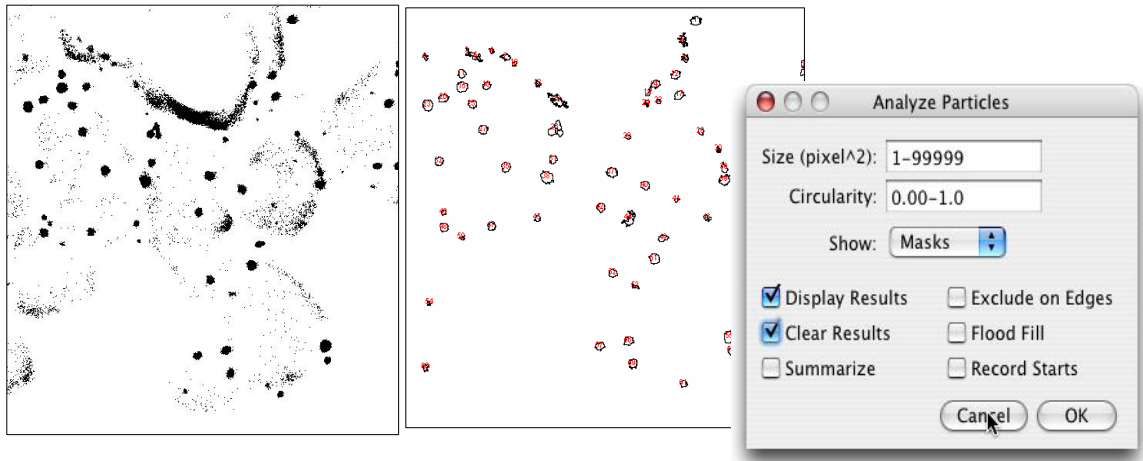


Figure 4.8 Process of Analysing Particle Size Distribution (adapted from ref [176])

Ashby and Ebeling [177] have proposed the most applicable method for determining the volumetric distribution of the spherical particle of the second phase from an extraction replica. If ideal extraction conditions are assumed, the direct measurement of particle size distribution should give the exact planar distribution of particle sizes. The volume fraction of second phase particles was calculated with accuracy from the following formula:

$$f = \frac{\pi}{6} N_s (\bar{x}^2 + \sigma^2) \quad (4.13)$$

where \bar{x} is the planar arithmetic mean, N_s is the number of particles per unit area, σ is the standard deviation, and N_v is the number of particles per unit volume.

4.7. Mechanical Testing

4.7.1. Micro-hardness testing

The micro-hardness tests were performed on a continuously cooled dilatometer specimen. The hardness of the material is defined as the resistance of a material to plastic deformation. The Vickers hardness testing constitutes a static indentation test whereby the diamond is pressed into a sample surface with a specific load and specific dwell time. The resulting deformation is measured and reported as Vickers Hardness Number in kg/mm^2 . The diamond surface has a pyramid shape with an angle of 136° between faces, which creates a square impression in the specimen under a 2D projection. Figure 4.9 shows the schematic of the diamond indenter used in Vickers hardness testing and the indentation it creates in a sample. The bulk hardness measurements were carried using a Mituyoto Vickers Hardness tester from indent generated by a load of 1 kg applied for a duration of the 20 sec. The average of two diagonal lengths of squared indentation was measured using a stage graticule. The hardness measurement (HV1) was calculated using a standard table provided by the manufacturer.

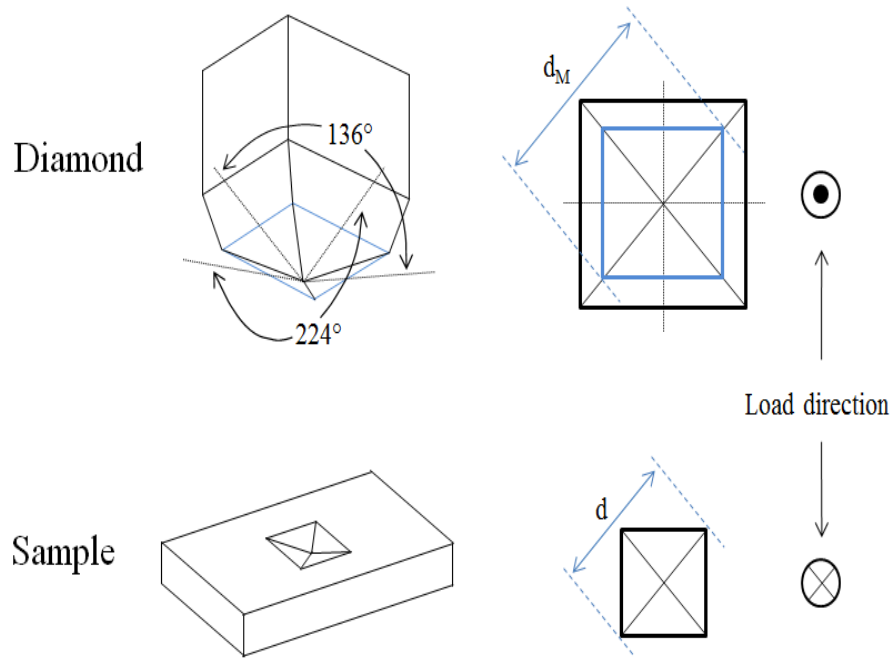


Figure 4.9 Schematic of the diamond used in Vickers hardness testing and the indentation it creates in a sample. 2D projections indicating the diagonals (d) of both the diamond and indentation are also displayed (adapted from ref [169])

The standard table uses the following equation for hardness conversion from measured diagonal:

$$HV1 = \frac{1.8544p}{\bar{d}^2} \quad (4.14)$$

Ten measurements were taken from each sample to minimize the uncertainty of measurement.

The standard deviation of measurement was estimated to calculate the standard error.

4.7.2. Compression Testing

The mechanical properties of dilatometer specimens were determined as a function of a cooling rate and dilute Nb concentrations through compression tests. The four cylindrical specimens of size 12 (D) x 15 (L) mm were sectioned for each heat-treated condition. The room temperature compression tests were performed on the TMTS simulator with the use of the round-flat parallel surface of axis-symmetric tools. The specimen was covered with the Teflon tape to reduce the friction condition between the tools and specimen surface. The specimen was placed on a flat surface of bottom tools, and an upper tool was moved for a true strain of 0.75. The constant strain rate of 0.05s^{-1} was applied during the test.

The load-displacement data was recorded using a high-speed data logger. The raw data were converted into an equivalent stress-strain curve using a standard practice guide for the axisymmetric test [157]. The yield strength of the material was determined with a 0.2% offset method. The compressive strength was estimated from at constant equivalent strain of 0.20.

This page is internationally left blank

Chapter 5

Results

5.1 Austenite Grain Coarsening Behaviour

Figure 5.1 - 5.4 shows the prior austenite grain size as a function of reheating temperature for steels B0-B3. These microstructures were obtained reheating to each respective temperature for 30 minutes and quenching in water. Steel B0-B3 exhibited a complete martensite microstructure, which is mostly a lath structure. There was no indication of pro eutectoid ferrite formation along the prior austenite grain boundaries. The series of micrographs for each steel indicate that the prior austenite grain size increases with an increase in reheating temperature. The quantitative measurement of grain sizes over a range of temperatures confirms this behaviour.

We measured the prior austenite grain size in RD (\bar{L}_3) and ND (\bar{L}_1) direction using the linear intercept method. The mean prior austenite grain size (L) was calculated assuming an axial symmetry of the grains from the above measurements with a relationship, $L = (L_1 * L_3)^{0.5}$. Table 5.1 shows the mean prior austenite grain size as a function of reheating temperature for each steel.

Table 5.1 Mean austenite grain size for as reheated and quenched steels

Deformation Temp °C	Austenite Grain Size (μm)			
	B0	B1	B2	B3
1000	80 ± 8	83 ± 7	78 ± 9	76 ± 6
1050	130 ± 15	123 ± 09	147 ± 13	171 ± 23
1100	160 ± 11	155 ± 12	126 ± 08	127 ± 08
1150	180 ± 22	159 ± 13	160 ± 13	153 ± 14
1200	162 ± 11	138 ± 09	137 ± 07	163 ± 12
1250	143 ± 13	147 ± 10	163 ± 09	158 ± 10

Figure 5.5 graphically depicts the quantitative data in the table for steel B0 and B1. It shows that grain coarsening occurs linearly up to a temperature of 1150°C, followed by secondary recrystallisation. Similarly, Figure 5.6 graphically depicts the grain coarsening behaviour for steel B2 and B3. The grain coarsening was observed for temperature up to 1050°C, followed by secondary recrystallisation.

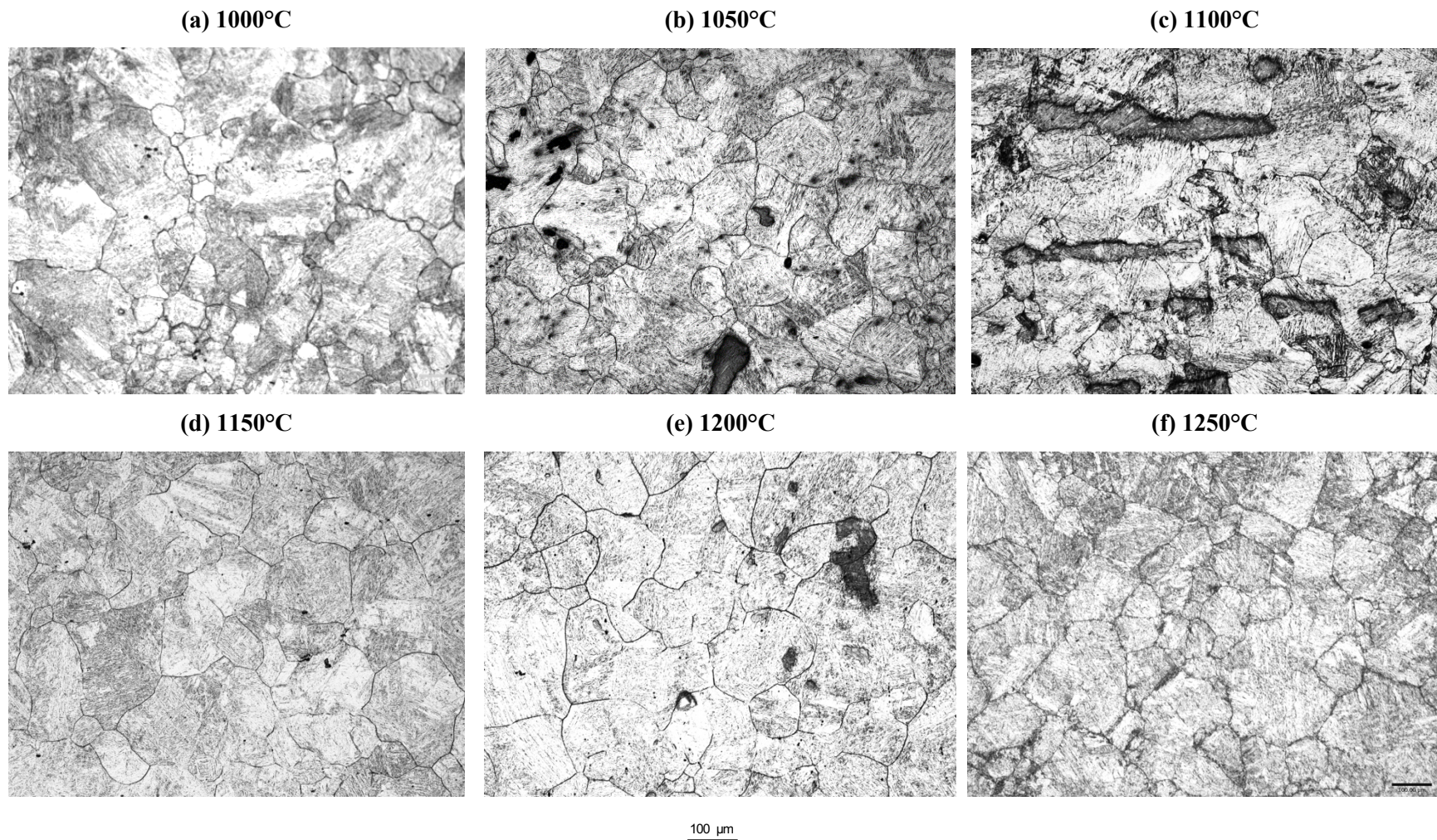


Figure 5.1 Prior austenite grain size for steel B0 at respective deformation temperature to the above reheating temperature and water quenching (Magnification: 100X)

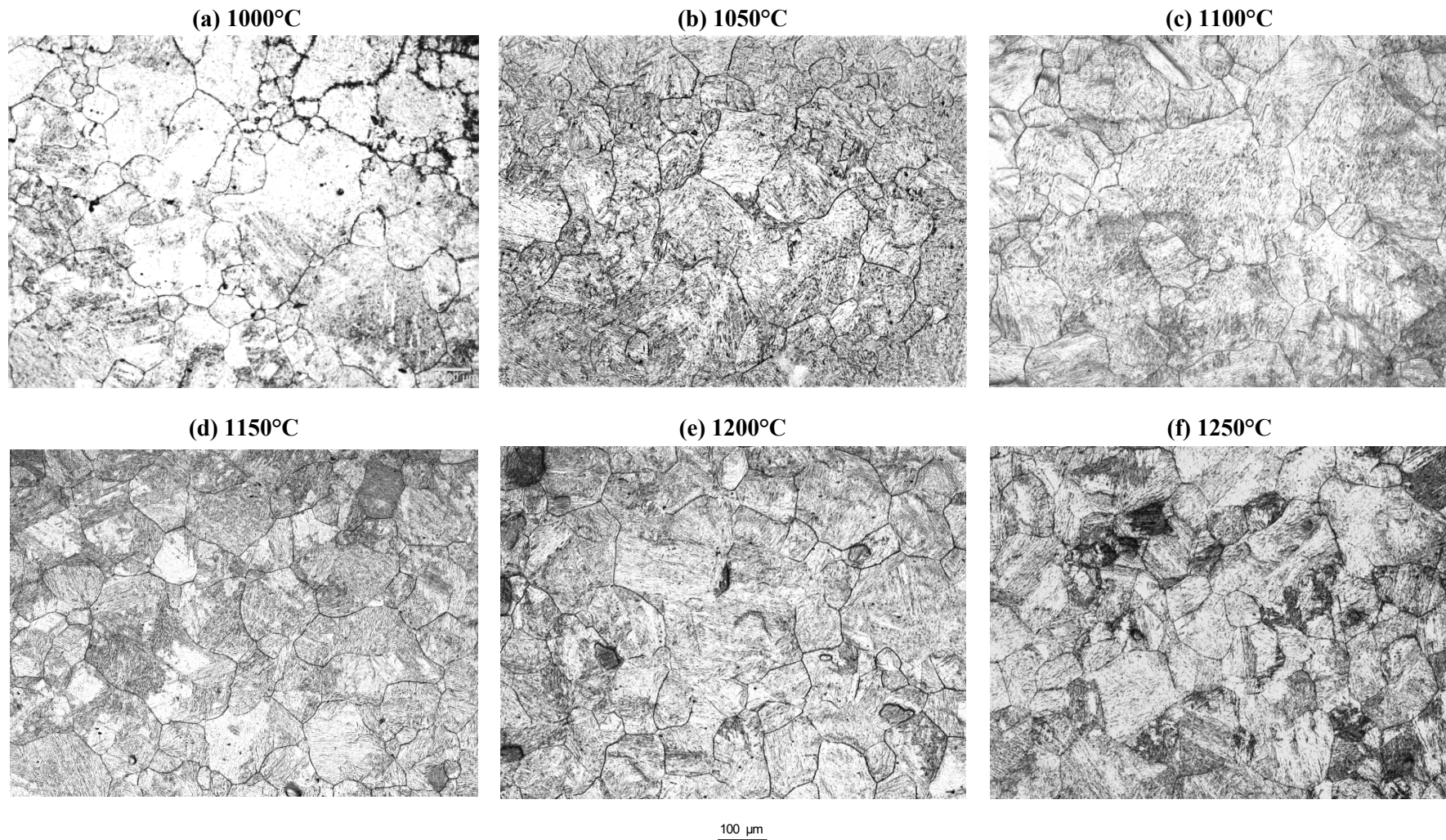


Figure 5.2 Prior austenite grain size for steel B1 at respective deformation temperature to the above reheating temperature and water quenching (Magnification: 100X)

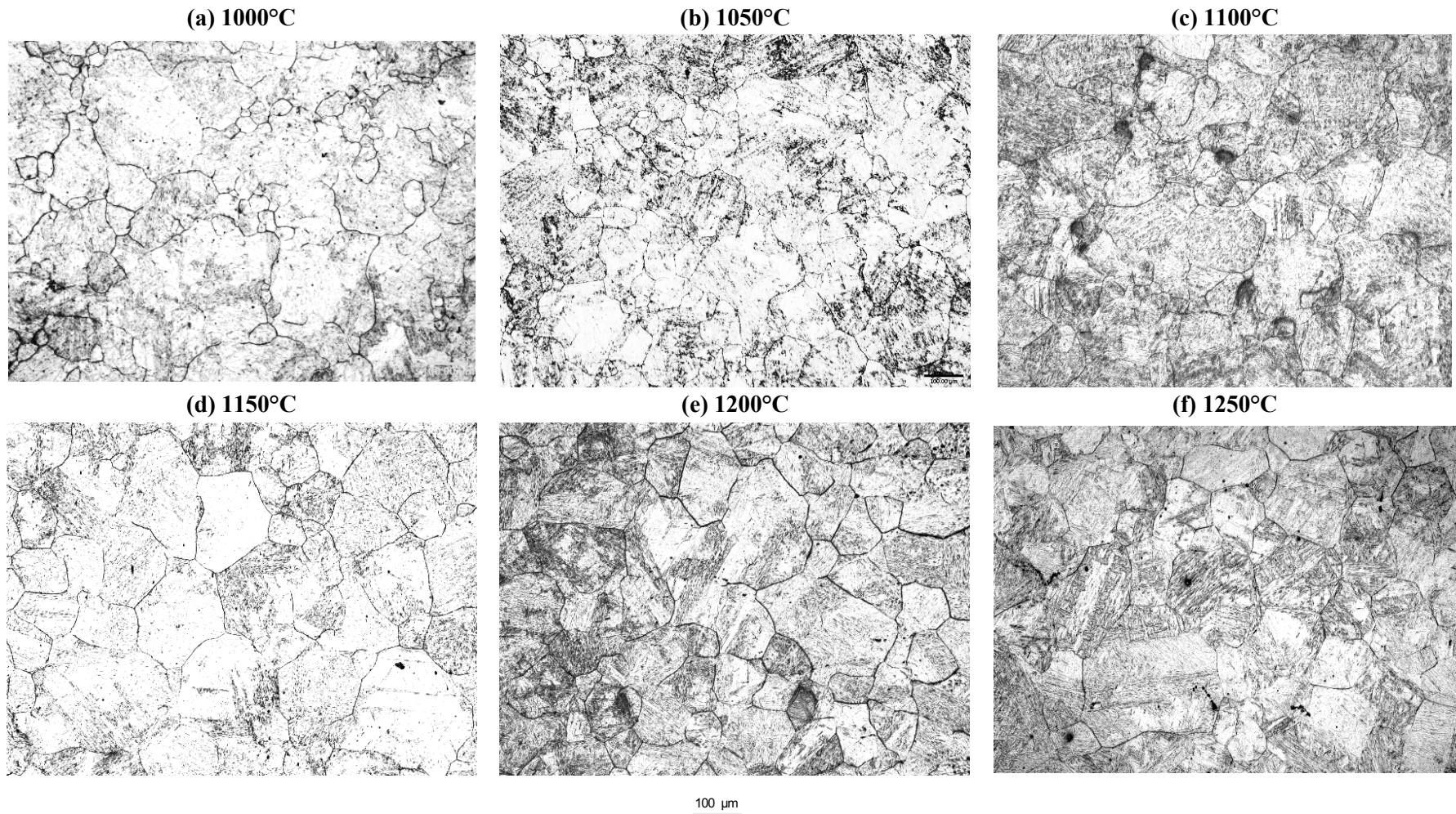
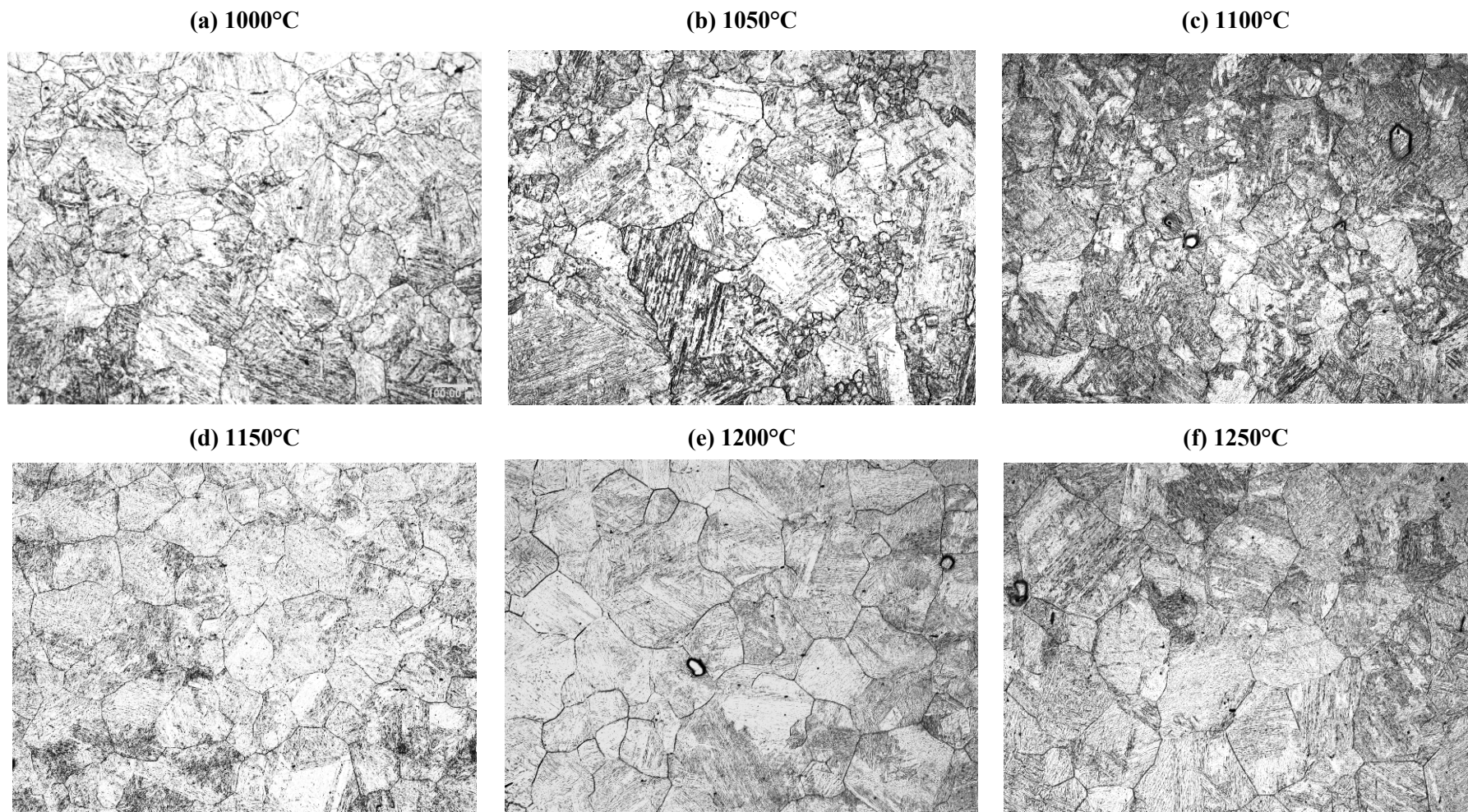


Figure 5.3 Prior austenite grain size for steel B2 at respective deformation temperature to the above reheating temperature and water quenching (Magnification: 100X)



100 μ m

Figure 5.4 Prior austenite grain size for steel B3 at respective deformation temperature to the above reheating temperature and water quenching (Magnification: 100X)

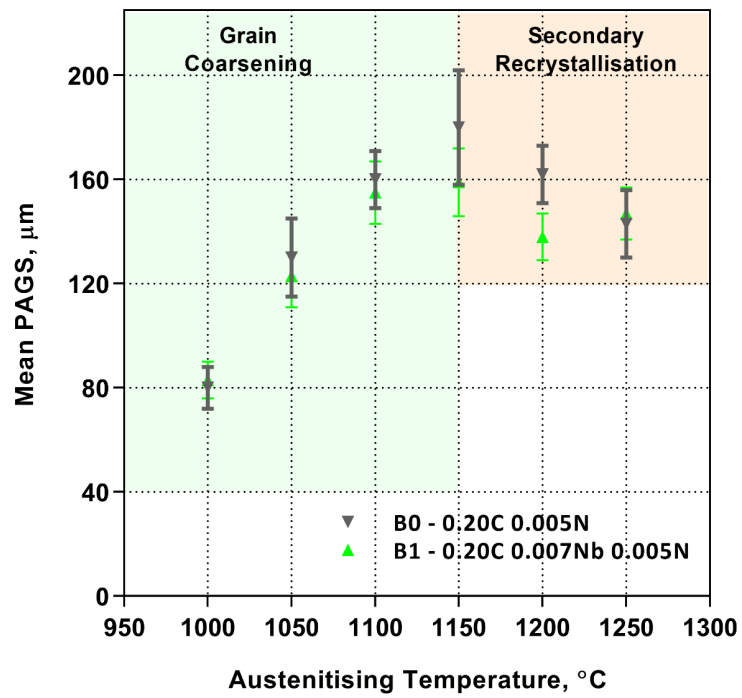


Figure 5.5 Mean austenite grain size as a function of reheating temperature for steel B0-B1

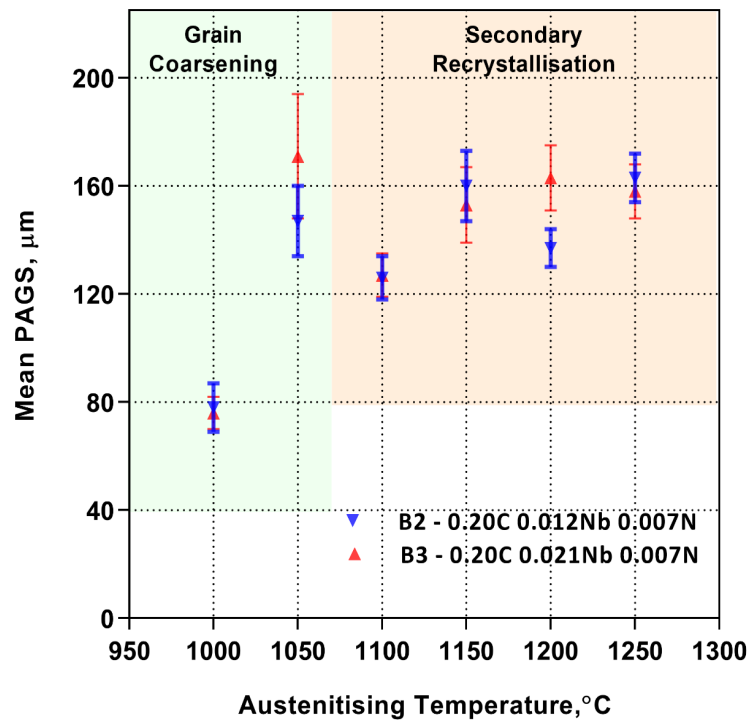
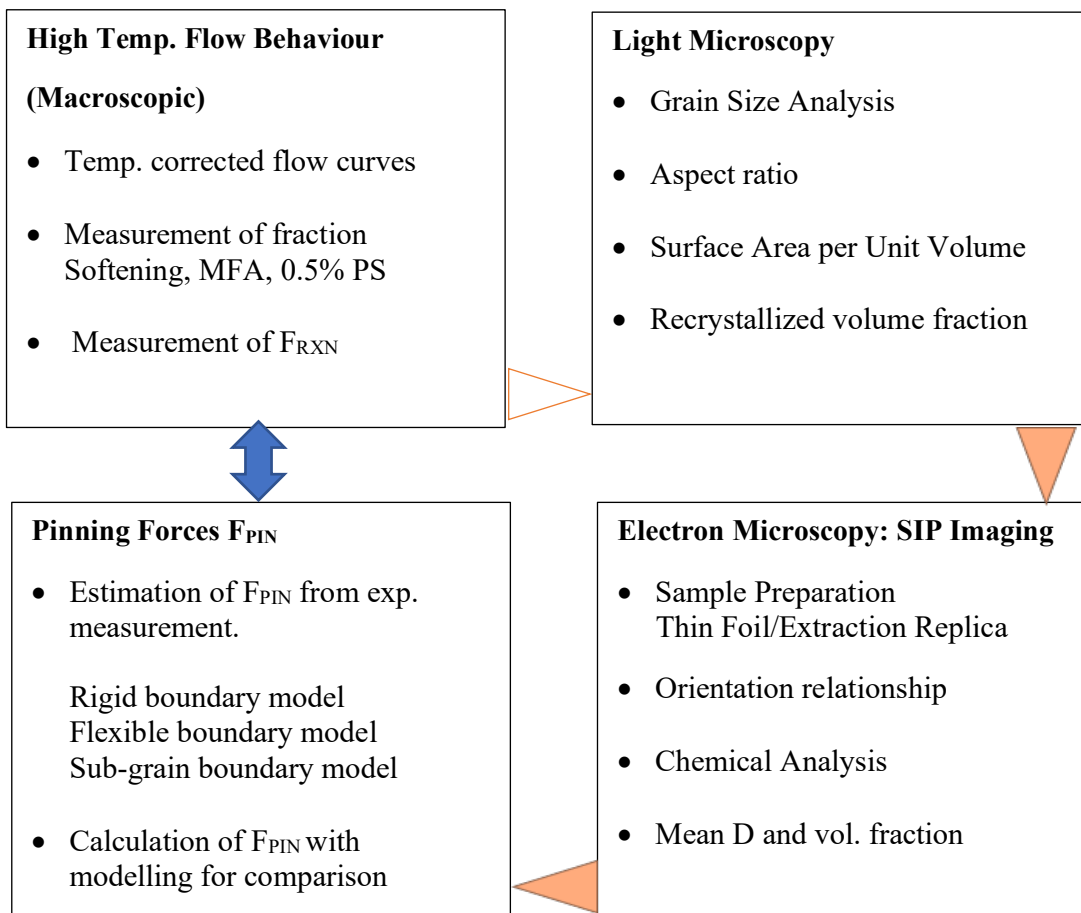


Figure 5.6 Mean austenite grain size as a function of reheating temperature for steel B2-B3

5.2 Static Softening Behaviour of Austenite

The fraction static softening behaviour of austenite was measured using a series of interrupted isothermal compression tests. The tests were performed with a prestrain of 0.10-0.40 for a hold time of 5 and 20 secs at a constant strain rate ($15s^{-1}$). These isothermal compression tests represented a significant portion of this research program. The understanding of fraction softening behaviour not only allowed determination of $T_{5\%}$ (i.e., recrystallisation-stop temperature) and $T_{95\%}$ (i.e., recrystallisation-limit temperature) but also provided a direct means to measure the driving force for recrystallisation, F_{RXN} for each of these steels.

Additionally, uninterrupted tests with an isothermal hold of 20 sec allowed experimental measurement Nb(CN) precipitate size and volume fraction for indirect determination of pinning force, F_{PIN} as a function of deformation processing variables. The result of softening studies is presented in a way that depicts the microstructure evolution of austenite during thermomechanical processing. The suppression of austenite static recrystallisation is correlated with Nb supersaturation and Nb(CN) precipitation at respective $T_{5\%}$ for each grade.



5.2.1 High-Temperature Flow Curves

Figure 5.7 shows the high-temperature flow curves of steel B3 from uninterrupted compression tests, $\epsilon = 0.80$ at different deformation temperatures. The amount of stress increases with decreasing deformation temperature for a given strain level. This flow behaviour is consistent with the Zener-Hollomon relationship [179]. Another notable feature is that we did not observe any dynamic recrystallisation in the present investigation at any deformation temperature. This observation is vital as static softening measured in the double-hit test will be exclusive of the static restoration event (i.e., recovery and recrystallisation) during the hold time. The area under the flow curves increases with decreasing deformation temperature, which means a large amount of stored energy is accumulated at a lower deformation temperature.

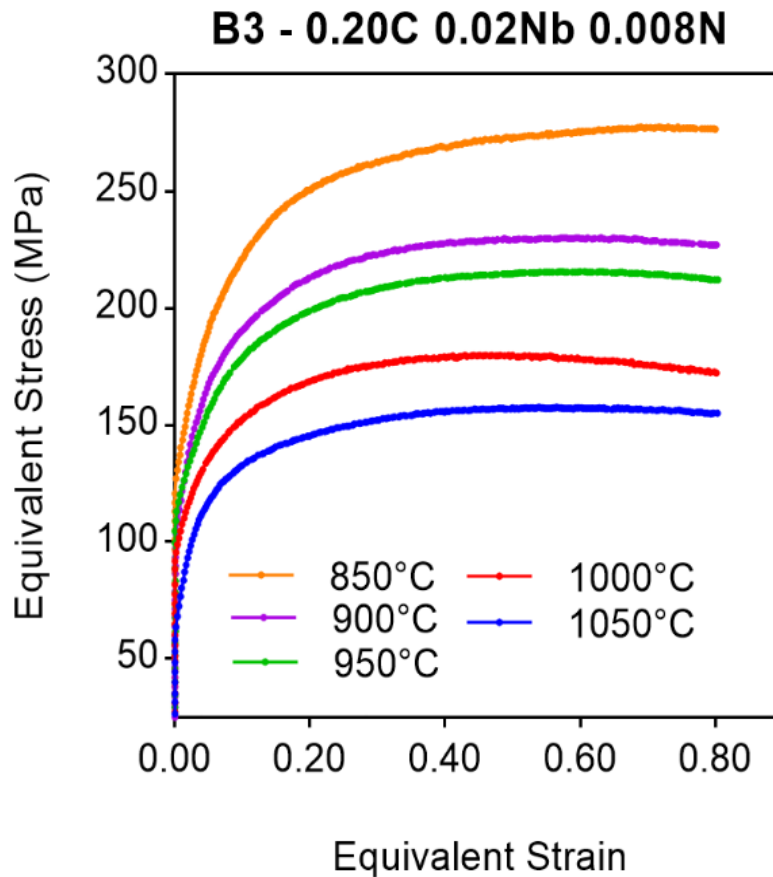


Figure 5.7 Flow stresses for steel B3 at different deformation temperatures during uninterrupted deformation ($\epsilon = 0.80$). A constant strain rate of 15 s^{-1} was applied.

Many of the earlier studies have used a laboratory rolling mill to deform the material [11,40, 48]. The direct measurement of flow stress was not possible in those cases leading to an inaccurate estimation of stored energy. In the present study, the use of a well-controlled TMC machine and PSC test enabled the more accurate determination of the increase in flow stress ($\Delta\sigma$) and corresponding stored energy. Palmiere *et al.* [154] proposed that flow stress at grain boundaries is 1.5 higher than the average flows stress obtained from mechanical testing.

This grain boundary flow stress assumption has been incorporated into the calculation of the change in dislocation density ($\Delta\rho$) from experimental flow curves for a true strain of $\varepsilon = 0.40$. The equation (2.17) and (2.19) were respectively used to calculate $\Delta\rho$ for steel B1-B3. Table 5.2 shows the values of $\Delta\rho$ estimated using Keh's relationship (Method 1) and Taylor's relationship (Method 2) for the same set of experimental data.

The driving force for static recrystallisation (F_{RXN}) is associated with the migration of recrystallisation front into the deformed region with the change in the dislocation density ($\Delta\rho$). The F_{RXN} was calculated according to equation (2.15) based on the model of strain-induced boundary grain motion [97-100]. Table 5.2 shows the values of F_{RXN} estimated for steel B1-B3. Figure 5.8 shows the evaluation F_{RXN} as a function of deformation temperature for steel B1-B3 based on data in the table.

Table 5.2 Driving force for recrystallisation (F_{RXN}) estimated from the flow curves at $\varepsilon = 0.40$

Deformation Temp °C	Steel B1			Steel B2			Steel B3		
	$\Delta\sigma$ (MPa)	$\Delta\rho$ (m ⁻²)	F_{RXN} (MPa)	$\Delta\sigma$ (MPa)	$\Delta\rho$ (m ⁻²)	F_{RXN} (MPa)	$\Delta\sigma$ (MPa)	$\Delta\rho$ (m ⁻²)	F_{RXN} (MPa)
Method 1-Keh's									
850	159.0	7.8E+15	7.02	152.0	7.1E+15	6.42	160.0	7.9E+15	7.11
900	129.0	5.1E+15	4.62	131.0	5.3E+15	4.77	135.0	5.6E+15	5.06
950	115.0	4.1E+15	3.67	112.0	3.9E+15	3.48	116.0	4.2E+15	3.74
1000	103.1	3.3E+15	2.95	100.2	3.1E+15	2.79	107.5	3.6E+15	3.21
1050	85.6	2.3E+15	2.04	92.5	2.6E+15	2.38	73.6	1.7E+15	1.50
Method 2-Taylor									
850	159.0	1.4E+15	2.92	152.0	1.3E+15	2.67	160.0	1.5E+15	2.96
900	129.0	9.5E+14	1.92	131.0	9.8E+14	1.98	135.0	1.0E+15	2.11
950	115.0	7.5E+14	1.53	112.0	7.2E+14	1.45	116.0	7.7E+14	1.56
1000	103.1	6.1E+14	1.23	100.2	5.7E+14	1.16	107.5	6.6E+14	1.34
1050	85.6	4.2E+14	0.84	92.5	4.9E+14	0.99	73.6	3.1E+14	0.63

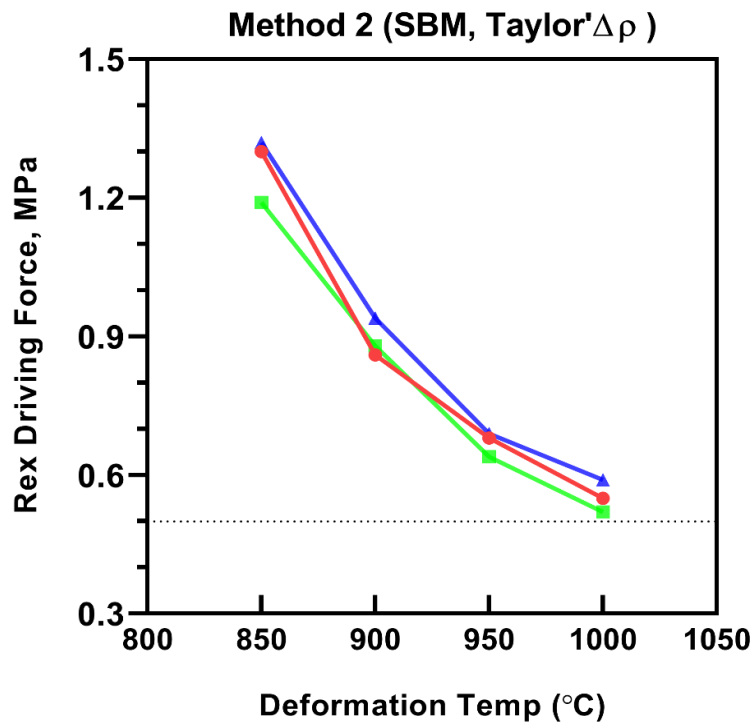
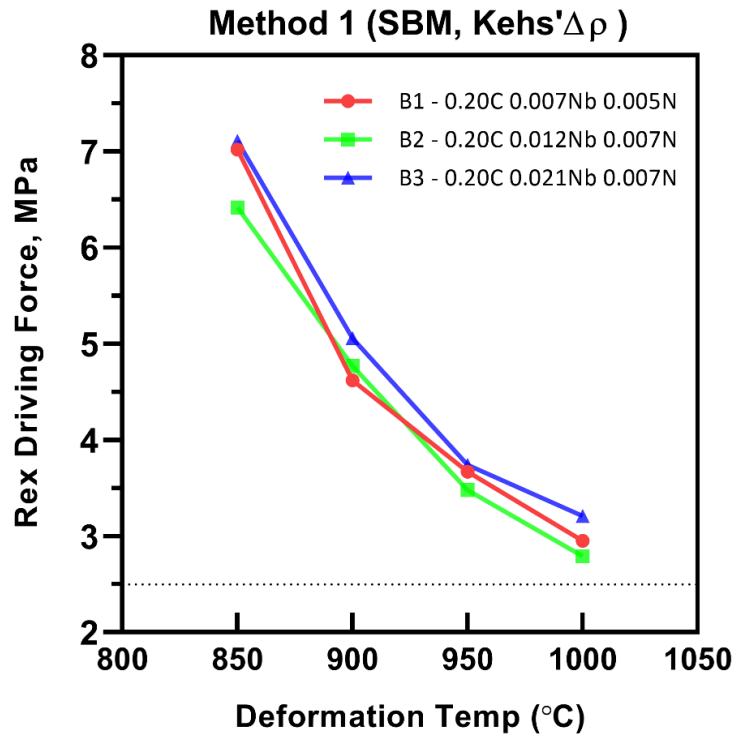


Figure 5.8 Recrystallisation driving force as a function of deformation temperature calculated from (a) Method 1 and (b) Method 2 for a true strain of $\epsilon = 0.40$ in steel B1-B3

Figures 5.9 - 5.12 shows the high-temperature flow curves respectively for steel B0-B3 from double hit tests at temperatures between 850-1050°C for a true strain, $\epsilon=0.40$ and a hold time of 20 sec. It is not feasible to include the flow curves for all strains and interpass timed due to the constraint of space. However, the flow curves at lower strains exhibit more or less similar flow behaviour.

The flow stresses increase with a decrease in deformation temperature, as seen in the single-hit deformation. The double deformation curves at specific temperatures, shown in Figures 5.9 - 5.12, vary only in Nb concentration and give a representation of softening/hardening kinetics. These flow curves are compared with the double deformation schematic, Figure 2.45, where areas relating to softening and hardening are identified.

Figure 5.9 shows the flow curves for steel B0 at a temperature between 850-1050°C. The flow curves in the second pass are approximately coincident of flow curves in the first pass. It indicates a complete static softening at all deformation temperatures for $\epsilon=0.40$. The softening increases with an increased hold time (area A_3 increases).

Figure 5.10 illustrates the flow curves for steel B1 at a temperature between 850-1050°C. At the lowest deformation temperature (i.e., 850°C), the flow stress in the second pass increased following the delay in comparison to the single-hit deformation curve. The apparent yield strength increase indicates the work hardening of austenite. As temperature increases further, the flow curves in the second pass match with the first pass for $T_{\text{def}} \geq 900^\circ\text{C}$, exhibiting complete softening similar to B0.

Figure 5.11 shows the flow curves for steel B2 at a deformation temperature of 850-1050°C. The flow curves exhibited complete softening for $T_{\text{def}} \geq 950^\circ\text{C}$ while a yield strength increase in a second pass was observed at low temperature, 850-900°C. The gradual change in second pass flow curves indicates the influence of Nb concentrations on recrystallisation kinetics.

Figure 5.12 illustrates the flow curves for steel B3 at a temperature between 850-1050°C. The significant austenite work hardening was observed at low deformation temperature, 850°C, for both interpass times, where the flow curves in the second pass were higher than continuous curves. The deformation at intermediate temperature showed increases in yield strength for a second pass. The flow curves exhibited complete softening for $T_{\text{def}} \geq 1000^\circ\text{C}$

The hold time in-between passes have a significant role to play in terms of an interaction between static restoration and precipitates. The hold time of 5 sec shows more strain hardening of austenite than 20 sec. Similarly, the true strain has a strong influence on static recrystallisation, i.e., softening kinetics. The flow curves at lower strain exhibited yield strength increment for certain test conditions compared to higher strains.

B0-0.20C-0.0Nb-0.005N/Base

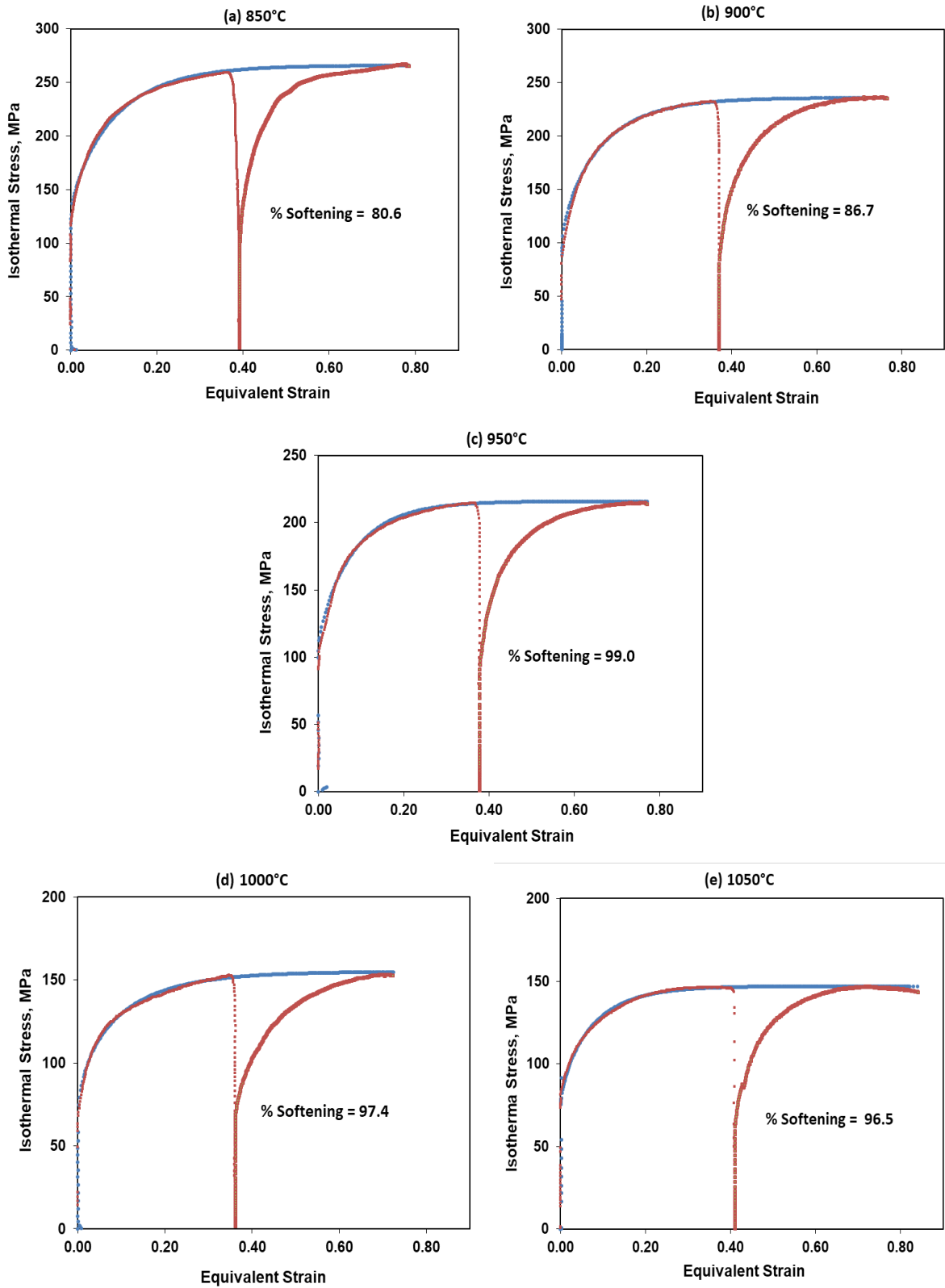


Figure 5.9 Flow Curves of steel B0 as a function of deformation temperature from interrupted compression tests, strain $\epsilon=0.40$ and IP= 20s (a) 850°C, (b) 900°C, (c) 950°C, (d) 1000°C and (e) 1050°C. All tests were carried out at constant strain rate $15s^{-1}$.

B1-0.20C-0.007Nb-0.005N

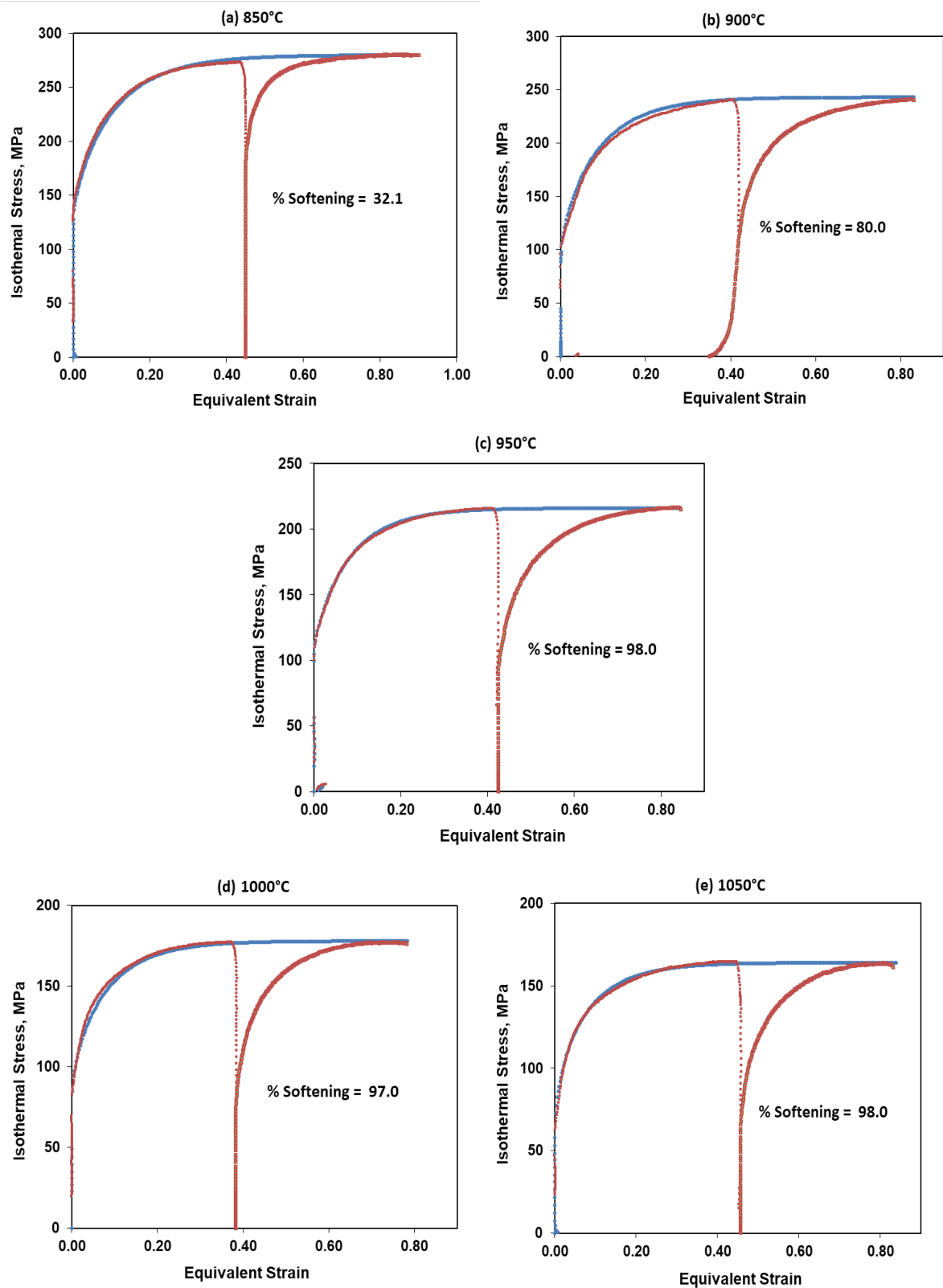


Figure 5.10 Flow Curves of steel B1 as a function of deformation temperature from interrupted compression tests, strain $\epsilon=0.40$ and $IP=20s$ (a) 850°C, (b) 900°C, (c) 950°C, (d) 1000°C and (e) 1050°C. All tests were carried out at constant strain rate $15s^{-1}$

B2-0.20C-0.012Nb-0.007N

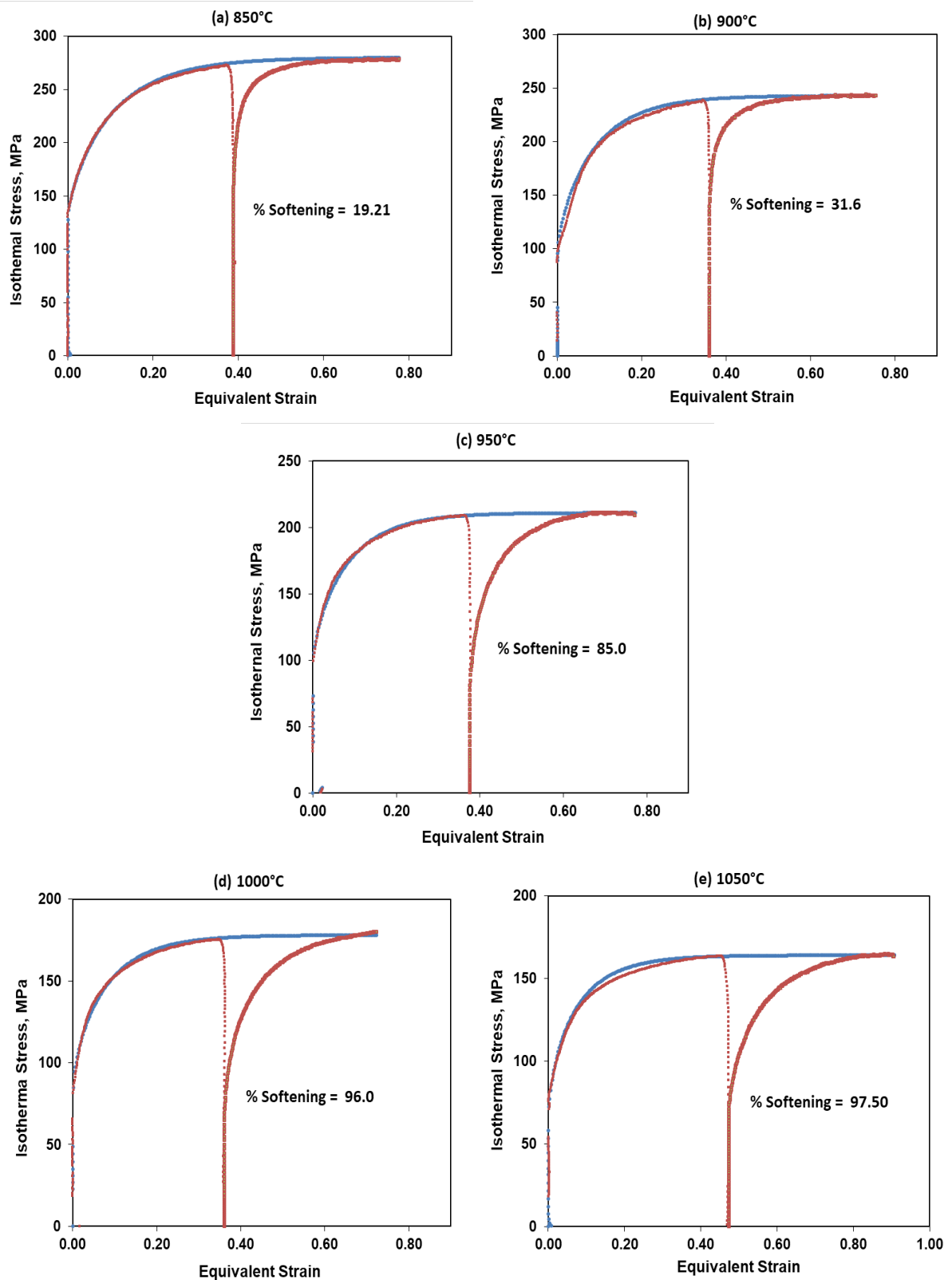


Figure 5.11 Flow Curves of steel B2 as a function of deformation temperature from interrupted compression tests, strain $\epsilon=0.40$ and IP= 20s (a) 850°C, (b) 900°C, (c) 950°C, (d) 1000°C and (e) 1050°C. All tests were carried out at constant strain rate $15s^{-1}$

B3-0.20C-0.021Nb-0.007N

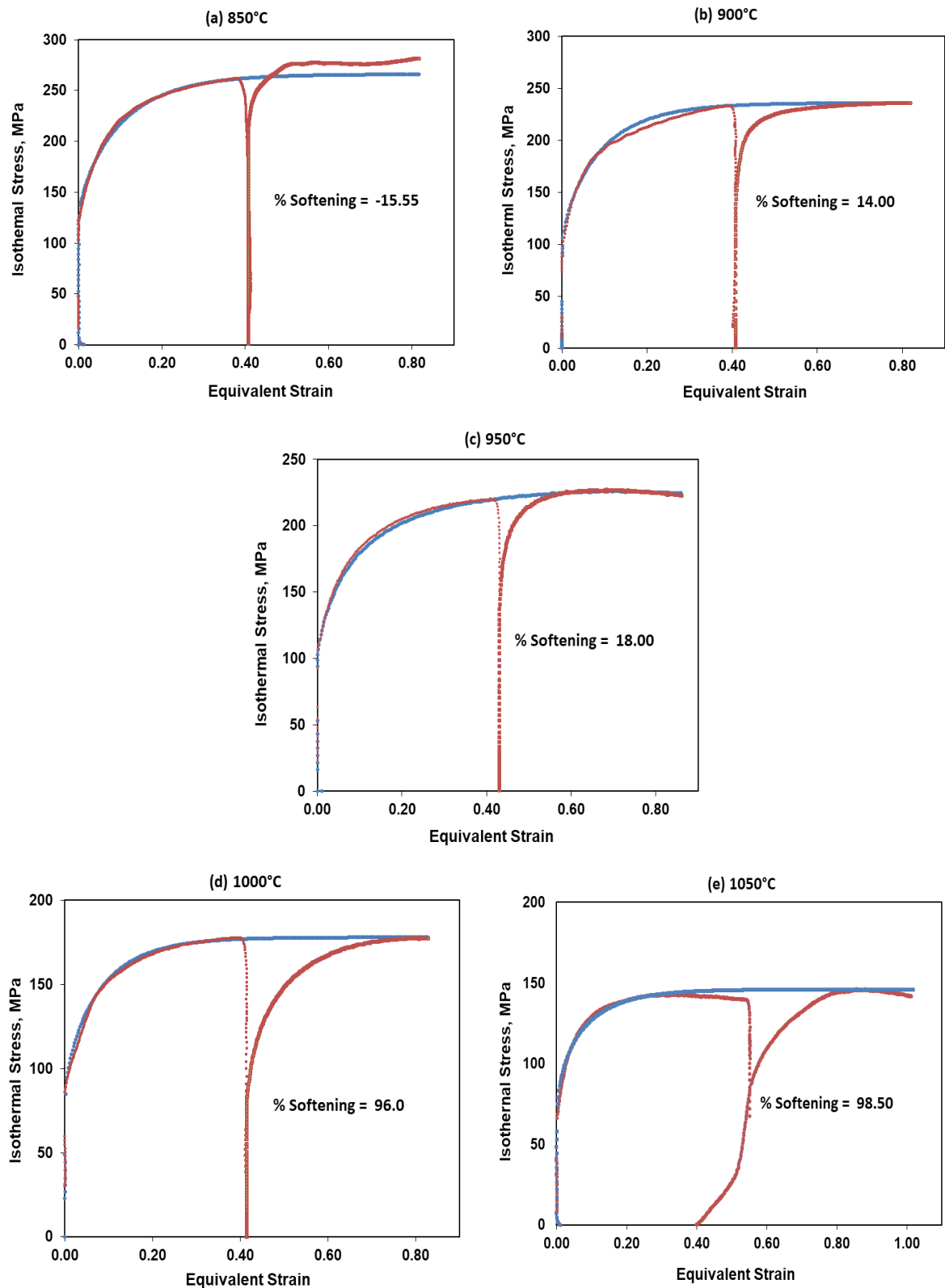


Figure 5.12 Flow Curves of steel B3 as a function of deformation temperature from interrupted compression tests, strain $\epsilon=0.40$ and IP= 20s (a) 850°C, (b) 900°C, (c) 950°C, (d) 1000°C and (e) 1050°C. All tests were carried out at constant strain rate $15s^{-1}$

5.2.2 Fractional Softening Behaviour

The overall softening behaviour of austenite is measured as a function of hold time from an area under the flow curves and parameter X_A (as described in section 2.7). Table 5.3 shows the percent fractional softening of steel B0-B3 as a function of deformation temperature and true strain during interrupted compression tests. Figure 5.13 graphically depicts the measured fractional softening for steel B0-B3 as a function of deformation temperature.

The fraction softening data in Figure 5.13 shows two types of behaviour based on the shape of softening curves. The first type of behaviour was characterized by sigmoidal form and observed in steel B0-B3 at all strain levels, except grade B3 at 850°C. The rate of fraction softening was slow initially (stage I), rises at an intermediate stage (stage II), and decreases as the static recrystallisation proceed to completion (stage III). The initial softening (up to 20% of total softening) is attributed to the static recovery process. The subsequent significant increase beyond this regime is caused by the initiation of static recrystallisation of austenite. The rate of fraction softening decreases with further temperature increase, and a plateau is observed indicating saturation of static recrystallisation process.

The second type of softening behaviour (i.e., deviation from the sigmoidal form) was only observed in steel B3 at 850°C. It showed a negative fraction softening (i.e., hardening) during the interpass time of 5 and 20 sec. This hardening was attributed to strain-induced precipitation of Nb(CN), as reported in earlier investigations on low carbon microalloyed steels [42,154,178]. The static restoration process is slow at this temperature; hence, precipitation hardening dominates. Dutta *et al.* [178] reported a similar level of fraction hardening up to -20% for hot deformation of austenite at 850 and 900°C in Nb microalloyed steel.

The austenite restoration process is thermally activated; hence, holding time in between passes has a significant influence on the recrystallisation kinetics. The static recrystallisation was not initiated for a hold time of 5 sec at low strains in steel B0-B2. However, holding time of 20 sec resulted in static softening for the same deformation condition.

Notably, Steel B0 (i.e., base composition) exhibited the fraction softening due to static recovery only at the lowest deformation temperature (850°C). The static recrystallisation was the dominant restoration mechanism and proceeded in a relatively uninhibited fashion for the rest of the deformation temperatures at all applied strains.

Table 5.3 Percent fractional softening of austenite as a function of deformation temperature. A negative value indicates the fractional hardening of austenite.

Deformation Temp	B0				B1				B2				B3			
	$\epsilon 0.10$	$\epsilon 0.20$	$\epsilon 0.30$	$\epsilon 0.40$	$\epsilon 0.10$	$\epsilon 0.20$	$\epsilon 0.30$	$\epsilon 0.40$	$\epsilon 0.10$	$\epsilon 0.20$	$\epsilon 0.30$	$\epsilon 0.40$	$\epsilon 0.10$	$\epsilon 0.20$	$\epsilon 0.30$	$\epsilon 0.40$

DHT – IP 5s

850	13.93	17.50	61.30	72.15	16.30	19.00	20.10	16.52	15.04	20.90	8.51	17.66	16.58	16.46	9.64	-2.70
900	19.00	46.15	78.00	80.52	18.00	20.97	37.29	52.38	15.74	16.75	23.73	22.15	14.50	10.43	12.30	10.12
950	28.00	76.00	84.00	93.00	26.10	56.00	87.00	96.00	26.00	21.00	58.82	77.15	24.00	18.00	19.30	22.57
1000	50.00	90.00	92.00	96.00	48.00	88.00	94.00	96.00	42.00	76.00	93.40	94.00	46.00	72.00	89.00	96.00
1050	62.30	84.91	93.95	94.40	58.00	86.00	96.00	97.00	44.00	81.00	98.62	99.10	48.96	78.12	99.38	98.50

DHT – IP 20s

850	18.00	20.00	65.69	78.36	19.20	16.90	21.55	36.13	18.50	20.55	18.79	19.20	16.55	13.81	1.51	-15.0
900	20.00	72.88	80.89	86.86	21.00	36.40	51.53	80.00	17.50	23.77	23.03	31.60	16.00	18.99	18.35	14.00
950	34.00	98.00	99.00	99.00	38.00	79.00	98.00	98.00	39.30	58.00	72.00	85.00	29.00	19.95	18.14	18.00
1000	50.00	94.00	92.00	96.00	54.00	91.00	97.00	96.00	51.00	84.00	86.00	92.00	58.00	82.00	92.00	96.00
1050	58.00	96.00	98.00	97.40	62.00	93.50	99.20	98.00	66.19	98.00	99.39	97.49	66.51	92.00	94.00	98.50



Non-recrystallised γ



Partially recrystallised γ



Fully recrystallised γ

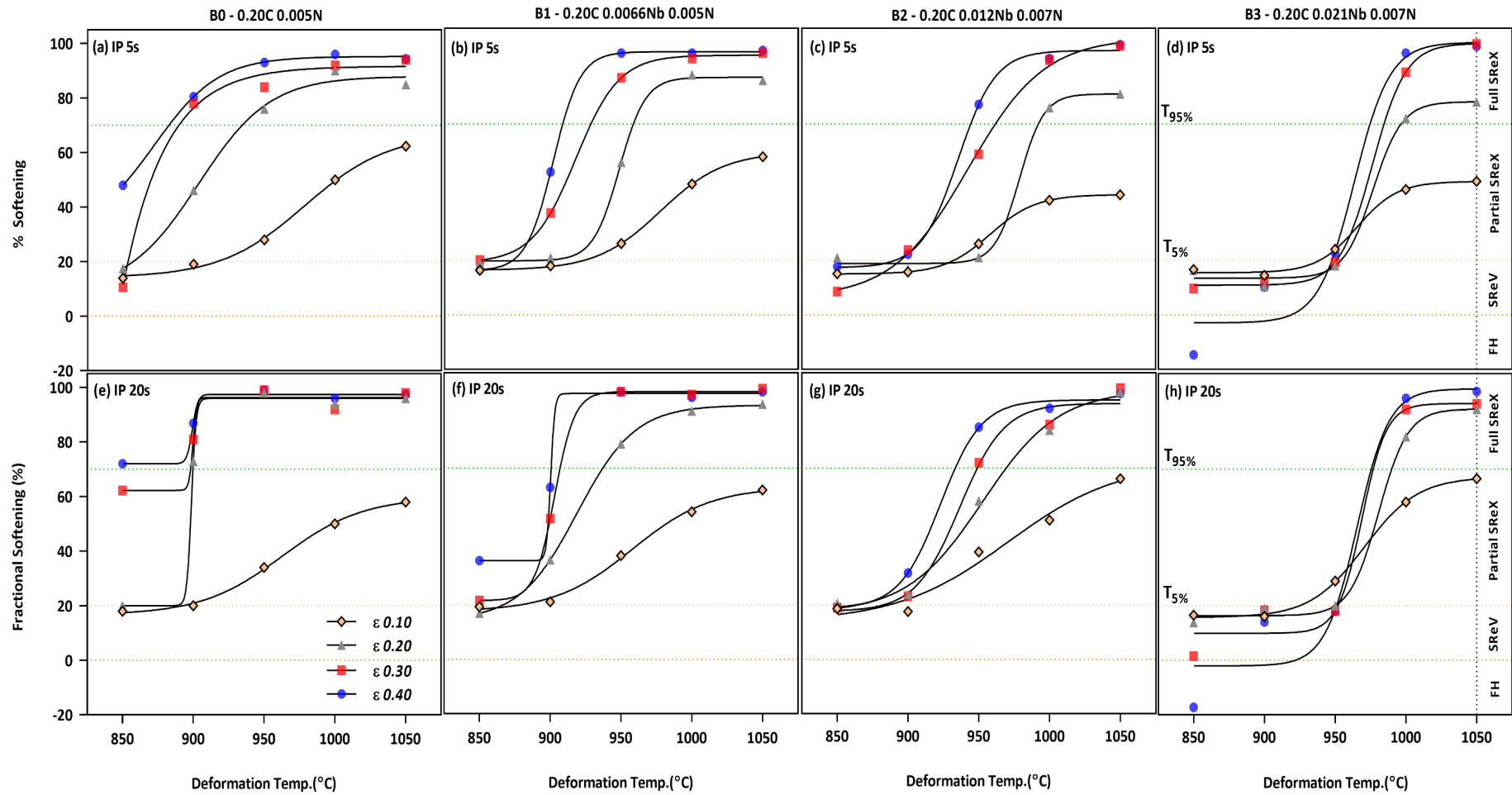


Figure 5.13 % Fractional softening of B0-B3 steel as a function of deformation temperature after interrupted compression testing for a hold time of 5 and 20 sec. All tests were carried out at a constant strain rate of 15 s^{-1} .

The $T_{5\%}$ (recrystallisation-stop temperature) for each steel has been identified for different strain using the softening criteria that 20% of overall softening corresponds to static recovery [66, 147, 154, 163, 178]. The complete retardation of the static recrystallisation is expected below 20% softening at given deformation temperature. The gradual extend beyond this value represents the onset of static recrystallisation event for a set hold time of 5 and 20 sec. The $T_{95\%}$ (recrystallisation-limit temperature) was determined from microstructure observation and corresponds to 70% overall fractional softening.

Table 5.4 presents the $T_{5\%}$ and $T_{95\%}$ temperatures determined as a function of pass strain from fractional softening criteria. The base steel exhibited static recrystallisation even at 850°C; hence, the $T_{5\%}$ was calculated by curve fitting the existing softening curves.

Table 5.4 $T_{5\%}$ and $T_{95\%}$ temperatures as a function of pass strain

Applied Strain	B0 0.0%Nb		B1 0.0066%Nb		B2 0.012%Nb		B3 0.021%Nb	
	$T_{5\%}$	$T_{95\%}$	$T_{5\%}$	$T_{95\%}$	$T_{5\%}$	$T_{95\%}$	$T_{5\%}$	$T_{95\%}$
IP 5 sec								
$\epsilon 0.10$	940	1050	945	970	965	1050	978	1050
$\epsilon 0.20$	875	933	904	959	955	994	972	996
$\epsilon 0.30$	835	890	893	929	925	961	965	985
$\epsilon 0.40$	825	881	873	908	910	944	950	980
IP 20 sec								
$\epsilon 0.10$	925	1050	935	960	960	1050	970	1050
$\epsilon 0.20$	865	897	890	937	925	969	965	990
$\epsilon 0.30$	830	870	870	910	910	949	955	976
$\epsilon 0.40$	820	870	855	907	900	933	943	976

Figure 5.14 shows both the upper and lower bound of the partial recrystallisation regime as a function of pass strain in the form of $T_{5\%}$ and $T_{95\%}$ temperature for interpass time of 5 and 20 secs. Both the $T_{5\%}$ and $T_{95\%}$ temperature decreases as pass strain increases for constant interpass time and strain rate conditions.

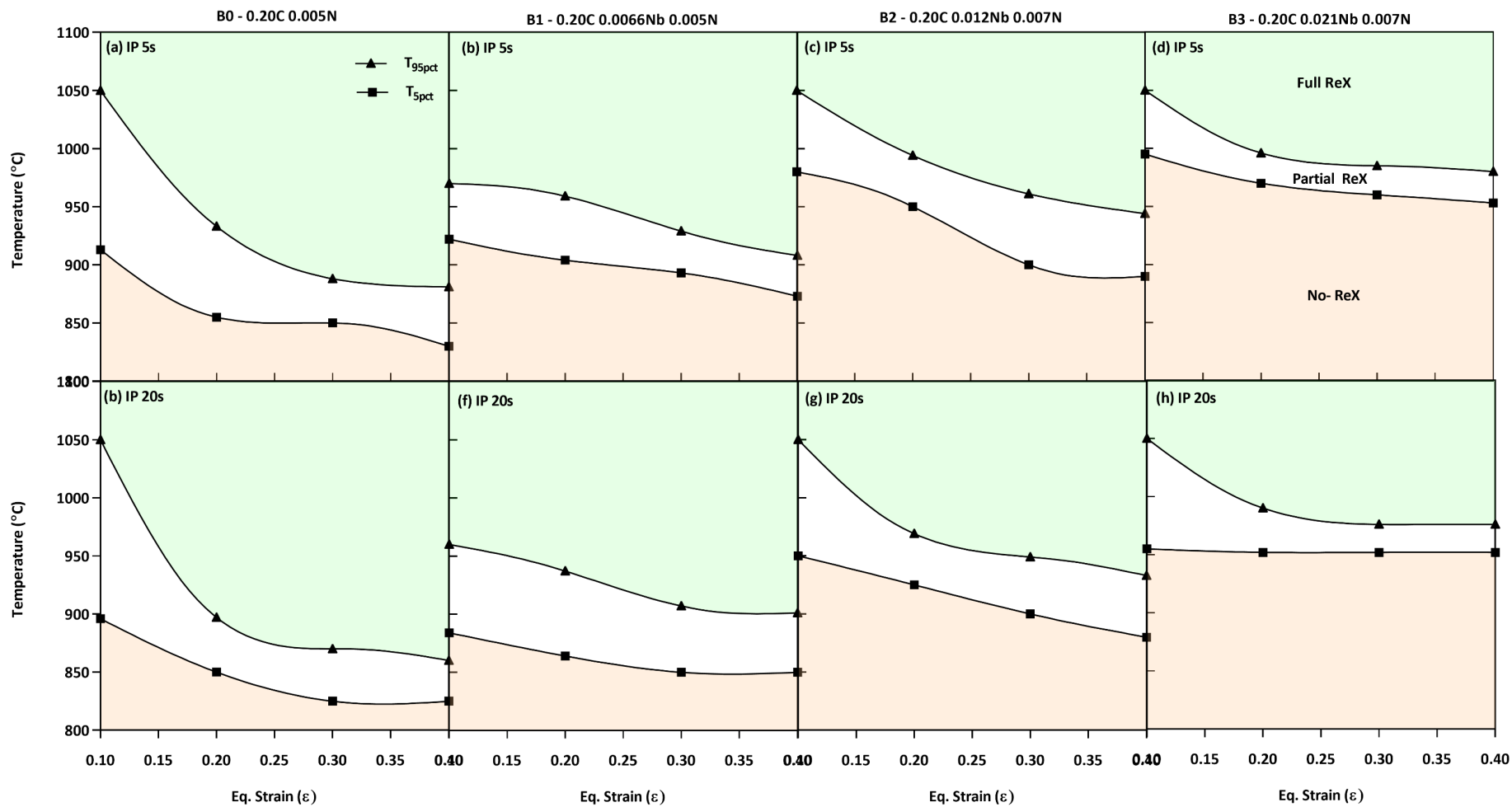


Figure 5.14 The $T_{5\%}$ and $T_{95\%}$ temperatures as a function of pass strain for a hold time 5 and 20 sec after interrupted compression testing. All tests were carried out at a constant strain rate of 15 s^{-1} .

5.2.3 Nb Supersaturation in Austenite

The Irvine *et al.* [127] solubility equation allows the calculation of Nb in solution in austenite at the respective reheating, $[Nb]_{\gamma}$, and deformation temperature, $[Nb]_{\epsilon}$. It is possible to determine the Nb supersaturation in austenite, $[Nb]_{SS}$ using the following relation:

$$[Nb]_{SS} = [Nb]_{\gamma} - [Nb]_{\epsilon} \quad (5.1)$$

Table 5.5 shows the estimated values $[Nb]_{SS}$ at the respective deformation temperature for steel B1-B3. The $[Nb]_{SS}$ is highest for the lowest deformation temperature and decreases as the deformation temperature increases for steel B1-B3. As shown in Figure 2.33, the solubility of Nb in austenite increases with temperature, which is subsequently reflected in lower $[Nb]_{SS}$ values at high temperatures. Also, $[Nb]_{SS}$ increases as the Nb concentration increases for a constant temperature, as seen in steel B1-B3. Steel B0 has no $[Nb]_{SS}$ available for precipitation at 1050°C, but the considerable potential exists for steel B3 at the same temperature.

Table 5.5 Nb supersaturation (wt %) as a function of deformation temperature

Deformation Temp °C	B0 0.0%	B1 0.007%	B2 0.012%	B3 0.021%
850	0.001	0.006	0.011	0.020
900	0.000	0.005	0.010	0.020
950	0.000	0.004	0.009	0.018
1000	0.000	0.002	0.007	0.017
1050	0.000	0.000	0.004	0.014

Note: The amount of Nb in solution at reheating and deformation temperature was calculated from Irvine et al. solubility equation [127]

The $[Nb]_{SS}$ in the present table (Table 5.5) and fractional softening data (Table 5.3) are combined as both being the function of deformation temperature. The aim was to understand the influence of $[Nb]_{SS}$ on the static softening behaviour of austenite. Figure 5.15 depicts the vital relationship between the % fractional softening of austenite and the corresponding $[Nb]_{SS}$ for a given deformation temperature. The $T_{5\%}$ increases with an increase of $[Nb]_{SS}$ in steel B1-B3 and shifts the retardation of static recrystallisation to high temperature.

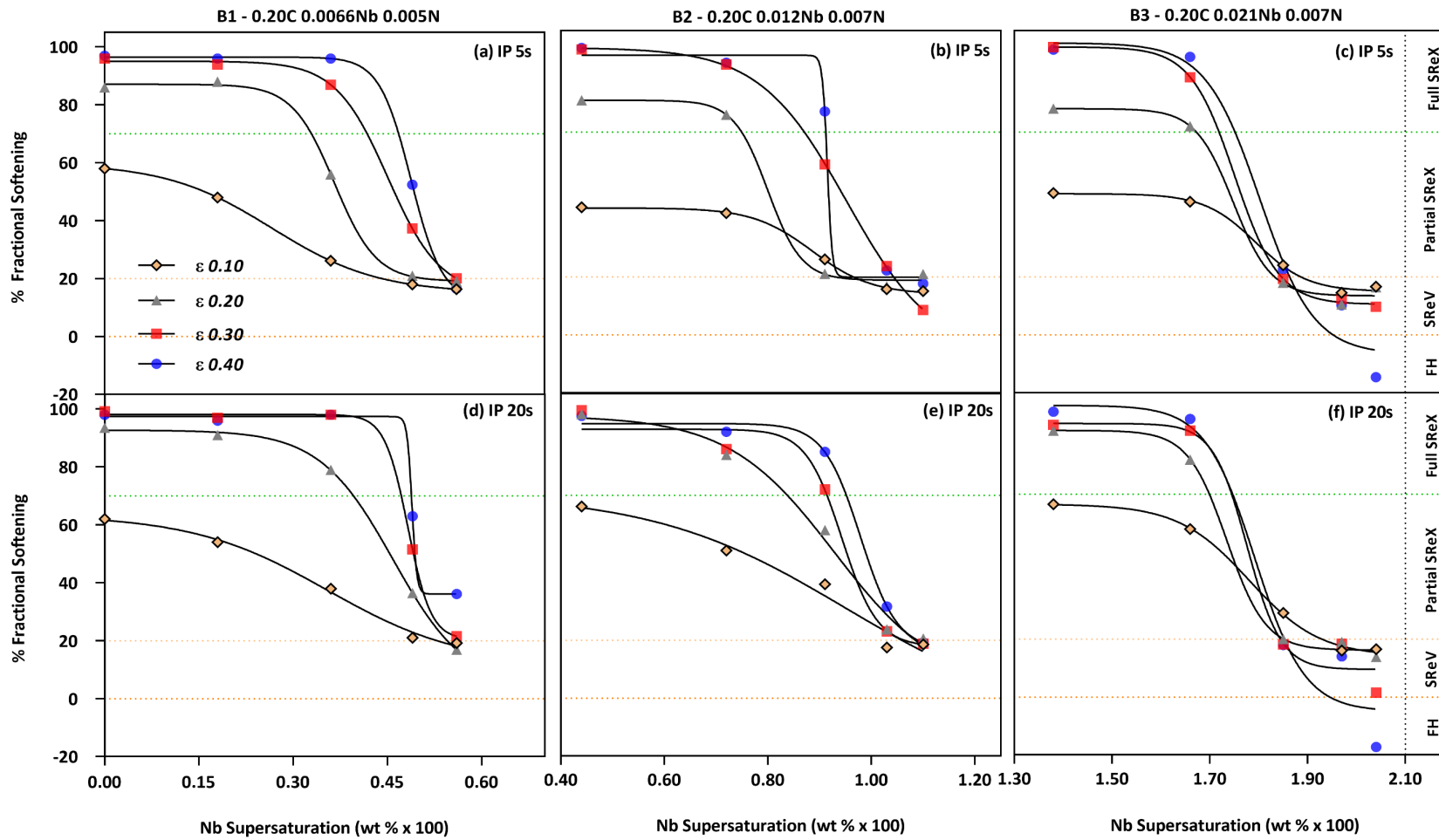


Figure 5.15 Percent fractional softening as a function of Nb supersaturation in austenite for steel B1-B3

Nb supersaturation ratio in austenite, $[Nb]_{SSR}$ is defined as being the ratio of the solubility product of Nb(CN) in austenite at reheating temperature to the solubility product of austenite at the deformation temperature. The relationship is as follows:

$$[Nb]_{SSR} = [Nb]_{\gamma} / [Nb]_{\epsilon} \quad (5.2)$$

Table 5.6 shows the estimated values of $[Nb]_{SSR}$ at the respective deformation temperature for steel B1-B3. $[Nb]_{SSR}$ decreases as the deformation temperature increases for steel B1-B3.

Table 5.6 Nb supersaturation ratio as a function of deformation temperature

Deformation Temp °C	B0	B1	B2	B3
850	1.87	6.87	12.59	22.41
900	1.04	3.82	7.01	12.48
950	0.61	2.23	4.09	7.29
1000	0.37	1.36	2.49	4.44
1050	0.23	0.86	1.58	2.81

Note: the amount of Nb in solution at reheating and deformation temperature was calculated from Irvin *et al.* solubility equation [127].

The $[Nb]_{SSR}$ of the present table (Table 5.6) and fraction softening data (Table 5.3) are combined as both the being function of deformation temperature. The aim is to establish the relationship between $[Nb]_{SSR}$ and the static softening behaviour of austenite. Figure 5.16 shows the relationship between $[Nb]_{SSR}$ and the percent fractional softening of austenite for steel B1-B3.

The fractional softening decreases as the $[Nb]_{SSR}$ increases at the respective deformation temperature. The result shows that the static recrystallisation was inhibited whenever $[Nb]_{SSR} \geq 6$ at the given deformation temperature.

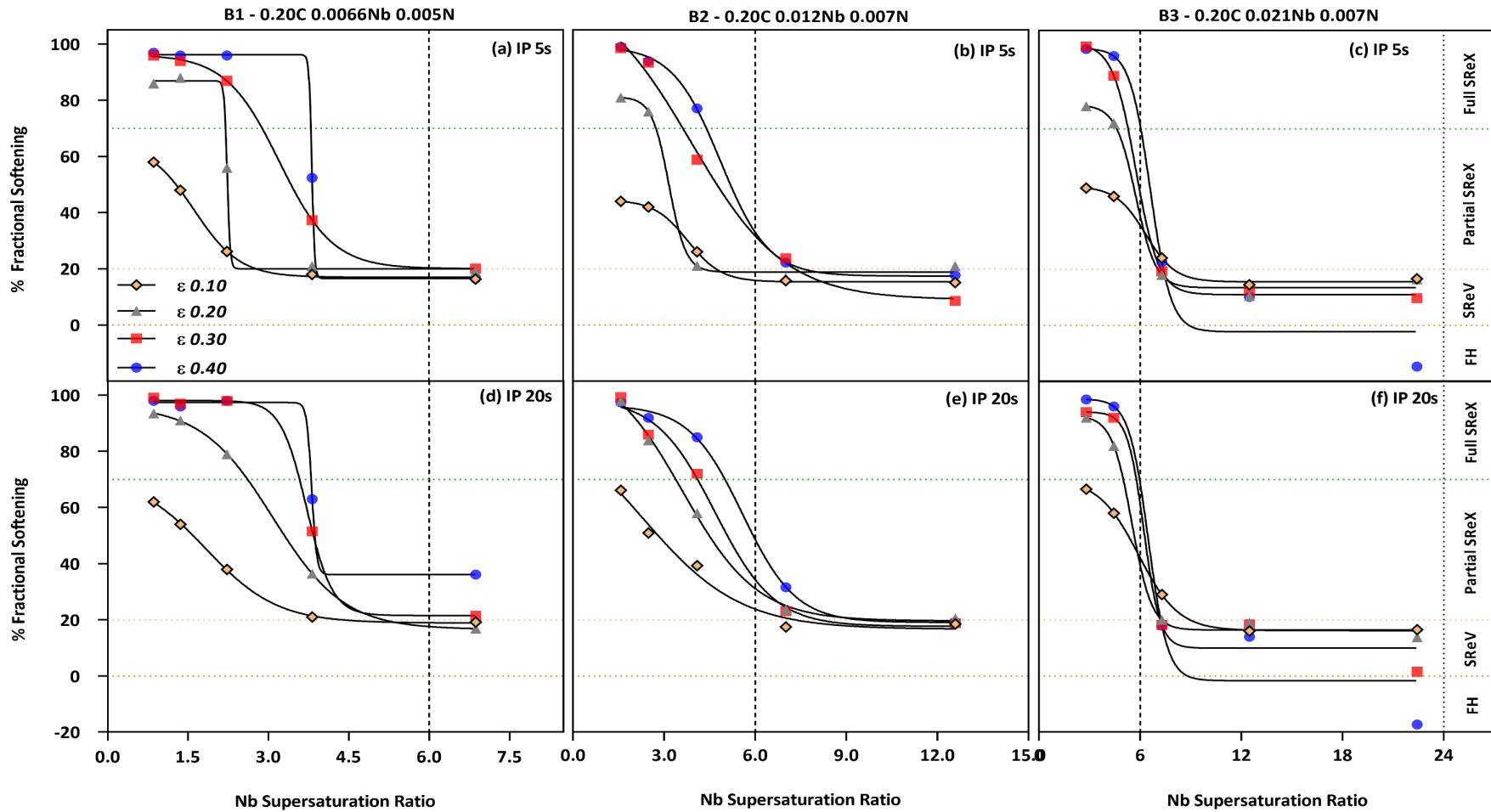


Figure 5.16 Percent fractional softening as a function of Nb Supersaturation Ratio for steel B1-B3

5.2.4 Microstructural Observation: Optical

The macroscopic flow behaviour was obtained over a sizeable deformed area (approx. 450 mm²) during hot compression testing. The quantitative metallography reveals the microscopic behaviour of austenite in a tiny area (approx. 1 mm²). The aim was to quantify the previously described agreement between the microstructure and percent fractional softening data.

5.2.3.1 Single-Hit Deformation, $\epsilon=0.20-0.80$

Figure 5.17 shows the series of micrographs of base composition (steel B0) subjected to a single hit deformation cycle of strain, $\epsilon=0.20-0.80$, in compression testing. The samples were immediately quenched to room temperature after the deformation. The microstructure appears to be fully martensite, mostly a lath structure. There was no indication of the formation of pro eutectoid ferrite along the prior austenite grain boundaries.

The austenite microstructure varies as a function of the Zener-Holloman parameter (Z), which is evident in optical micrographs. A deformed and unrecrystallised austenite microstructure was observed at the lowest deformation temperature of 850°C for a true strain, $\epsilon=0.20-0.40$ (high Z). The complete recrystallised microstructure was observed at deformation temperature, $T_{\text{def}} \geq 900^\circ\text{C}$, (low Z) for all strains.

The linear intercept grain sizes, \bar{L}_3 , was measured from the counts in ND directions for different strains. Figure 5.18 shows the \bar{L}_3 as a function of deformation temperature for steel B0 at the end of single hit deformation. The figure clearly shows the effect of lighter reductions, i.e., strains on broader grain size distribution observed at 950°C for strain $\epsilon=0.20$ and 0.40.

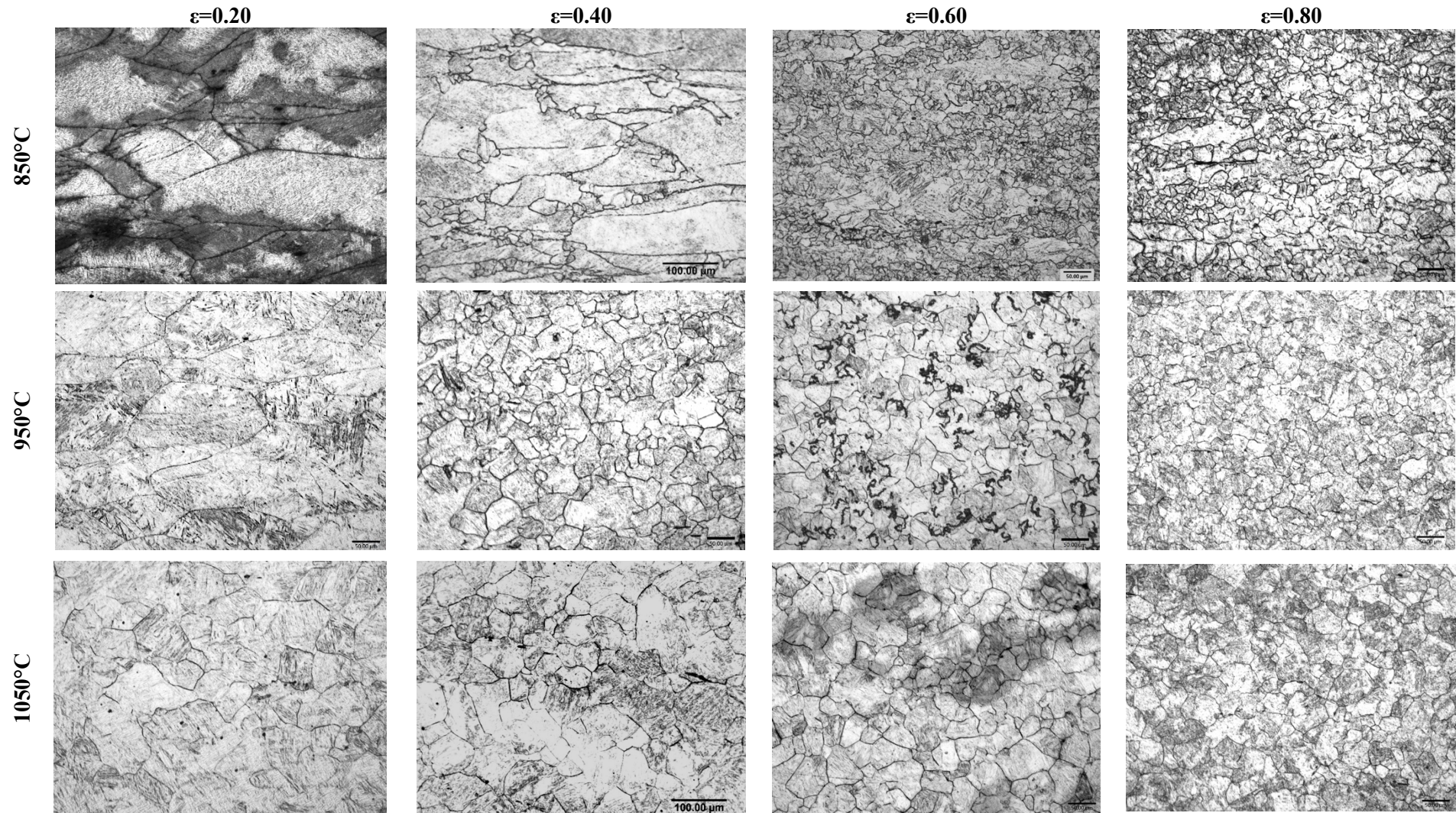


Figure 5.17 Microstructure evaluation of steel B0 at the respective deformation temperature in a single hit deformation cycle. The microstructure was obtained after reheating to 1250°C, uninterrupted compression testing at different strain, $\epsilon=0.20-0.80$ and immediate WQ (Magnification 200X)

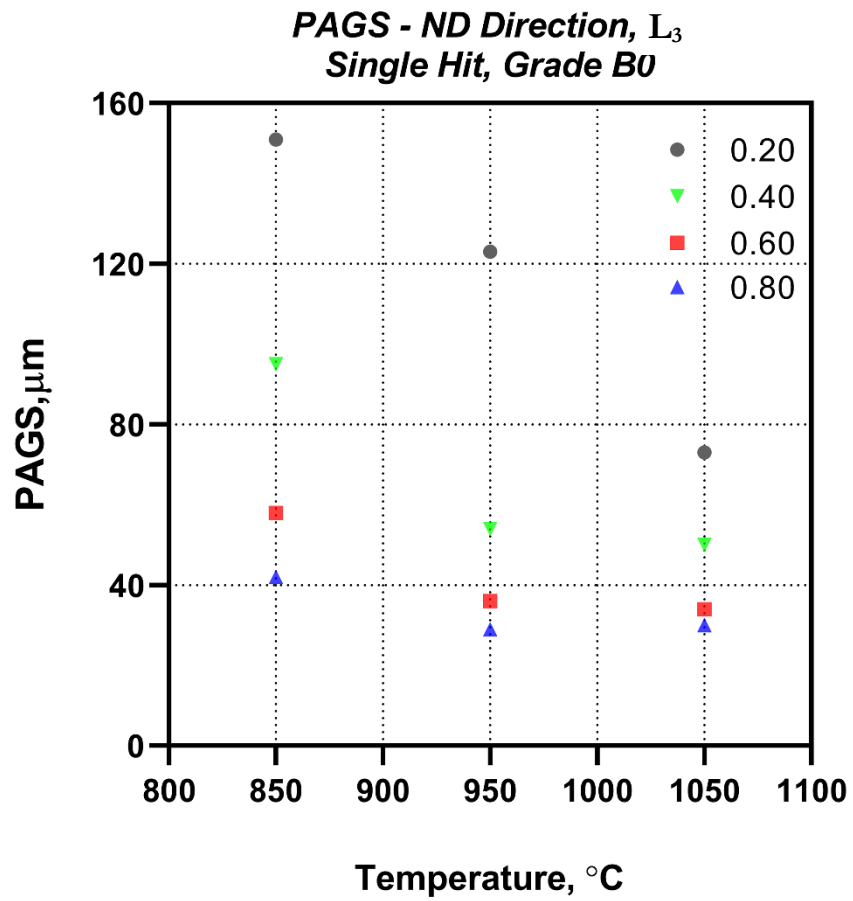


Figure 5.18 Linear intercept grain size \bar{L}_3 (ND) as a function of deformation temperature for steel B0 at different pass strains in a single hit deformation cycle.

5.2.3.2 Single-Hit Deformation, $\epsilon=0.80$

The high-temperature flow curves exhibited steady-state conditions at all temperatures, which indicates that dynamic recovery was the only operating restoration mechanism during this single-hit deformation. The resulting microstructure should be elongated grain structure with poor subgrain boundary development at all deformation temperatures.

Figure 5.19 shows the series of micrographs of steel B1-B3 subjected to a single hit deformation cycle of maximum strain, $\epsilon=0.80$ in hot compression testing. Steel B1-B3 showed a completely deformed and unrecrystallised austenite microstructure at the lowest deformation temperature of 850 and 900°C (except B1 at 900°C). However, the equiaxed recrystallised grains were observed for deformation temperature, $T_{\text{def}} \geq 950^\circ\text{C}$, for steel B1-B3.

This discrepancy could be a result of the delay in quenching the specimen after the hot deformation. The delay time between the end of deformation and quenching is approximately 1.0-1.5 secs. The time for 5% recrystallisation ($t_{5\% \text{ rex}}$) was using Sellars empirical equation [70] and found to be 0.10 sec for a true strain, $\epsilon=0.80$ at 950°C. The static recrystallisation was initiated and completed in a short time (< 1.0 sec), even before quenching due to a higher driving force for recrystallisation. Hence, the estimation of $t_{5\% \text{ rex}}$ supports the observation of equiaxed recrystallised grains observed at high temperature due to rapid static recrystallisation.

Figure 5.20 shows the linear intercept grain size \bar{L}_3 as a function of deformation temperature for steel B1-B3 at the end of single hit deformation. The recrystallised grain size decreases linearly for steel B1-B3 as the deformation temperature decreases. The linear intercept grain size, \bar{L}_3 , for unrecrystallised austenite is in the range of 35-40 μm for low-temperature hot deformation, i.e. 850-900°. The steel B1-B3 exhibits similar grain size values.

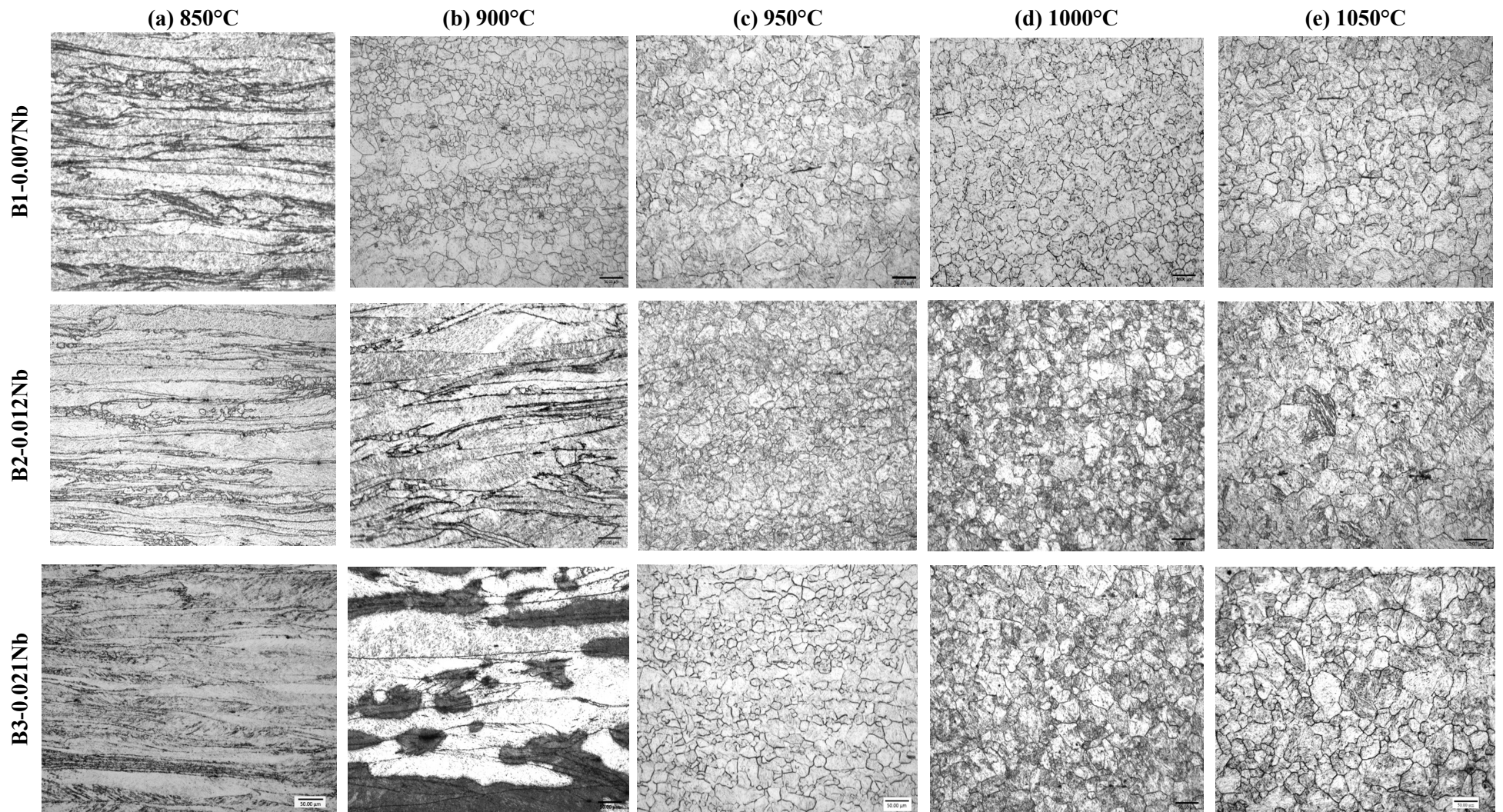


Figure 5.19 Microstructure evaluation of steel B1-B3 at respective deformation temperature in a single hit deformation cycle. The microstructure was obtained after reheating to 1250°C, uninterrupted compression testing at a maximum strain, $\epsilon=0.80$ and immediate WQ (Magnification 200X)

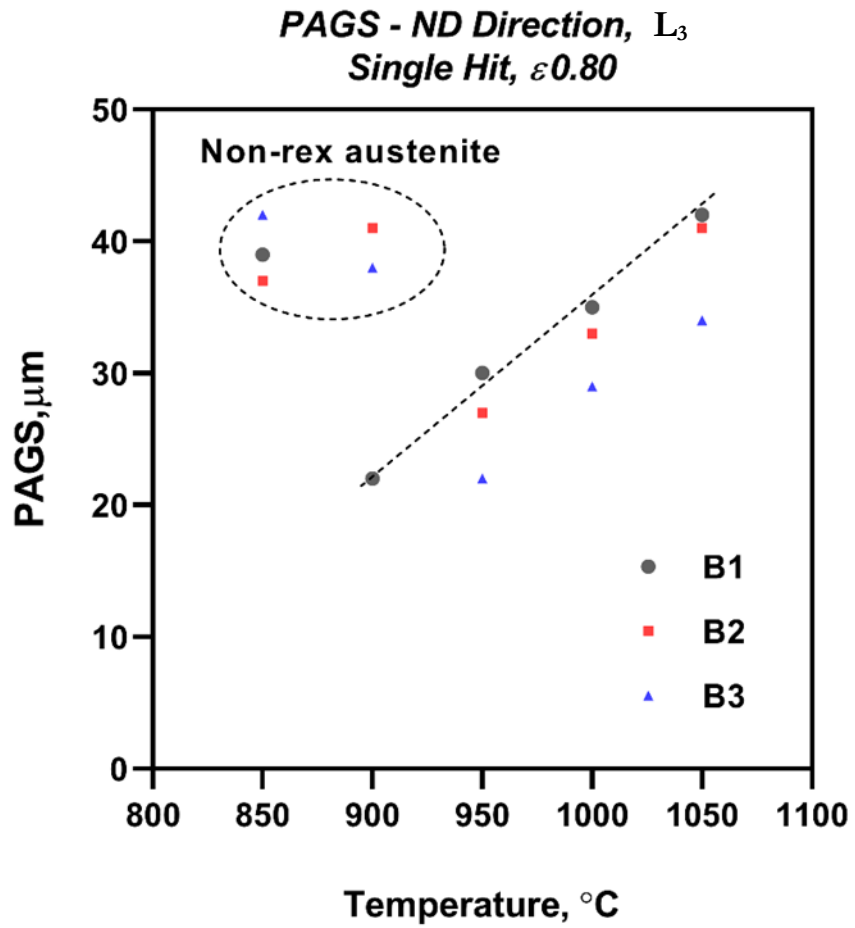


Figure 5.20 Linear intercept grain size \bar{L}_3 (ND) as a function of deformation temperature for steel B1 - B3 in a single hit compression testing at a maximum strain, $\epsilon=0.80$.

5.2.3.3 Single-Hit Deformation Plus Isothermal hold ($\epsilon=0.40$, IP=20s)

Figure 5.21 - Figure 5.23 shows the microstructures of steel B1-B3, respectively subjected to a single hit cycle of strain, $\epsilon=0.40$ with an isothermal hold of 20 sec. The microstructures were obtained after the immediate end of isothermal hold time.

The excellent agreement is obtained between microstructure (Figure 5.21 - Figure 5.23) and fraction softening data (Figure 5.13) from compression tests. These microstructures evaluation verified the correspondence between $T_{5\%}$ and 20% fractional softening criteria. At temperature below the $T_{5\%}$, a complete unrecrystallised austenite microstructure was observed in steel B1-B3. At temperature above the respective $T_{95\%}$ for each steel, a complete recrystallised austenite microstructure consisting of small equiaxed grains was observed. The $T_{95\%}$ temperature corresponds to 70% overall fractional softening of austenite.

For example, the $T_{5\%}$ and $T_{95\%}$ for steel B1 was identified as 850°C and 900°C from fractional softening curves for a true strain, $\epsilon=0.40$, and hold time of 20 sec. These temperatures fit well with the sequence of microstructure for steel B1, as shown in Figure 5.21. The microstructure at 850°C reveals a completely deformed and unrecrystallised prior austenite structure elongated in a perpendicular direction to the axis of compression. The micrographs at 900°C exhibits a complete recrystallised austenite microstructure consisting of small equiaxed grains.

A similar correspondence between compression test results and microstructure was found for steels B2. The $T_{5\%}$ and $T_{95\%}$ for steel B2 was identified as 890°C and 930°C from fraction softening curves for a true strain, $\epsilon=0.40$. The DHT tests were done in temperature increment of 50°C, the microstructure at 900°C, close to $T_{5\%}$, reveal a deformed and unrecrystallised prior austenite structure. While the micrographs at 950°C, just above $T_{95\%}$, exhibits a complete recrystallised austenite microstructure (Figure 5.22).

The $T_{5\%}$ and $T_{95\%}$ for steel B3 was identified as 953°C and 980°C from fraction softening curves for a true strain, $\epsilon=0.40$. These temperatures fit well with the sequence of microstructure for steel B3, as shown in Figure 5.23. The microstructure at 950°C reveals a completely deformed and unrecrystallised prior austenite structure elongated in a perpendicular direction to the axis of compression. The micrographs at 1000°C exhibits a complete recrystallised austenite microstructure consisting of small equiaxed grains.

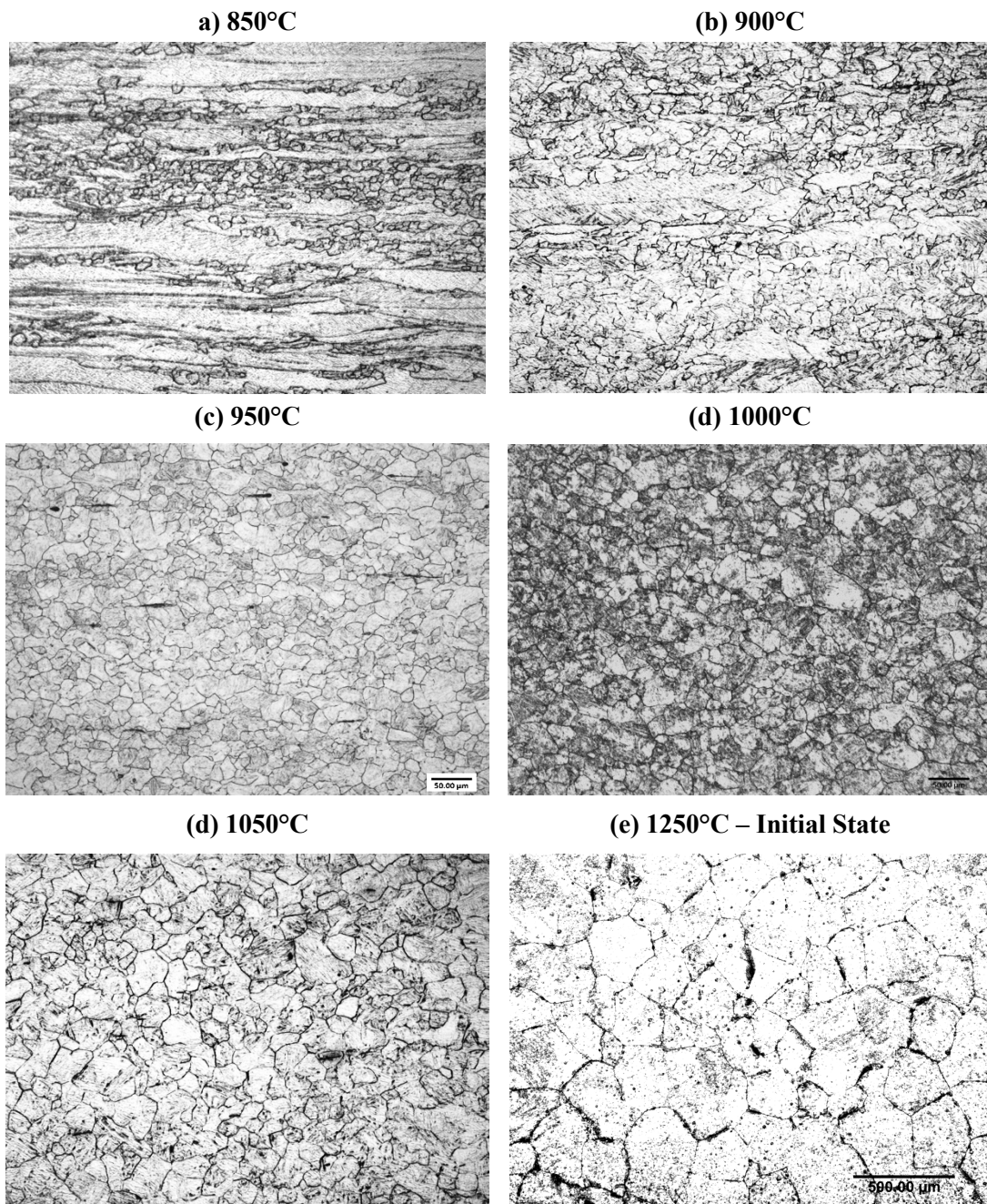


Figure 5.21 Microstructure evaluation of grade B1 at the respective deformation temperature. The microstructure was obtained after reheating to 1250°C, single hit deformation at strain $\epsilon=0.40$, an isothermal hold of 20 secs, and WQ. The constant strain rate of $15s^{-1}$ was applied. This steel had a $T_{5\%}$ of 855°C as measured from fraction softening studies.

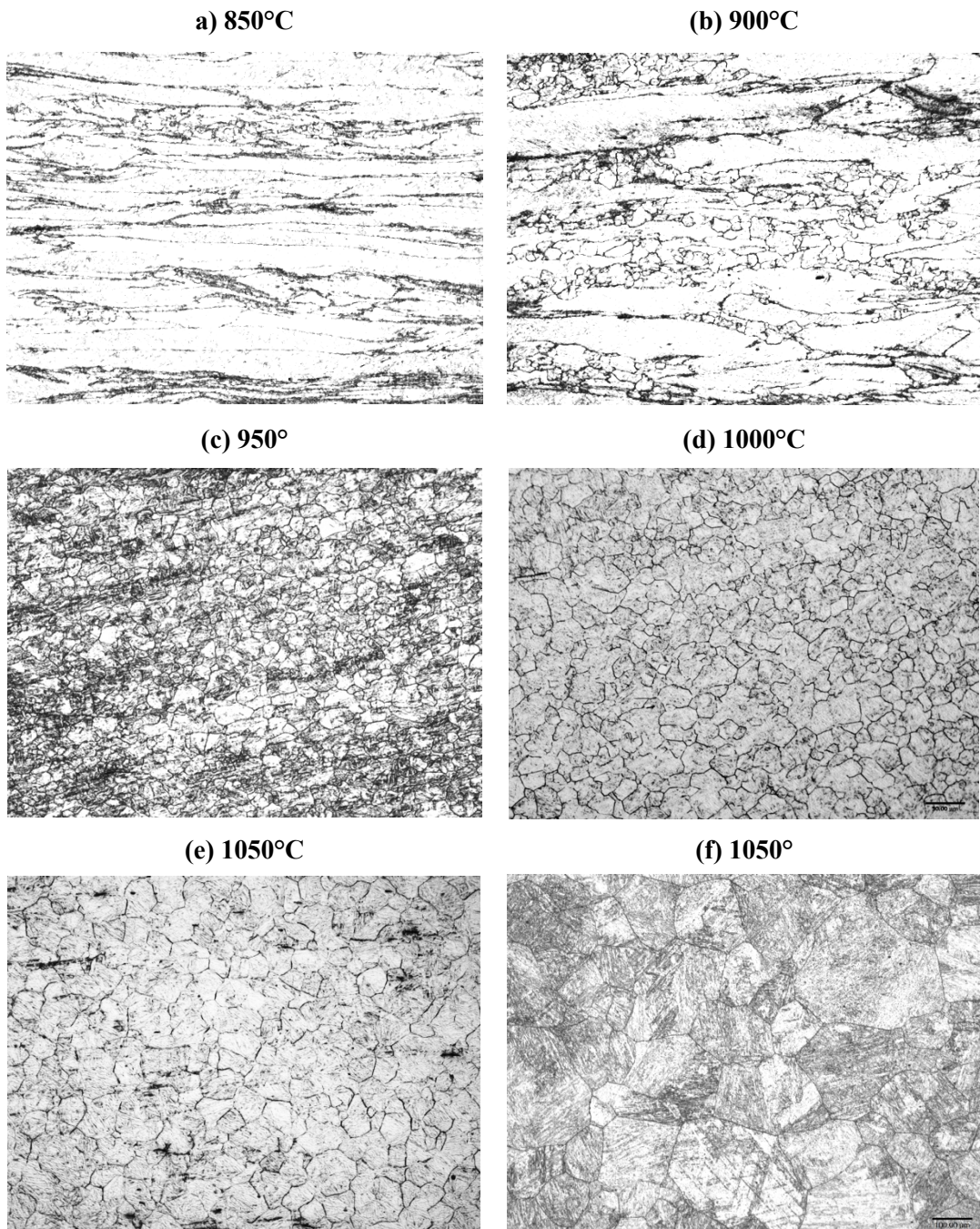


Figure 5.22 Microstructure evaluation of grade B2 at the respective deformation temperature. The microstructure was obtained after reheating to 1250°C, single hit deformation at strain $\epsilon=0.40$, an isothermal hold of 20 secs, and WQ. The constant strain rate of 15 s^{-1} was applied. This steel had a $T_{5\%}$ of 900°C as measured from fraction softening studies.

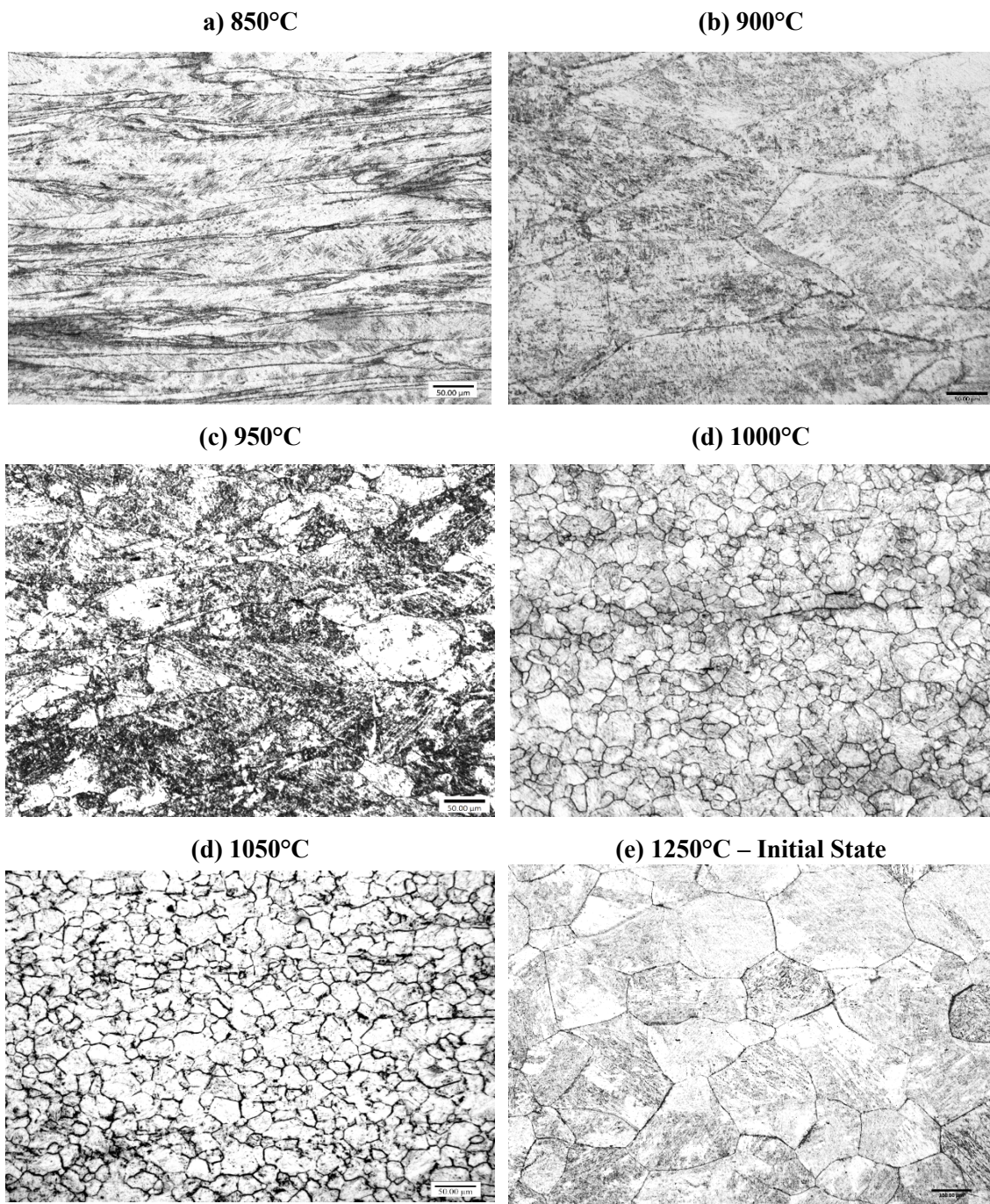


Figure 5.23 Microstructure evaluation of grade B3 at the respective deformation temperature. The microstructure was obtained after reheating to 1250°C, single hit deformation at strain $\epsilon=0.40$, an isothermal hold of 20 secs, and WQ. The constant strain rate of $15s^{-1}$ was applied. This steel had a $T_{5\%}$ of 943°C as measured from fraction softening studies

5.2.3.4 Double-Hit Deformation (Isothermal Hold of 5 and 20 sec)

Figure 5.24 (a)-(d) shows the microstructure of steel B0 after isothermal deformation (850-1050°C) for a true strain, $\epsilon=0.10-0.40$, and hold time of 20 sec. The deformed samples were immediately quenched after the second deformation to retain the austenite condition. The unrecrystallised austenite was observed at all temperatures for the lowest true strain, $\epsilon=0.10$. As applied strain increased, the complete recrystallised austenite microstructure was observed for the majority of test conditions, even at the lowest deformation temperature of 850°C. At higher true strain, $\epsilon > 0.30$, the recrystallised austenite was observed for all test temperatures.

Figure 5.25 (a)-(d) shows the microstructure of steel B1 after isothermal deformation (850-1050°C) for a true strain, $\epsilon=0.10-0.40$, and IP=20 sec. The complete deformed and unrecrystallised austenite was observed at all strains for the lowest deformation temperature of 850°C. Similarly, the unrecrystallised austenite was observed at all temperatures for the lowest true strain, $\epsilon=0.10$. For the rest of the test conditions, the recrystallised austenite was observed after the deformation.

Figure 5.26 (a)-(d) shows the microstructure of steel B2 after isothermal deformation (850-1050°C) for a true strain, $\epsilon=0.10-0.40$, and IP=20s. The complete deformed and unrecrystallised austenite was observed at all strains for the lowest deformation temperature of 850 and 900°C. Similarly, the unrecrystallised austenite was observed for the lowest true strain, $\epsilon=0.10$ at 950 and 1000°C. At higher true strain, $\epsilon > 0.20$, the recrystallised austenite was observed for these temperatures.

Figure 5.27 (a)-(d) shows the microstructure of steel B3 after isothermal deformation (850-1050°C) for a true strain, $\epsilon=0.10-0.40$, and IP=20s. The unrecrystallised austenite was observed for deformation temperature up to 950°C. The complete recrystallised austenite was observed at higher deformation temperatures, i.e., 1000°C. The steel B3 has a $T_{5\%}$ of 943°C (measured from fraction softening studies), the DHT microstructures fit well with the sequence of single hit microstructure shown in Figure 5.23

The linear intercept grain sizes \bar{L}_1 and \bar{L}_3 were measured from the counts in RD and ND directions, respectively, after the second hit deformation cycle. The means PAGS $(\bar{L}_1 * \bar{L}_3)^{0.5}$ and aspect ratio (\bar{L}_1 / \bar{L}_3) were calculated assuming an axial symmetry of the grains from the above measurements. Table 5.7 presents mean PAGS of all steels as a function of deformation temperature for double-hit tests with a hold time of 5 and 20 secs.

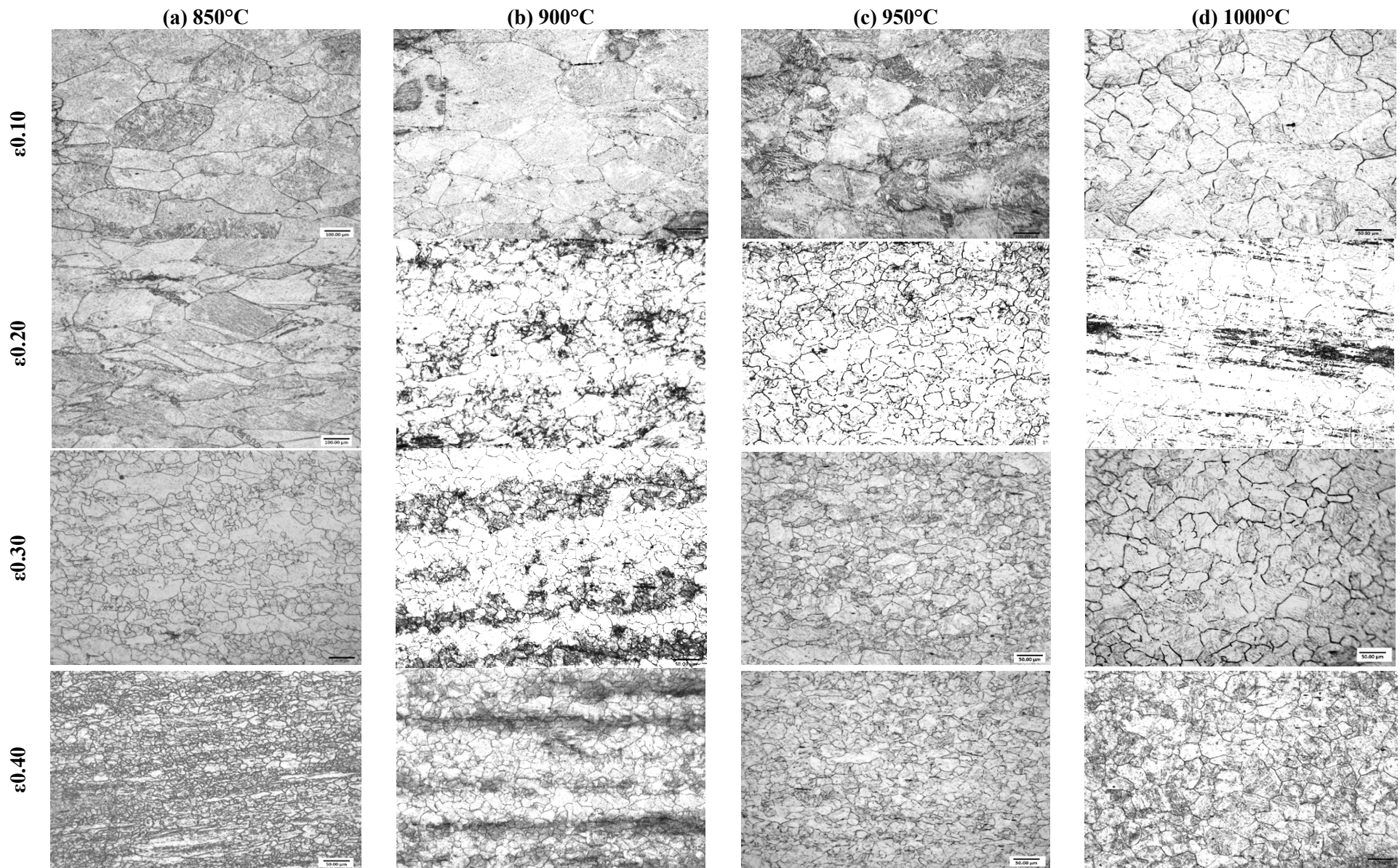


Figure 5.24 Microstructure evaluation of grade B0 at the respective deformation temperature after DHT tests. Samples were reheated to 1250°C, interrupted compression testing at strain ϵ 0.10-0.40 for isothermal hold of 20 secs and WQ. The constant strain rate of $15s^{-1}$ was applied.

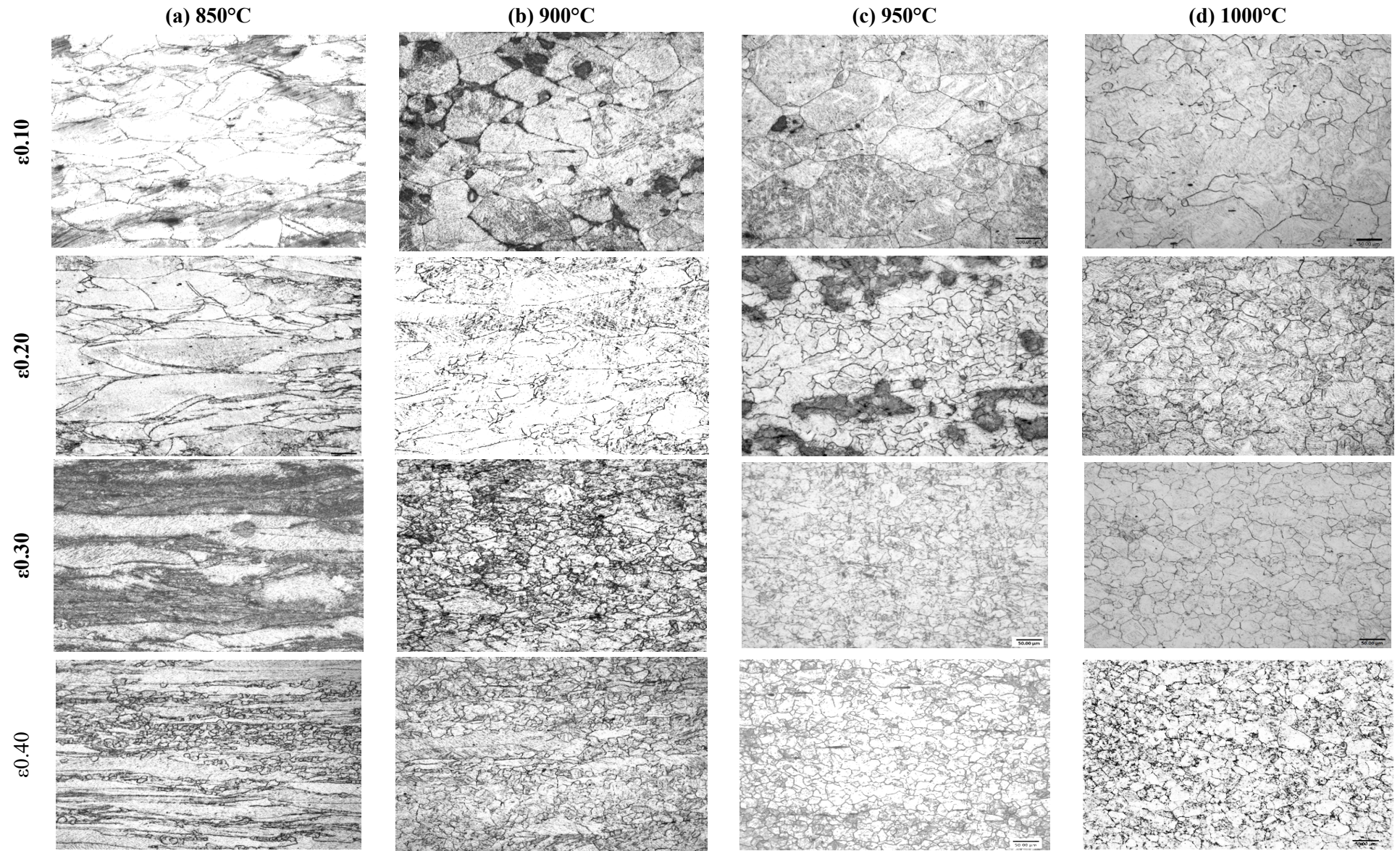


Figure 5.25 Microstructure evaluation of grade B1 at the respective deformation temperature after DHT tests. Samples were reheated to 1250°C, interrupted compression testing at strain $\epsilon 0.10$ - 0.40 for isothermal hold of 20 secs and WQ. The constant strain rate of $15s^{-1}$ was applied.

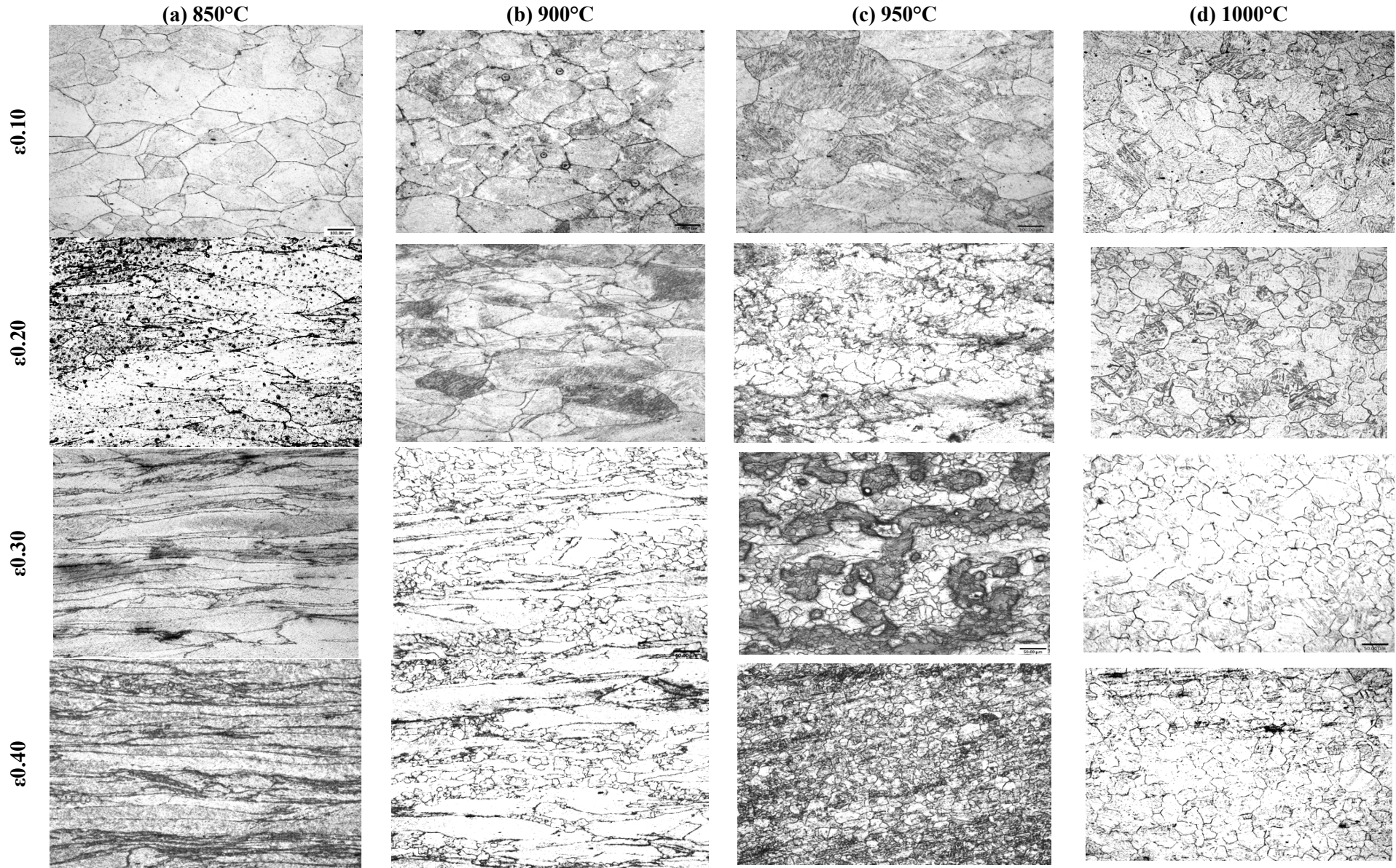


Figure 5.26 Microstructure evaluation of grade B2 at the respective deformation temperature after DHT tests. Samples were reheated to 1250° interrupted compression testing at strain ϵ 0.10-0.40 for isothermal hold of 20 secs and WQ. The constant strain rate of $15s^{-1}$ was applied.

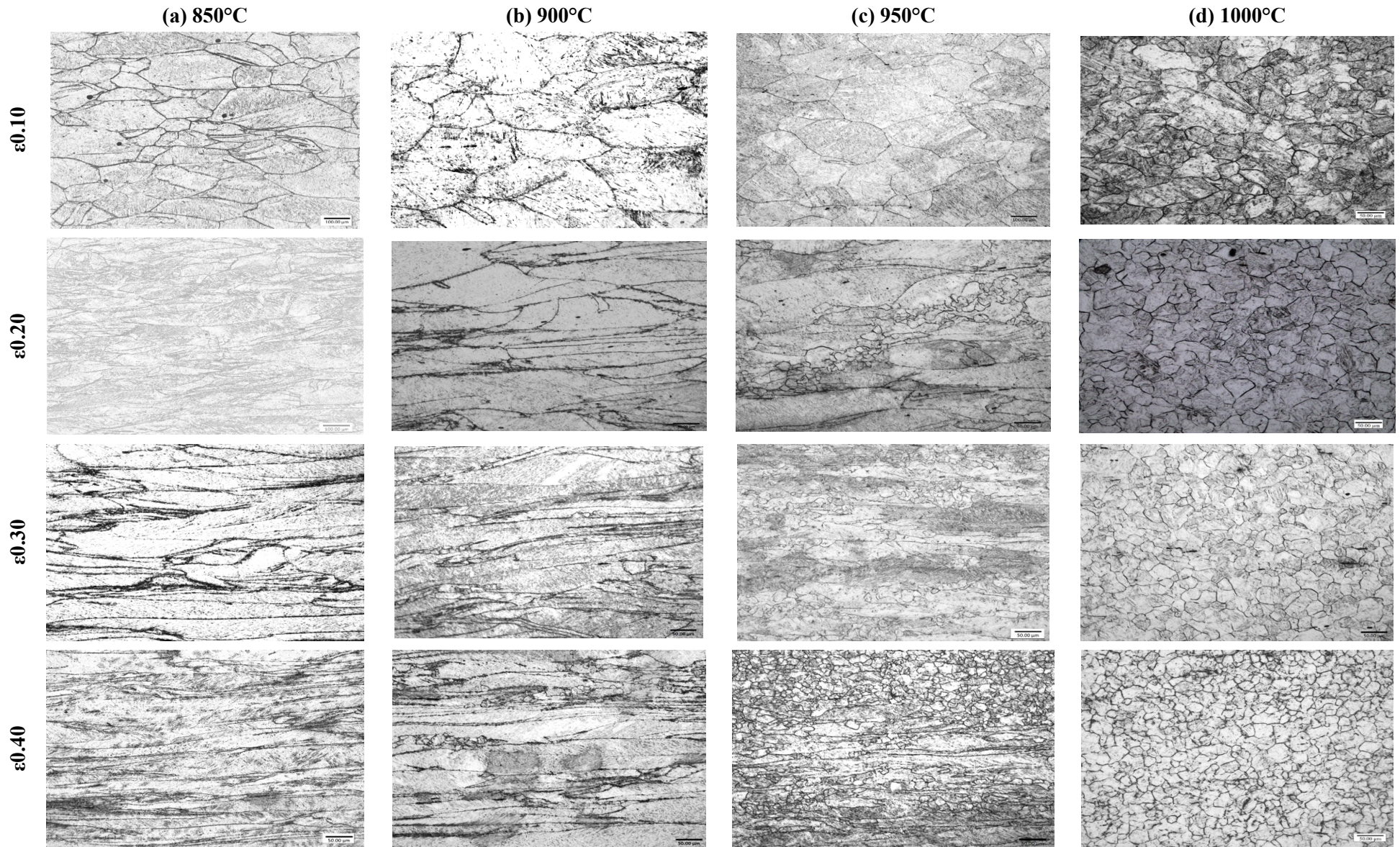


Figure 5.27 Microstructure evaluation of grade B3 at the respective deformation temperature after DHT tests. Samples were reheated to 1250°C, interrupted compression testing at strain $\epsilon 0.10$ -0.40 for isothermal hold of 20 secs and WQ. The constant strain rate of $15s^{-1}$ was applied.

Table 5.7 Mean PAGS of steel B0-B3 as a function of deformation temperature interrupted compression testing

Deformation Temp	B0				B1				B2				B3			
	$\epsilon 0.10$	$\epsilon 0.20$	$\epsilon 0.30$	$\epsilon 0.40$	$\epsilon 0.10$	$\epsilon 0.20$	$\epsilon 0.30$	$\epsilon 0.40$	$\epsilon 0.10$	$\epsilon 0.20$	$\epsilon 0.30$	$\epsilon 0.40$	$\epsilon 0.10$	$\epsilon 0.20$	$\epsilon 0.30$	$\epsilon 0.40$

A. DHT – 5s

850	167 ± 12	174 ± 20	25 ± 2	21 ± 1	157 ± 18	171 ± 11	129 ± 19	130 ± 15	154 ± 19	159 ± 13	130 ± 19	131 ± 17	174 ± 13	148 ± 25	137 ± 18	122 ± 18
900	172 ± 14	34 ± 4	26 ± 2	25 ± 1	173 ± 10	169 ± 15	152 ± 19	25 ± 2	160 ± 10	167 ± 12	165 ± 16	147 ± 16	158 ± 11	152 ± 18	157 ± 17	149 ± 20
950	169 ± 16	39 ± 2	29 ± 2	30 ± 2	172 ± 14	32 ± 2	27 ± 1	24 ± 2	162 ± 13	168 ± 14	31 ± 3	27 ± 2	156 ± 15	154 ± 12	152 ± 18	132 ± 18
1000	58 ± 3	44 ± 2	38 ± 1	29 ± 1	51 ± 3	43 ± 2	38 ± 2	27 ± 1	53 ± 3	40 ± 2	37 ± 1	28 ± 1	52 ± 3	38 ± 1	34 ± 1	26 ± 1
1050	67 ± 6	50 ± 3	39 ± 2	31 ± 1	60 ± 3	47 ± 1	42 ± 1	28 ± 1	59 ± 4	44 ± 3	41 ± 2	27 ± 1	57 ± 4	41 ± 2	37 ± 2	25 ± 1

B. DHT – 20s

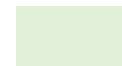
850	159 ± 14	175 ± 16	28 ± 1	29 ± 2	147 ± 11	178 ± 20	133 ± 19	144 ± 17	153 ± 14	170 ± 23	129 ± 18	133 ± 10	161 ± 12	151 ± 10	138 ± 21	138 ± 17
900	171 ± 13	35 ± 4	26 ± 1	23 ± 1	178 ± 15	180 ± 24	30 ± 2	25 ± 2	168 ± 13	194 ± 12	47 ± 9	137 ± 16	165 ± 12	174 ± 17	162 ± 24	145 ± 15
950	167 ± 11	36 ± 2	30 ± 2	22 ± 2	172 ± 14	35 ± 2	31 ± 3	22 ± 2	187 ± 16	46 ± 4	26 ± 2	22 ± 1	164 ± 11	179 ± 12	152 ± 18	131 ± 18
1000	61 ± 3	47 ± 2	41 ± 1	29 ± 1	60 ± 3	48 ± 2	38 ± 2	30 ± 1	58 ± 3	42 ± 2	36 ± 1	28 ± 1	56 ± 4	41 ± 1	33 ± 1	26 ± 1
1050	70 ± 2	50 ± 3	44 ± 2	31 ± 1	67 ± 3	48 ± 1	42 ± 1	31 ± 1	66 ± 4	42 ± 2	37 ± 2	30 ± 2	61 ± 3	40 ± 2	37 ± 2	25 ± 1



Non-recrystallised γ



Partially-recrystallised γ



Fully-recrystallised γ

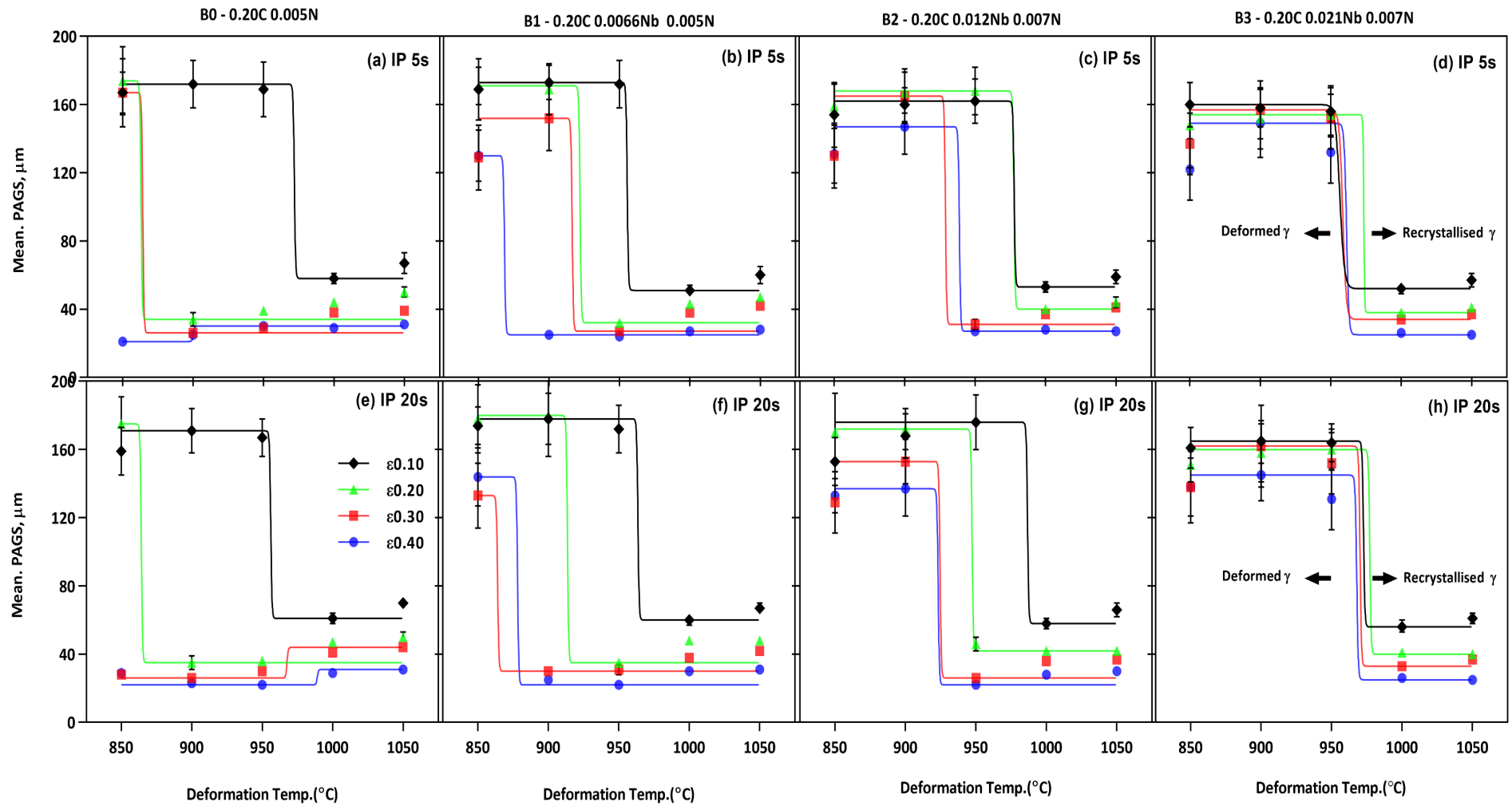


Figure 5.28 Mean PAGS of B0-B3 steel as a function of deformation temperature under different prestrain and hold time of 5 and 20 sec after double-hit compression testing. All tests were carried out at a constant strain rate of 15 s^{-1} .

Figure 5.28 graphically illustrates the data presented in Table 5.7. The mean PAGS exhibits the sigmoidal curve shape separating the non-recrystallised and recrystallised austenite condition. The mean PAGS of the non-recrystallised austenite microstructure was in the range of 130-150 μm while the grain size of the recrystallised austenite was in the range of 25-35 μm .

Table 5.8 shows the aspect ratio of austenite grains as a function of deformation temperature after the second hit deformation cycle. The aspect ratio of 15-20 was obtained for unrecrystallised austenite microstructure at the lowest deformation temperature. The aspect ratio decreases as temperature increases and is approximately 1.2 at higher deformation temperature 1000-1050°C for a fully recrystallised austenite microstructure.

Figure 5.29 shows the graphical representation of the data in Table 5.8. The plateau of aspect ratio for steel B3 in between 900-950°C complements the observation in fractional softening behaviour.

Table 5.8 Aspect Ratio as a function of deformation temperature

Deformation Temp	B0				B1				B2				B3			
	$\epsilon 0.10$	$\epsilon 0.20$	$\epsilon 0.30$	$\epsilon 0.40$	$\epsilon 0.10$	$\epsilon 0.20$	$\epsilon 0.30$	$\epsilon 0.40$	$\epsilon 0.10$	$\epsilon 0.20$	$\epsilon 0.30$	$\epsilon 0.40$	$\epsilon 0.10$	$\epsilon 0.20$	$\epsilon 0.30$	$\epsilon 0.40$

A. DHT – 5s

850	2.05	3.25	7.25	1.48	2.00	4.21	12.15	17.98	2.06	4.62	11.71	17.74	2.93	5.79	12.37	15.80
900	2.12	1.46	1.51	1.20	2.00	3.53	7.67	1.50	2.06	3.99	4.96	8.98	2.14	4.49	8.86	9.64
950	1.32	1.43	1.26	1.30	1.45	1.60	1.51	1.34	1.91	4.00	1.49	1.53	3.32	2.37	7.32	12.56
1000	1.19	1.38	1.23	1.24	1.24	1.12	1.33	1.33	1.24	1.25	1.30	1.26	1.22	1.20	1.26	1.18
1050	1.15	1.30	1.25	1.18	1.20	1.32	1.31	1.14	1.15	1.40	1.27	1.10	1.30	1.27	1.33	1.20

B. DHT – 20s

850	2.09	3.78	1.21	1.27	3.13	4.23	11.82	14.10	1.90	4.56	11.36	17.07	2.76	5.18	13.00	20.00
900	1.72	1.51	1.13	1.20	1.70	3.39	1.45	1.45	1.67	4.00	3.32	6.90	2.12	4.15	7.73	10.83
950	1.80	1.15	1.30	1.31	1.96	1.51	1.67	1.37	1.91	1.91	1.46	1.28	2.20	4.27	7.50	10.96
1000	1.19	1.38	1.25	1.25	1.30	1.17	1.33	1.14	1.24	1.25	1.30	1.26	1.22	1.20	1.26	1.18
1050	1.26	1.21	1.20	1.15	1.30	1.17	1.26	1.19	1.61	1.24	1.20	1.12	1.27	1.25	1.38	1.16



Non-recrystallised γ



Partially-recrystallised γ



Fully-recrystallised γ

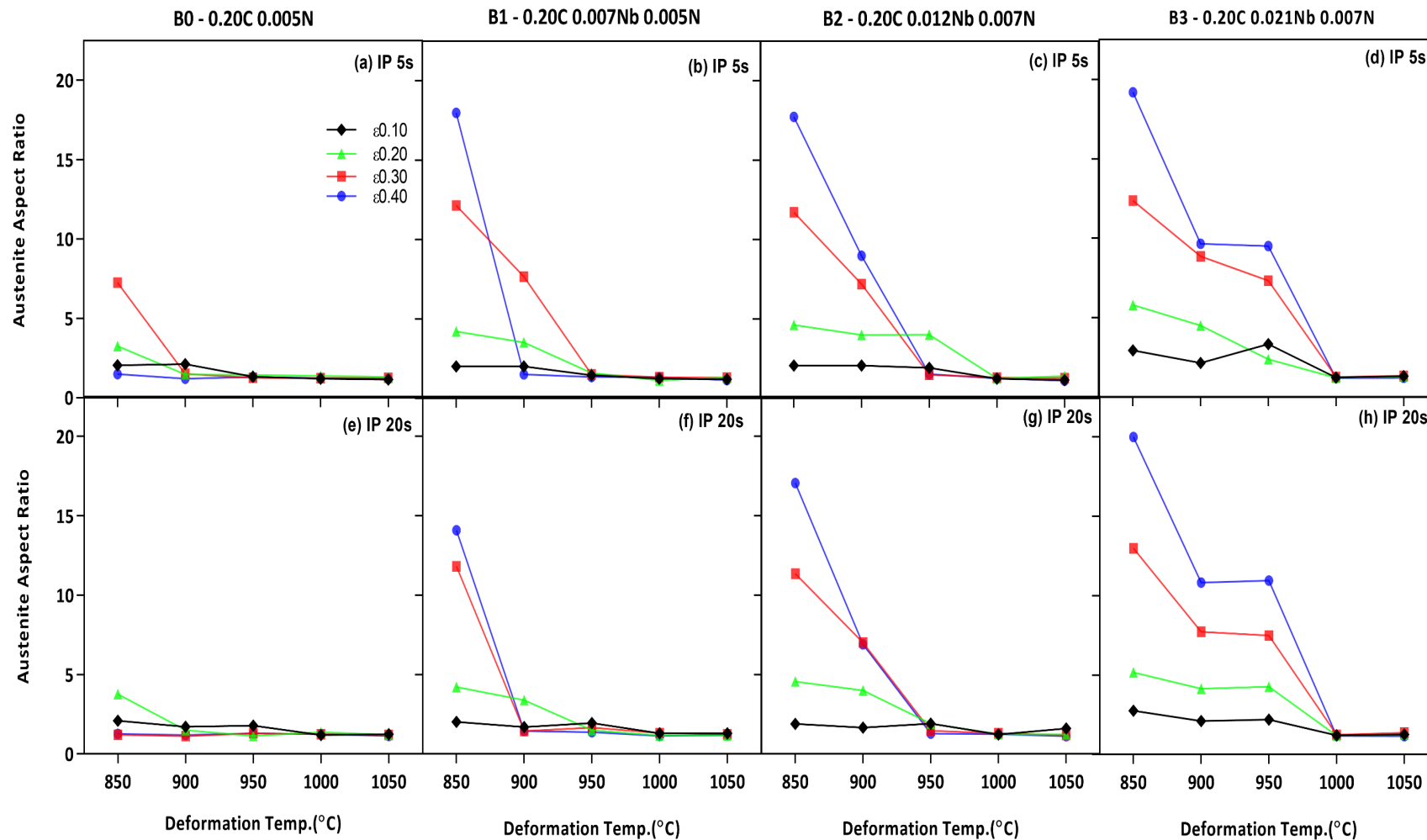


Figure 5.29 Aspect ratio of B0-B3 steel as a function of deformation temperature under different prestrain after interrupted compression testing for a hold time of 5 and 20 sec. All tests were carried out at a constant strain rate of 15 s^{-1} .

5.3 Nb(CN) Precipitation: Quantitative TEM

The strain-induced precipitation of Nb(CN) on austenite grain boundaries inhibits the static recrystallisation of deformed austenite. It is essential to study the precipitate evolution as a function of deformation temperature, inter pass time, and applied strain. The pinning force exerted by precipitates can be calculated if the precipitate size, distribution, and volume fraction are known.

The TEM is the preferred technique to determine the size and distribution of strain-induced precipitates of Nb(CN) in austenite. The precipitation kinetics are evaluated as a function of deformation temperature for a constant applied strain, $\epsilon=0.40$ and isothermal hold time of 20 sec. The results in the following section present the quantitative description of Nb(CN) precipitation observed in hot deformed austenite. In particular, the location of Nb(CN) precipitation was assessed quantitatively to determine the precipitate size and volume fraction.

5.3.1 Thin Foils

Figure 5.30 shows an example of the microstructure exhibited by each steel following isothermal compression and hold time of 20 secs, followed by immediate water quenching to room temperature. The microstructure is characteristic of low carbon martensite (α') and often referred to as lath martensite due to lath or plate-like morphology. The lath thickness of the microstructure was found to be 0.20-0.50 μm .

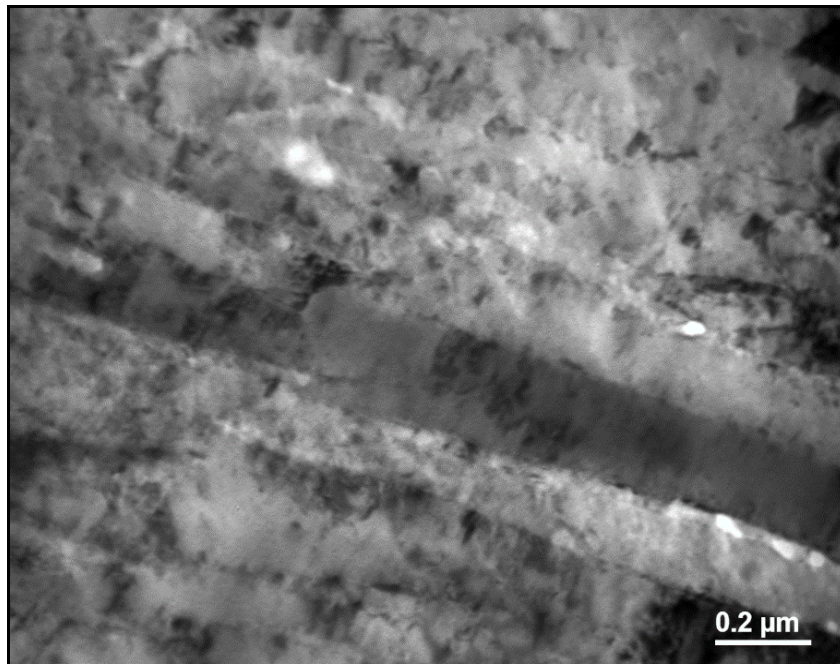


Figure 5.30 Bright-field TEM micrograph depicting low carbon (lath) martensite in steel B3. The microstructure resulted from deformation at 950°C, an isothermal hold of 20 sec followed by immediate water quenching.

The bright field imaging of the Nb(CN) precipitates in thin foil samples is challenging due to a high dislocation density associated with lath martensite microstructure. Also, the SIPs are incoherent with the martensite matrix being formed in the austenite phase and lose the orientation relationship during the phase transformation. Hence, the centre dark-field imaging mode was employed to obtain a diffraction pattern and orientation relationship between strain induced Nb(CN) precipitate and lath martensite matrix.

The softening studies have shown the full static recrystallisation behaviour in all grades for high-temperature deformation, $T_{\text{def}} \geq 1000^{\circ}\text{C}$. It points out the limited potential of SIP at high temperatures; hence, these conditions were subsequently not considered for OR analysis. If Nb(CN) precipitation occurs during deformation as a function of strain then it should obey the K-S orientation relationship [180] with quenched matrix. If the precipitation occurs during phase transformation, then Baker-Nutting orientation relationship will be applicable [181].

Figure 5.31 shows the centred bright-field micrographs for steel B3 deformed at 950°C . It depicts the localised SIP of Nb(CN) along the prior austenite grain boundaries and subgrain boundaries in the matrix. The corresponding selective area diffraction pattern (SADP) reveals both matrix and precipitate reflections. The SADP has been used to analyse the orientation relationship between the SIP and the ferrite matrix.

Figure 5.32 (a, b, and c) shows the bright and dark-field images of steel B2 following deformation at 850°C . The SIP in low carbon martensite/ferrite, α could be identified from the $(1\bar{1}\bar{1})$ NbC reflection, shown in the dark-field image in Figure 5.32 (b). These strain-induced precipitations were localised in nature, often located on dislocations and subgrain boundaries. The sample deformed at 900°C also exhibits the unrecrystallised austenite structure.

Figure 5.32 (d, e, and f) shows bright and dark-field images of precipitates at 900°C which showed the same orientation relationship between SIP and ferrite matrix. The sample deformed at 950°C showed a partially recrystallised structure. Figure 5.32 (g, h, and i) shows the Nb(CN) precipitation was formed on grain boundaries and within grains. The dark-field images were taken from $(\bar{2}02)$ NbC reflection. In summary, the evidence indicates that the precipitation in steel B2 was SIP after deformation at 850°C and 900°C .

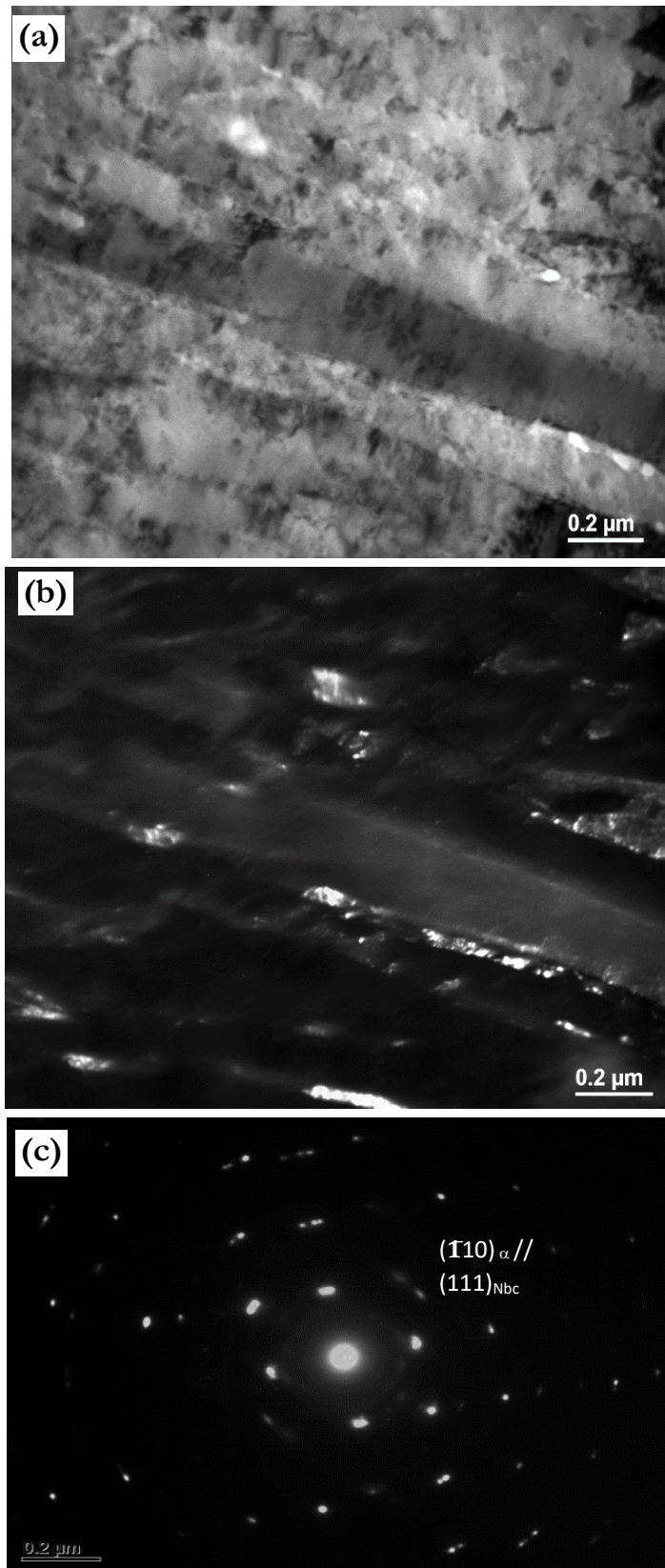


Figure 5.31 (a) bright-field TEM micrograph of Nb(CN) precipitates (b) dark-field TEM micrograph of (a) depicting Nb(CN) precipitation along austenite subgrain boundaries and (c) SADP Microstructure resulted from deformation at 950°C, the isothermal hold of 20 secs followed by immediate water quenching for steel B3.

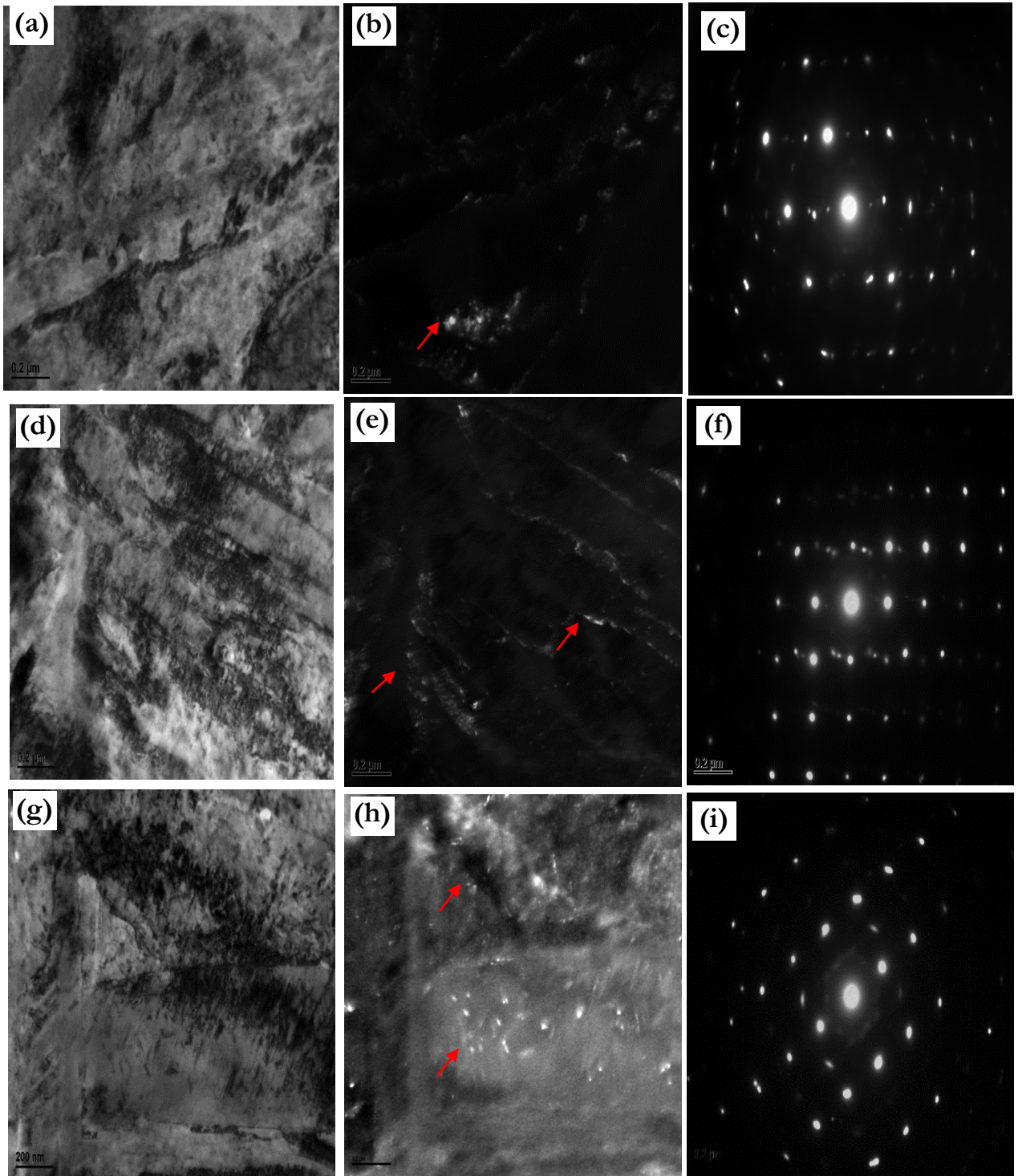


Figure 5.32 TEM images of B2 steel deformed at 850°C to 950°C, $\epsilon=0.40$ and hold 20 sec + WQ
 (a) a bright-field image at 850°C; (b) Centered-dark-field image of the same region of (a); and (c) the corresponding SADP of SIP and ferrite matrix from (a) for deformation temperature at 850°C;
 (d) a bright-field image 900°C; (e) Centered-dark-field image formed the same region of (d); and (f) the corresponding SADP of SIP and ferrite matrix from (d) for the deformation temperature at 900°C
 (g) a bright-field image 950°C; (h) Centered-dark-field image formed the same region of (g); and (i) the corresponding SADP of SIP and ferrite matrix from (g) for the deformation temperature at 950°C

High-resolution TEM (HRTEM) was used to investigate the Nb(CN) precipitation in steel B2 after deformation at 850°C. Figure 5.33(a) shows the bright-field TEM image of Nb(CN) precipitate in steel B2. Figure 5.33(b) shows the high-resolution lattice image of Nb(CN) precipitation observed in a sample. Figure 33 (c) shows the inverse fast Fourier transformation (IFFT) of Nb(CN) particles shown in Figure 33 (b). Figure 33 (d) shows corresponding fast Fourier transformed diffractogram to analyse the OR between precipitate and matrix.

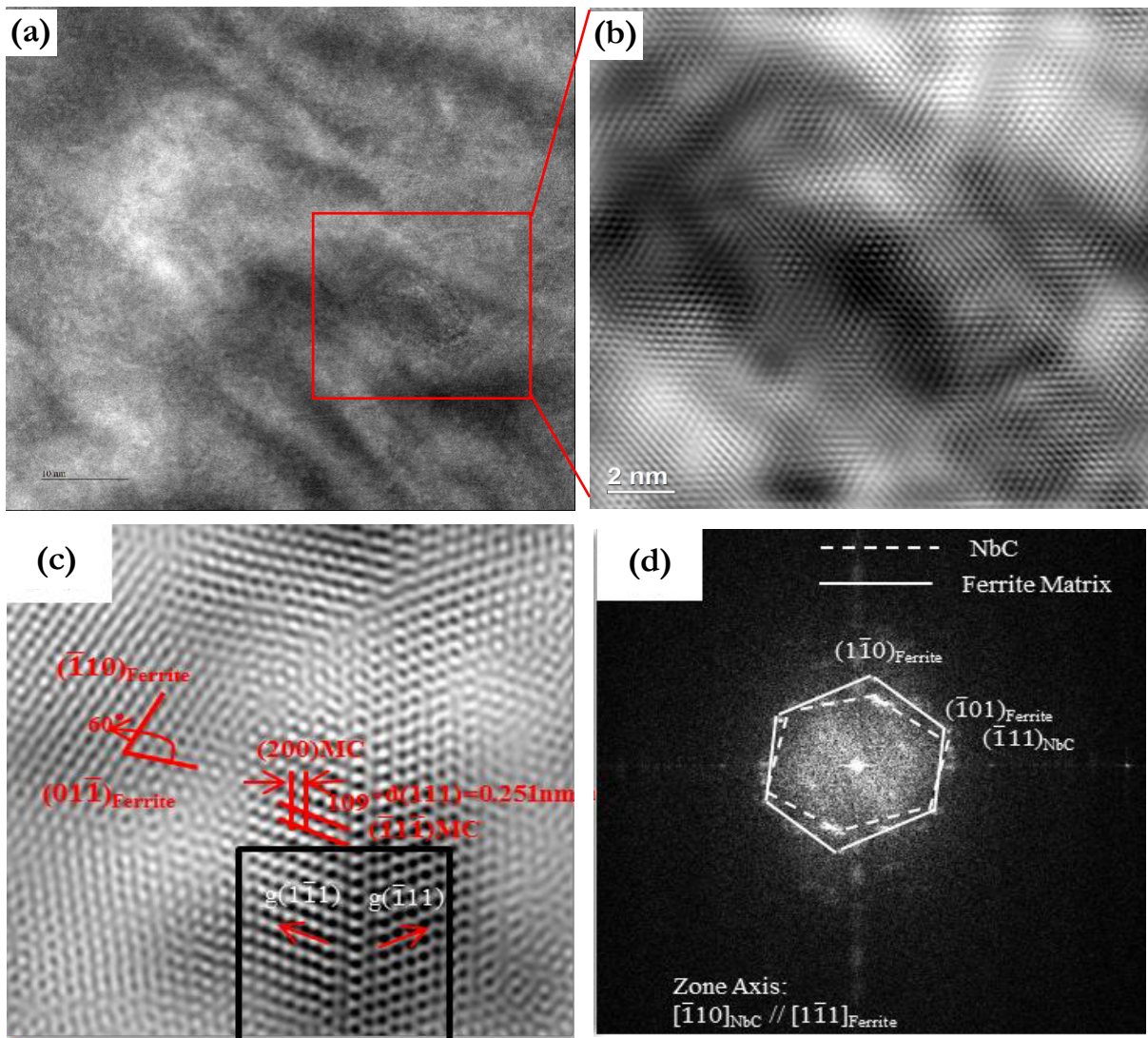


Figure 5.33 HRTEM image and IFFT lattice image of the nanosized sized carbide in steel B3 (a) obtained after deformation at 850°C with water quenching immediately; (b) HRTEM image of the fine Nb(CN); (c) IFFT lattice image in the range of red line of (a), (d) the corresponding fast Fourier transformed diffractogram from (b).

In the dark field image, some of the particles may be invisible, and the number of particles appearing in the image varies depending upon the orientation of the specimen along the zone axis. Therefore, the size distribution of precipitates was mainly investigated using the carbon extraction replica technique.

5.3.2 Extraction Replicas

The carbon extraction replicas were analyzed to determine the morphology, size distribution, and volume fraction of Nb(CN) precipitates as a function of deformation processing variables (temperature, holding time, and location) for each of the Nb-microalloyed steels. The mean diameter of the precipitate, its confidence limits, and the number of precipitates per unit area (N_s) were determined directly from precipitate size measurements over multiple locations. An average of 200 particles was measured to determine the precipitate size distribution in the planar section.

5.2.3.3 Steel B1

Figure 5.34 (a) shows the bright field micrographs depicting the Nb precipitation in steel B1 deformed at 850°C, ϵ 0.40, and isothermally hold for 20 sec before WQ. It is evident from Figure 5.34 that a large number of precipitates are present close to austenite subgrain boundaries. Similar trends are displayed with increasing deformation temperature. This has been shown in Figures 5.34 (c), (e), and (g) for steel deformed at 900°C, 950°C, and 1000°C, respectively.

The particle size measurements were performed on the micrographs using the ImageJ software. The lognormal particle size distribution was observed for all the deformation test conditions, as shown in Figure 5.34 (b), (d), and (h). The Woodhead analysis method [173] was used to calculate the number of precipitates per unit area (N_s) and per unit volume (N_v). The volume fraction of precipitate (V_f) was calculated using the relationship proposed by Ashby *et al.* [177], given by equation (4.12).

Table 5.9 shows the quantitative measurement of precipitates, volume fraction, and corresponding F_{PIN} for the experimental conditions. The precipitate formed at lower deformation temperature is finer compared to one formed at a higher temperature. In a similar line, the volume fraction of precipitates increases with decreasing deformation temperature irrespective of precipitation had occurred locally on the grain boundary or in the matrix. This has reflected in the values of F_{PIN} .

Table 5.9 Quantitative measurement particle size and volume fraction for steel B1

Def. Temp. (°C)	Local Precipitate Distribution Data Experimental Measurement				Precipitate Pinning Forces (MPa)		
	Diam. (nm)	N_s (m ⁻²)	N_v (m ⁻³)	Local f_v	RBM	FBM	SBM
850	12.1 ± 2.2	5.3 x 10 ¹²	4.3 x 10 ²⁰	4.2 x 10 ⁻⁴	0.11	7.5 x 10 ⁻⁰⁶	2.18
900	16.2 ± 2.3	1.8 x 10 ¹²	1.1 x 10 ²⁰	2.5 x 10 ⁻⁴	0.05	2.0 x 10 ⁻⁰⁶	0.74
950	18.6 ± 1.9	6.8 x 10 ¹¹	3.7 x 10 ¹⁹	1.2 x 10 ⁻⁴	0.02	4.2 x 10 ⁻⁰⁷	0.27
1000	16.9 ± 1.9	9.9 x 10 ¹⁰	5.9 x 10 ¹⁸	1.5 x 10 ⁻⁵	0.00	6.8 x 10 ⁻⁰⁹	0.04

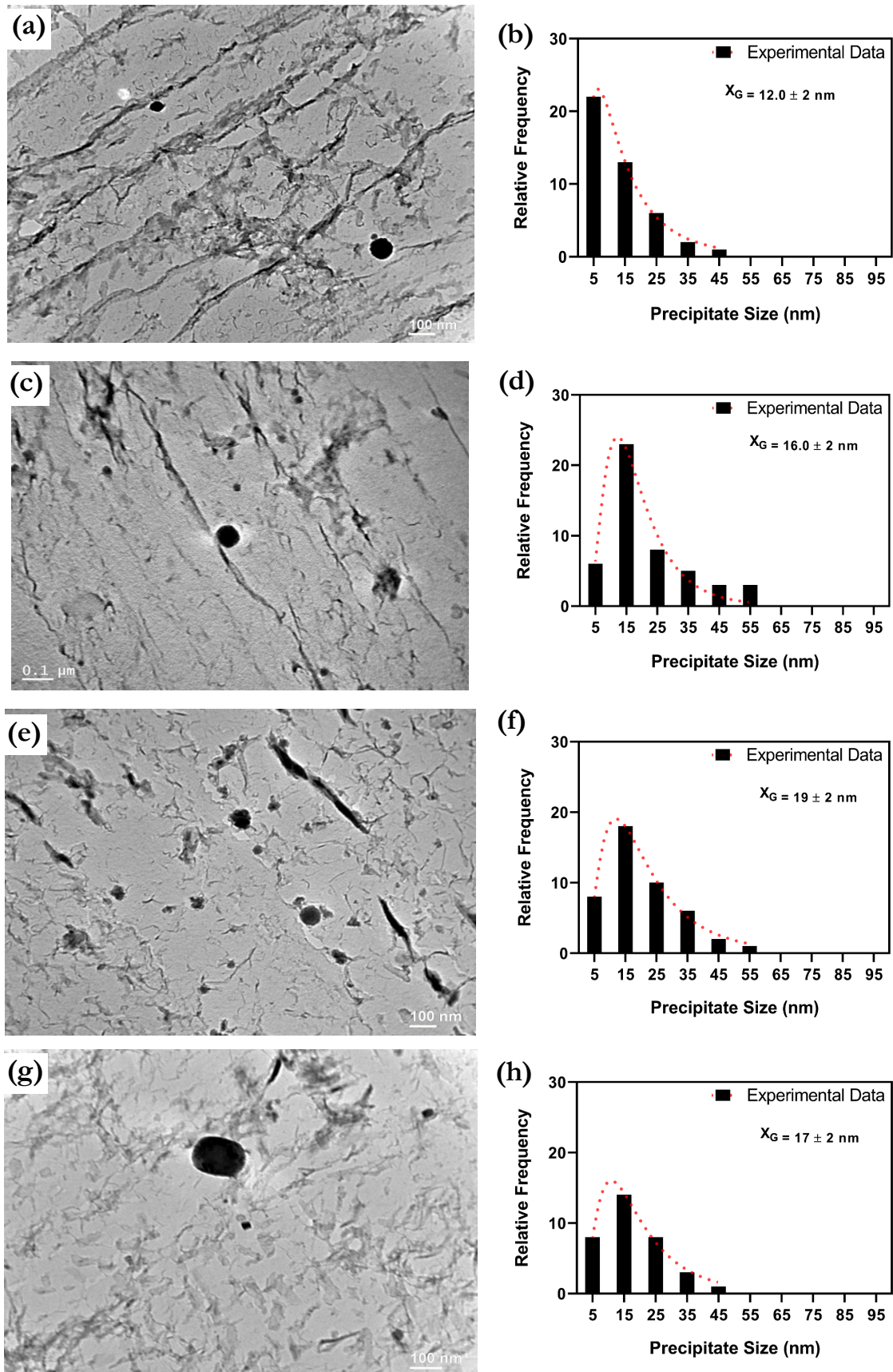


Figure 5.34 TEM micrographs depicting Nb(CN) precipitation in austenite sub-grain boundaries and size distribution for steel B1 at various deformation temperature: (a) – (b) 850°C, (c) –(d) 900°C, (e)- (f) 950°C & (g) –(h) 1000°C from extraction replica. The specimen was reheated at 1250°C, deformed ϵ 0.40 and isothermally hold for 20 sec before WQ.

The local pinning forces, F_{PIN} were calculated using the sub-grain boundary model (SBM) of Hansen *et al.* [41], given by equation (2.43). All input values (r , f_v , l) were experimentally measured in this research project, with the exception of interfacial energy between the Nb(CN) and austenite. The average mean linear intercept between austenite subgrain boundaries was determined to be 0.50 μm from thin foil microscopy. Figure 5.30 illustrates an example of a subgrain structure in steel B3, deformed at 950°C.

The local pinning forces were also estimated using the rigid boundary model (RBM) and the flexible boundary model for a comparison purpose. The pinning forces estimation with these models is given by equation (2.40) and (2.41), respectively. The measured F_{PIN} reflects the real condition of the austenite after the hot deformation irrespective of the pinning force model used for analysis.

5.2.3.2 Steel B2

The precipitation behaviour of steel B2 was analyzed similarly to the electron microscopy investigation of the low Nb-bearing steel B1. The original intent was to compare the precipitation potential in these steels at similar deformation temperature and strain.

Figure 5.35 shows the bright-field TEM micrographs along with corresponding size distribution of steel B2, deformed at 850-1000°C respectively for ϵ 0.40, and isothermally held for 20 sec before WQ. The precipitation behaviour of Nb(CN) in steel B2 is similar to that found in steel B1. A higher concentration of precipitates was observed on prior austenite and sub-grain boundaries at any given temperature.

Table 5.10 shows the quantitative measurement of precipitate size fraction and the corresponding volume fraction. The lognormal distribution of particle size was observed for given deformation conditions. The volume fraction of precipitates is significantly higher compared to steel B1. The f_v increases as the deformation temperature decreases.

Table 5.10 Quantitative measurement particle size and volume fraction for steel B2

Def. Temp. (°C)	Local Precipitate Distribution Data Experimental Measurement				Precipitate Pinning Forces MPa		
	Diam. (nm)	N_S (m^{-2})	N_V (m^{-3})	Local f_v	RBM	FBM	SBM
850	17.7 ± 1.9	7.2×10^{12}	4.1×10^{20}	1.2×10^{-3}	0.21	4.1×10^{-05}	2.91
900	15.7 ± 1.8	5.5×10^{12}	3.5×10^{20}	7.2×10^{-4}	0.14	1.7×10^{-05}	2.24
950	25.8 ± 2.2	1.6×10^{12}	6.2×10^{19}	5.6×10^{-4}	0.07	6.2×10^{-06}	0.65
1000	24.0 ± 1.4	4.9×10^{11}	2.1×10^{19}	1.5×10^{-4}	0.02	4.8×10^{-07}	0.20

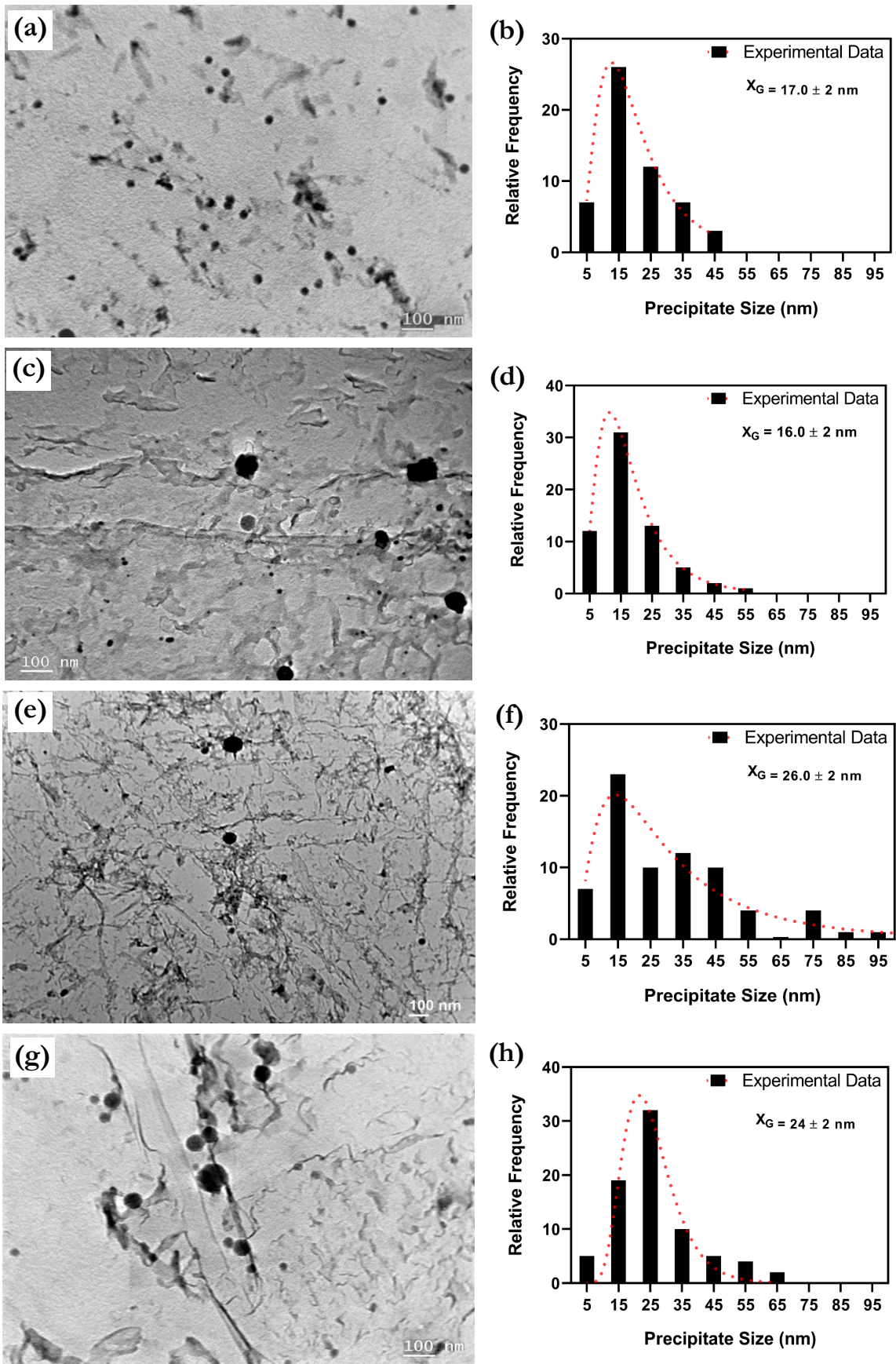


Figure 5.35 TEM micrographs depicting Nb(CN) precipitation in austenite sub-grain boundaries and size distribution for steel B2 at various deformation temperature: (a) – (b) 850°C, (c) –(d) 900°C, (e)-(f) 950°C & (g) –(h) 1000°C from extraction replica. The specimen was reheated at 1250°C, deformed $\epsilon 0.40$ and isothermally held for 20 sec before WQ.

5.3.2.1 Steel B3

Figure 5.36 – 39 shows morphology and compositions of precipitates observed in steel B3 after deformation at 850-1000°C, $\epsilon=0.40$ and isothermally hold for 20 sec before water quenching. A large number of fine Nb(CN) precipitates appeared to be formed in the highly localized fashion along with some matrix precipitates. The EDX spectrum further demonstrated that these particles contain Nb and C/N elements. The lognormal particle size distribution was observed for all the deformation test conditions (Figure 5.36 -38).

Table 5.11 presents the quantitative measurement from carbon extraction replicas of steel B3, showing particle size and volume fraction. The precipitation kinetics behaviour of Nb(CN) in steel B3 is similar to that found in steel B1 and B2, however, the observed volume fraction is significantly higher.

Table 5.11 Quantitative measurement particle size and volume fraction for steel B3

Def. Temp. (°C)	Local Precipitate Distribution Data Experimental Measurement				Precipitate Pinning Forces MPa		
	Diam. (nm)	N_s (m^{-2})	N_v (m^{-3})	Local f_v	RBM	FBM	SBM
850	16.2 ± 1.8	17×10^{13}	1.1×10^{21}	2.4×10^{-3}	0.45	1.8×10^{-04}	6.97
900	18.7 ± 2.1	1.1×10^{13}	6.0×10^{20}	2.1×10^{-3}	0.34	1.2×10^{-04}	4.54
950	26.1 ± 2.1	4.6×10^{12}	1.7×10^{20}	1.6×10^{-3}	0.19	5.2×10^{-05}	1.83
1000	21.7 ± 1.2	1.9×10^{12}	8.5×10^{19}	4.6×10^{-4}	0.06	4.9×10^{-06}	0.74

The HRTEM imaging technique was used to analyze the crystal structure and coherency of SIP with the matrix for selected test conditions. Figure 5.40 shows an HRTEM image of a nanometer-sized particle in steel B3 with a size less than 20 nm. The sample was deformed at 900°C, strain $\epsilon=0.40$ isothermal hold of 20 secs, followed by immediate water quenching. The d-spacing of coherent precipitate was measured and found to be 0.257 nm. The equilibrium Nb(CN) has $d_{(111)}$ equal to 0.258 nm, which fits well with experimental measurement.

The EDX spectrum further demonstrated that the particles contain Nb and C. The HRTEM and EDS results indicate that the observed particles are strain-induced precipitates of Nb(CN). The strain-induced precipitation is localised in nature and they preferentially nucleate on austenite subgrain boundaries

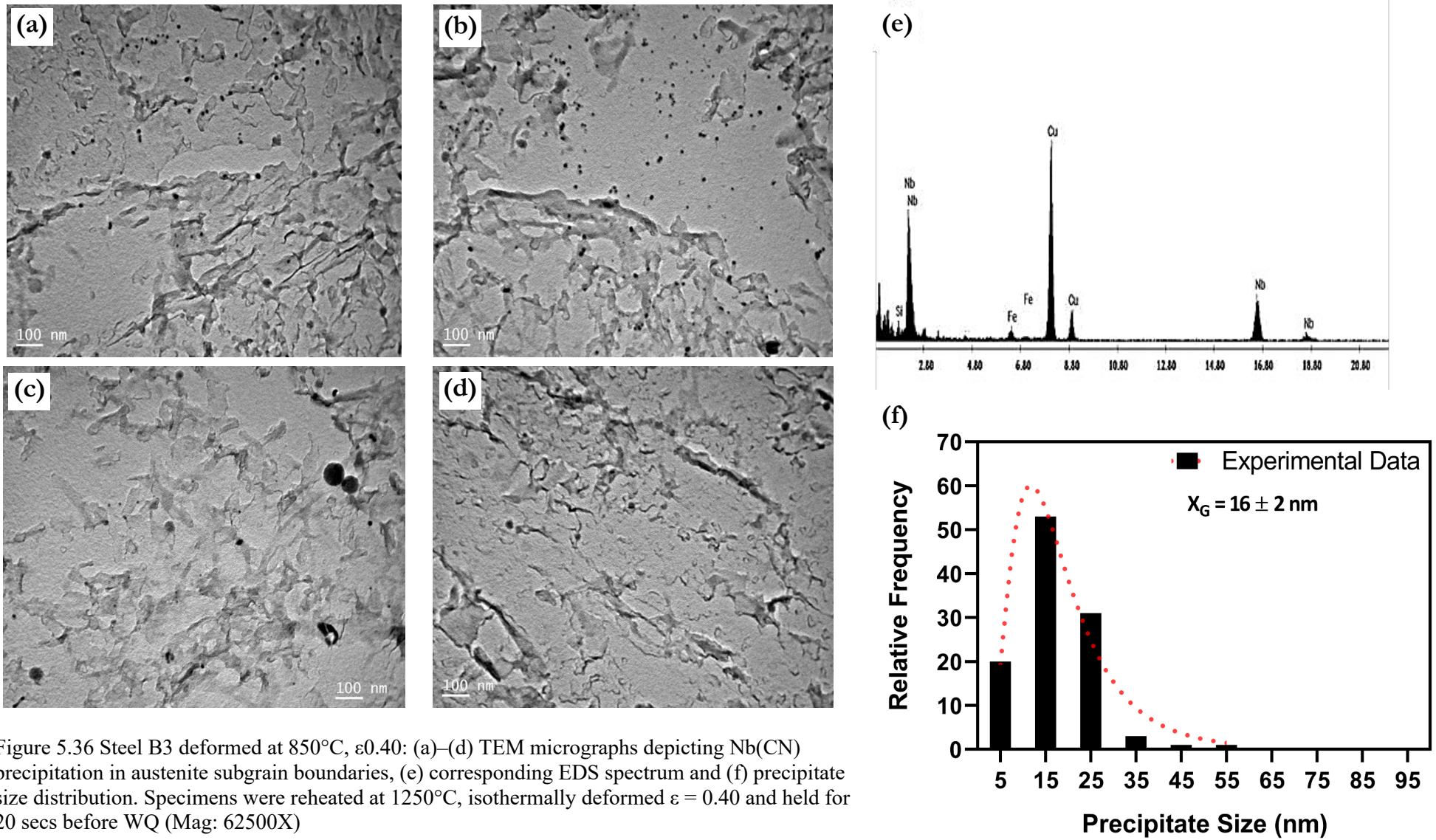


Figure 5.36 Steel B3 deformed at 850°C, ϵ 0.40: (a)–(d) TEM micrographs depicting Nb(CN) precipitation in austenite subgrain boundaries, (e) corresponding EDS spectrum and (f) precipitate size distribution. Specimens were reheated at 1250°C, isothermally deformed $\epsilon = 0.40$ and held for 20 secs before WQ (Mag: 62500X)

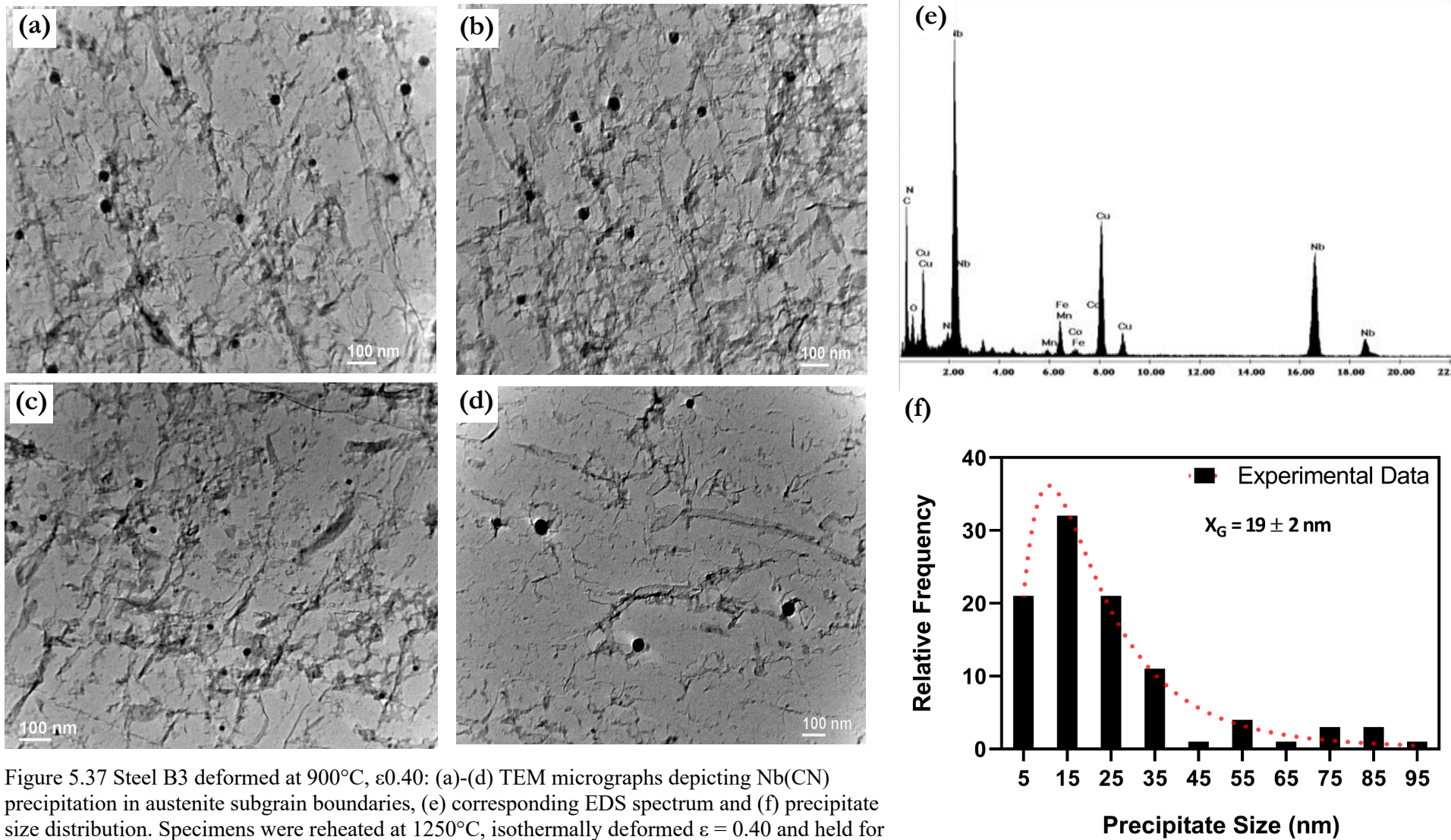


Figure 5.37 Steel B3 deformed at 900°C, ϵ 0.40: (a)-(d) TEM micrographs depicting Nb(CN) precipitation in austenite subgrain boundaries, (e) corresponding EDS spectrum and (f) precipitate size distribution. Specimens were reheated at 1250°C, isothermally deformed $\epsilon = 0.40$ and held for 20 secs before WQ (Mag: 62500X)

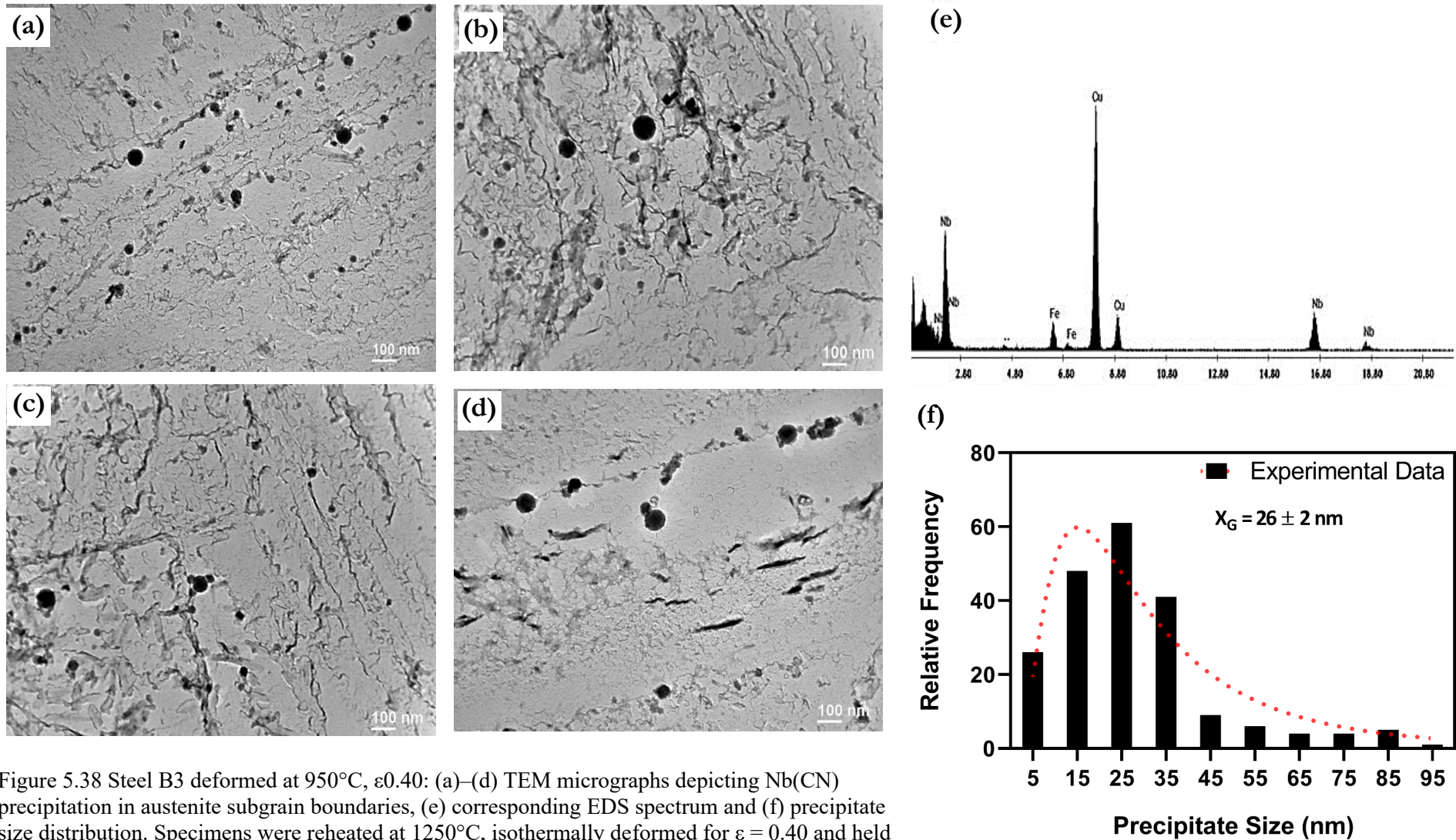


Figure 5.38 Steel B3 deformed at 950°C, ϵ 0.40: (a)–(d) TEM micrographs depicting Nb(CN) precipitation in austenite subgrain boundaries, (e) corresponding EDS spectrum and (f) precipitate size distribution. Specimens were reheated at 1250°C, isothermally deformed for $\epsilon = 0.40$ and held for 20 secs before WQ (Mag: 51000X)

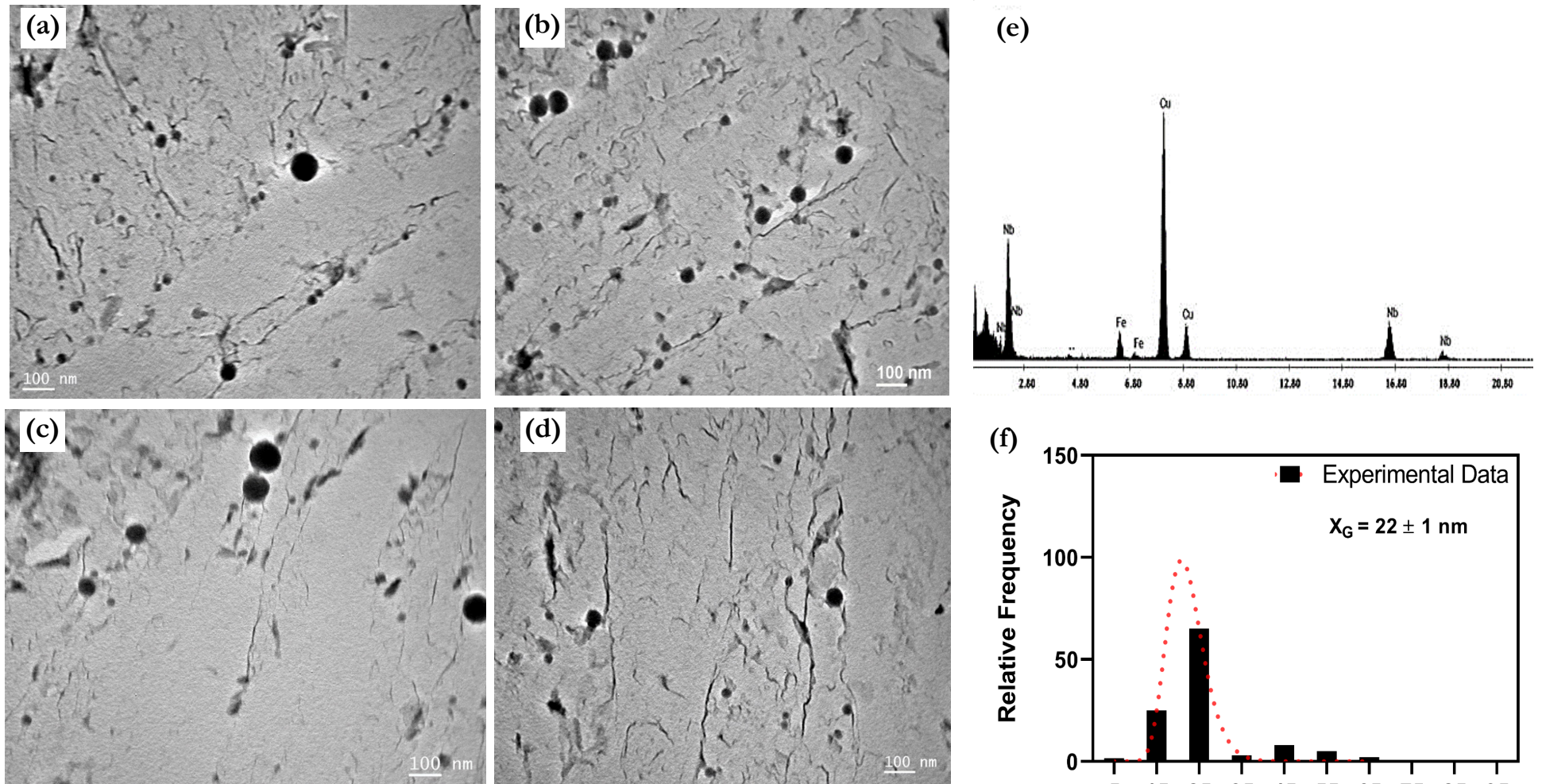


Figure 5.39 Steel B3 deformed at 1000°C, ϵ 0.40: (a)–(d) TEM micrographs depicting Nb(CN) precipitation in austenite subgrain boundaries, (e) corresponding EDS spectrum and (f) precipitate size distribution. Specimens were reheated at 1250°C, isothermally deformed for $\epsilon = 0.40$ and held for 20 secs before WQ

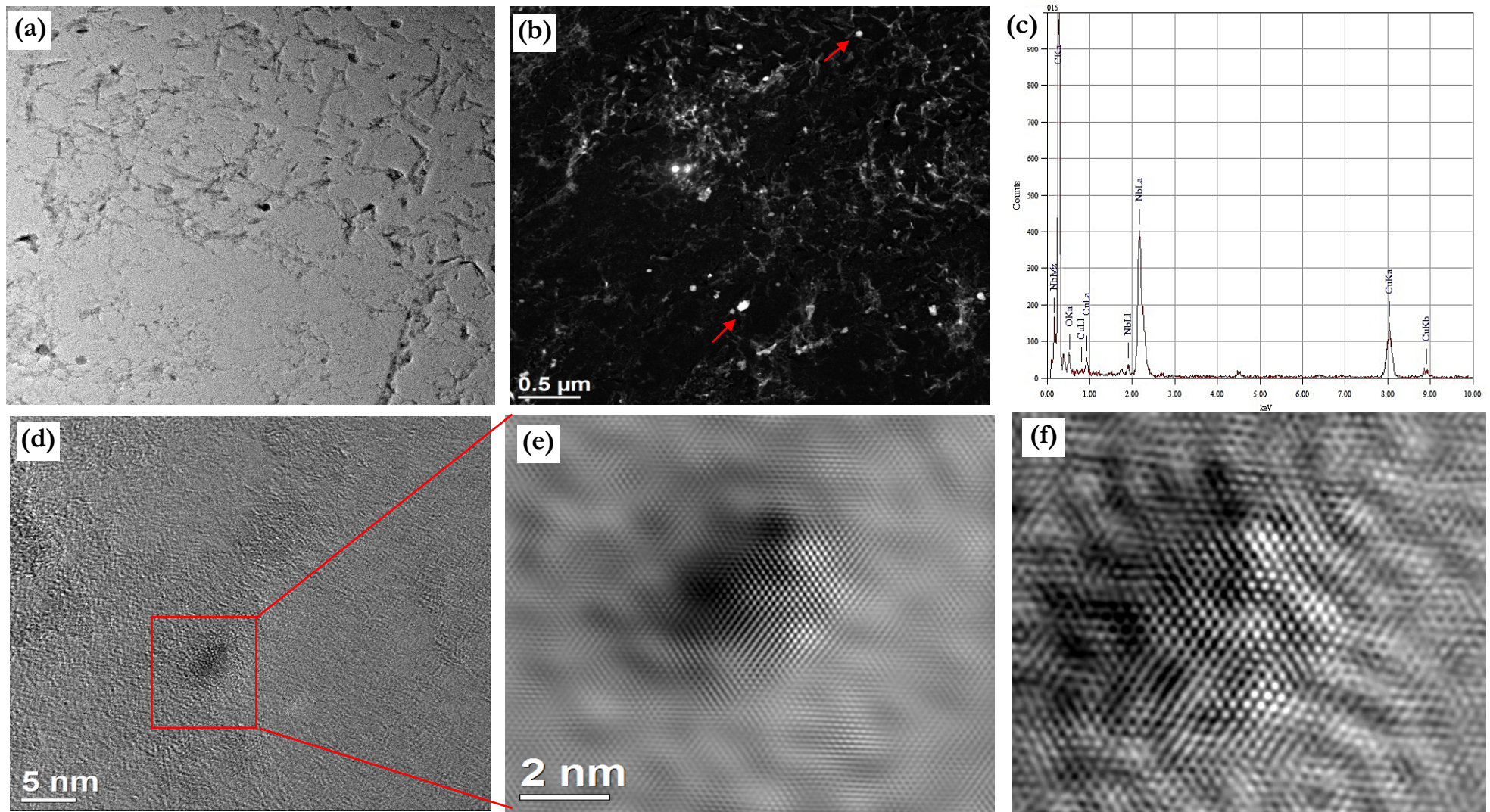


Figure 5.40 TEM micrograph of showing the morphology of precipitate formed at 900°C for steel B3 (a) bright-field image (b) dark-field image of the same area; (c) an EDS spectrum of marked precipitates, (d) fine NbC particle and (e)-(f) a high-resolution TEM image

5.3.3 Precipitate Pinning Forces (F_{PIN})

The strain-induced precipitation significantly retards recrystallisation by locking the substructure, thereby preventing the evolution of austenite recrystallisation grains via the process of dislocation and subgrain boundary migration. The precipitate location is essential, as they provide much more pinning potential if they are located on subgrain boundaries rather than located randomly throughout the matrix [40].

Table 5.9 - 5.11 presents the local F_{PIN} calculated using pinning force models for steel B1-B3. The high localised volume fraction of Nb(CN) at austenite subgrain boundaries results in higher local F_{PIN} . The F_{PIN} calculated with the SBM model is more practical over the underestimated F_{PIN} given values by RBM and FBM. The present results with the SBM model are in agreement with the previous investigation which validates the acceptance of SBM as the most realistic pinning model.

For a given composition, the local F_{PIN} increases with decreasing deformation temperature for steel B1-B3. The volume fraction of Nb(CN) precipitates increases with decreasing deformation temperature because of high Nb supersaturation and nucleation rate. Figure 5.41 illustrates the relationship between local F_{PIN} and volume fraction, f_v for steel B3. The higher volume fraction is reflected in the higher local F_{PIN} values at low deformation temperature. The similar behaviour is observed for steel B1 and B2. So, the precipitation pinning force also exhibits the temperature dependence similar to recrystallisation driving force.

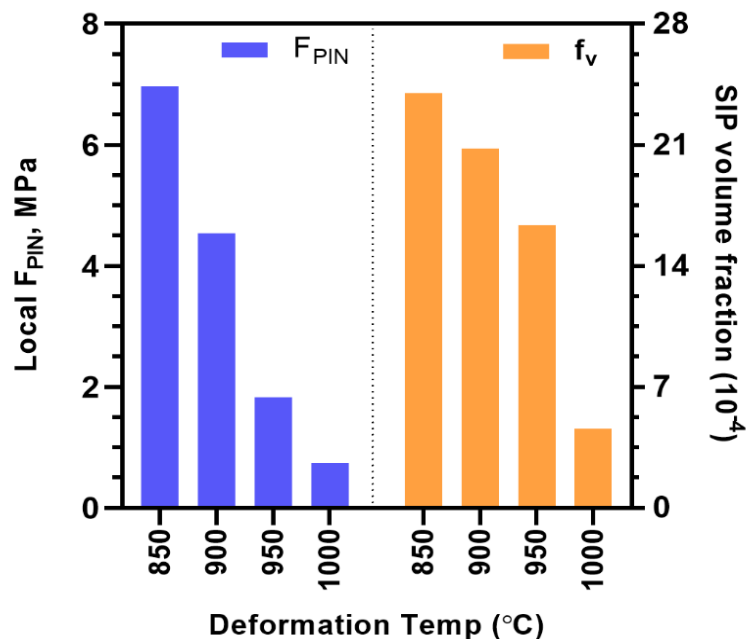


Figure 5.41 Relationship between volume fraction and pinning force at different deformation temperature for steel B3. The samples were deformed in a single hit for a true strain, $\epsilon = 0.40$, isothermally held for 20 secs, and immediately water quenched.

5.4 Transformation Behaviour of Austenite

The present work aims to determine the effect of soluble Nb on the transformation behaviour of austenite for selected 0.20%C composition. It is expected that these studies would allow us to determine the quantitative expression for the soluble Nb effect on austenite transformation kinetics. The following three sections present the results of the transformation behaviour of austenite:

5.4.1 Dilatometry

The austenitizing temperature and cooling rate were chosen to represent a typical finish rolling temperature and post-cooling for structural steels like rebar and beams. However, the current investigation is focused on undeformed austenite contrary to deformed austenite observed in practical situations.

The progress of austenite phase transformations under continuous cooling conditions was estimated from plots of linear strain vs. temperature based on data collected from MTS. Figure 5.42 shows an example of resulting linear strain vs. temperature graphs for steel B1 for a cooling rate of 0.5 and 5°C/s. It can be seen that the strain decreases approximately linearly until a transformation starts. The start and finish of various microstructure constituents were estimated from inflections in the slope of the linear strain vs. temperature plot.

Table 5.12 lists the summary of transformation temperatures obtained from a dilatometry experiment. It also details the type of transformation measured (further evidence substantiating these assignments is presented later in the metallography section).

Table 5.12 Dilatometry data for continuous cooling experiments

CR	Steel	Allotriomorphic Ferrite Onset °C	Allotriomorphic Ferrite End °C	Widmanstätten Ferrite Start °C	Widmanstätten Ferrite End °C
0.5°C/s	B0	798	760	720	645
	B1+0.006Nb	800	762	717	648
	B2+0.012Nb	789	763	706	645
	B3+0.021Nb	786	761	707	642
5°C/s	B0	780	710	640	600
	B1+0.006Nb	770	700	640	567
	B2+0.012Nb	765	700	640	570
	B3+0.021Nb	760	700	636	544

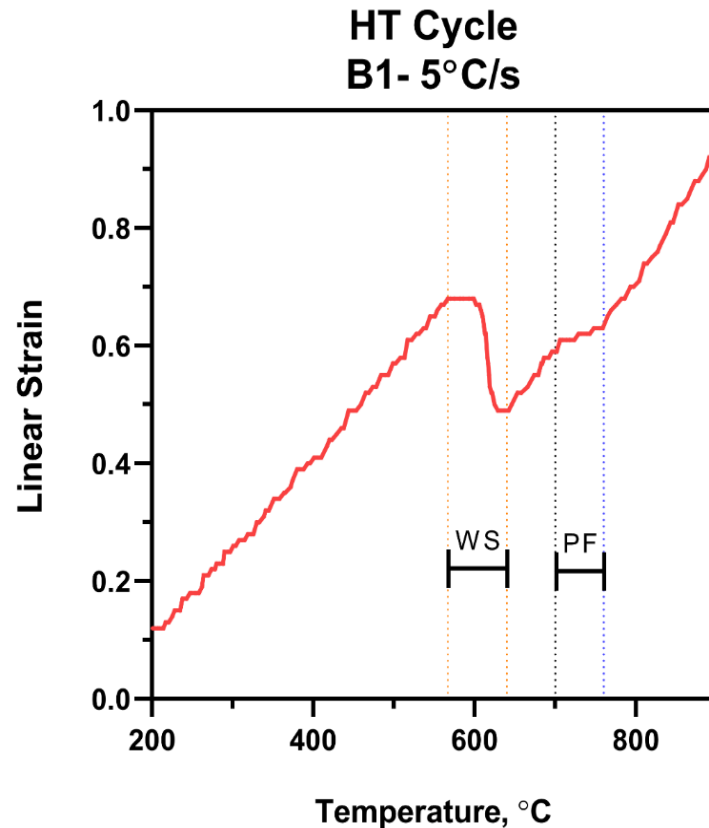


Figure 5.42 Strain vs. Temperature curve for steel B1 showing the phase transformation temperature

The allotriomorphic and Widmanstätten ferrite onset temperatures for steel B2 and B3 were lower (between 10 and 15°C) than those of steel B0 and B1. Figure 5.43 graphically illustrates the data in Table 5.12. The temperature range consisting of allotriomorphic and Widmanstätten ferrite onset and end is higher compared to the cooling rate of 0.5°C/s. The following observation can be made on the effect of solute Nb on transformation temperatures in present investigation:

- For a cooling rate of 0.5°C/s, a transformation consistent with allotriomorphic ferrite was observed between 760 and 800°C. The transformation event present between 640 and 720°C was associated with Widmanstätten ferrite formation. This transition was consistently reproduced, and an average transformation end temperature of 645°C was observed for steel B0-B3.
- For a cooling rate of 5°C/s, a transformation consistent with allotriomorphic ferrite was observed between 700 and 780°C. The transformation event present between 540 and 640°C is associated with Widmanstätten ferrite formation. The Widmanstätten ferrite transition composed of two stages: the first leading to an increase in linear strain between 640 and 600°C and the second giving very little change in linear strain from 600°C until around 545°C.

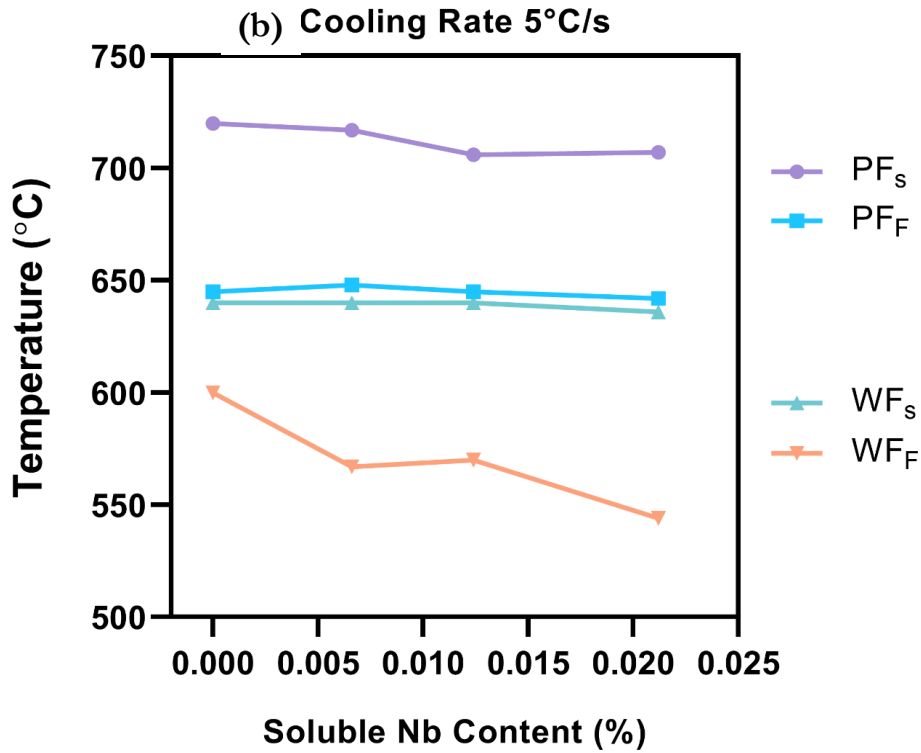
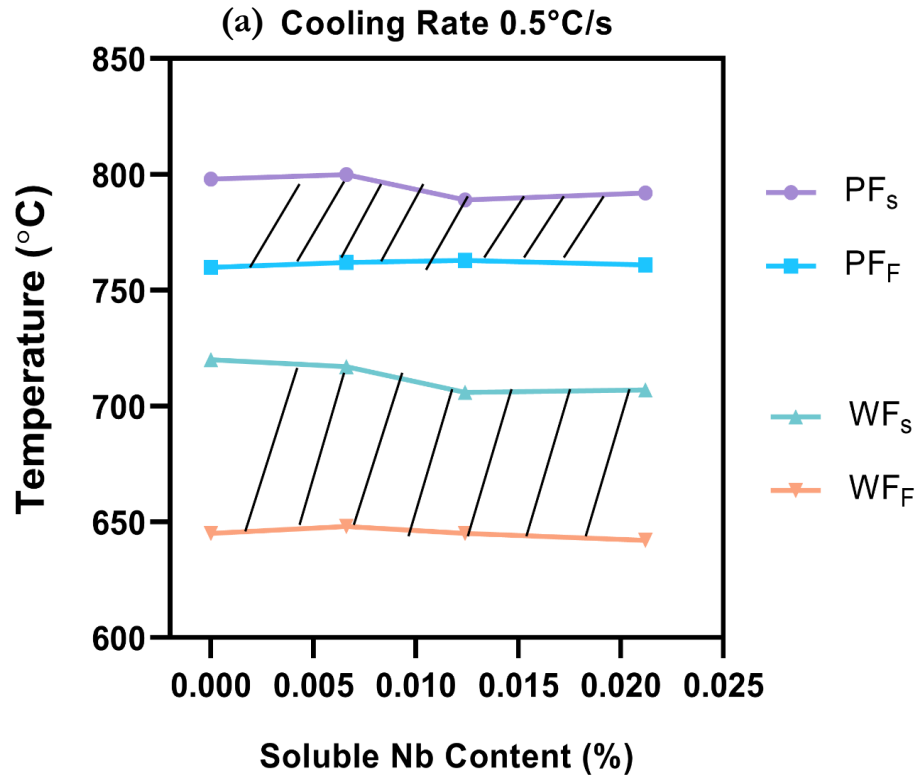


Figure 5.43 Effect of cooling rate on phase transformation temperature in steel B0-B3 as a function of Nb content

5.4.2 Microstructure Observations

Figure 5.44 (a)-(d) shows the microstructure of B0-B3 steels after solution treatment. These microstructures were obtained reheating to the temperature of 1250°C for 45 minutes and quenching in water. The selection of this temperature was crucial to dissolve the precipitates of Nb(CN) and to have complete Nb in austenite solution. All microstructure appears to be fully martensite, mostly a lath structure. There was no indication of pro eutectoid ferrite formation along the PAGB. The mean PAGS of grades B0-B3 were determined to be $145 \pm 12 \mu\text{m}$.

Figure 5.44 (e)-(h) and (i)-(l) illustrate microstructures of steel B0-B3 cooled at 0.5 and 5°C/s and respectively. The solution treated samples were austenitized at 900°C for 5 min and then controlled cooled to room temperature in MTS. The evaluation of continuously cooled microstructure has confirmed the identities of the transformation measured by dilatometry. The microstructure consisting of three distinct phases allotriomorphic ferrite, Widmanstätten ferrite, and pearlite in all cases as follows:

- The first distinct feature consisted of allotriomorphic ferrite primarily formed on coarse prior austenite grain boundaries. The allotriomorphic ferrite grain size was calculated by measuring the thickness of grain boundary allotriomorphs over multiple random locations.
- The second distinct feature consisted of either primary or secondary Widmanstätten ferrite plates grown from allotriomorphic ferrite. The Widmanstätten ferrite plates appeared to be clean (free of carbides) and appeared to be fine in thickness. The plates were stretched and intersecting within the prior austenite grains.
- The prior formation of allotriomorphic and Widmanstätten ferrite enriches the residual austenite with carbon, which transforms to pearlite at A_{r1} temperature. It was challenging to resolve the pearlite in most cases due to the formation higher volumes of Widmanstätten ferrite. The perlite fraction is overestimated due to overlap with Widmanstätten ferrite and carbide structure.

Table 5.13 presents the quantitative metallography data (e.g., the volume fraction of allotriomorphic/polygonal ferrite, Widmanstätten structure, and pearlite) for steel B0-B3 for each cooling condition. The volume fraction of allotriomorphic and Widmanstätten ferrite was calculated using the point-counting method.

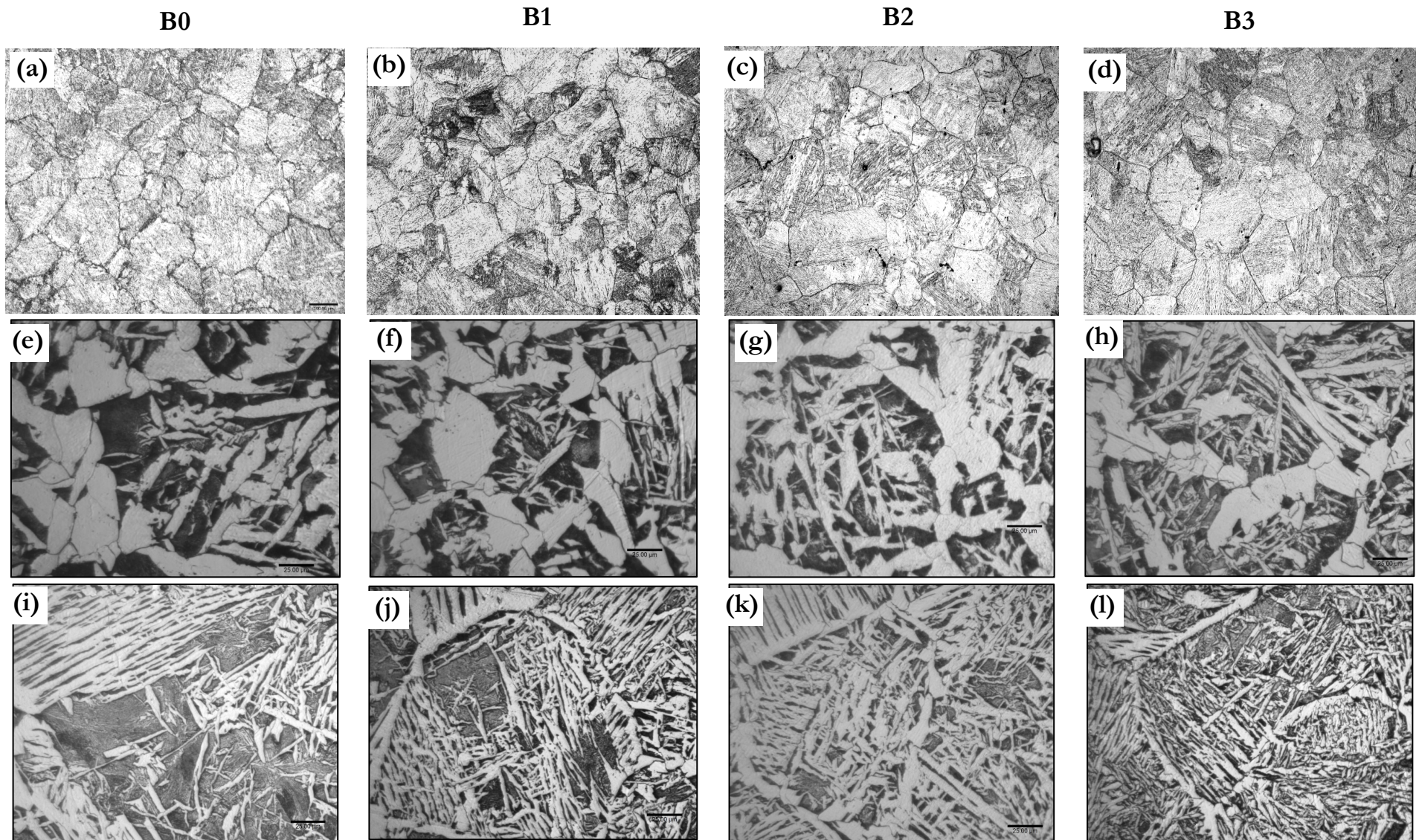


Figure 5.44 (a)-(d) Prior austenite microstructure after solution treatment for steel B-B3 respectively, (e)-(h) microstructure after cooling at 0.5°C/s for steel B0-B3 respectively and (i)-(l) microstructure after cooling at 5°C/s of steel B0-B3 respectively. (Magnification: 200X)

Table 5.13 Metallography data for steel B0-B3 specimens after dilatometry experiments

	Steel	Allotriomorphic Ferrite GS, μm	Allotriomorphic Ferrite (%)	Widmanstätten Ferrite (%)	Pearlite/ Carbide (%)
0.5°C/s	B0	18.4 ± 1.5	33.7 ± 6.3	28.5 ± 5.1	37.9 ± 2.4
	B1+0.006Nb	16.1 ± 1.4	27.4 ± 2.3	33.3 ± 3.6	39.3 ± 1.4
	B2+0.012Nb	15.2 ± 2.5	28.5 ± 4.3	35.2 ± 5.1	36.4 ± 1.8
	B3+0.021Nb	17.2 ± 1.7	27.2 ± 2.3	31.0 ± 4.2	41.8 ± 2.5
5°C/s	B0	9.4 ± 1.8	21.3 ± 1.5	35.2 ± 4.0	43.5 ± 3.1
	B1+0.006Nb	6.2 ± 1.0	16.6 ± 2.0	41.9 ± 3.0	41.5 ± 4.7
	B2+0.012Nb	7.9 ± 0.7	18.0 ± 1.2	43.8 ± 2.8	38.2 ± 1.7
	B3+0.021Nb	7.8 ± 1.2	13.2 ± 4.3	51.8 ± 5.3	35.0 ± 5.1

Figure 5.45 graphically illustrates the quantitative data in Table 5.13. The percentage of Widmanstätten structure increases with an increase in cooling rate and Nb addition to steel B0-B3. The following observation can be made about the ferrite transformation product:

Allotriomorphic Ferrite

- For a given cooling rate, the volume fraction of allotriomorphic ferrite decreases with an increase in Nb addition in the following order: B0, B1, B2, and B3. The grade B3 exhibits the lowest allotriomorphic ferrite for a given cooling rate as it has the lowest transformation temperature range.
- For a given composition, the allotriomorphic ferrite grain size and volume fraction decrease as the cooling rate increases. The austenite decomposition began at higher temperatures in a slow cooling rate, which could be the primary reason for larger grain size and volume fraction of allotriomorphic ferrite in the final microstructure.

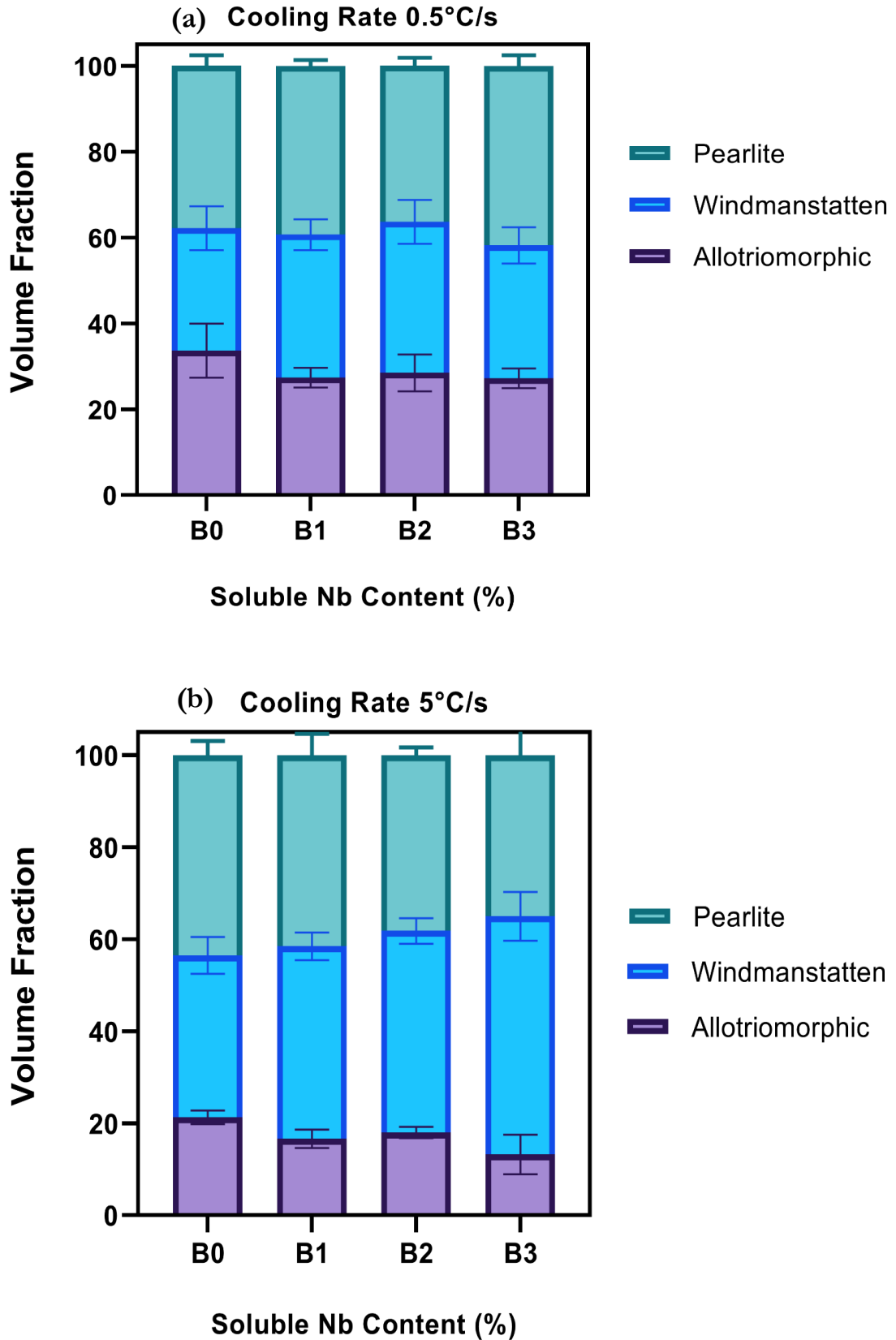


Figure 5.45 Volume fraction of micro constituents of steel B0-B3 as a function of niobium content for a cooling rate of (a) 0.5°C/s and (b) 5°C/s

5.4.3 Mechanical Properties

The heat-treated cylindrical specimens were deformed at room temperature in the TMTS simulator. The true strain, $\epsilon=0.80$, was applied with a constant strain rate of $0.05s^{-1}$. For each steel grade, three specimens were deformed for reproducibility. The load-displacement curves were converted into equivalent stress-strain curves bases on standard practice guide.

Figure 5.46-5.47 shows the equivalent stress-strain curves of steel B0-B3 after room-temperature compression tests for a cooling rate of 0.5 and $5^{\circ}C/s$, respectively. All samples exhibited continuous yielding behaviour except steel B0 at $0.5^{\circ}C/s$. For a given cooling rate, yield strength increases with the increase in Nb addition in the following order: B0, B1, B2, and B3. The grade B3 exhibits the highest yield strength of 458 MPa, which corresponds to an increase of 160 MPa over steel B0 (297 MPa).

For a given composition, the yield strength increases as the cooling rate increases. The strength incremental is in the range of $20-30$ MPa over a slower cooling rate of $0.5^{\circ}C/s$. Table 5.14 summarises the mechanical properties of steel B0-B3 for both the cooling rates.

Table 5.14 Mechanical properties of steel B0-B3 specimens after dilatometry cooling experiments

Cooling Rate	Steel Grade	Average 0.2% YS MPa	Average CS @ $\epsilon = 0.20$ MPa
$0.5^{\circ}C/s$	B0	297	660
	B1	326	675
	B2	360	708
	B3	457	770
$5^{\circ}C/s$	B0	280	655
	B1	360	725
	B2	384	745
	B3	453	766

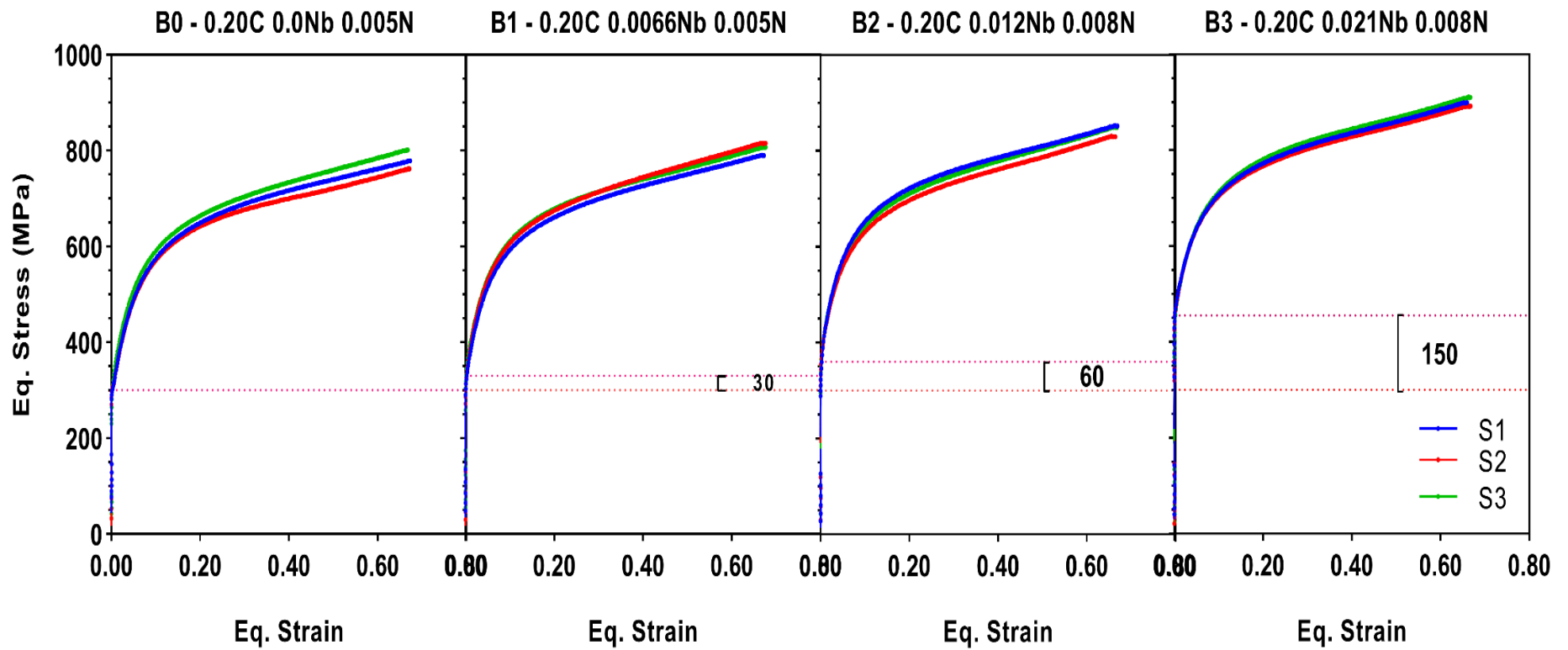


Figure 5.46 Plots of the stress-strain curve from compression tests of steel B0-B3 cooled at 0.5°C/s

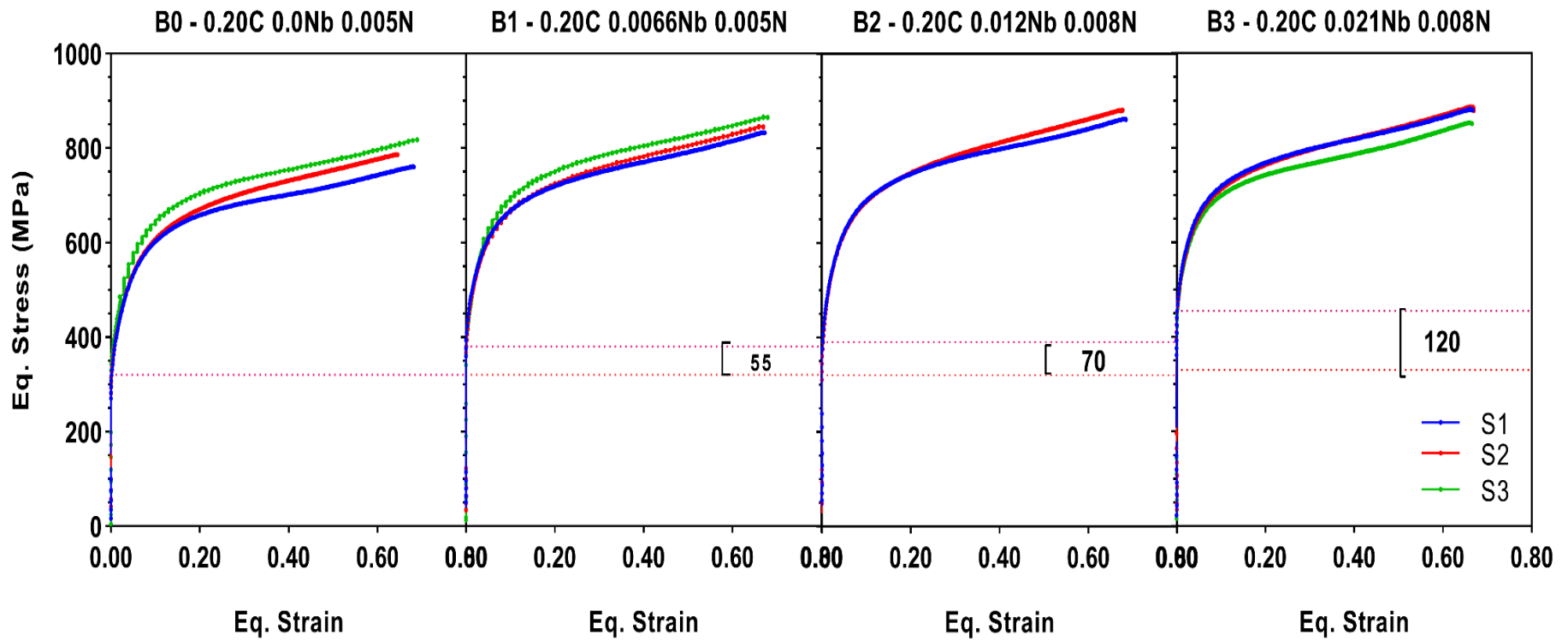


Figure 5.47 Plots of the stress-strain curve from compression tests of steel B0-B3 cooled at 5°C/s

Chapter 6

Discussion

6.1 Grain Coarsening of Austenite

There have been numerous investigations [55,126-127,130,151] regarding the grain coarsening behaviour of plain C-Mn steels, microalloyed steels, or Al-containing steels during reheating in the range 900-1300°C. All of these investigations show results similar to those of Figure 5.1-Figure 5.4 for plain carbon and microalloyed steels. The grain coarsening behaviour of steel B0 and B1 is indicative of typical grain coarsening behaviour. The grain size continuously increases with increasing temperature without any formation of bimodal grain distribution.

The microalloyed steel B2 and B3 exhibited abnormal grain coarsening in a temperature range of 1000-1100°C, followed by secondary recrystallisation. The three regimes of grain coarsening behaviour can be defined for steel B2-B3 representing (1) unimodal distribution of initial grains at lower temperatures (~900-1000°C), (2) a bimodal grain distribution primary and abnormally coarsened grains at intermediate temperatures (~1000-1100°C), and (3) unimodal grain distribution of abnormally coarsened grains at high temperatures (> ~ 1150°C).

For the curves in Figure 5.6, the beginning of T_{GC} (grain coarsening temperature) is identified as corresponding to the onset of the second regime. It represents the temperature where there is a discontinuity in grain growth resulting in bimodal austenite grain diameter/size. This bimodal grain distribution was observed at T_{GC} which is reflected in scatter of standard deviation. The T_{GC} depending upon chemical composition (Nb in present investigations) dictates the presence of second phase particles. As illustrated in Figure 5.6, the T_{GC} for steel B2 and B3 is identified as 1050°C and 1100°C, respectively.

At temperature below the T_{GC} of each steel, austenite grain growth is suppressed by the presence of Nb(CN) particles and results in uniform distribution of fine grains. However, Gladman and Hillert have shown that the Ostwald ripening of precipitates occurs with time, leading to the onset of abnormal grain growth, given in equation (2.31). When a precipitate coarsening gives a value of $r > r_c$, the giant austenite grain will grow consuming the smaller neighboring grains. The abnormal grain growth starts when the precipitates coarsen and go into the austenite solution, with a corresponding decrease in volume fraction.

As the reheating temperature increases further above T_{GC} , the grain coarsening curves shown in Figure 5.6, assume an appearance indicative of the normal grain growth. At 1150°C, most of Nb(CN) precipitates are dissolved in the austenite solution hence results in the normal grain growth. A very small volume fraction of precipitates remains to retard to grain growth; however, they are ineffective due to their coarser size and large interparticle spacing. The combined effect of having a coarser size with large interparticle spacing renders the growth of austenite grains to behave in a manner similar to the growth single-phase austenite.

The trend for increasing T_{GC} with increased Nb levels is observed for steel B1-B3 in the present investigation. This trend is in agreement with an observation from previous studies [130, 160]. The implication is that a higher T_{GC} will result in those systems which contain the most thermodynamically stable Nb(CN) precipitate. The result shows that high stability precipitates as a function of Nb content effectively retard austenite grain coarsening as they are the less soluble in austenite. This higher volume fraction of stable precipitate retards grain growth at higher temperatures.

6.2 Static Recrystallisation of Austenite

The present investigation result, as shown in Figure 5.13 - 5.17, are unique and provides insight into the effect of dilute Nb concentrations on austenite softening. We have measured the static fraction softening of austenite as a function of deformation temperature under a constant interpass time. The interpass time of 5 and 20 sec represents the typical long product processing conditions, e.g., sections, bars, and rails. The strain rates in industrial rolling vary in range from 10-500 s^{-1} ; thus, the applied strain rate of 15 s^{-1} was very close to the industrial process conditions.

6.2.1 Solution Treatment

The dissolution temperature of Nb(CN) mainly depends on the carbon content as well as precipitate's size and their origin. We estimated the dissolution temperature for Nb(CN) using published solubility products, as reviewed in section 2.5. The austenitizing temperature of 1250°C was selected to ensure complete dissolution of Nb(CN) in austenite solution. The solution temperature not only dictates the amount of Nb in solution but also determines austenite grain size before deformation.

Figure 6.1 shows the solubility of Nb in austenite for steel B3 at different reheating temperatures. The employed solubility equations predict the complete dissolution of Nb in a range of 0.023 – 0.032 % at 1250°C. The Irvin *et al.* [127] solubility equation predicts the higher solubility of Nb in austenite at all temperature range in comparison to other equations. Hence, the steel B1-B3 should

have all Nb in austenite solution irrespective of which solubility equation is employed from the literature.

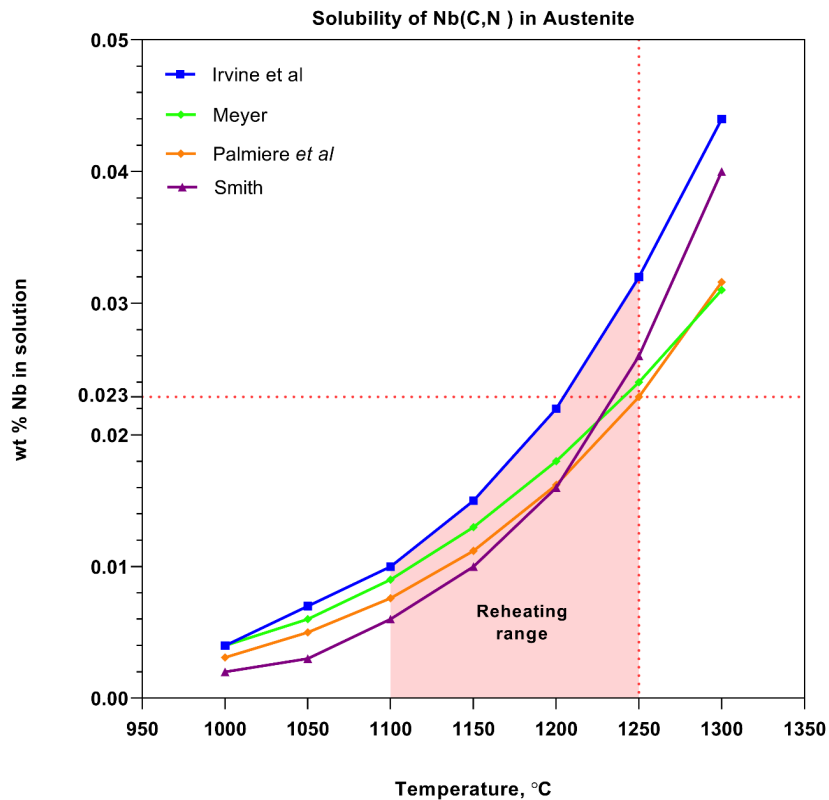


Figure 6.1 Solubility of Nb(CN) in austenite for steel B3 (0.20C-0.021Nb-0.007N) as a function of reheating temperature

We further validated the predicted solution temperature with real heat treatment trials. The samples from steel B3 were soaked in a muffle furnace at 1250°C with different soaking times (30, 60, and 90 mins). The samples were quenched in water immediately after the end of soaking time. The optical and TEM analysis confirmed that the dissolution of Nb(CN) precipitation occurred after austenitizing at 1250°C. The observed grain structure showed uniform grain size distribution, indicating that Nb(CN) has been completely dissolved in solution.

Various investigations studied the effect of austenitizing/soaking temperature on the kinetics of recrystallisation [182-184]. These studies showed that the lower austenitizing temperatures resulted in more rapid recrystallisation rates in comparison to higher austenitizing temperature. The two factors responsible for the difference in recrystallisation behaviour may be the initial grain size, and amount of microalloying element dissolved in the austenite solution.

The effect of initial grain size on static recrystallisation during hot working has received considerable attention [77,80]. The density of favourable nucleation sites increases with a decrease in prior austenite grain size (d_0) since nucleation takes place preferentially on the grain boundaries

[77]. The static recrystallisation kinetics generally follow the Avrami relationship, with a data fitted with Avrami exponent $k=2$.

Barraclough *et al.* [80] examined the effect of initial grain size on static recrystallisation kinetics for austenitic stainless-steel specimens. They observed a systematic decrease in k values when the initial grain size increased above $200 \mu\text{m}$, as shown in Figure 6.2. The prior deformation tends to be inhomogeneous for coarser grain sizes, particularly in the region of grain boundaries. The recrystallised grain will nucleate and grow in the regions of higher local strain, but then the growth rate will fall when growth proceeds into regions of lower local strain.

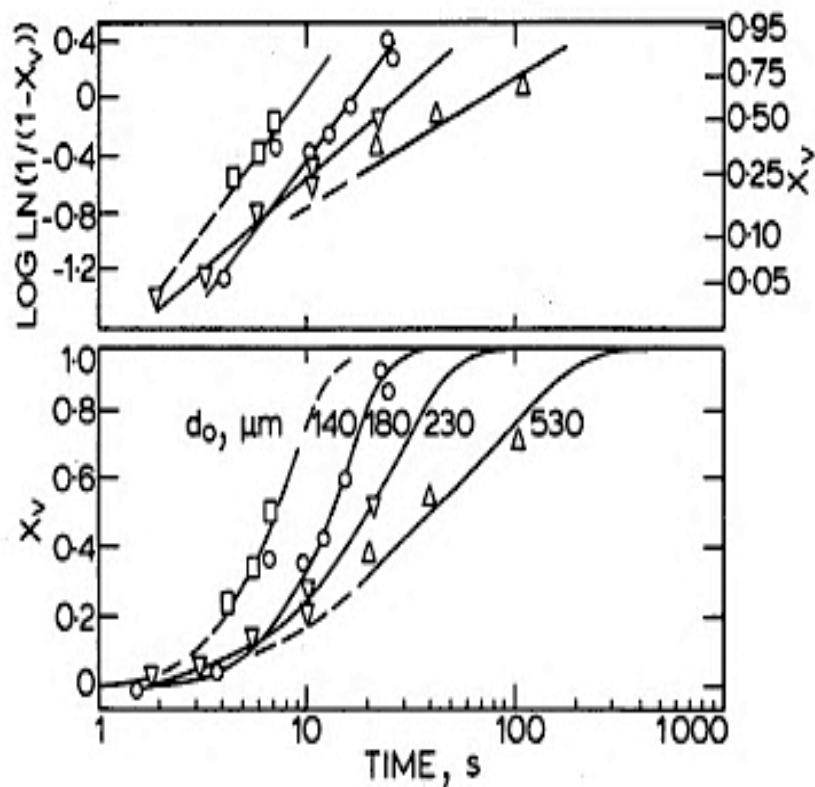


Figure 6.2 Effect on initial grain size on the static recrystallisation curves for a specimen deformed to an equivalent strain 0.50 at 1050°C and 1 s^{-1} (adapted from ref [80])

The complete dissolution of $\text{Nb}(\text{CN})$ precipitates is essential to maximize the retarding effect of Nb on static softening. Stewart *et al.* [183] investigated the effect of Nb and V additions on the softening of austenite during the two-stage deformation cycle with continuous cooling. Figure 6.3 shows the stress softening ratio versus the first deformation temperature for X65 steel for the three different soaking temperatures. The austenite softening occurred at lower deformation temperature for a lower soaking condition. In his experiment, higher softening means recrystallisation was inhibited since the author calculated the softening ratio based on the yield strength. The low softening means the static recrystallisation was the dominant restoration mechanism.

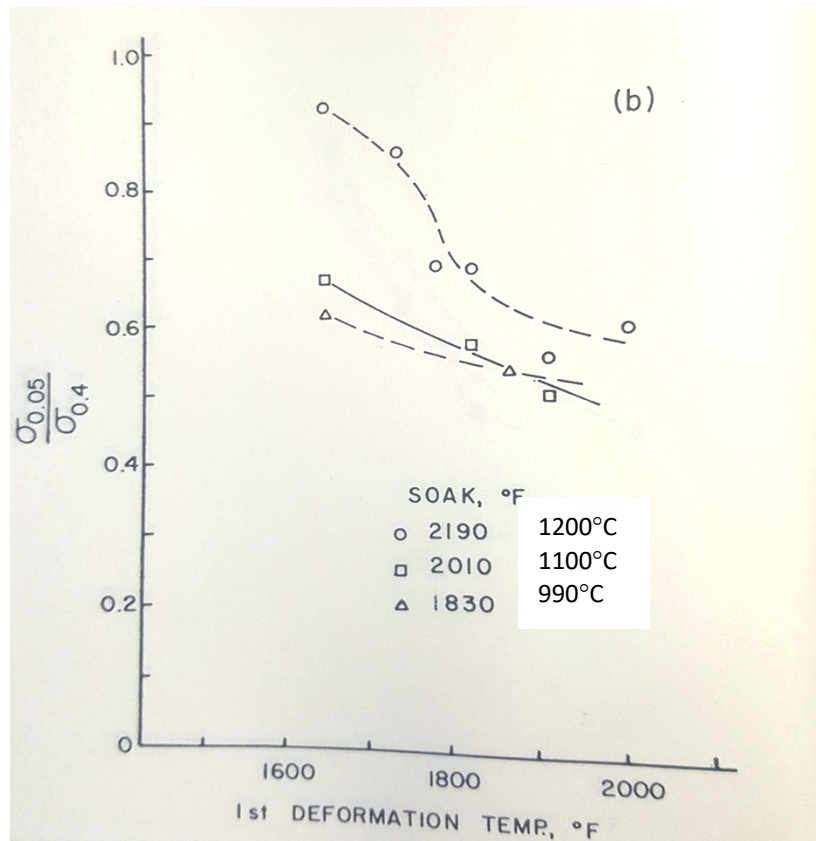


Figure 6.3 The softening ratio versus the first deformation temperature for the X65 steel, a true strain of 0.44, 18 s^{-1} . The second deformation pass was at 900°C (adapted from ref [183]).

Stewart *et al.* [183] recommended higher soaking temperature if no recovery and recrystallisation is desired in hot rolling. The Nb supersaturation will be higher for the highest soaking temperature, resulting in the higher Nb(CN) precipitation potential, and hence the static softening will be retarded to a greater extent.

Double austenitizing heat treatment was used in the present study to eliminate the effect of initial grain size on recrystallisation kinetics. The PSC specimens were further reheated in the TMC machine at 1250°C for 2 mins. The prior austenite grain size was measured after double austenitising treatment and found to be $230 \mu\text{m}$ for steel B0-B3. We expect that the recrystallisation kinetics will follow typical Avrami kinetics with exponent value = 2.

This double austenitizing treatment not only controlled the initial grain structure but also ensured the complete dissolution of Nb(CN) precipitates. In summary, the solution treatment ensured the complete dissolution of Nb(CN) to maximise the retarding effect of Nb through solute drag or by the formation of strain-induced Nb(CN) precipitates.

6.2.2 Recrystallisation Driving Force (F_{RXN})

The change of dislocation density ($\Delta\rho$) during hot deformation is one of the most important microstructural change in the austenite. In present investigation, the $\Delta\rho$ is estimated from an increase in flow stress ($\Delta\sigma$) of the first-pass deformation. The value of $\Delta\sigma$ is obtained from subtracting the initial flow stress from the maximum flow stress reached in the σ - ϵ curve of the first deformation pass.

Numerous investigations [94-99] have shown that the $\Delta\rho$ of hot-worked austenite exhibits a strong dependence on temperature, strain rate, and amount of strain. The present investigation result agrees quite well with the above finding. The $\Delta\rho$ increases as the deformation temperature decrease for steel B1-B3, irrespective of the type of empirical equation used.

Table 5.2 presents the estimated values of $\Delta\rho$ as a function of deformation temperature for steel B1-B3. The equation (2.17) overestimated the value of $\Delta\rho$ in comparison to equation (2.19) for the same input $\Delta\sigma$ value. A minimal change in the estimated $\Delta\rho$ value can cause a substantial effect in F_{RXN} prediction for different deformation condition.

The measured flow stress reflects the complicated physical phenomenon involving the interaction between dislocations, grain boundaries and other microstructural factors. The flow stress in PSC tests can vary for similar isothermal deformation conditions, mainly due to variable friction condition. The flow stress increases with reduction in friction coefficient and vice versa. The simplified mathematical formulae linking $\Delta\sigma$ to $\Delta\rho$ can't reflect the complicated conditions of flow stress. The thin foil sample preparation itself includes 30 % intrinsic error resulting in overall 50% deviation range for $\Delta\rho$ values [185]. In comparison, the flow stresses in PSC testing don't vary significantly for identical deformation condition and can cause deviation of only 5-10% in $\Delta\rho$ values.

The evaluation of dislocation density with time during the restoration event has not received considerable attention. There is hardly any quantitative analysis for austenite recovery behaviour during the actual hot rolling process of steel. The various researchers have adopted a modelling approach to determine the dislocation density evaluation as a function of interpass time [102,145,185]. Akamatsu *et al.* [185] proposed a model to calculate the $\Delta\rho$ due to static recovery as a function of the deformation, interpass time and Nb content based on experimental double-hit tests. He suggested that the amount of decrease in $\Delta\rho$ at 900°C would be small during interpass time of 8-15 sec (typical to plate and section mill rolling).

The driving force for recrystallisation (F_{RXN}) is directly related to stored energy during hot working. A higher F_{RXN} is expected at lower deformation temperature than higher temperatures. As expected,

the F_{RXN} increases as the deformation temperature decrease for steel B1-B3. The Nb addition does not influence the F_{RXN} as the steel B1-B3 shows similar values of F_{RXN} . The calculated F_{RXN} is in the range of 2-9 MPa for steel B1-B3 with Δp estimated from equation (2.17), Method 1. This is in magnitude two to three times higher than the conservative estimate of 0.3-1.3 MPa obtained from the estimation of Δp with equation (2.19), Method 2.

Table 2.9 presents the value of F_{RXN} reported in the literature. It can be seen that errors in the estimation of the driving pressure are significant, considering the variance in the data. The behaviour of measured F_{RXN} is consistent with theoretical predictions even though calculated values may not be absolute. The measured F_{RXN} via Method 2 is in close agreement with the observation of Dutta and coworkers [178]. Hence, the F_{RXN} estimated based on equation (2.18) will be considered for interaction with the pinning force.

6.2.3 Fractional Softening Parameter

The fractional softening measured during PSC testing corresponds to the total net softening of austenite during a set hold time of 5 and 20 secs, which comprises of all softening due to static recovery and recrystallisation as well as hardening due to precipitation.

When the applied strain is less than ϵ_c^R , the softening occurs by classical recovery. The stored energy of deformation is released during static recovery although not large enough to activate any high angle grain boundary motion. The fraction softening due to static recovery would be small in carbon steels because the stacking fault energy of austenite is relatively low (75 mJ/m²) and in effect have more difficulty of dislocation cross slips [94]. In earlier studies, the fractional softening observed before the initiation of recrystallisation was found to be < 20% for a low carbon steel [66,154,162-163]. The non-recrystallised austenite microstructure was observed in these investigations whenever a fractional softening was $\leq 20\%$.

In present study, the fractional softening of approximately 30% was observed before the initiation of the static recrystallisation. The higher softening corresponds to greater $\epsilon_c^f/\epsilon_c^R$ ratio and may be attributed to the solute drag effect of carbon atoms on the occurrence of recovery and recrystallisation in given 0.20%C steels. Kwon *et al.* [42] reported a similar impurity effect in high and commercial purity Al and Cu. The observed fraction softening before the initiation of recrystallisation was approximately 20% for commercial purity Al, but was only about 5% for high purity Al.

As a result of above, the overall static softening behaviour showed in Figure 5.13 mainly represents the softening due to the static recrystallisation of austenite. It is apparent for each steel, the amount of fractional softening increases with increasing temperature for a constant strain, strain rate, and

hold time. Additionally, the amount of fraction softening increases with an increase in pass strain for a given deformation temperature. Dutta *et al.* [178] reported similar behaviour for a low carbon microalloyed steel.

Steel B0-B3 exhibited a typical sigmoidal shape of softening curves as a function of deformation temperature. The steel B3 only showed fractional hardening at the lowest deformation temperature of 850°C. The fractional softening curves of steel B1-B3 revealed the influence of Nb supersaturation on the static restoration process in comparison to the base grade. The systematic gradual shift in retardation temperature validates the role of Nb for a given composition.

Steel B1 (B0+0.007% Nb) showed a plateau in softening curves for a true strain, $\varepsilon \leq 0.20$, and temperature up to 900°C. These results imply that the static recrystallisation was inhibited at lower strains for steel B1, mainly due to Nb addition. The observed fraction softening was lower at higher strains $\varepsilon > 0.20$ in comparison to steel B0 for the same deformation conditions.

Steel B2 (B0+0.012%Nb) exhibited the plateau of softening curves for all strains at 900°C. Also, the static recrystallisation was inhibited for temperature up to 950°C at lower strains, $\varepsilon \leq 0.20$. Again, this positive effect could be directly linked to the Nb addition.

Steel B3 (B0+0.021%Nb) showed the most potent effect of Nb on retarding static recrystallisation. The recrystallisation was inhibited up to a deformation temperature of 950°C for all strain conditions. The static recrystallisation was the dominant mechanism at higher temperatures.

It is difficult to compare the results of Figure 5.13 directly with the majority of previous investigations on low and high carbon steels [11,71-75,108]. The previous investigations concentrated on understanding the kinetics of softening, which occurs during delay time in multi-pass deformation conditions. The investigations measured the fractional softening of austenite at a constant temperature as a function of interpass time. Additionally, the previous investigation conducted deformation at lower strain rates ($\leq 1s^{-1}$) and under low Z conditions where dynamic restoration process may occur before any static restoration event. The present research measured the fraction softening of austenite at constant interpass time as a function of deformation temperature.

There are two investigations [154, 178] from which direct comparison could be made with the results of Figure 5.13, particularly of steel B3. These investigations had a composition similar to steel B3 of the present study, with the exception of carbon concentration (0.10 wt. %). The austenite static softening behaviour can be compared due to similarity in reheating temperature, isothermal DHT technique, and deformation parameters.

Palmiere *et al.* [154] had studied the static softening of microalloyed steel composition, Fe-0.080C-1.4Mn-0.020Nb-0.008N for deformation parameters of $\epsilon=0.30$, $\dot{\epsilon}=10\text{s}^{-1}$ and delay time =10 sec. A softening plateau of 10-20% belonging to the static recovery was reported in steel E3 for $T_{\text{def}} \leq 950^\circ\text{C}$, similar to steel B3 of the present investigation. The full softening corresponding to static recrystallisation was reported for deformation at a higher temperatures, $T_{\text{def}} \geq 1000^\circ\text{C}$, which again is in agreement with present investigation results.

Dutta *et al.* [178] investigated the static softening of a steel composition, Fe-0.10C-1.4Mn-0.030Nb-0.005N for deformation parameters of $\epsilon=0.10-0.40$, $\dot{\epsilon}=10\text{s}^{-1}$ and delay time = 10 sec. The reported overall austenite softening behaviour is in total agreement with the results of steel B3 even though their steel has higher Nb content. All the softening curves at 850°C exhibited fractional hardening while curves exhibited a plateau between 900 and 950°C temperatures.

Figure 6.4 illustrates the % fractional softening of steel B3, hold time = 5 sec as a function of deformation temperature. The fractional softening curves of Palmiere *et al.* [154] and Dutta *et al.* [178] investigations are superimposed for the comparison purposes. A favorable agreement was obtained between the % fractional softening of austenite for all three compositions at temperature, $850-1050^\circ\text{C}$. It is interesting to note that the higher carbon concentration has not affected the softening results for steel B3. It suggests that there is no significant difference in Nb(CN) precipitation potential for 0.10 vs. 0.20 % carbon level if the Nb is completely dissolved in austenite.

There are some investigations [18, 92] in the literature concerning static recrystallisation of austenite microalloyed with dilute Nb additions similar to steel B1 (66 ppm) and steel B2 (120 ppm). However, these investigations involved the multi-pass rolling simulations under continuous cooling conditions through hot torsion testing. Therefore, the results of the present investigation cannot be compared based on differences in test principles.

6.2.4 Recrystallisation Processing Window

The fraction softening attributed to static recovery (up to 20%) is in agreement with findings from previous investigators [66,154,162-163] who also had reported a similar level of softening due to static recovery. The measurement of static fraction softening as a function deformation temperature allows the easy and direct estimation of $T_{5\%}$ based on 20% fraction softening criteria. Table 5.4 presents the value of $T_{5\%}$, and $T_{95\%}$ estimated from softening criteria for steel B0-B3. The steel B0/base grade exhibited static recrystallisation even at 850°C ; for $\epsilon \geq 0.20$. Hence, we calculated the $T_{5\%}$ for base steel B0 via curve fitting the real softening curves below 850°C .

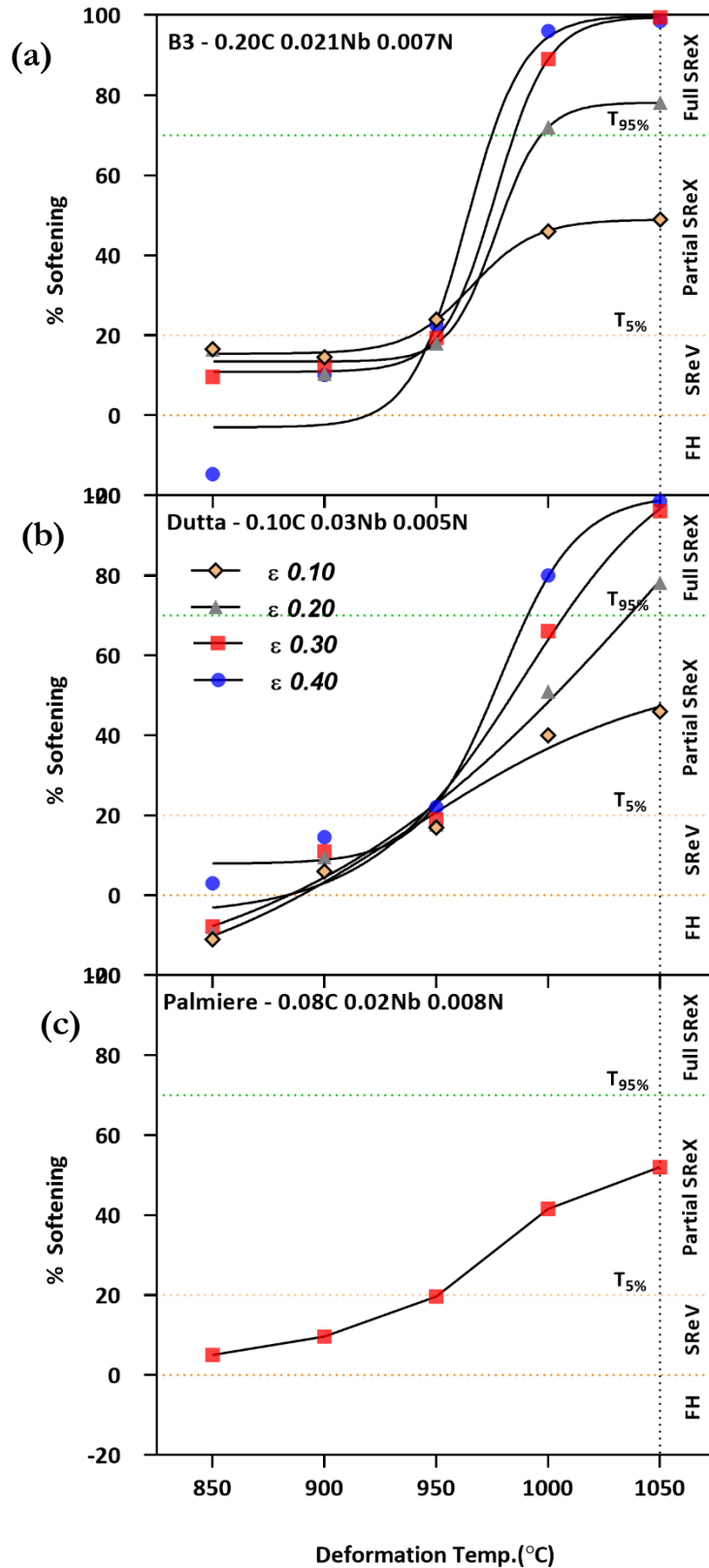


Figure 6.4 Fractional softening curves comparison (a) steel B3-present investigation (b) Dutta *et al.* and (c) Palmiere *et al.* for isothermal deformation and hold (reproduced from ref [154, 178])

Figure 5.14 illustrates the dependence of $T_{5\%}$ and $T_{95\%}$ on first pass strain for steel B0-B3 at set interpass time of 5 and 20 secs. The $T_{5\%}$ and $T_{95\%}$ temperatures decreased with an increase in pass strain for steel B0-B3. The effect of pass strain on recrystallisation rates arises from its direct influence on nucleation density and growth of new grains. The RST also decreased with an increase in interpass time for the same deformation condition.

The $T_{95\%}$ curve for steel B0 exhibits the exponential decay shape, i.e., steeply going downward as pass strain increases. However, $T_{95\%}$ for Nb bearing steels is shifted rightwards, and it does not decrease drastically as a function of strain. It could be due to the interaction between recrystallisation and precipitation, which delays the completion of static recrystallisation. The temperature range ($T_{95\%} > T_{def} > T_{5\%}$) where partial recrystallisation can occur for steel B1-B3 decreases as the Nb content increases. As a result, steel B3 has a very narrow range of partial recrystallisation regime of 30°C.

There has been little quantitative experimental work to determine the $T_{5\%}$ (RST) and $T_{95\%}$ (RLT) as a function of pass strain, interpass time, and strain rate for isothermal conditions. Dutta *et al.* reported a similar strain dependence of $T_{5\%}$ and $T_{95\%}$ in his investigations on low carbon steels [178]. They proposed the following relationship between $T_{5\%}/T_{95\%}$ and the amount of deformation (ϵ) from mathematical fit to data: $T_{5\%} = 936 \times \epsilon^{-0.014}$ and $T_{95\%} = 916 \times \epsilon^{-0.07}$. This relationship was derived from the experimental fractional softening data and is valid only for the investigated composition. The equation predicts value closed to measured $T_{5\%}$ and $T_{95\%}$ for steel B3 at higher value of applied strain.

Bai *et al.* [147] investigated the influence of deformation processing variables (i.e., strain, strain rate, interpass time and chemical composition) on the RST for short and long interpass time under continuous cooling condition. They observed that the $T_{5\%} / RST$ decreases with time for short interpass range as solute drag controls the recrystallisation. However, the $T_{5\%} / RST$ increased with time for long interpass time since the Nb(CN) precipitation retarded the recrystallisation. The relationship between RST and processing parameter was derived in their work which is as follows:

$$\begin{aligned} RST &= (A \log [Nb]_{eq} + B) \epsilon^{-0.12} \dot{\epsilon}^{-0.01} t^{-0.1} && \text{for } t < 12 \\ RST &= (A' \log [Nb]_{eq} + B') \epsilon^{-0.12} \dot{\epsilon}^{-0.01} t^{0.04} && \text{for } t > 12 \end{aligned} \quad (6.1)$$

where, $A = 88.1^\circ\text{C}$ per wt.%, $B=1156^\circ\text{C}$, $A' = 63.5^\circ\text{C}$ per wt.% and $B'=885^\circ\text{C}$ are fitting constants determined from experimental tests. The equation predicted a high value of $T_{5\%} / RST$ for deformation condition in present investigation consisting of interpass time of 5 and 20 secs. The equation was based on higher precipitation stability hence predicted higher $T_{5\%}$.

The $T_{5\%}$ increases with an increase in amount of Nb added to the base steel in the following order: 835°C (0Nb), 870°C (0.007Nb), 900°C (0.012Nb) and 953°C (0.021Nb) for a maximum pass strain, $\epsilon = 0.40$ and IP=5 sec. An increase of 120°C in RST for steel B3 over base grade is significant, considering the levels of dilute Nb additions. Figure 6.5 illustrates the influence of Nb concentration on measured $T_{5\%}$ for steel B1-B3.

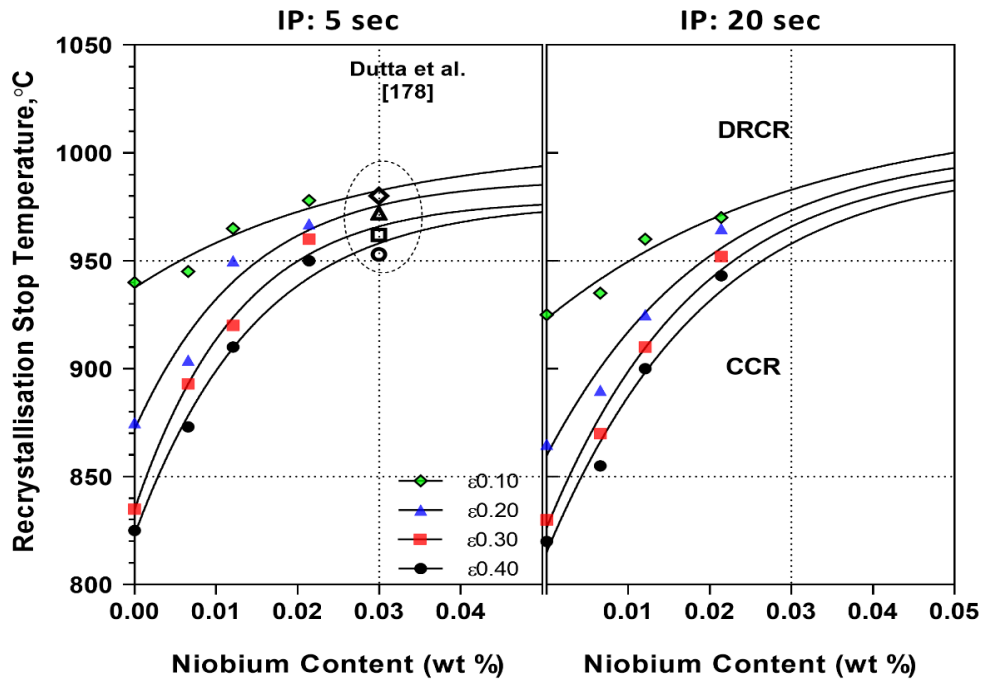


Figure 6.5 Effect of initial niobium content on recrystallisation stop temperature for different pass strains. The circled area shows the reported values of $T_{5\%}$ in Dutta *et al.* [178] investigation.

Cuddy [11] examined the effect of microalloying concentration on the recrystallisation of austenite during hot deformation. The RST (i.e., $T_{5\%}$) was determined using simulated multipass rolling for a variety of microalloyed steels, which had each been soaked at several temperatures to obtain a range of initial solute levels. The samples were subjected to multipass rolling comprising of 5 sequential PSC of 10-17% reduction per pass with a temperature interval of 40-50°C. The strain rates ranged from 5-10 s^{-1} with interpass time of 10-16 sec. The results showed that only the Nb effect is strong enough to allow control rolling at high temperatures. The RST per gram of solute atom increased in the order of V < Al < Ti < Nb. He suggested that finish passes should begin at least 50°C below the RST to avoid partial recrystallisation regime.

Figure 6.6 compares the values of RST obtained from the present investigation for $\epsilon = 0.40$ with the Cuddy's results. A very satisfactory agreement is obtained between the RST values for Nb levels in the present investigation. As mentioned earlier, the Cuddy's experiments involved multipass rolling with total strain, $\epsilon = 1.0$ (5 x 0.20) at different temperature while the present study had two isothermal deformation passes with total strain $\epsilon = 0.80$ (2 x 0.40). However, the strain rates,

interpass time, and method of deformation were similar which is one of the main reasons for favorable agreement. The RST is expected to be higher for strain $\epsilon \leq 0.25$ (15-25% reduction), which is typical of plate or section mill rolling compared to below Cuddy results.

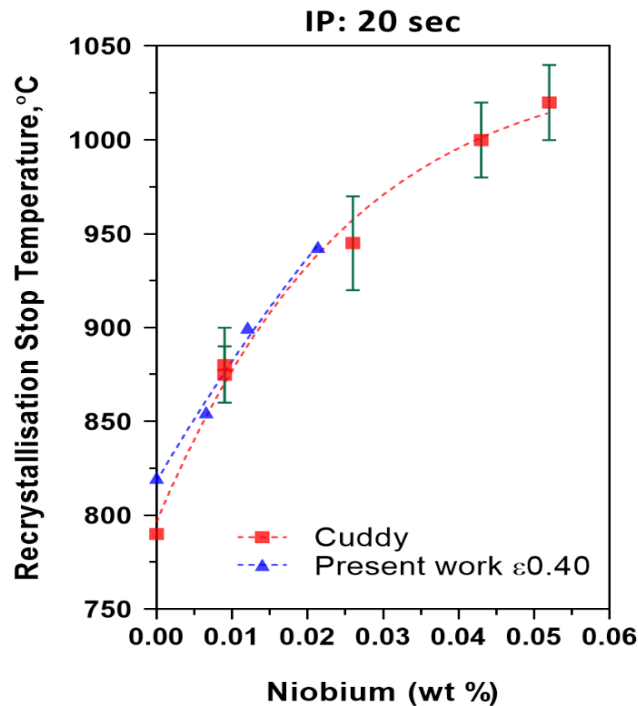


Figure 6.6 Effect of initial Nb content on recrystallisation stop-temperature (reprod. from ref [11])

6.2.5 Nb Supersaturation, $[Nb]_{ss}$

Figure 5.15 depicts the critical relationship between Nb in a supersaturated solution, $[Nb]_{ss}$ before hot deformation, and % fractional softening for steel B1-B3. The curves exhibit typical sigmoidal kinetics similar to deformation temperature. At high temperature, the static recrystallisation is the dominant mechanism even for the steel B3 having an $[Nb]_{ss} \sim 0.015$. As the deformation temperature decreases, the $[Nb]_{ss}$ levels had a significant influence on static softening behavior and particularly on the regime of partial recrystallisation for all steels.

Steel B3 exhibited a low fractional softening at 950°C since the $[Nb]_{ss}$ of 0.019 % is sufficient for strain-induced precipitation to proceed and retard static recrystallisation of hot deformed austenite at $\epsilon = 0.40$. Steel B2 exhibited high softening at 950°C as $[Nb]_{ss}$ of 0.010 % is not sufficient to retard recrystallisation. However, it exhibited low softening at 900°C with the same amount of $[Nb]_{ss}$ in austenite.

Similarly, steel B1 exhibited low softening for deformation at 850°C with $[Nb]_{ss}$ of 0.0056 % whereas base composition showed complete softening at this temperature. The electron microscopy studies have validated the role of $[Nb]_{ss}$ on strain-induced precipitation which will be discussed in detail in sections 6.3.

Table 6.1 compares the relationship between $T_{5\%}$ (i.e., RST) vs. $[Nb]_{ss}$ levels before deformation at $\epsilon=0.4$ for steel B1-B3. The $T_{5\%}$ increases as the $[Nb]_{ss}$ increases for steel B1-B3 respectively for a constant strain and interpass time. The $[Nb]_{ss}$ of 0.006, 0.010, and 0.018 wt.% were observed for steel B1-B3, respectively, at their corresponding $T_{5\%}$ (RST). The Nb microalloying addition increased the $T_{5\%}$ at a rate of 40°C per 0.006 % $[Nb]_{ss}$.

Table 6.1 Comparison of $T_{5\%}$ vs. $[Nb]_{ss}$ for steel B1-B3 at $\epsilon=0.40$ and hold time of 20 sec

Parameter	B1	B2	B3
$T_{5\%}, ^\circ\text{C}$	855	900	943
Nb soluble at 1250°C, wt % (1)	0.0066	0.0121	0.0214
Nb soluble at $T_{5\%}$, wt % (2)	0.0010	0.0017	0.0027
Nb supersaturation at $T_{5\%}$, wt % (1)-(2)	0.0056	0.0103	0.0187
Nb supersaturation ratio (1)/(2)	6.46	7.01	7.84

Figure 6.7 depicts the $[Nb]_{ss}$ at respective $T_{5\%}$ for each steel at strain $\epsilon=0.10-0.40$ and hold time of 20 sec. For a constant applied strain, the $T_{5\%}$ increases with increasing $[Nb]_{ss}$ for steel B1 to B3 respectively (B1 being the lowest). This clearly demonstrates an effect of higher $[Nb]_{ss}$ on precipitation kinetics which in turn inhibits the progress of recrystallisation.

For a constant composition, there is no significant $[Nb]_{ss}$ difference prior to deformation at $T_{5\%}$ for different strain levels. However, the $T_{5\%}$ decreases with increasing applied strain for all the steel composition. These results validate the effect of pass strain not only on precipitation kinetics but also on recrystallisation rates. Assuming parabolic hardening leads to a linear increase in dislocation density with strain and hence in driving force for grain boundary migration. The three-dimensional dislocation nodes being preferred sites for precipitate nucleation, the kinetics of strain-induced precipitation are also accelerated with increase in strain. The decrease in $T_{5\%}$ with increases in applied strain is more significant for steel B1 and B2 as there is not enough $[Nb]_{ss}$ available for precipitation.

According to Hansen *et al.* [40], “The degree of Nb supersaturation concerning Nb(CN) precipitation is believed to be a critical factor in determining whether or not an effective recrystallisation/precipitation interaction will take place at a particular temperature.” He suggested a critical degree of supersaturation must be exceeded for profuse strain-induced Nb(CN) precipitation to retard austenite recrystallisation at $T_{5\%}$. Palmiere *et al.* [154] found that an $[Nb]_{ss}$ was not constant at respective $T_{5\%}$ and ranged in value between 0.019 to 0.045 wt.% for their work on low carbon steels.

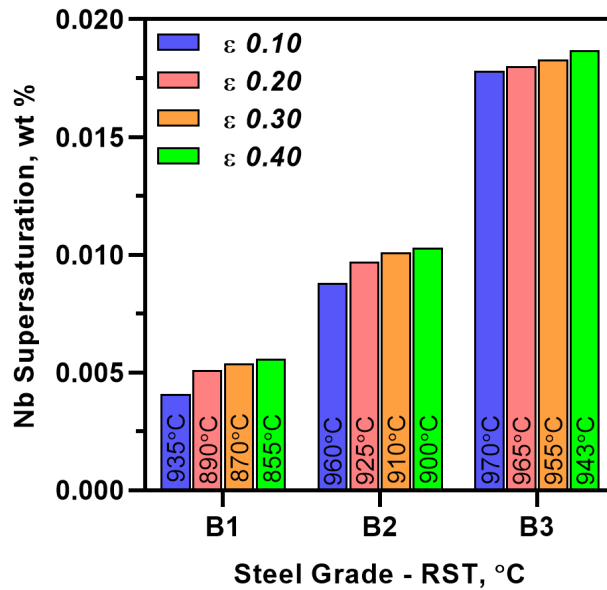


Figure 6.7 Nb supersaturation in austenite at respective RST/ $T_{5\%}$ for steel B1-B3

The present result is in favorable agreement with both the above findings with the view that retardation of recrystallisation is not associated with unique $[Nb]_{ss}$ as seen in Figure 6.7. The recrystallisation and precipitation are competing processes during high-temperature deformation, and the rate of each process depends upon which process is occurring preferentially. The precipitation process is the one which is significantly influenced by available $[Nb]_{ss}$ prior to deformation at that particular temperature.

6.2.6 Nb Supersaturation Ratio, $[Nb]_{SSR}$

Figure 5.16 highlights the relationship between Nb supersaturation ratio, $[Nb]_{SSR}$, and % fractional softening for steel B1-B3. Steel B3 exhibited low softening values at 950°C with an $[Nb]_{SSR} = 7.8$ whereas an $[Nb]_{SSR} = 4.1$ in steel B2 was not sufficient to retard recrystallisation. However, the recrystallisation was retarded whenever the $[Nb]_{SSR}$ exceeded a constant value of 5 for steel B1-B3 at a particular deformation temperature. As shown in Table 6.4, an $[Nb]_{SSR}$ of 6.5, 7.0 and 7.8 were observed for steel B1-B3, respectively, at their corresponding $T_{5\%}$ (RST) for $\epsilon=0.40$.

Figure 6.8 depicts the $[Nb]_{SSR}$ at respective $T_{5\%}$ for each steel at strain $\epsilon=0.10-0.40$ and hold time of 20 sec. The critical $[Nb]_{SSR}$ for retardation of recrystallisation increases with pass strain for a constant level of Nb supersaturation. The critical $[Nb]_{SSR}$ of 4.5, 5.0 and 6.0 were observed for steel B1, respectively, at corresponding $T_{5\%}$ (RST) for the strain of 0.20, 0.30 and 0.40. A similar pattern is seen for the steel B2 and B3. The recrystallisation was inhibited whenever the critical $[Nb]_{SSR}$ was exceeded at a particular temperature.

Hansen *et al.* [40] suggested that the retardation of recrystallisation was associated with a similar Nb supersaturation ratio in austenite. Their investigations on Fe-0.10C-1.35Mn-0.03Nb-0.010N has shown that a 0.03 % Nb in solution with an $[\text{Nb}]_{\text{SSR}}$ of 7.5 retarded static recrystallisation at 950°C, through strain-induced precipitation. The retardation effect declined as the soluble Nb decreased to 0.02%Nb with corresponding an $[\text{Nb}]_{\text{SSR}}$ of 5.0. Both of these steels were reheated at 1250°C, deformed at 950°C in a single pass of strain, $\varepsilon=0.70$. The solubility equation of Irvine *et al.* [127] was adopted to calculate the Nb in austenite solution. He suggested that the critical supersaturation limit must fall between these two $[\text{Nb}]_{\text{SSR}}$ values for deformation conditions in their study.

Cuddy [11] calculated the $[\text{Nb}]_{\text{SSR}}$ ratio at the respective $T_{5\%}$ for several steels which were simulated in multipass deformation. These steels were soaked at several temperatures (950-1200°C) to obtain a range of initial solute levels. The $[\text{Nb}]_{\text{SSR}}$ was not constant and ranged in value between 5–40 at respective $T_{5\%}$. He reported uncertainty in reported results because the soluble Nb in austenite was calculated from the Nordberg *et al.* [118] solubility product. However, Cuddy calculated the $[\text{Nb}]_{\text{SSR}}$ as a ratio of solubility product (k_s) instead of Nb content which yielded wrong values. The correct values of $[\text{Nb}]_{\text{SSR}}$ are in the range of 3.10–6.20 at respective $T_{5\%}$ based on the Irvin solubility product.

These present study results have a satisfactory agreement with the work of Hansen and Cuddy. The results show that the critical Nb supersaturation ratio is independent of Nb supersaturation levels at respective $T_{5\%}$ however they vary with pass strain for steel B1-B3. The recrystallisation was inhibited whenever critical $[\text{Nb}]_{\text{SSR}}$ exceeded at a particular temperature for steel B1-B3. It is expected that there will be a sufficient volume fraction of Nb(CN) precipitates at critical $[\text{Nb}]_{\text{SSR}}$, leading to the necessary pinning force to inhibit the progress of recrystallisation. This finding has significant importance showing the role of Nb supersaturation, critical Nb supersaturation ratio and associated precipitation potential in retarding the static recrystallisation.

6.2.7 Optical Microstructure Studies

Figure 5.20 illustrates linear intercept grain size, \bar{L}_3 (ND) as a function of deformation temperature for microstructure after single hit-deformation, $\varepsilon=0.80$ for steel B1-B3. The \bar{L}_3 of the recrystallised grains decreases as the deformation temperature decreases for a constant strain.

Various researchers [64,68] have studied the conventional subgrain structures of austenite in low carbon steels. During high-temperature deformation (low Z), the grain boundary migrates locally in response to subgrain structure and dislocation density variations. The subgrain size of the dynamically recovered material is related to the steady-state flow stress. The larger subgrain is

formed at lower stress values and vice versa. As a result, larger subgrain sizes are seen at higher temperatures (low Z), leading to coarser prior austenite grains for a constant strain [68].

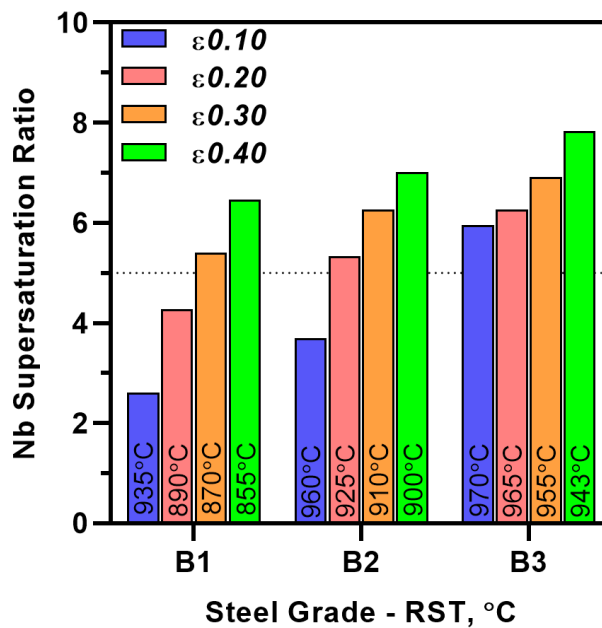


Figure 6.8 Nb supersaturation ratio in austenite at respective RST/ $T_{5\%}$ for steel B1-B3

Under low-temperature deformations (high Z), the work hardening dominates, resulting in large scale formation of deformation bands. It is well known that the static recrystallisation preferentially nucleates on grain boundary as well as deformation bands and twins [70, 77-80]. The finer grain size at lower deformation temperature could be the result of the intragranular nucleation on deformation bands.

The fraction softening data was further supported through quantitative metallography observation in Figure 5.21-5.23 for precipitate analysis conditions. It was necessary to verify the correspondence between 20% fractional softening criteria and $T_{5\%}$. All steels showed good agreement between the microstructure and mechanical softening data. At a temperature below the respective $T_{5\%}$ for each steel (corresponding to a temperature where 20% fraction softening was measured after 5 or 20 sec hold time), a fully deformed and unrecrystallised prior austenite microstructure is observed. The austenite grains are elongated in a perpendicular direction to the axis of compression.

At temperature immediately above $T_{5\%}$ for each steel, the presence of duplex microstructure should be observed, depicting both equiaxed and elongated prior austenite grains. This type of microstructure is indicative of material that has experienced partial recrystallisation. These microstructures are not observed for steel B1 and B3 because of the 50°C deformation temperature increments. However, one clear example of the duplex microstructure is depicted in Figure 5.22 of steel B2.

Figure 5.22 shows series of microstructures for steel B2 deformed, $\epsilon=0.40$ at various temperatures. The $T_{5\%}$ and $T_{95\%}$ for steel B2 was identified as 900°C and 933°C from interrupted compression testing. The microstructure corresponding to the deformation temperature of 900°C exhibits unrecrystallised prior austenite predominately. With an increase in deformation temperature to 950°C, the partially recrystallised microstructure was observed. The small equiaxed grains were nucleated on grain boundary with some deformed and elongated austenite grains. At the next highest deformation temperature of 1000°C, a complete recrystallised microstructure is observed. The sequence of the microstructure of steel B2 suggests that the temperature range of partial recrystallisation is narrow and no greater than 50°C.

Figure 5.24 – 5.27 shows austenite microstructure after the double hit deformation (hold time of 20 sec) for steel B0-B3. A good correspondence was obtained between these microstructures and fraction softening data. Although the mean PAGS after the solution treatment is different for B0-B3, the recrystallised austenite grain size does not vary after the deformation. This proves that the applied strain has a more dominant effect of grain size rather than the initial austenite grain size.

Figure 5.28 – Figure 5.29 shows the mean PAGS and aspect ratio respectively of austenite microstructure deformed in double hit deformation. These parameters were taken as indicators of the degree of recrystallisation or work in the grains. For example, a drastic decrease in the mean PAGS coupled with an aspect ratio = 1.0 indicates complete static recrystallisation. Similarly, a constant mean PAGS with an increase of aspect ratio indicates the work hardening of the austenite.

6.3 Nb(CN) Precipitation in Austenite

Both the thin foil and extraction replica technique have identified the morphology, location, size, and chemical composition of strain induced Nb(CN) precipitates.

6.3.1 Crystallography of Precipitation

Nb(CN) can precipitate in both austenite and ferrite depending upon available supersaturation and deformation parameters. Several studies [181-190] have shown that the lattice of Nb(CN) precipitate with the NaCl crystal structure is parallel to the FCC lattice of the parent austenite in austenitic stainless steel, i.e.

$$\begin{aligned} (100)_{\text{Nb(CN)}} &\parallel (100)_{\gamma} \\ [010]_{\text{Nb(CN)}} &\parallel [010]_{\gamma} \end{aligned}$$

Davenport *et al.* [133] have provided direct evidence that this same relationship holds true for the strain induced precipitation of NbC in deformed austenite in a microalloyed steel. When Nb(CN)

precipitates in ferrite [181, 187] or martensite, [186] it does so with the Baker-Nutting orientation relationship (181):

$$\begin{aligned} (100)_{\text{NbC}} &\parallel (100)_{\alpha} \\ [110]_{\text{NbC}} &\parallel [110]_{\alpha} \end{aligned}$$

So in principle, the orientation relationship observed between the Nb(CN) and ferrite can be used to distinguish whether the precipitate had nucleated in austenite or in ferrite. As was noted above, Nb(CN) forms in austenite with a parallel orientation relationship and in ferrite with the B-N orientation relationship. Therefore, Nb(CN) precipitates showing the B-N relationship must have formed in the ferrite while the Nb(CN) that forms in austenite will not have the B-N relationship with the ferrite.

When austenite transforms into ferrite or martensite, it does so with a Kurdjumov-Sachs (K-S) orientation relationship [180]. As a result, the orientation of prior austenite and the strain-induced Nb(CN) precipitates that formed in the deformed austenite would be related to the ferrite or lath martensite by the K-S orientation relationship.

$$\begin{aligned} (111)_{\gamma} &\parallel (110)_{\alpha} \\ [110]_{\gamma} &\parallel [111]_{\alpha} \end{aligned}$$

The six variants of orientation relationship between SIP and ferrite matrix can be derived as there are six two-fold rotation axes of $\{110\}$ in the bcc matrix. Table 6.2 list the possible variants of orientation relationship between SIP and ferrite matrix when observed at room temperature [187]. Therefore, the precipitates that formed in the austenite can be identified if they obey K-S OR with the lath martensite in quenched deformed specimen.

The orientation of austenite grain will change if any static recrystallisation occurs during hold time or by grain rotations accompanying deformation. In this case, there would be no rational crystallographic relationship between the Nb(CN) precipitation that had formed in the austenite before the restoration process and the final martensite matrix. The localised SIP of Nb(CN) generally suppress the static recrystallisation of the deformed austenite. In theory, the austenite grain orientations after strain-induced precipitation would not be a commonplace occurrence.

The bright and dark-field images in Figure 5.31–Figure 5.32 showed that precipitates were often located on the dislocation and austenite subgrain boundaries. The SADP analysis in Figure 5.31(d) revealed the orientation relationship between the precipitate and matrix. The close-packed directions from both the precipitate and matrix were found to be parallel, $[110]_{\text{NbC}} \parallel [111]_{\alpha}$. The observed precipitate exhibits the K-S orientation relationship with matrix which signifies that they were formed in hot-worked austenite as a function of applied strain.

Table 6.2 Orientation relationship between Nb(CN) and matrix (adapted from ref [187])

Ferrite-NbC Variant	Plane BCC//FCC	Direction BCC//FCC
1a 1b	(011)bcc//(111)fcc	[111]bcc//[110]fcc [111]bcc//[110]fcc
2a 2b	(101)bcc//(111)fcc	[111]bcc//[110]fcc [111]bcc//[110]fcc
3a 3b	(110)bcc//(111)fcc	[111]bcc//[110]fcc [111]bcc//[110]fcc
4a 4b	(110)bcc//(111)fcc	[111]bcc//[110]fcc [111]bcc//[110]fcc
5a 5b	(101)bcc//(111)fcc	[111]bcc//[110]fcc [111]bcc//[110]fcc
6a 6b	(011)bcc//(111)fcc	[111]bcc//[110]fcc [111]bcc//[110]fcc

Figure 5.33 was imaged along a $[110]_{MC}$ zone axis with the measured d spacing about 0.251 nm, which is close to published values for the $d_{(111)}$ spacing of NbC of 0.258 nm. The orientation relationship had been identified by the fast Fourier transformed (FFT) diffractogram as shown in Figure 5.33(d). The $[111]$ direction of ferrite matrix is parallel with the $[110]$ zone axis of carbides, i.e. $[110]_{NbC} // [111]_f$. The observed orientation relationship between the precipitates and the matrix matches well with the calculated K-S OR presented in Table 6.2.

The lattice parameter of SIP was measured from the recorded electron diffraction patterns. The measured lattice parameter showed a wide scattering of values between 4.42-4.46 Å showing NaCl type crystal structure. However, most of these values fall in between lattice parameters of pure NbC and NbN compound. Furthermore, the multiple EDX spectrum analysis on second phase particles demonstrated the particles contain Nb L line, as the main element along with C and N.

The EELS quantitative analysis would have confirmed the presence of a lighter element, C and N, with better accuracy. Unfortunately, the EELS analysis could not be performed due to equipment downtime. The structure and EDX results suggest that the observed nanometer-sized particles are strain induced Nb(CN) precipitation formed after hot deformation of austenite.

The composition of Nb(CN) precipitates vary depending upon the steel composition and thermal condition of formation, i.e., deformation, continuous cooling or isothermal [117,122,126,129,134]. DeArdo had reviewed the work of Meyer *et al.* on composition Nb(CN) precipitates at different temperatures. Meyer suggested that the Nb(CN) precipitates contain more carbon if they are formed at high temperatures for the steel with a larger C/N ratio. In the present investigation, the C/N ratio of 25 is expected to give higher carbon content in strain-induced precipitates ($NbC_{0.80}N_{0.20}$) compared to typical HSLA steels. Again, this prediction could not be experimentally verified in the present investigation due to a lack of EELS analysis.

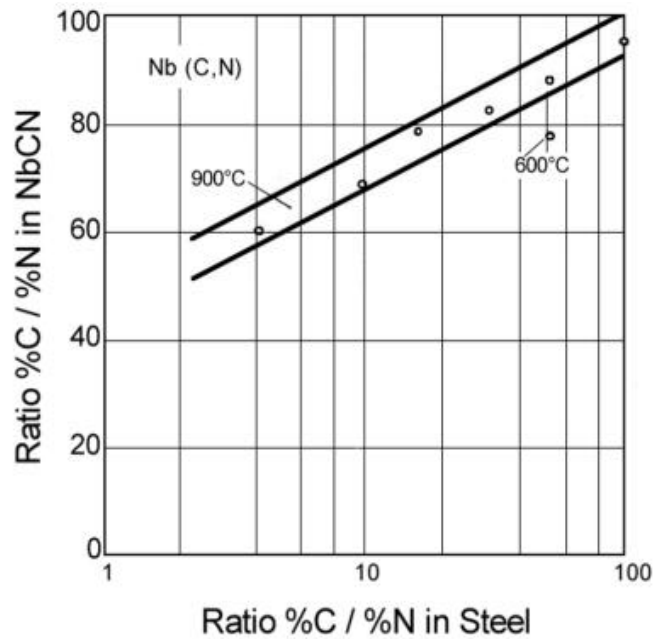


Figure 6.9 Influence of ratio of %C/%N on Nb(CN) precipitate composition in microalloyed steel (adapted from ref [8])

6.3.2 Precipitate Location

Both thin foil and extraction replica TEM micrographs show localised non-random precipitation, either in a cell-like manner or in more linear arrays (e.g., Figures 5.37 and 5.36). These localised areas include prior austenite grain boundaries, deformation bands, subgrain boundaries [40,154] or upon the dense dislocation walls of microbands [107], depending on the substructure present. The heterogeneous Nb(CN) precipitation at non-equilibrium defects was not surprising considering classical nucleation theory. Less energy is required for the nucleation of second phase particles at microstructure heterogeneities compared to homogenous nucleation at grain interior or matrix. Also, there may be segregation of Nb solute atoms towards these microstructure inhomogeneities before Nb(CN) formation [107].

A localized distribution of Nb(CN) particles seems to be the typical nature of Nb(CN) precipitation in deformed austenite. This behaviour has been reported in numerous investigations on low carbon Nb microalloyed steels over the last five decades [40-41,154]. Davenport *et al.* [133] found fine-scale precipitates heterogeneously distributed in a cell-like manner, suggesting precipitation on subgrain boundaries in Fe-0.03C-0.10Nb microalloyed steels after hot deformation at 900-1000°C.

Hansen and coworkers [40, 41] reported two stages for the strain-induced precipitation of Nb(CN) in deformed austenite. In the first stage, precipitation forms on grain boundaries and deformation band, while in the second stage, intense precipitation takes place in unrecrystallised austenite. The present investigation is in agreement with the above reported data. The localized precipitation of

Nb(CN) was frequently observed within the prior austenite grains delineating what may have been subgrains for steel B1-B3.

It was postulated that the relatively large initial austenite grain size creates a shortage of grain boundary areas hence promotes the formation of Nb(CN) on austenite subgrain boundaries [133,186]. This hypothesis had been incorrect, and an explanation for this has been provided elsewhere [42]. Dutta *et al.* [107] proposed that most probable precipitation nucleation sites were dislocation nodes within subgrain boundaries but could not provide direct evidence in conventional C-Mn microalloyed steel. It is challenging to resolve fine-scale precipitation on dislocation structures because the dislocation also provides contrast in dark-field TEM imaging which may be confused with particles.

Fritzmeier *et al.* [186] have studied the hot worked subgrain size in type 304 stainless steel. Their result showed that the subgrain size increases with a decrease in Z values (i.e., higher temperature and lower strain rate deformation). They reported the subgrain size of around 1-2 μm in diameter for deformation at 1000°C. The subgrain size in the present investigation is found to be 0.20-0.40 μm however, a direct comparison is not valid due to differences in materials. Sun *et al.* [145] investigated the influence of initial grain size, strain, and Z-value the subgrain diameter (d_{SUB}) and proposed an empirical relationship between them. The empirical equation gives a $d_{\text{SUB}} \sim 0.50 \mu\text{m}$ for steel B1-B3 under isothermal deformation test conditions.

There has been considerable interest in understanding the hot deformed austenite microstructure, particularly shear and microbands, in line with Al and Mg alloy. A “microband” is an elongated subgrain structure comprising cell blocks surrounded by dense dislocation walls (DDWs). Rainforth *et al.* [188] investigated precipitation of NbC in a model austenitic alloy (Fe-30Ni-0.1C-0.1Nb) through electron spectroscopy imaging (ESI). The result showed that precipitation occurs entirely on dislocations, present principally as a microband wall but also as an original subgrain structure. There was no evidence of precipitation within microbands core, which remains supersaturated with Nb leading to strain-induced precipitation of Nb(CN) during the next deformation and interpass time.

6.3.3 Size and Distribution of Nb(CN)

Figure 5.34-39 shows the measured mean size and distribution of Nb(CN) precipitate of steel B1-B3 using the carbon extraction replica technique. All the steels were deformed in a single hit for a true strain, $\varepsilon = 0.40$, isothermally held for 20 secs, and immediately water quenched.

Table 5.11 – 5.13 shows the quantitative description of Nb(CN) precipitation in steel B1-B3. The mean particle sizes range from 15-30 nm after a holding time of 20 secs in the present investigation.

The lognormal particle size distribution was observed for all the deformation test conditions. The measured particle size and distribution were typical of strain-induced precipitation in microalloyed steels. The particle size decreases as deformation temperature decreases (high Z). This dependence arises because of the direct influence of the Zener Hollomon parameter on the density of nucleation sites.

The present results are in agreement with the work of Yamamoto *et al.* [139] and Luton *et al.* [189] on low carbon Nb microalloyed steels. Yamamoto *et al.* [139] observed a bimodal particle size distribution of Nb(CN) precipitation in austenite. Large particles of a mean size 25 nm were found on austenite grain boundaries, while fine particles of a mean size 10 nm observed along the subgrain boundaries. Luton *et al.* [189] reported an average particle size of 25.9 nm after deforming to a true strain, $\varepsilon=0.25$ at 0.1/sec followed by an isothermal hold of 20 sec.

However, a markedly fine particle size in a range of 3–10 nm was reported in most of the earlier investigations on low carbon steels [40, 74, 133]. Davenport *et al.* [133] reported the mean particle size of 5-10 nm following a hot reduction of 40% at 900-1000°C. Lebon *et al.* [74] and Hansen *et al.* [40] have also reported the precipitate mean size in the range of 3-5 nm after the hot deformation of austenite. APFIM studies [190-191] have reported the NbC as fine as 1 nm in C-Mn microalloyed steels deformed in the range of 780-890°C.

In the present work, no precipitates were observed with a diameter less than 2 nm due to the resolution limit of conventional TEM. The smallest precipitate diameter detected in the TEM micrograph was 3.5 nm at 850°C for steel B2-B3. It is challenging to distinguish contrast in TEM micrographs from small precipitate sizes (< 5 nm). If finer precipitates would have been detected efficiently, the mean size of precipitates will undoubtedly have decreased from the current value.

The earlier work has shown that the presence of dislocations causes a significant acceleration in heterogeneous nucleation and growth of strain-induced precipitates [86, 146]. As the precipitates have very short nucleation and growth regime, the particles enter into growth and coarsening regime as soon as nucleation ceases. The coarsening of precipitates is influenced by accelerated pipe diffusion along with the dislocation core (not the bulk diffusion).

Dutta *et al.* [107] proposed a model to predict the complete precipitation kinetics for Nb microalloyed steels using classical nucleation theory and incorporating the influence of dislocations. The model predictions were in good agreement with the experimental observations for the size evaluation of the precipitate. The model used r^3 law for coarsening using a combined/effective diffusion coefficient instead of the bulk diffusion coefficient.

However, it is known that pipe diffusion is faster than capillary (bulk) diffusion, and consequently, it can be assumed that pipe diffusion should produce precipitates of larger radius than that produced by bulk diffusion. Nagarajan *et al.* [192] extended the work of Dutta *et al.* and put together the multipass model for strain-induced precipitates. The model determined the precipitate coarsening kinetics considering both the grain boundary diffusion (r^4 law) or the pipe diffusion (r^5 law).

Figure 6.10 illustrates the evaluation of precipitation radius after single pass deformation ($\epsilon=0.80$) as a function of time with pipe diffusion (r^5 law). The precipitates significantly coarsened in from 1 nm to 10 nm radius an isothermal hold of 15 sec at 1050°C. The predicted precipitate diameter of 20 nm agrees well with the result of the present investigation.

Whatever the coarsening theory applied, the mean radius of precipitates at any given time, t , will depend upon the initial supersaturation of the diffusing species (Nb in the present case) and concentration of solute in the precipitate (C and N). The role of later has not been researched well, particularly for higher carbon content observed in long products (C : 0.20-0.80%). The questions remain whether the final size of Nb(CN) precipitates will decrease or increase with increasing carbon level of steel for a given isothermal time and temperature after deformation. Thus, these two effects would narrow down the gap between the expected and the measured values for precipitate diameter.

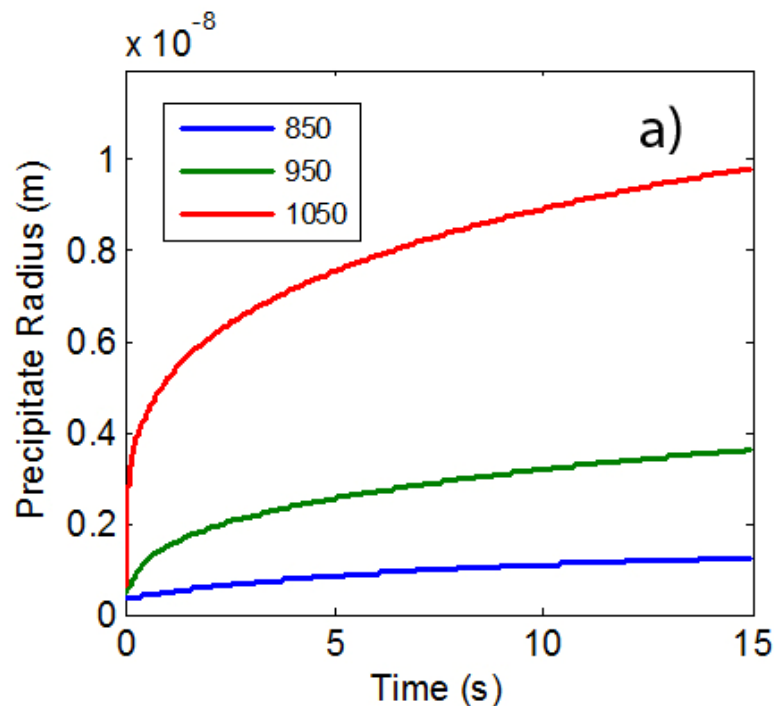


Figure 6.10 Time evolution of precipitate radius as a function of temperature for a microalloyed steel, Fe-0.084C-0.06Nb-0.015N (adapted from ref [192])

6.3.4 Precipitate Volume Fraction

Table 5.9 - 5.11 presents the local precipitate volume fraction (f_v) data for steel B1-B3 as a function of deformation temperature. The measured f_v varies from 8.7×10^{-4} to 5.8×10^{-3} which appears to be on the higher side when compared with values reported in the literature and expected equilibrium volume fraction based on thermodynamics. The higher f_v values are presumably an artefact of the carbon replication technique. The chemical extraction can pull out more than just the surface particles, giving the overestimated volume fraction readings [177, 188]. Although the f_v values obtained agree with earlier research [40, 86, 154], they cannot be accepted wholly for rationalising macroscopic findings.

The measured f_v increases with decreasing deformation temperature for steel B1-B3. This is practically possible considering a high nucleation rate and Nb supersaturation associated with lower deformation temperature. Both of these conditions in effect accelerate the kinetics of strain-induced precipitation, particularly below the nose of the PTT curve. A volume fraction in the range of $2-3 \times 10^{-3}$ is observed for steel B3 at lower deformation temperature which is significantly higher.

The equilibrium volume fraction of the precipitates was calculated, assuming a stoichiometric NbC composition and assuming uniform dispersion of particles [10, 193]. Valdes *et al.* [193] suggested that for each wt. % of Nb precipitates only 0.13 wt. % of carbon is taken from the austenite solid solution. The excess C/N ratio in the steel compositions allows the determination of the equilibrium volume fraction based on the thermodynamic principle with the following equation:

$$V_V = \frac{M_{Fe}(V_m)_{Nb(CN)}}{100M_{Nb}(V_m)_{Fe}} [\%Nb] (1 - 1/k_s) \quad (6.2)$$

where M_{Fe} and M_{Nb} are the molar masses of iron and niobium, $(V_m)_{Nb(CN)}$, and $(V_m)_{Fe}$ are the molar volumes of Nb(CN) and austenite. The equilibrium volume fractions were calculated with input values of 56 and 93, and 1.28×10^{-5} and $7.3 \times 10^{-6} \text{ m}^3 \text{ mol}^{-1}$, respectively.

Figure 6.11 shows the comparison between an experimentally measured volume fraction (Exp) and equilibrium volume fraction (Eqm) values for steel B1-B3 as a function of deformation temperature. The experimentally measured f_v values are around ten times higher than equilibrium f_v at any given temperature. Steel B1 with just 66 ppm Nb addition had measured f_v two-three times higher than equilibrium f_v .

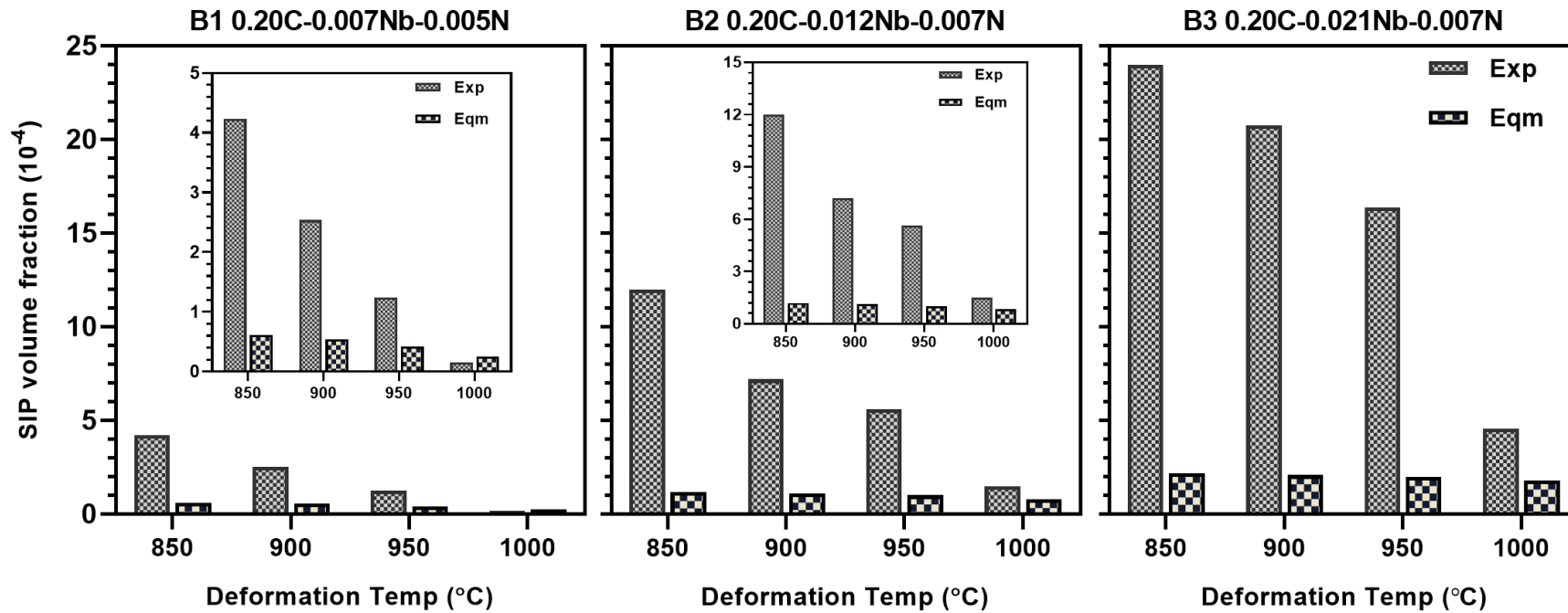


Figure 6.11 Experimental (Exp) measured versus Equilibrium (Eqm) volume fraction at different deformation temperature in Steel B1-B3. All the steels were deformed in a single hit for a true strain, $\epsilon = 0.40$, isothermally held for 20 secs, and immediately water quenched.

6.3.5 Nb(CN) Pinning Forces

The selection of similar deformation temperatures and hold time enabled comparison of precipitation kinetics in steel B1-B3 as a function total Nb content and related supersaturation in austenite. It is clear from quantitative measurement that higher Nb supersaturation resulted in a higher volume fraction of Nb(CN) precipitate at constant temperature and time condition. At any given temperature, the local F_{PIN} increases with increasing Nb concentration from steel B1 to B3. The measured Nb(CN) volume fraction in steel B3 is 2-3 times higher than steel B1 and B2, which is reflected in higher values of local F_{PIN} .

RBM and FBM pinning forces models assume a uniform distribution of particles throughout the matrix and subgrain boundaries based on the thermodynamic system. It means that the volume fraction of precipitates at the austenite subgrain boundary will be identical to the volume fraction within the grains or bulk matrix. However, electron microscopic investigations [40-42,117,154,160] have revealed that the distribution of Nb(CN) precipitates appears to be localised, preferentially on prior-austenite grain boundaries, subgrain boundaries, and deformation bands.

The calculated local F_{PIN} based on RBM and FBM is too low compared to measured F_{RXN} for steel B1-B3 (Table 5.9-5.11). Hence, the present results render the assumption of uniform precipitate distribution invalid and associated pinning force models.

Besides this, some of the previous investigations [11,18, 108] calculated the precipitate pinning force, F_{PIN} based on the equilibrium volume fraction. In order to make a comparison, the equilibrium F_{PIN} was calculated for the present investigation based on the SBM model using the equilibrium volume fraction and average particle radius measured for steel B1-B3, respectively. Table 6.3 presents the experimentally measured and equilibrium F_{PIN} at different deformation temperature for steel B1-B3.

Table 6.3 Experimentally measured vs. Equilibrium F_{PIN} at austenite subgrain boundary, calculated by SBM of Hansen et al. [40]

Def. Temp. (°C)	Exp. Measured Local F_{PIN} (MPa)			Equilibrium F_{PIN} (MPa)		
	B1	B2	B3	B1	B2	B3
850	2.18	2.91	6.97	0.31	0.29	0.63
900	0.74	2.24	4.54	0.16	0.35	0.46
950	0.27	0.65	1.83	0.09	0.12	0.22
1000	0.04	0.20	0.74	0.07	0.11	0.29

Figure 6.12 shows the comparison between experimentally determined local F_{PIN} and equilibrium F_{PIN} for steel B1-B3, respectively. The static recrystallisation was inhibited whenever local F_{PIN} at $T_{5\%}$ was greater than 1.6 MPa. The experimental local F_{PIN} was higher than the equilibrium F_{PIN} in the present investigation for all the steel composition at any given temperature. The calculated equilibrium pinning forces were far too low (0.10-0.60 MPa) to retard static recrystallisation of austenite at any deformation temperature. The equilibrium F_{PIN} also shows an increasing trend for steel B1-B3 as a function of Nb, but the difference is insignificant.

The equilibrium volume fraction estimation based on thermodynamic systems and the assumption of uniform precipitation leads to a lower value of equilibrium F_{PIN} . As we know, the strain-induced precipitation is a time-temperature dependent phenomenon that makes uniform precipitation assumption invalid. The typical interpass times are short during practical operations, which means precipitate volume fraction never reaches the equilibrium value due to discontinuity in kinetics. Hence, the F_{PIN} based on the equilibrium volume fraction will always overestimate the magnitude for a given interpass time.

The local pinning forces, F_{PIN} were estimated from the local precipitate size and distribution in the planar TEM image using the carbon extraction replica technique. The extraction replica technique contains some inherent drawbacks. Some of the particles may be stripped off from the replica, and some may be dissolved in the etching solution during the preparation of replicas. The replica technique is considered reliable for removing the particles with a diameter > 3 nm [188]. Some research groups use the extraction efficiency factor to account for the loss of smaller particles.

Also, some of the particles may be too small to observe during TEM analysis. The lower limit of detectable particle size in conventional TEM is considered to be 2 nm [40,188-189]. The small particles less than 2 nm known as clustering or pre-precipitation [190] are considered to be distributed on a very fine scale; hence pinning effect of these particles would be substantial. Brenner *et al.* [191] have reported the fine distribution of Nb(CN) particles as small as 0.4 nm in diameter using the atom probe technique. The pinning forces increase significantly as precipitate size decreases; hence the contribution of missing particles should be accounted for extraction efficiency factor.

Considering the inherent drawbacks of the extraction replica technique, the high-resolution synchrotron X-ray experiments should have been carried out to accurately measure the Nb(CN) volume fraction after hot deformation studies. Even synchrotron studies have limitations and precipitations of different phases overlap strongly which makes identification of Nb(CN) more challenging

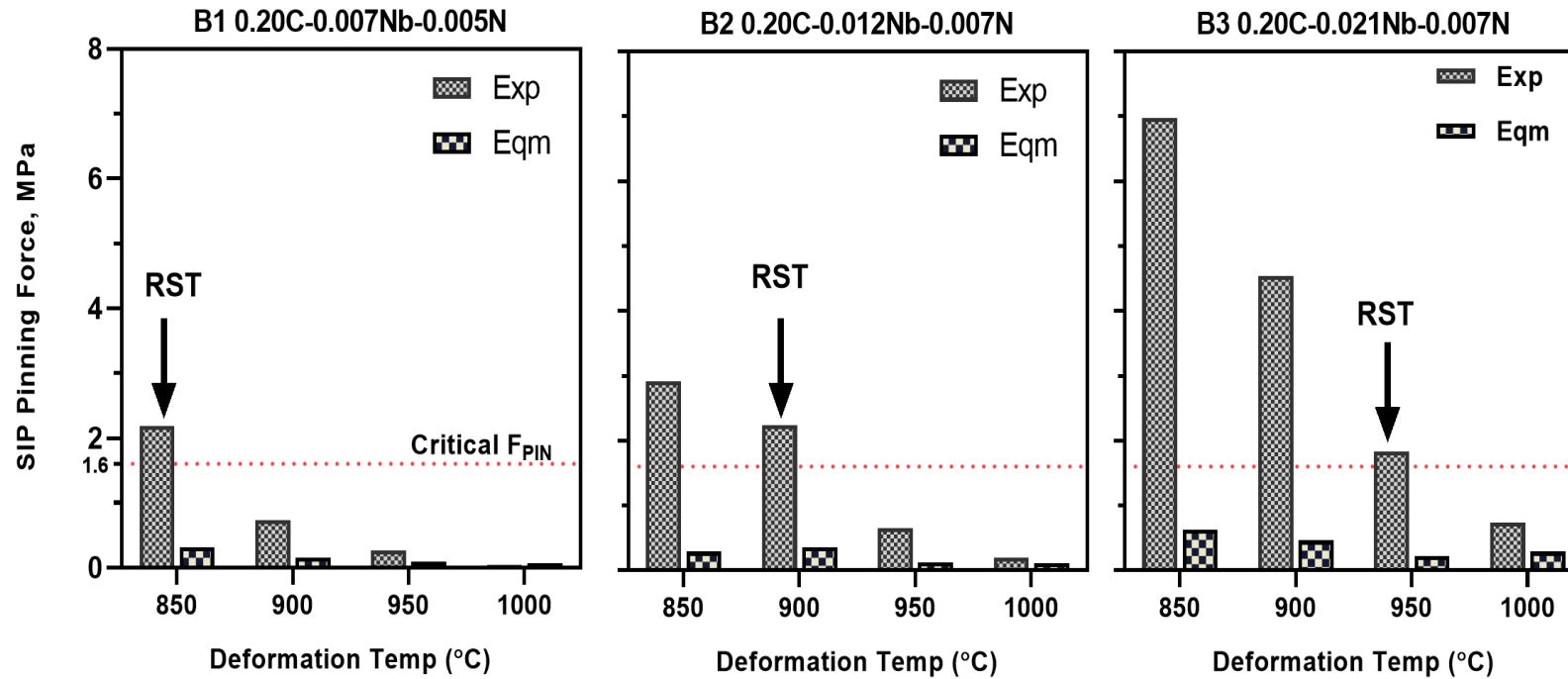


Figure 6.12 Comparison between experimental measured (Exp) and equilibrium (Eqm) pinning forces at different deformation temperature for steel B1-B3. The precipitate pinning forces were calculated based on the subgrain boundary model, as proposed by Hansen *et al.* [40]. All the steels were deformed in a single hit for a true strain, $\epsilon = 0.40$, isothermally held for 20 secs, and immediately water quenched.

6.3.6 Relationship between F_{PIN} and F_{RXN}

The recrystallisation is retarded only when the precipitate pinning forces (F_{PIN}) become higher than recrystallisation driving force (F_{RXN}). If the precipitation occurs before the onset of recrystallisation, significant retardation in the recrystallisation kinetics is achieved. Figure 6.13 shows the interactions of both precipitate-pinning forces, F_{PIN} and driving force for recrystallization growth, F_{RXN} as a function of deformation temperature for an isothermal hold of the 20 sec after a true strain of $\varepsilon=0.40$.

The measured pinning forces for steel B2 and B3 showed a good agreement with fraction softening and quantitative metallography studies. At temperature below the respective $T_{5\%}$, the F_{PIN} appears to be of comparable magnitude or higher to the F_{RXN} for deformation. The close agreement validates that observed local precipitation and corresponding size and volume fraction are in the right range to retard static recrystallisation. Additionally, the accurate estimation of F_{RXN} and F_{PIN} rationalizes the interaction between the recrystallisation and precipitation process.

The steel B2 showed a fully unrecrystallised microstructure at corresponding $T_{5\%}$ of 900°C. The F_{PIN} was slightly higher than F_{RXN} for deformation at temperature $< T_{5\%}$ due to small Nb supersaturation available in steel B2. If the $T_{5\%}$ is defined as the intersection of F_{PIN} and F_{RXN} curves, then it gives a value of 920°C. The predicted value is very close to one measured from fraction softening curves, $T_{5\%} = 900^\circ\text{C}$. The pinning force corresponding to an estimated $T_{5\%}$ is 1.8 MPa, which must be exceeded for complete retardation of static recrystallisation. The local F_{PIN} is 2.2 MPa at 900°C which is almost equal to the F_{RXN} of 2.1 MPa. As discussed earlier, the local F_{PIN} would always be higher than the current value considering the volume fraction of missing fine precipitates (2 nm).

Similarly, the steel B3 showed a fully unrecrystallised microstructure for a $T_{def} \leq 950^\circ\text{C}$. The TEM analysis has revealed a localised Nb(CN) precipitation at austenite subgrain boundaries and deformation bands. The measured local F_{PIN} was significantly higher than F_{RXN} for a $T_{def} \leq 950^\circ\text{C}$. Again, the estimated $T_{5\%} = 960^\circ\text{C}$ from the pinning force curve very well agrees with the one measured from fractional softening curves, $T_{5\%} = 943^\circ\text{C}$. At an estimated $T_{5\%}$, the pinning force is 1.6 MPa which very well matches with the corresponding measured value for steel B2.

The favorable agreement was not obtained in steel B1 as the measured F_{PIN} were lower than F_{RXN} at all temperatures. The steel B1 showed a fully unrecrystallised microstructure only at a corresponding $T_{5\%}$ of 855°C. The TEM analysis have shown the presence of strain-induced precipitation in deformed austenite at 850°C. However, the observed volume fraction of precipitates was very low which resulted in lower values of local F_{PIN} , equal to 2.18 MP.

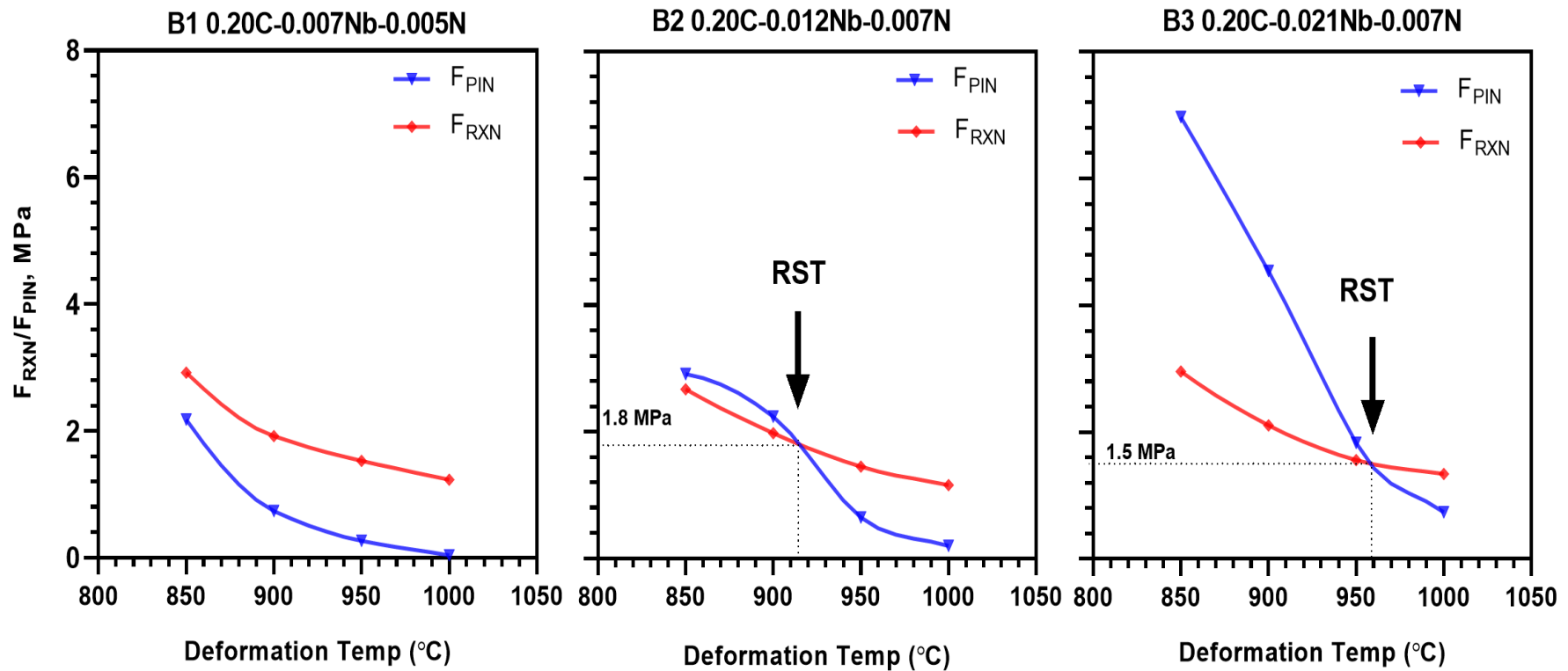


Figure 6.13 Interaction between F_{PIN} and F_{RXN} versus deformation temperature for steel B1-B3. Data to the left of the intersection point will result in complete suppression of austenite recrystallisation. Data to the right of intersection point will result in partially or fully recrystallised austenite microstructure. All the steels were deformed in a single hit for a true strain, $\epsilon = 0.40$, isothermally held for 20 secs, and immediately water quenched.

At the other extreme, the measured F_{PIN} for steel B1-B3 is less than the F_{RXN} for deformation at 1000°C. This is attributed to the small Nb supersaturation available at 1000°C for all the steel. The steel B1 essentially had a zero F_{PIN} , which was in agreement with solubility predictions using the Irvine *et al.* equation. The steel B2 had a very small Nb supersaturation at 1000°C considering the temperature was very close to precipitate dissolution temperature. The steel B3 had a considerable Nb supersaturation at 1000°C which resulted in a local F_{PIN} of 0.70 MPa. As seen in Figure 6.13, this F_{PIN} was still insufficient to pin the austenite grain boundaries and retard recrystallisation completely.

As mentioned previously, the steel B1-B3 exhibited a different Nb supersaturation in austenite at their respective $T_{5\%}$. This has been summarized in Table 6.4, along with calculated values for F_{PIN} at $T_{5\%}$. The table indicates that steel B3 had an Nb supersaturation in austenite which was 83% larger than steel B2. The difference in Nb supersaturation subsequently resulted in different precipitate volume fraction as shown in Figure 6.11.

Steel B3 exceeded a critical pinning force of 1.6 MPa at $T_{5\%}$ because of this both coupled phenomena. However, at their respective $T_{5\%}$, steel B2 and B1 showed a similar value of F_{PIN} in a range of 1.8-2.5 MPa. Additionally, steel B1-B3 exhibited a critical Nb supersaturation ratio ≥ 6 resulted at their respective $T_{5\%}$ for $\varepsilon=0.40$.

Table 6.4 Comparison of parameters, as measured for this investigation at $\varepsilon=0.40$ for steel B1-B3.

Parameter	B1	B2	B3
$T_{5\%}, ^\circ\text{C}$	855	900	943
Aspect ratio	14.01	11.30	10.96
F_{PIN} (MPa)	2.18	2.24	1.83
F_{RXN} (MPa)	2.95	1.98	1.56
Bulk Nb Concentration, wt %	0.0066	0.0121	0.0214
Nb soluble at 1250°C, wt %	0.0066	0.0121	0.0214
Nb soluble at $T_{5\%}$, wt %	0.0011	0.0019	0.0029
Nb supersaturation at $T_{5\%}$, wt %	0.0055	0.0101	0.0185
Nb supersaturation ratio	6.08	6.27	7.29

6.4 Microstructure Modelling

The microstructure modelling based on physical metallurgy principles is well developed and widely being used for off-line optimization of processing conditions. It allows rapid determination of controlled rolling regime, which can be easily implemented in an industrial practice over intense laboratory simulation.

6.4.1 Model for predicting microstructure

The recrystallisation and precipitation are competing for processes during high-temperature deformation, and the rate of each process depends upon which process is occurring preferentially. The time for 5% recrystallisation ($t_{0.05X}$) and precipitation ($t_{0.05P}$) were calculated using the Sellars empirical relationships [70,86], given in equation (2.13) and (2.30) respectively.

If $t_{0.05P}$ is less than $t_{0.05X}$ then the Nb(CN) precipitates will retard the recrystallisation provided there is enough volume fraction available. Additionally, the recrystallisation will also be suppressed if $t_{0.05X}$ is higher than interpass time (t_d), which is generally observed for low-temperature deformations. Hence, the unrecrystallised austenite microstructure will be obtained after deformation if either of these conditions or both are fulfilled. Table 6.5-6.8 shows the results predicted by these conditions for steel B1-B3, respectively and draws a comparison with present experimental observation.

An excellent agreement is obtained at all deformation temperatures for higher strain levels ($\epsilon \geq 0.20$), except at 950°C, $\epsilon = 0.20$ in steel B2. In the case of later, the model predicts initiation of the static recrystallisation after 39 secs for a true strain, $\epsilon = 0.20$, which is higher than actual interpass times in the present investigation. The optical microstructure observation showed partially and fully recrystallised austenite grains (see Figure 5.26) for interpass time of 5 and 20 secs, respectively. The fractional softening studies also revealed 80% overall softening which validates the presence of static recrystallisation.

These results show that the factual recrystallisation kinetics in steel B2 were faster than one predicted by equation (2.13). The equation predicted recrystallisation delay of 19 secs as a function of solute Nb in steel B2 (calculated in reference to steel B1), which is a gross overestimation in a practical sense. The preceding discussion indicates that there is a need to review the validity of equation (2.13)/ $t_{0.05X}$ for all Nb concentrations. However, this issue is beyond the scope of the present investigation.

In contrast to good agreement discussed previously, there is a distinct discrepancy between experimental results and model prediction for lower strains $\epsilon = 0.10$. The proposed model predicts

absence of the static recrystallisation at a deformation temperature of 1000°C and 1050°C based on slower recrystallisation kinetics. The model estimated $t_{0.05X}$ at $\varepsilon=0.10$ is twenty times higher than the actual delay time of 20 secs for steel B1-B3. However, the fractional softening and microstructure results revealed fully recrystallised austenite for both the deformation temperatures.

It implies that the equation (2.13) has overestimated the values $t_{0.05X}$ for lower strain, $\varepsilon=0.10$, and the actual time for onset of static recrystallisation could be less than the 20 secs. The reason behind this discrepancy could be the strain-dependent exponent ($t_{0.05X} \propto \varepsilon^p$, $p=4$) or grain size exponent ($t_{0.05X} \propto d^2$, $m=2$) used in equation (2.13). The equation (2.13) for $t_{0.05X}$ was initially developed based on higher rolling reduction levels associated with the industrial practice for low carbon microalloyed steels.

Recently, Sanz *et al.* [194] investigated the static recrystallisation behavior of low carbon Nb-Ti microalloyed steel through torsion studies at low strain levels, $\varepsilon=0.10$. They reported that a value of strain exponent (p) close to 4 from a slope of $\log t_{0.05X}$ versus $\log \varepsilon$. The Sellars equation has incorporated the same exponent value for Nb microalloyed steels. However, there is considerable spread in reported values of p in literature for low carbon steels with and without microalloying additions.

The initial grain size plays a significant role in the nucleation and growth of recrystallised austenite grains. However, the equation (2.13) may be overestimating the effect of initial grain size ($t_{0.05X} \propto d^2$, $m=2$) on recrystallisation kinetics at lower strain levels. The driving force for this effect could be minimal. The presiding discussion indicates that there is a need to review the influence of initial grain size on $t_{0.05X}$ at low strain levels ($\varepsilon \leq 0.10$). However, this issue is beyond the scope of the present investigation.

The results indicate that $t_{0.05P}$ occurs after a delay time of 32 secs at 850°C, following a $\varepsilon = 0.40$ prestrain for steel B1. It can be recalled that the delay time was kept constant at 20 secs for all the precipitate evaluation testing conditions in the present study. The localised precipitation of Nb(CN) was observed on austenite subgrain boundaries in TEM analysis. Microstructural evidence also revealed that the austenite was unrecrystallised after a delay time of 20 secs at 850°C, following a 0.40 strain. Additionally, the steel B1 exhibited a 20% fractional softening at 850° for deformation $\varepsilon = 0.40$. This suggests that there is also a necessity to review the validity of equation (2.30)/ $t_{0.05P}$ for dilute Nb concentrations.

Table 6.5 Calculated values of t_{rxn} and t_{pin} along with predictions and experimental observation of resulting microstructure for steel B1

Model Input			Model Output		PREDICTION			EXP Observations (Has SReX started?)		
Temp.	Strain	t_d	$t_{rxn} / t_{0.05X}$	$t_{pin} / t_{0.05P}$	$t_d < t_{rxn}$	$t_{pin} < t_{rxn}$	SReX Prediction	Fractional Softening	Micro-structure	Comment
850	0.10	20	4775	129.78	yes	no	no	no	no	
	0.20	20	298	64.89	yes	no	no	no	no	
	0.30	20	59	43.26	yes	no	no	no	no	
	0.40	20	21	32.45	yes	no	no	no	no	
900	0.10	20	1133	1825.56	yes	no	no	no	no	
	0.20	20	71	912.78	yes	no	no	no	no	
	0.30	20	14	608.52	no	no	yes	yes	yes	
	0.40	20	4.43	456.39	no	no	yes	yes	yes	
950	0.10	20	302.37	6.86E+06	yes	no	no	no	no	
	0.20	20	18.90	3.43E+06	no	no	yes	yes	yes	
	0.30	20	3.73	2.29E+06	no	no	yes	yes	yes	
	0.40	20	1.18	1.71E+06	no	no	yes	yes	yes	
1000	0.10	20	89.53	5.32E+27	yes	no	no	yes	yes	Low Strain
	0.20	20	5.60	2.66E+27	no	no	yes	yes	yes	
	0.30	20	1.11	1.77E+27	no	no	yes	yes	yes	
	0.40	20	0.35	1.33E+27	no	no	yes	yes	yes	
1050	0.10	20	29.06	-	yes	no	no	yes	yes	Low Strain
	0.20	20	1.82	-	no	no	yes	yes	yes	
	0.30	20	0.36	-	no	no	yes	yes	yes	
	0.40	20	0.11	-	no	no	yes	yes	yes	

Table 6.6 Calculated values of t_{rxn} and t_{pin} along with predictions and experimental observation of resulting microstructure for steel B2

Model Input			Model Output		PREDICTION			EXP Observations (Has SReX started?)		
Temp.	Strain	t_d	$t_{rxn}/t_{0.05X}$	$t_{pin}/t_{0.05P}$	$t_d < t_{rxn}$	$t_{pin} < t_{rxn}$	SReX Prediction	Fractional Softening	Micro-structure	Comment
850	0.10	20	10845	13.37	yes	yes	no	no	no	
	0.20	20	678	6.69	yes	yes	no	no	no	
	0.30	20	134	4.46	yes	yes	no	no	no	
	0.40	20	42	3.34	yes	yes	no	no	no	
900	0.10	20	2430	28.81	yes	yes	no	no	no	
	0.20	20	152	14.40	yes	yes	no	no	no	
	0.30	20	30	9.60	yes	yes	no	no	no	
	0.40	20	9.49	7.20	no	yes	no	no	no	
950	0.10	20	615.15	185.42	yes	yes	no	no	no	
	0.20	20	38.45	92.71	yes	no	no	yes	yes	Grain Size
	0.30	20	7.59	61.81	no	no	yes	yes	yes	
	0.40	20	2.40	46.36	no	no	yes	yes	yes	
1000	0.10	20	173.50	29019.01	yes	no	no	yes	yes	Low Strain
	0.20	20	10.84	14509.51	no	no	yes	yes	yes	
	0.30	20	2.14	9673.00	no	no	yes	yes	yes	
	0.40	20	0.68	7254.75	no	no	yes	yes	yes	
1050	0.10	20	53.85	1.66E+13	yes	no	no	yes	yes	Low Strain
	0.20	20	3.37	8.30E+12	no	no	yes	yes	yes	
	0.30	20	0.66	5.53E+12	no	no	yes	yes	yes	
	0.40	20	0.21	4.15E+12	no	no	yes	yes	yes	

Table 6.7 Calculated values of t_{rxn} and t_{pin} along with predictions and experimental observation of resulting microstructure for steel B3

Model Input			Model Output		PREDICTION			EXP Observations (Has SReX started?)		
Temp.	Strain	t_d	t_{rxn}	t_{pin}	$t_d < t_{rxn}$	$t_{pin} < t_{rxn}$	SReX Prediction	Fractional Softening	Micro-structure	Comment
850	0.10	20	17167	3.46	yes	yes	no	no	no	
	0.20	20	1073	1.73	yes	yes	no	no	no	
	0.30	20	212	1.15	yes	yes	no	no	no	
	0.40	20	67	0.87	yes	yes	no	no	no	
900	0.10	20	3490	4.22	yes	yes	no	no	no	
	0.20	20	218	2.11	yes	yes	no	no	no	
	0.30	20	43	1.41	yes	yes	no	no	no	
	0.40	20	13.63	1.06	no	yes	no	no	no	
950	0.10	20	808.32	7.44	yes	yes	no	no	no	
	0.20	20	50.52	3.72	yes	yes	no	no	no	
	0.30	20	9.98	2.48	no	yes	no	no	no	
	0.40	20	3.16	1.86	no	yes	no	no	no	
1000	0.10	20	210.00	27.7	yes	yes	no	yes	yes	Low Strain
	0.20	20	13.13	13.9	no	no	yes	yes	yes	
	0.30	20	2.59	9.2	no	no	yes	yes	yes	
	0.40	20	0.82	6.9	no	no	yes	yes	yes	
1050	0.10	20	60.41	691	yes	yes	no	yes	yes	Low Strain
	0.20	20	3.78	346	no	no	yes	yes	yes	
	0.30	20	0.75	230	no	no	yes	yes	yes	
	0.40	20	0.24	173	no	no	yes	yes	yes	

6.4.2 RPTT Diagram

The interaction between recrystallisation and precipitation has traditionally been explained with the aid of the RPTT diagram [40, 42, 115] for a constant strain and strain rate condition. Both curves of time for the start of recrystallisation and precipitation are overlapped as a function of deformation temperature for a given steel composition.

Figure 6.14–6.16 shows the RPTT diagrams of steel B1-B3, respectively, as a function of the different deformation temperature and strain level used in the present investigation. The time for 50 and 95% recrystallisation were estimated from a value of $t_{0.05X}$ using the JMAK principle, equation (2.11) with appropriate values of the initial constant. With the identification of $T_{5\%}$ and $T_{95\%}$, the three-stage interaction behavior between static recrystallisation and precipitation is observed for all the steels at the constant interpass time of 5 and 20 sec. Similar behavior has been reported in earlier investigations into the low carbon Nb microalloyed steels [111], as shown in Figure 2.42.

In stage I regime ($T_{95\%} \leq T_{\text{def}} \leq T_{\text{sol}}$), the static recrystallisation ($t_{0.05X}$) is completed before the start of precipitation ($t_{0.05P}$) and is not expected to be influenced by the formation of Nb(CN) precipitates. This behaviour was demonstrated by steel B1-B3 deformed at 900°C, 950°C, and 1000°C, respectively. The full static recrystallised austenite was observed due to accelerated recrystallisation kinetics. It is proposed that the Nb solute atoms would delay the start of static recrystallisation by solute drag mechanism at this temperature [115-116,139]. However, the solute drag effect could not be verified for isothermal deformation in the selected temperature regime.

In the stage II regime ($T_{95\%} \leq T_{\text{def}} \leq T_{5\%}$), precipitation occurs after partial recrystallisation. Steel B2 exhibited this behaviour in the present investigation for a deformation temperature of 950°C, $\epsilon_{0.20-0.30}$. The overall precipitation process could be sluggish due to the formation of dislocation free new recrystallised austenite grains. As a result, the progress of recrystallisation was delayed due to Nb(CN) precipitation, and the recrystallisation finish curve was shifted to the right resulting in partially recrystallised microstructure during the hold of 5 and 20 secs. The partially recrystallised microstructure is not desirable from the view of grain uniformity and mechanical properties in the final product. Hence, the finishing passes for steel B2 should be completed below 930°C to avoid rolling in partial recrystallisation region.

In the stage III regime ($T_{\text{def}} \leq T_{5\%}$), the precipitation occurs prior to the onset of recrystallisation. Steel B1-B3 exhibited this behaviour at deformation temperature below the $T_{5\%}$ of each steel. The recrystallisation finishing curve is shifted to longer times due to precipitate pinning. In summary, the quantitative metallography and electron microscopy observation complements the findings from the RPTT diagram.

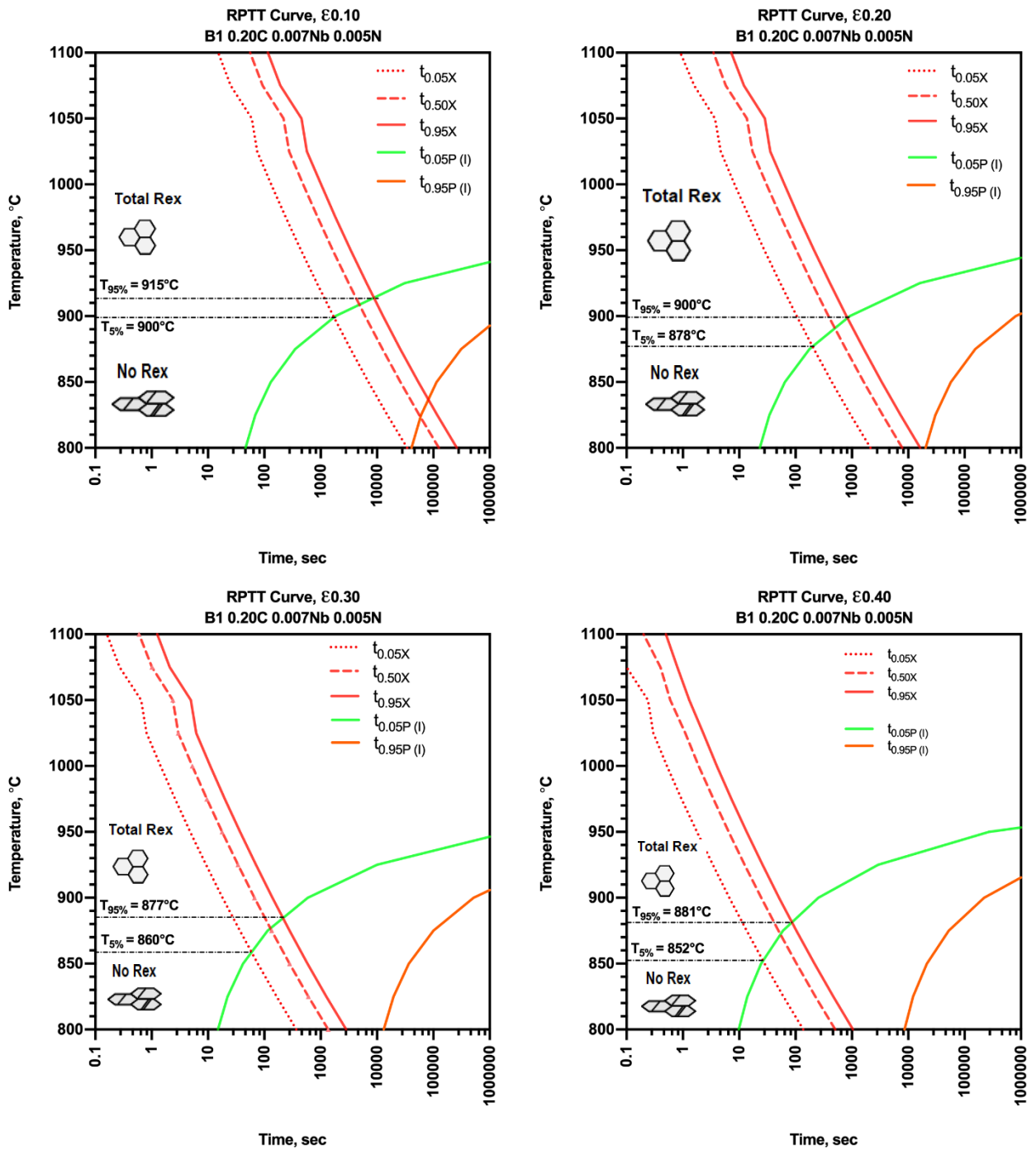


Figure 6.14 RPTT diagram showing the interaction between recrystallisation and precipitation for steel B1 at a true strain, $\epsilon = 0.10- 0.40$.

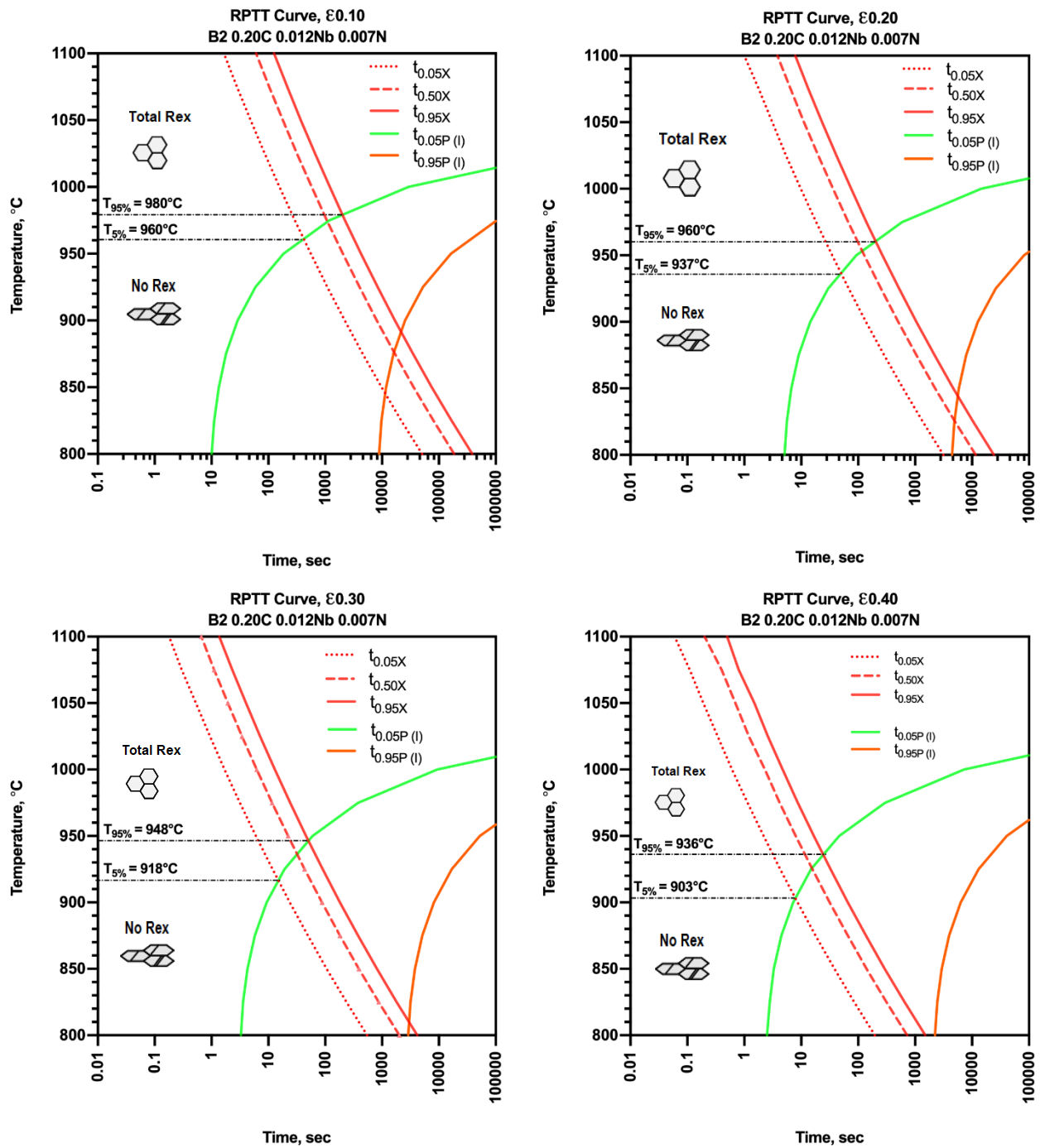


Figure 6.15 RPTT diagram showing the interaction between recrystallisation and precipitation for steel B2 at a true strain, $\epsilon = 0.10-0.40$.

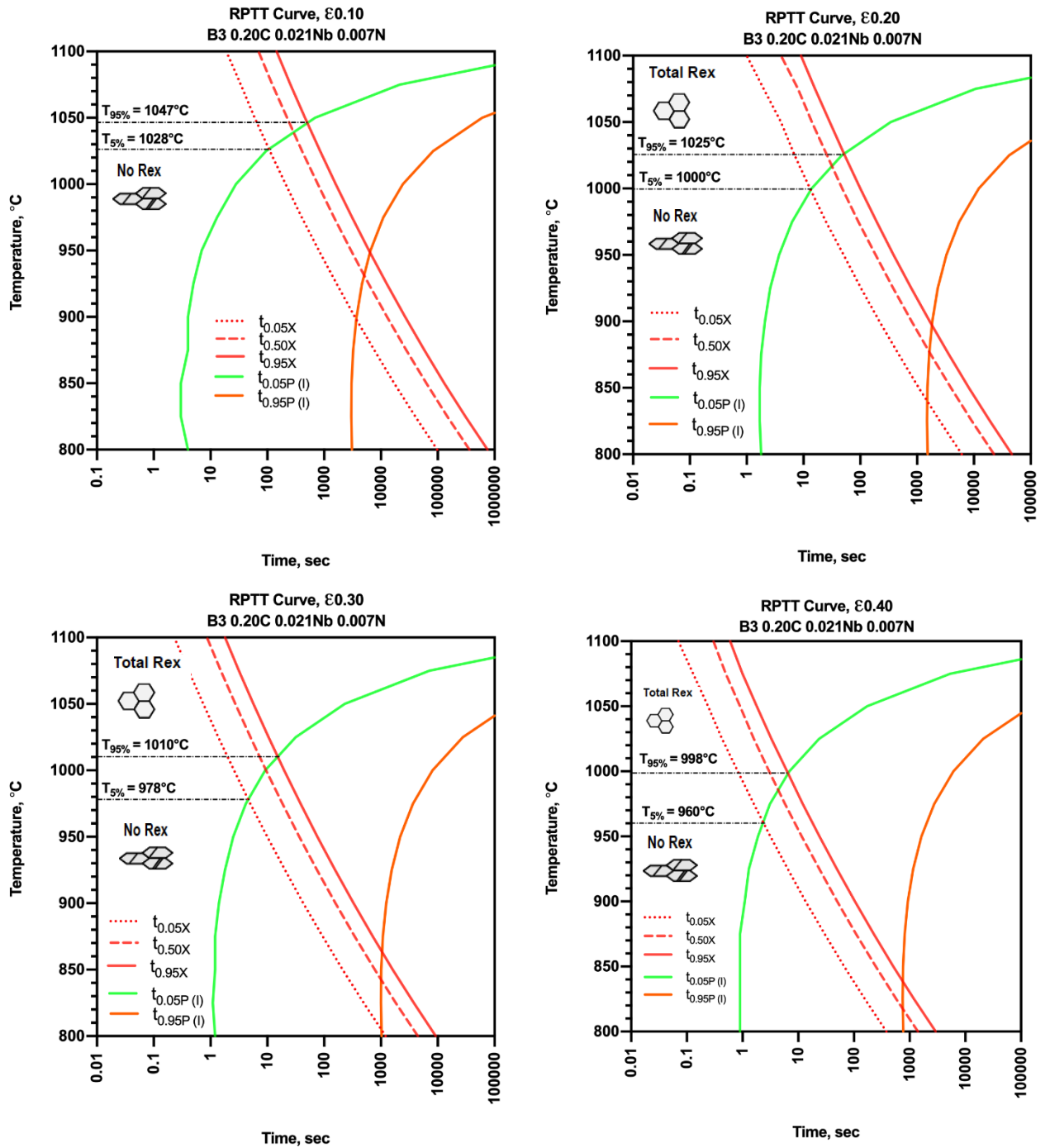


Figure 6.16 RPTT diagram showing the interaction between recrystallisation and precipitation for steel B3 at a true strain, $\epsilon = 0.10-0.40$.

The RST ($T_{5\%}$) is defined as the intersection of the precipitation starts curve ($t_{0.05P}$) and the recrystallisation start curve ($t_{0.05X}$). Similarly, the intersection of recrystallisation finish curves ($t_{0.95X}$) with precipitation starts curve ($t_{0.05P}$) is defined as RLTT ($T_{95\%}$). Table 6.8 lists the estimated value of $T_{5\%}$ and $T_{95\%}$ from the RPTT diagram for steel B1-B3 at strain $\epsilon=0.10-0.40$.

Table 6.8 $T_{5\%}$ and $T_{95\%}$ temperatures as a function of pass strain, determined from RPTT diagram

Applied Strain	B1 0.0066%Nb		B2 0.012%Nb		B3 0.021%Nb	
	$T_{5\%}$	$T_{95\%}$	$T_{5\%}$	$T_{95\%}$	$T_{5\%}$	$T_{95\%}$
$\epsilon 0.10$	922	970	980	1050	995	1050
$\epsilon 0.20$	904	959	950	994	970	996
$\epsilon 0.30$	893	929	900	961	960	985
$\epsilon 0.40$	873	908	890	944	953	980

Figure 6.17 depicts the RST determined RPTT diagram, based on equation (2.11) and (2.19) for steel B1-B3. As expected, the RST decreases with an increase in pass strain for steel B1-B3 for isothermal deformation conditions. The effect of strain or rolling reduction on the RST in the first finishing pass has been studied experimentally in the present investigation. The experimentally measured RST for constant interpass time of 5 and 20 secs has been superimposed in Figure 6.17.

For steel B1-B2, there is a close agreement for predicted RST and experimentally measured for interpass time of 20 secs at all strain levels. However, the experimental measured $T_{5\%}$ is higher than predicted RST for a shorter interpass time of 5 secs at a lower strain. The increase in $T_{5\%}$ at 5 secs is mainly due to delay in the onset start of recrystallisation even without the occurrence of strain-induced precipitation.

For steel B3, the predicted RST was higher than experimentally measured at all strain levels and interpass time. There is a significant difference between experimental and predicted values (40-60°C) at low strain levels ($\epsilon \leq 0.20$). Again, the reason for this discrepancy could be the value of the strain-dependent exponent in equation (2.11) and the overestimation of a solute Nb concentration effect on recrystallisation kinetics. As a result, the equation (2.11) overestimates the $t_{0.05X}$ and in turn undermines the recrystallisation rates.

The RPTT curves analysis highlights the importance of the effect of Nb(CN) precipitation on the softening mechanisms. The precipitation significantly influences the progress of recrystallisation even if the $t_{0.05X} < t_{0.05P}$. Therefore, the criterion for selecting the recrystallisation stop temperature as an intersection of the $t_{0.05P}$ and $t_{0.05X}$ curves is not a requirement [40]. The continuous evolution of the precipitation process with time is the determining factor for retarding the static recrystallisation. Consequently, the precipitate pinning force will also vary with interpass time as a function of precipitate size and volume fraction.

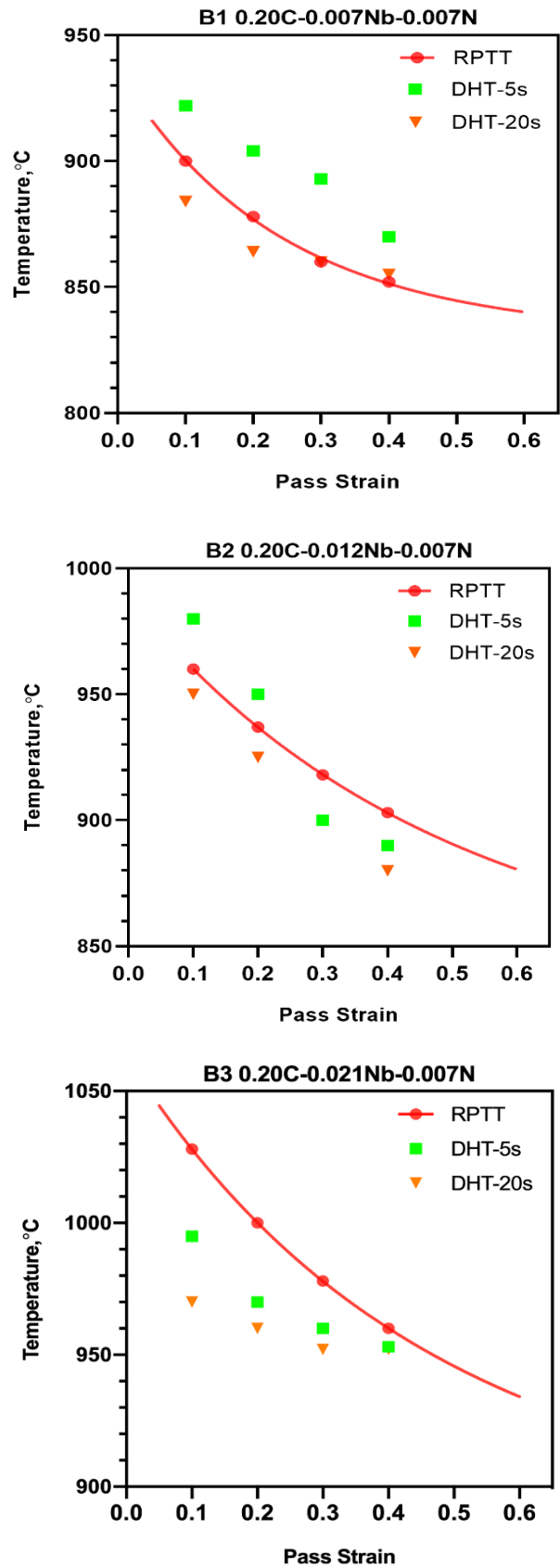


Figure 6.17 Effect of pass strain on estimated RST ($T_{5\%}$) for steel B1-B3. The experiment measured RST for 5 and 20 sec are superimposed for comparison purpose

6.4.3 Strain-induced Precipitation Model

The presiding discussion indicates that the interaction between recrystallisation and precipitation process is the foundation of conventional controlled rolling (CCR). The fundamental mechanism involved with these processes is complex and is still an important research topic within the steel industry. The deformation processing variables of temperature, strain, strain rate and interpass time have a significant effect on the kinetics of both recrystallisation and precipitation process.

Various researchers [86, 146, 193] have studied the mechanism of strain-induced precipitation in great detail. Dutta and Sellars [86] presented the details illustration of the mechanism and kinetics of strain-induced precipitation based on thermodynamic and experimental observation. Dutta *et al.* [146] followed up with the earlier precipitation work and reviewed the coarsening of Nb(CN) particles. He proposed that the coarsening of precipitate on dislocations node begins at the very early stage due to pipe diffusion. Dutta *et al.* [107] presented a comprehensive mathematical model to predict complete precipitation kinetics in Nb microalloyed steels. The model was based on classical nucleation theory with the assumption of heterogeneous precipitation upon dislocation nodes.

Nagarajan *et al.* [190] refine the work of Dutta *et al.* [107] and developed a multi-pass model for strain-induced precipitation. The model provides a complete description of the precipitate size and volume fraction evaluation as a deformation processing variable. Hence, this model can be coupled with the recrystallisation model to obtain a realistic view of the interaction between recrystallisation and precipitation during the high-temperature deformation. The simulation of precipitate radius and volume fraction as a function of time allows estimation of F_{PIN} during hold time on a continue basis.

Figure 6.18 presents the results from this computer model simulating precipitate evaluation in steel B1 for isothermal deformation at 850°C (measured $T_{5\%}$), strain $\epsilon=0.40$ and hold of 20 sec. The precipitation number density, radius, and volume fraction evaluations are shown as a function of time. The precipitate number density reaches a maximum very early and subsequently starts decreasing after a hold of 5 secs. In contrast, the precipitation volume fraction continuously increases with time until it reaches the equilibrium fraction. The Nb concentration continuously diminishes in the austenite matrix, first as a result of nucleation of precipitates and later as a coarsening of precipitates.

Figure 6.19 and 6.20 illustrates the precipitate evaluation for steel B2 and B3 at their respective $T_{5\%}$. The steel B2 and B3 exhibited Similar nucleation and growth behaviour. However, a higher volume fraction of Nb(CN) precipitate is predicted due to higher Nb supersaturation.

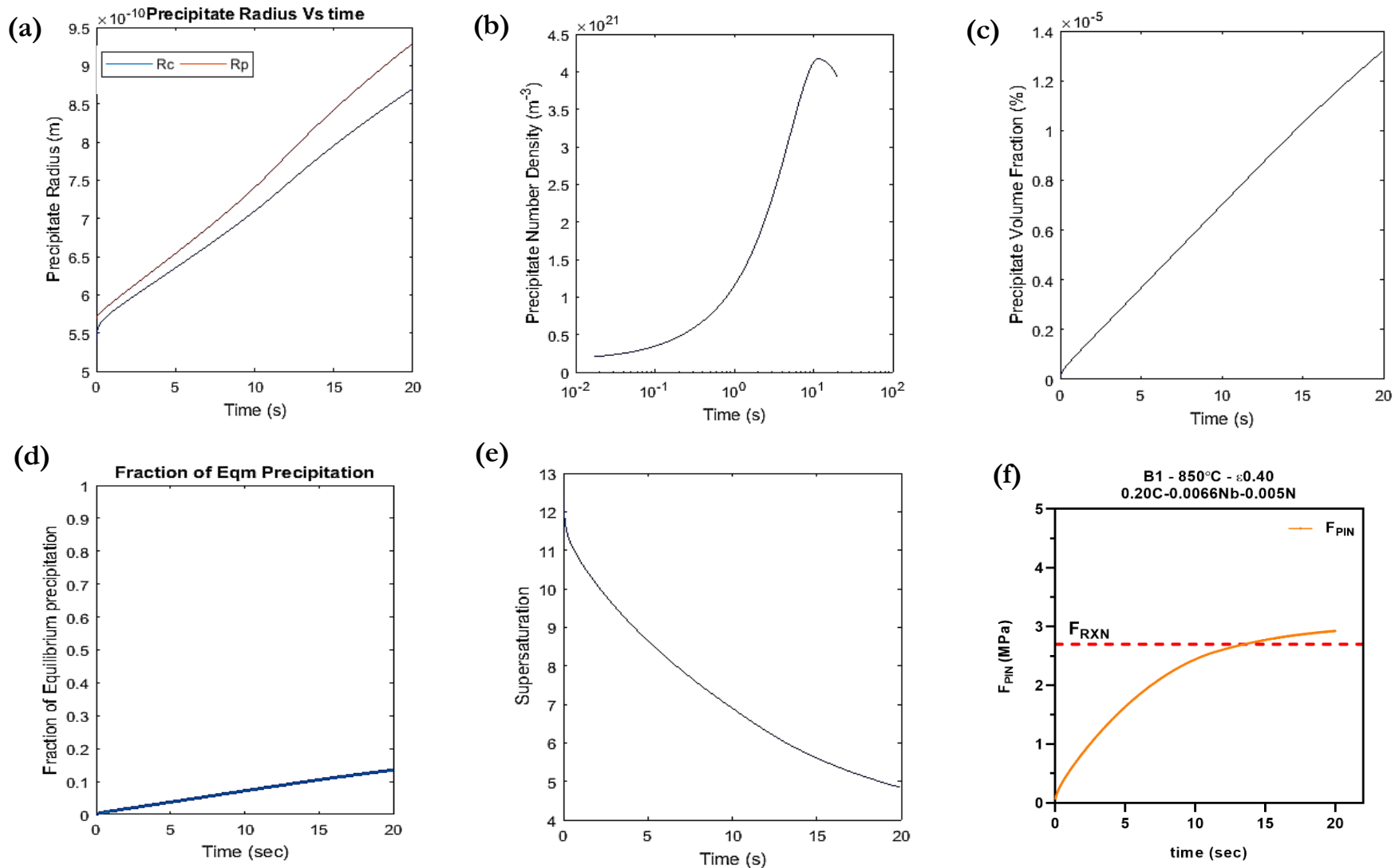


Figure 6.18 Illustration of results from a computer model for steel B1: deformation at 850°C, $\epsilon 0.40$ and held for 20 sec, (a) precipitate radius evaluation, (b) precipitate number density, (c) precipitate volume fraction (d) fraction of equilibrium precipitation (precipitation fraction), (e) Nb_{SSR} and (f) F_{PIN}.

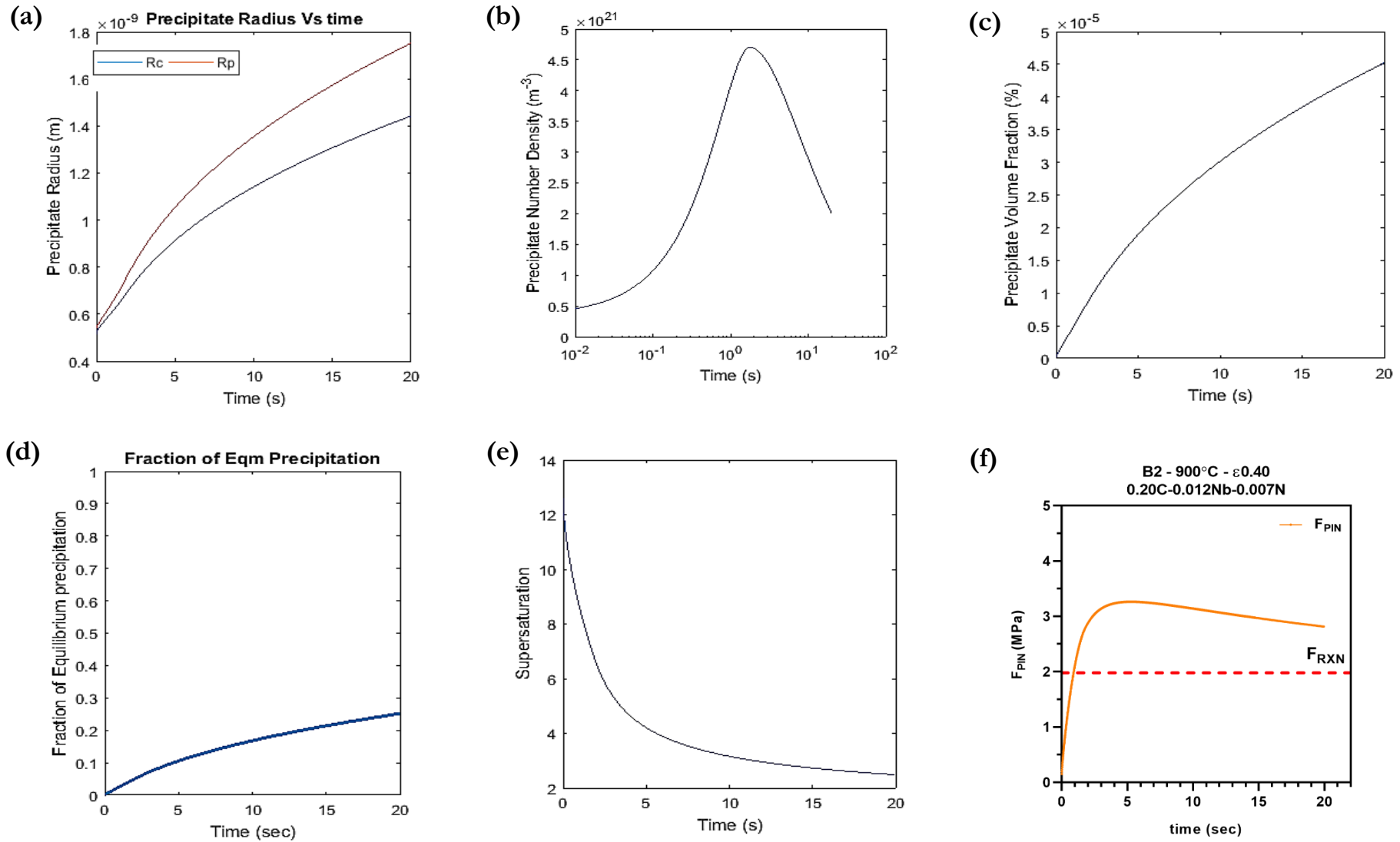


Figure 6.19 Illustration of results from a computer model for steel B2: deformation at 900°C, $\epsilon 0.40$ and held for 20 sec, (a) precipitate radius evaluation, (b) precipitate number density, (c) precipitate volume fraction (d) fraction of equilibrium precipitation (precipitation fraction), (e) N_{bSSR} and (f) F_{PIN}

XX

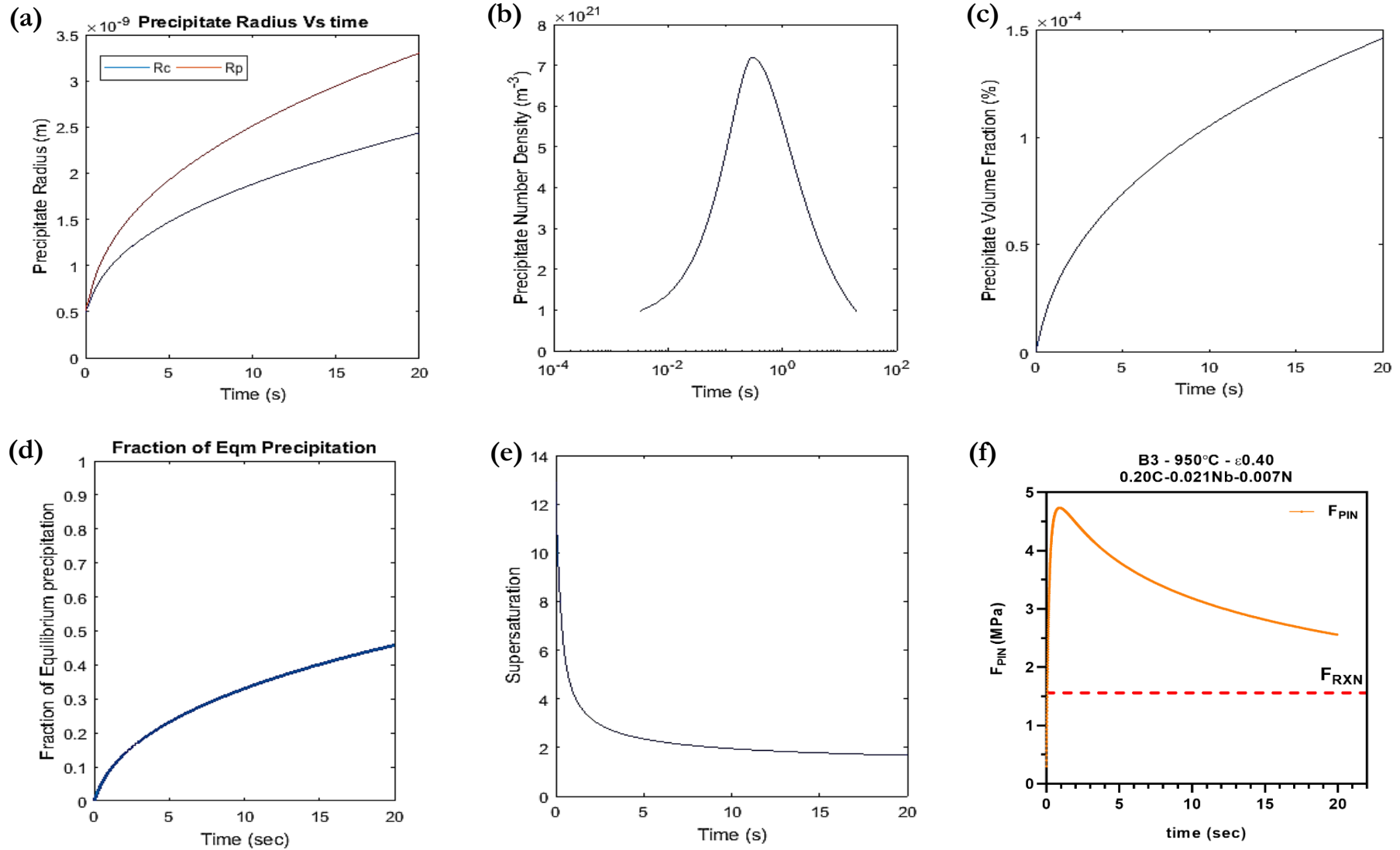


Figure 6.20 Illustration of results from a computer model for steel B3: deformation at 950°C, $\epsilon 0.40$ and held for 20 sec, (a) precipitate radius evaluation, (b) precipitate number density, (c) precipitate volume fraction (d) fraction of equilibrium precipitation (precipitation fraction), (e) N_{bSSR} and (f) F_{PIN}

XX

In the previous models [86, 107, 146], the precipitate number density was computed using the classical nucleation equation. Typically, for homogeneous nucleation, all the lattice points act as a potential site for precipitate nucleation. However, the dislocation nodes in the microbands are highly favoured as nucleation sites for Nb(CN) due to the higher reduction in the total energy associated with nucleation on such heterogenous sites. But it is difficult to know the correct value for the total number of active nucleation sites for SIP.

Hence, the SIP number density (N) is computed indirectly from the volume constraint (mass balance) equation in the multipass SIP model. It is a floating variable which changed according to the laws of precipitate growth and the flux of solute atoms reaching the microbands.

$$N = \frac{XV_0}{(4/3)\pi R_p^3} \quad (6.3)$$

where X is the precipitation fraction, V_0 is the equilibrium volume fraction and R_p is the precipitate radius. The precipitate volume fraction is calculated for every iteration from the solute concentration profile and the precipitate number density is computed according to equation 6.2 to comply with the precipitate growth rate equation. As seen in Figure 6.19 and 6.20, the maximum precipitate number density is reached in a fraction of a second after first pass deformation. It could be assumed that precipitation is instantaneous and no further nucleation takes place during the interpass hold time.

As discussed earlier, the critical factor in retarding recrystallisation is the continuous evaluation of precipitation and recrystallisation process with time. Most of the early researchers [?] have calculated single F_{PIN} values at the end of holding time-based on experimentally measured or equilibrium volume fraction. In contrast, the multi-pass SIP model provides a unique opportunity for evaluation an F_{PIN} as a function of holding time with an accurate estimation of precipitate size and volume fraction. The F_{PIN} was estimated using the subgrain boundary model proposed by Hansen *et al.* [40].

Figure 6.18(f) - 6.20(f) shows the variation of precipitate pinning force F_{PIN} per unit area as a function of time for the steel B1-B3 isothermally held at respective $T_{5\%}$ after prestrain of 0.40. The F_{PIN} gradually increases as the precipitation proceeds until the precipitate number density reaches the maximum value. With further isothermal hold, the precipitate number density starts to decrease due to the coarsening of the precipitates. The pinning force also decreases as a function of precipitate size even though the volume fraction increases with time.

The estimated F_{PIN} is higher than measured F_{RXN} during the entire hold time for all the steels. The predicted F_{PIN} agrees well with experimental measured F_{PIN} for steel B1 and B3 even though the

model predicts a very fine size of precipitates. For steel B3, the predicted pinning forces are two times higher than the measured local F_{PIN} . The estimation of the precipitate pinning force with interpass time makes the SIP model a significant development.

The model predicts low volume fraction based in line with the thermodynamic system; however, the predicted pinning forces are still higher. The pinning forces are directly proportional to precipitate volume fraction and inversely proportional to the square root of the precipitate radius. The precipitate size has a stronger effect on the pinning forces than the volume fraction. The fine precipitate size of 2-6 nm has resulted in pinning forces comparable to or greater than recrystallisation driving force.

The recrystallisation will be retarded whenever the pinning force becomes greater than the recrystallisation driving force. The precipitates can effectively pin the subgrain boundary whenever a critical volume fraction is achieved. The austenite recovery and recrystallisation are thermally activated processes. There will be a continuous decrease in the dislocation density with interpass time hence a deceleration in recrystallisation and precipitation kinetics. The modelling approach for evaluation of dislocation density as a function of time is sophisticated and beyond the scope of this investigation.

6.5 Transformation Behaviour of Austenite

6.5.1 Allotriomorphic Ferrite Nucleation

The effect of soluble Nb on austenite to allotriomorphic ferrite transformation has been studied extensively in the last four decades [195-199]. It is agreed that Nb in solution retards the austenite to ferrite transformation and thus lowers the A_{r3} temperature. Lee *et al.* [196] suggested that solute Nb strongly segregates to the austenite/ferrite phase boundary and reduces the ferrite growth kinetics due to the solute drag effect. Abe *et al.* [197] reported that the Nb microalloying addition lowered the A_{r3} at a rate of 10°C per 0.01% dissolved Nb.

In the present work, steel B1-B3 had three different amounts of Nb in solution after the austenitising heat treatment, but they had similar prior austenite grain size. Hence, any enhancement in hardenability after transformation should be directly related to soluble Nb as the initial grain size is similar. As shown in Figure 5.43, the A_{r3} of steel B3 (0.021%Nb) was found to be about 20°C lower than that of the base grade for a cooling rate of $5^{\circ}\text{C}/\text{s}$. It implies that dissolved Nb lowers the A_{r3} at a rate of 10°C per 0.01% solute Nb in line with previous investigations.

Several research workers have proposed the mechanism of ferrite growth retardation based on the segregation of carbide forming elements (Mo, Nb, V, etc.) at ferrite/austenite interfaces [195-199]. According to Aaronson *et al.* [198], this segregation takes place whenever there is a significant difference between the size of substitutional atoms and the interstitial solutes. The presence of substitutional solute reduces the activity of interstitial solutes in the matrix (austenite). The decrease of carbon activity in the matrix near ferrite interfaces lowers the driving force for ferrite diffusion in the austenite and ferrite growth rate.

Yan and Bhadeshia [199] recently studied the effect of soluble Nb on austenite-ferrite transformation in a low carbon-high Nb line pipe steel. A 0.021 wt. % of soluble Nb lowered the A_{r3} by 40°C at a cooling rate of $20^{\circ}\text{C}/\text{s}$. They proposed the mechanism that Nb segregates at the prior austenite grain boundaries and reduces the austenite grain boundary energy ($\sigma_{\gamma\gamma}$). A reduction of the γ/γ interfacial energy per unit area makes the grain boundaries less potent sites for heterogeneous nucleation of allotriomorphic ferrite. This leads to a dramatic reduction in the activation energy for nucleation and retardation of the nucleation rate. A reduction $\Delta\sigma$ in $\sigma_{\gamma\gamma}$ was found to be 0.286 J m^{-2} per wt. % of soluble Nb.

6.5.2 Widmanstätten Ferrite

There have been numerous investigations about the occurrence of Widmanstätten ferrite in steel as a function of chemical composition, austenite grain size, and cooling rate during continuous cooling transformation [200-203]. It is consequently well-established that Widmanstätten ferrite is favored in austenite with a large grain structure [200, 202]. Widmanstätten ferrite forms in a temperature range where reconstructive transformation becomes relatively sluggish and gives way to para-equilibrium displacive transformation.

For a small grain size, the prior formation of allotriomorphic ferrite enriches the residual austenite with carbon, which transforms to pearlite at A_{r1} temperature. So, it is not surprising that a small grain size ($< 30 \mu\text{m}$) suppresses the Widmanstätten ferrite formation. For the same reason, an increase in the cooling rate will tend to favor the formation of Widmanstätten ferrite. Figure 6.21 illustrates the influence of austenite grain size on the propensity of Widmanstätten formation.

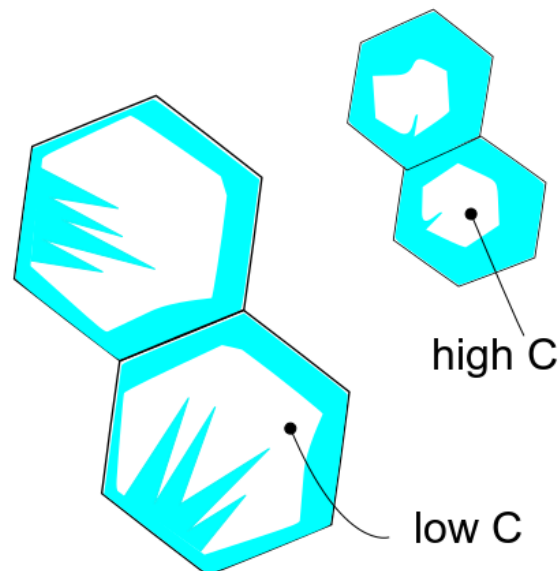


Figure 6.21 Effect of prior austenite grain size on Widmanstätten ferrite formation (adapted from ref [204])

Bodnar *et al.* [200] reported the effect of austenite grain size and cooling rate on Widmanstätten ferrite formation in the 0.20%C low alloy steels from a series of controlled experiments. Their studies demonstrated that the volume fraction of the Widmanstätten structure increases with an increase in austenite grain size and cooling rate. The austenite grain size had a more significant effect than the cooling rate on the amount of Widmanstätten ferrite formed. They proposed adequate refinement of prior austenite grain size (e.g., $\leq 30 \mu\text{m}$) during the rolling process to avoid the formation of coarser Widmanstätten structure in both plain carbon and microalloyed steel. The Nb microalloying addition promoted the formation of Widmanstätten structure in comparison to V and Ti.

Figure 5.45 depicts that the volume fraction of Widmanstätten ferrite increased with the increase in cooling rate for constant grain size and composition. At the same time, the volume fraction and grain size of allotriomorphic ferrite decreased with increasing cooling rate. This observation is consistent with the general trend reported in earlier investigations [200, 202]. It was also observed that the volume fraction of allotriomorphic ferrite decreases with an increasing Nb concentration in the following order: B0, B1, B2 and B3 for a given cooling rate. This in turn leads to an increase in the volume fraction of Widmanstätten ferrite as a function of undercooling.

Bhadeshia *et al.* [204, 205] suggested that substitutional alloy elements like Mn, Ni, Cr, Nb have negligible effects upon the displacive transformation products. The substitutional solute does not partition during displacive transformation, and their role is to influence the thermodynamic stability of the austenite. As a result, the substitutional elements would not retard the formation of Widmanstätten ferrite.

6.5.3 Mechanical Properties

A microstructure predominant with an allotriomorphic ferrite phase typically exhibits the discontinuous yielding behavior and a low YS/UTS ratio (typically < 0.7). It has been traditionally regarded as providing a safety margin against failure by plastic collapse or fracture in the post-yield area. It has been claimed [201-202] that the presence of Widmanstätten ferrite changes the deformation behavior from discontinuous to continuous yielding during tensile deformation. The low volume fraction of Widmanstätten ferrite reduces the 0.2% yield offset, while a relatively large volume fraction leads to continuous yielding and increased yield strength [202].

In the present investigation, all samples exhibited continuous yielding behaviour except steel B0 at 0.5°C/s. This result is in agreement with the finding of other researchers [201-202]. However, a direct comparison cannot be made due to the difference in the mode of mechanical testing. The compression testing was employed for present studies contrary to traditional tensile testing in earlier research. Also, the presence of lower transformation product was not investigated with electron microscopy characterization which may be present in small amounts.

Bodnar *et al.* [206] studied the effect of Widmanstätten ferrite on the mechanical properties of plain C-Mn steel as a function of austenite grain size and different cooling rates. There was an improvement in both the strength and toughness when the microstructure was changed from one which is predominantly allotriomorphic ferrite to one containing Widmanstätten ferrite. This was attributed to an increase in the volume fraction of Widmanstätten ferrite and associate microstructure refinement. All the samples consisting of Widmanstätten ferrite microstructures showed discontinuous yielding behavior. He suggested that in cases where continuous yielding has

been reported in the literature [201-202], the microstructures may have contained a sufficient amount of lower transformation products (i.e., bainite or martensite) to mask the deformation behavior of Widmanstätten ferrite.

The present study is in agreement with earlier findings [201-202, 206] that Widmanstätten ferrite is not detrimental to the mechanical properties of C-Mn steels. Both yield strength and hardness increase with an increasing volume fraction of Widmanstätten ferrite. For a given cooling rate, both yield strength and hardness increase with the grades in the following order: B0, B1, B2, and B3. This ordering is mainly due to the positive influence of Nb on Widmanstätten ferrite formation. For example, the steel B3 has the largest volume fraction of Widmanstätten ferrite and hence, the highest strength and hardness level.

Some of the strength increments may be due to fine NbC precipitation in the ferrite during cooling. These fine precipitates significantly contribute to strength increment depending upon their size and volume fraction. However, estimating the strengthening potential of precipitate in finished products is beyond the scope of this investigation. Figure 6.22 shows the yield strength increment in steel B1-B3 over base steel as a function of niobium concentration. The steel B3 showed a maximum increase; however, the steel B1 has a notable jump considering the level of Nb addition.

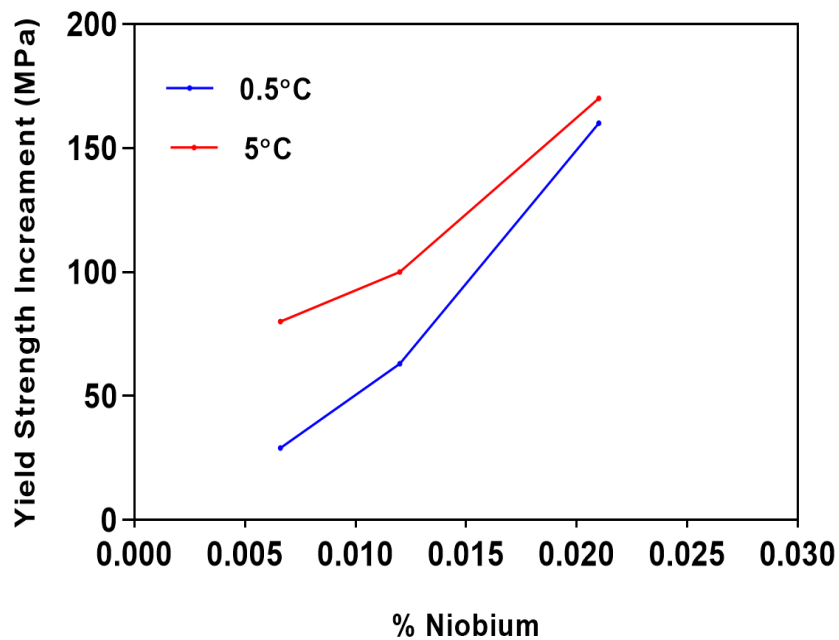


Figure 6.22. Influence of Nb concentration on yield strength improvement in steel B1-B3

This page is internationally left blank

Chapter 7

Application to commercial processing

The microalloying technology enabled the development of High Strength Low Alloy (HSLA) steels via the process of thermomechanical processing. It represents a group of low carbon microalloyed steels with yield strength over 355 MPa in the as-rolled condition. The lower carbon levels of HSLA steels gives them excellent weldability and formability compared to mild steel. Such steels have been hugely successful, and it has been estimated that they now constitute around 10% of total world steel production

Even though the Nb microalloying technology is very well established in the case of flat products, there are still known unknowns in the case of mainstream hot rolled long products. Due to the limited solubility of Nb in austenite at normal carbon levels (0.20-0.30%C) of structural steels, the use of Nb has been somewhat limited and applied only when higher strength is required. The present study was primarily designed to investigate the influence of dilute Nb microalloying additions (50-200 ppm) on static restoration behaviour of structural steels and to gain better control of microstructural changes occurring during deformation.

This study showed that the recrystallisation stop temperature ($T_{5\%}$) increases with increasing Nb in steel and related Nb supersaturation in austenite. The $T_{5\%}$ increased at a rate of 40°C per 0.006 % Nb supersaturation in austenite for steel B1–B3. The increased supersaturation resulted in the high volume fraction of Nb(CN) precipitates which in turn lead to higher values of pinning forces F_{PIN} . Even a dilute level of 66 ppm Nb at 0.20%C could retard the static austenite recrystallisation under certain deformation conditions.

The present study has contributed to advancing our existing knowledge of the interplay between solute supersaturation and Nb(CN) volume fraction on $T_{5\%}$ for a given structural steel composition. It is possible to develop a unique TMCP deformation schedule for a given structural steel composition (0.20%C-1.0%Mn) to best benefit from dilute Nb additions. The ultimate result would be an enhancement of the final product regarding both microstructure and properties. The generic strategy for a different type of rolling process is presented below:

7.1 Heavy Sections (Beam-IPE and Crane Rail)

The adaptation to Nb-microalloyed approach will allow higher strengths to be easily developed (e.g. S420 and S460) without any major changes in the production. The Nb addition would not only enhance the yield strength (due to a finer grain size; the Hall-Petch relationship) but would also further decrease the low temperature impact properties (as grain refinement is the only mechanism to achieve this). In particular both of these mechanisms would be beneficial for the heavier gauge sections that are near the specified minimum yield strength.

→ The following chemistry is recommended for production of high strength heavy sections:

C	Mn	Si	P	S	Al	Nb	N
0.18 0.20	1.10 1.25	0.25	< 0.018	< 0.010	0.020	0.020 0.025	< 0.007

→ The furnace reheating temperature should be between 1240-1250°C allowing all of the Nb to enter into the austenite solid solution. The bloom/billet should be not held excessively in the furnace once it is believed that core of billet has reached 1250°C to achieve uniform prior austenite grain size before rolling.

→ As established, the actual $T_{nr} / T_{5\%}$ is expected to occur somewhere during the finishing pass sequence. With the addition of 0.021 % Nb, the T_{nr} was found to be in the region of 980-950°C based on experimental softening results for a $\varepsilon=0.20-0.40$ respectively at interpass time of 20 sec. Based on the RPTT diagrams (Figure 7.1), the T_{nr} is predicted to start at 960°C for a maximum strain of a $\varepsilon=0.40$ which very well matches with experimental observation.

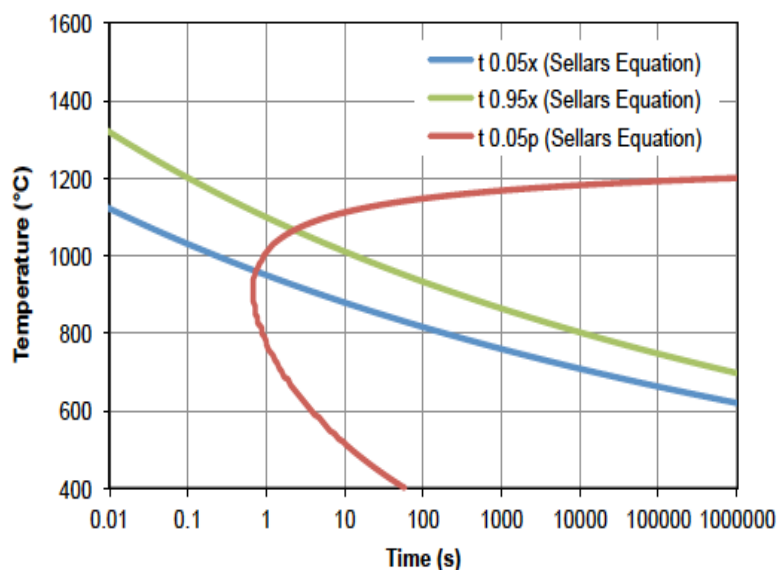


Figure 7.1 Predicted RPTT diagram for proposed steel chemistry

Patel *et al.* [207] proposed that all roughing passes should be completed above 980°C and the finishing passes do not start until 940°C if the T_{nr} point is approximately 950°C. Figure 7.2 highlights the demarcation applicable in reference to control rolling of heavy sections in a rolling mill.

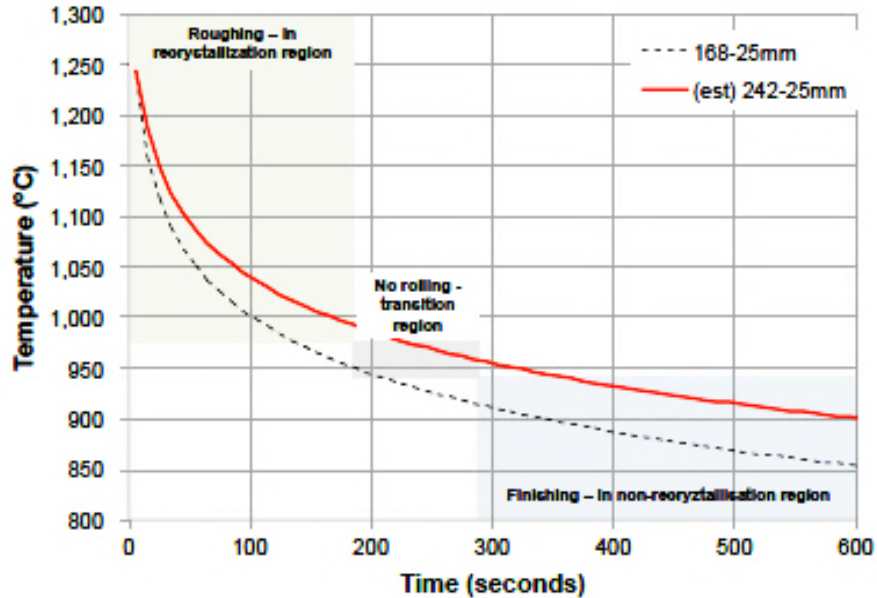


Figure 7.2. Temperature evaluation of rolled bloom/billet through the section mill [207]

→ During roughing, the interpass times must be maintained to ensure that complete static recrystallization of the austenite occurs through the thickness. Naturally, this will be challenging, as long interpass times will mean a reducing stock temperature whilst balancing the fact that all roughing passes must be completed before the temperature drops below 980°C.

→ The rolling mill loads and temperature along the process line should be recorded to help the identify T_{nr} for actual rolling schedule and product size.

→ The strength increment would be further higher in an industrial practice considering a heavy reduction applied below $T_{5\%}$. Using a 0.030-0.035% Nb would serve to further increase the T_{nr} which in turn will permit greater levels of austenite conditioning (and retain strain) and again, an improvement in strength and ITT.

Note: The steels in the present investigation were processed under the principles of CCR through DHT tests at 880°C, $\epsilon=0.40$, hold time = 20 sec and controlled cooled at 5°C/s after the second deformation. The ferrite grain size of 15 μm and 10.7 μm were obtained in the final product for steel B0 and B3 respectively, as shown in Figure 7.3.

The effect of polygonal ferrite grain on yield strength has been well known and can be described by the Hall-Petch relationship [22] for typical C-Mn structural steels. Based on this relationship, the increase in yield strength developed from the fine ferrite grain size of 4.3 μm would be equivalent to 27 MPa.

Additionally, the strain-induced precipitation in deformed austenite contributes to dispersion strengthening based on size and volume fraction in the final product. Based on TEM results in the present investigation, the dispersion strengthening contribution is estimated at around 45 MPa using the Ashby-Orowan relationship [10]. So, the strength of plain C-Mn steel may be improved by 70 MPa with just an addition of 0.021%Nb and subsequent application of controlled rolling practice.

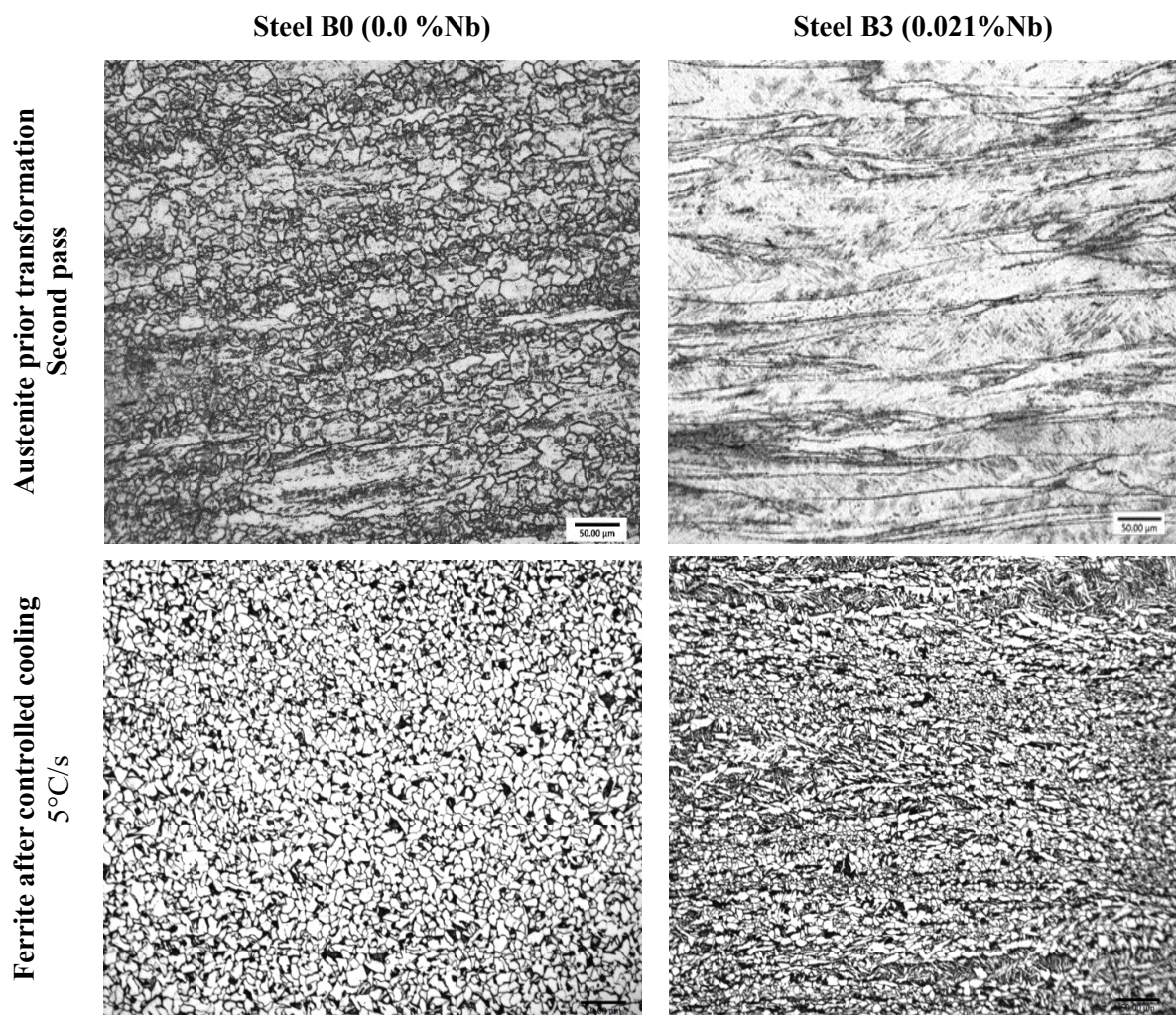


Figure 7.3 Microstructure of the grade B0 and B3, which were deformed in DHT test at 850°C, $\epsilon=0.40$, hold of 20 sec and cooled at 5°C/s after second deformation pass.

7.2 Light or Medium Sections (Equal Angle and Channel - PFC)

The introduction of Nb microalloying to the existing commercial TLT angle section would enable refinement of polygonal ferrite grain size and pearlite colony size.

→ The following chemistry can be recommended for value-added light sections:

C	Mn	Si	P	S	Al	Nb	N
0.18 0.20	1.25	0.25	< 0.018	< 0.010	0.020	0.010 0.012	< 0.007

→ A furnace reheating temperature of 1150-1180°C should be applied even for the largest billet size (160 x 160 mm and 250 x 250 mm). For a 0.01%Nb addition, all the Nb is expected to be in complete solution at a temperature of 1140°C, therefore a lower reheating temperature can be easily be employed and thus saving fuel costs. This is in addition to the other microstructure and material performance benefits.

→ With the addition of 0.010 % Nb, the T_{nr} is around 890-900°C based on experimental results in present study for a $\epsilon=0.20-0.40$ and hold time = 20 sec. The austenite pancaking will occur for majority of the finishing passes in the light gauge equal angle sections (6-12 x110 x 110 mm) as shown in Figure 7.4. Some austenite conditioning will take place for heavier gauge sections (20-25 x 200 x 200 mm).

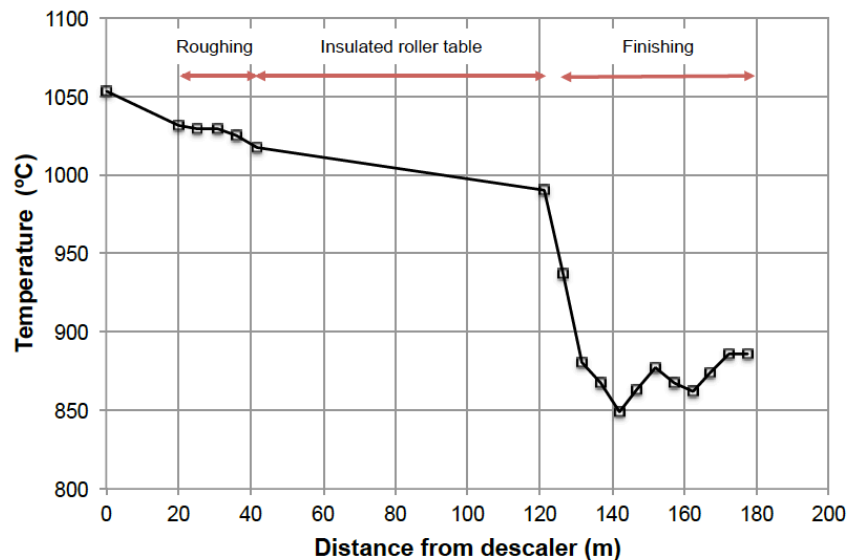


Figure 7.4 Measured temperature run-down of the light gauge angle through the mill [207]

→The austenite will start to accumulate strain owing to the lack of recrystallisation in finishing passes. As discussed earlier, the pancaked austenite will give the ferrite grain refinement thus contributing to the improved yield strength and toughness. The yield strength increment of 25-30 MPa is practically achievable with a simple 0.01%Nb addition to plain C-Mn steel.

7.3 Rebar

Steel rebar remains a primary construction material used in many civil engineering applications. Rebar are typically rolled with DRCR practice involving higher finishing temperature ($> 950^{\circ}\text{C}$) and strain rates. Even in this case, dilute Nb addition can support the grain refinement through the solute drag effect considering most of Nb remains in solution at typical processing temperatures.

→ The following chemistry can be recommended for high strength rebars:

C	Mn	Si	P	S	Al	Nb	N
0.20 0.25	1.00 1.25	0.25	< 0.018	< 0.010	0.020	0.010 0.020	< 0.007

→ In present study, the steel B2 with 0.012%Nb exhibited a T_{nr} of 940°C at $\epsilon=0.20$ (typical finishing mill strain in each pass). The shorter interpass time in rebar rolling will push the $T_{5\%}$ even further provided critical strain for dynamic recrystallisation is not reached. It is worth validating this proposed change in a laboratory to generate more data before any industrial application.

→ Due to higher finish rolling temperature, grain refinement effect is lower than anticipated in rebar rolling as discussed in earlier sections. In the meanwhile, Nb in solution decrease ferrite transformation temperature thus pearlite volume fraction increases. Nb microalloying is more effective to improve upon tensile-to-yield ratio due to this solute Nb effect on transformation.

→ The Nb remaining in austenite solution precipitates in ferrite during or after phase transformation and provides precipitation strengthening (hardening) as a function of precipitate size and volume fraction. The rough approximation of precipitation strengthening contribution in yield strength is 30 MPa per 100 ppm Nb addition. However, the strength increment of 60 MPa per 100 ppm of Nb was observed from the dilatometry experiment (which is almost double of a typical norm) in present study. But these conditions also had a significant amount of Widmanstätten ferrite which may have increased the yield strength.

In summary, it has been demonstrated through laboratory studies that ‘small’ and even ‘dilute’ additions of Nb in the solution can support grain refinement through the mechanism of strain-induced precipitation and solute drag. the addition of dilute Nb concentration is beneficial for structural steels irrespective of broader rolling practices adopted in industrial production. Application of dilute Nb concept can reduce the overall material and construction costs fulfilling the challenges of safe, healthy and sustainable construction. The physical metallurgical principles of dilute Nb addition can be applied to the number of other hot deformation processes like forging.

Chapter 8

Concluding Remarks

Based on the present investigation and results reported herein, the following conclusions can be made concerning the effect of dilute Nb concentrations on suppression recrystallisation in hot deformation of austenite:

Role 1: Grain Coarsening Behavior

1. Steel B0 and B1 exhibited typical grain coarsening behaviour of plain carbon C-Mn steels. The austenite grain growth increased linearly until 1150°C as a function of reheating temperature. The austenite grains become uniformed post 1150°C because of secondary recrystallisation.
2. Steel B2 and B3 exhibited abnormal grain growth upon reheating at high temperatures. The T_{GC} corresponding to mixed grain structure was found to be between 1050-1100°C for steel B2-B3. Post this temperature, the austenite grain attains uniform structure due to secondary recrystallisation.

Role 2: Inhibition of Recrystallisation

3. The fractional softening increased with an increase in deformation temperature and equivalent strain at constant strain rate and interpass time. This is consistent with the trend reported from earlier investigators [154,178]. However, the present result indicates that the deformation temperature has a more significant effect on initiation of the static restoration events than the equivalent strain.
4. The isothermal PSC testing proved to be an easy and straightforward method for determining recrystallisation-stop ($T_{5\%}$) and recrystallisation-limit ($T_{95\%}$) temperatures. The $T_{5\%}$ was associated with a 20% fractional softening of austenite. A $T_{5\%}$ of 825, 855, 900 and 943°C was measured for steel B0, B1, B2, and B3 respectively for a strain of $\epsilon=0.40$ and hold time of 20 sec. The $T_{5\%}$ increased at a rate of 40°C per 0.006 % Nb supersaturation in austenite for steel B1–B3. The level of Nb supersaturation was not constant at the respective $T_{5\%}$ for steel B1-B3.
5. An excellent agreement is obtained between quantitative microstructure studies and fraction softening results from the hot compression tests. The microstructure below the $T_{5\%}$ exhibited unrecrystallised prior austenite structure. A fully recrystallised microstructure consisting of a small equiaxed grain was observed at temperature 30-70°C above $T_{5\%}$. The quantitative metallography validated the softening criteria that the $T_{5\%}$ is equal to 20% fractional softening.

6. Upon double-hit tests, the mean PAGS were in the range of 130-150 μm for unrecrystallised austenite microstructure with an aspect ratio of 15-20 in all steels. The aspect ratio of unrecrystallised austenite increased with an increase in strain. The mean PAGS of recrystallised austenite was in the range of 22-35 μm with an aspect ratio of approximately 1.0-1.2.
7. These parameters are indicators of the degree of recrystallisation or work hardening in the austenite grains. For example, a drastic decrease in the mean PAGS coupled with an aspect ratio = 1.0 indicated complete static recrystallisation. Similarly, a constant mean PAGS with an increase of aspect ratio indicated the work hardening of the austenite.
8. Electron microscopy investigation indicated a high, localized volume fraction of Nb(CN) precipitation at austenite subgrain boundaries in carbon extraction replica. No evidence was found for Nb(CN) precipitation in the matrix, i.e. within the prior austenite grains. HRTEM and EDX techniques have confirmed the chemical composition and morphology of Nb(CN) precipitates.
9. The extensive strain-induced Nb(CN) precipitation was observed in thin foil dark fields for unrecrystallised austenite structure. The strain-induced precipitates exhibited the K-S orientation relationship with a quenched ferrite (α') matrix. The SADP analysis suggests that these carbides have a NaCl type crystal structure with a lattice parameter of 0.447 nm. These observations are consistent with a trend reported from earlier investigations in low carbon microalloyed steels.
10. The measured volume fraction of Nb(CN) precipitates at austenite subgrain boundaries was 5-10 times higher than predicted volume fraction based on thermodynamic equilibrium. This high volume fraction of Nb(CN) at prior austenite grain boundaries translated into high values of precipitate pinning force (F_{PIN}). The pinning forces were experimentally determined based on the subgrain boundary pinning mechanisms [40]. At any given temperature and strain, the local F_{PIN} increases with increasing dilute Nb concentration from steel B1 to B3
11. The driving force for recrystallisation (F_{RXN}) was determined using the SIBM model from isothermal compression testing for steel B0-B3. Values of F_{RXN} were calculated from an increase in flow stress at $\epsilon = 0.40$ prior to holding. The change in dislocation density ($\Delta\rho$) estimated via Taylor's equation gave a good reasonable estimate of F_{RXN} . At any given temperature, the F_{RXN} was similar for all steels independent of Nb additions and showed a strong dependence on deformation temperature. A value ranging from 1.5 MPa (at 1000°C, low Z) to 3 MPa (at 850°C, high Z) was observed depending upon Z conditions.

12. The interaction between F_{PIN} and F_{RXN} showed good correspondence with fraction softening and quantitative metallography measurements. The static recrystallisation was inhibited when $F_{PIN} \geq F_{RXN}$ at respective $T_{5\%}$, corresponding to the critical pinning force of 1.6 MPa. This agreement confirms the validity of precipitate pinning in suppressing the static recrystallisation of austenite during interpass time by essentially locking the substructure.
13. The static recrystallisation was the dominant mechanism at high temperature ($\geq 1000^{\circ}\text{C}$) which is also demonstrated by fraction softening studies. The measured F_{PIN} was far less than F_{RXN} for the steel B3 even with available Nb supersaturation of 0.017%. As expected, steel B2 showed much less precipitation at 1000°C due to lower Nb supersaturation.
14. The Nb supersaturation ratio, $[Nb]_{SSR}$ concerning Nb(CN) precipitation, is a critical factor in determining whether an effective recrystallisation and precipitation interaction will take place at a particular temperature. The recrystallisation was inhibited in those deformation conditions where an $[Nb]_{SSR}$ exceeded a critical value of 4.5, 5.0 and 6.0, at corresponding $T_{5\%}$ (RST) for a true strain of 0.20, 0.30 and 0.40 respectively.

Role 3: Transformation Behavior

15. At a constant grain size, the Nb in austenite solution retarded the allotriomorphic ferrite transformation and the start of transformation is shifted to a lower temperature. The transformation temperature decreased with an increase in soluble Nb in the following order: B3, B2, B1 and B0. The dissolved Nb lowered the A_{r3} at a rate of 10°C per 0.01 wt % solute Nb.
16. The possible explanation for the retardation effect is that Nb segregates at the prior austenite grain boundaries and reduces the austenite grain boundary energy. The resulting increase in activation energy leads to retardation in the nucleation rate.
17. The Widmanstätten ferrite is favored in austenite with a large grain structure. The volume fraction of the Widmanstätten structure increased with an increase in the cooling rate through the transformation range for constant grain size. These observations are consistent with the general trend reported by the earlier investigators [200]. For a given cooling rate and grain size, the presence of soluble Nb promoted Widmanstätten ferrite formation as it lowered the transformation temperature.
18. For a given cooling rate, the yield strength increased with steel in the following order: B0, B1, B2, and B3. This ordering is primarily due to the positive influence of Nb on Widmanstätten ferrite formation. The NbC may have precipitated in the ferrite during cooling which could have also improved strength.

This page is internationally left blank

Chapter 9

Scope for Future Work

1. Many of the popular solubility products for Nb(CN) available in the literature are limited to ranges of steel chemistries investigated, keeping in mind the developments of line pipe and automotive steel up to the 1980s. The quantitative electron microscopy techniques were limited when most of these solubility products were investigated and published. Atom Probe Tomography /quantitative TEM can be carried out to develop a solubility product that is directly applicable to a 0.20–0.25wt.% carbon steel (in the first instance) and Nb contents up to 0.025wt.%,
2. The $T_{5\%}$ and $T_{95\%}$ processing map in the present investigation was determined from isothermal hot PSC tests based on DHT techniques. This processing map identified a regime of partial recrystallisation as a function of constant strain which should be avoided to achieve better toughness in steels. However, the finish rolling in the industry always takes place in continuous cooling conditions and multiple passes. It would be worth simulating the industrial finishing schedule for selected composition, followed by control cooling to room temperature. The TMC machine allows the 4-5 multi-pass simulation for an initial PSC sample thickness of 10 mm with a maximum true strain of 1.1.
3. The present studies investigated the effect of Nb supersaturation on the static restoration behaviour of austenite concerning TMCP synergy. A large amount of structural steel tonnage is rolled at a higher finishing temperature; hence it will be worthwhile to investigate the role of Nb in case of a reference to DRCR practice.
4. The extraction replica technique has two inherent drawbacks, the first depth of etching is unknown leading to variation in the volume fraction of SIP for the same deformation conditions and second inability to extract $SIP < 2$ nm. The synchrotron X-ray experiments should be carried out to overcome the problem associated with the extraction replica technique. The high energy synchrotron X-ray of 100 - 60 keV ($\sim 0.12 - 0.20 \text{ \AA}$) offers statistical relevance as volumes of several cubic millimetres can be analysed. A very high angular resolution power allows accurate measurement of size distribution and volume fraction of SIP. Additionally, the synchrotron technique enables in-situ observation of the precipitation in the austenite matrix.

5. The empirical equation for the onset of static recrystallisation ($t_{0.05X}$) needs to be reviewed for higher carbon and low niobium content in typical structural steels. The equation (2.11) for $t_{0.05X}$ overestimates the start of recrystallisation due to the soluble Nb effect; hence the isothermal recrystallisation kinetics as a function of hold time should be evaluated for a range of Nb levels. In a similar line, the exponent values for initial grain size needs reconsideration at low strain levels ($\epsilon \leq 0.10$)
6. Similarly, the empirical equation for the onset of precipitation ($t_{0.05P}$) predicts very long incubation times at dilute Nb concentrations (< 100 ppm). However, the TEM studies have shown the accelerated precipitation kinetics in these steels. The empirical equation needs reevaluation for dilute Nb levels in structural steels.
7. The effect of soluble Nb on austenite-ferrite transformation varies primarily with cooling rate and, to some extent, with grain size. In the present investigation, the solution treatment was performed on the material to completely dissolve the Nb into an austenite solution, which resulted in the coarse austenite grains ($140 \mu\text{m}$). It will be sensible to analyse the effect of soluble Nb on phase transformation kinetics when austenite grains are in the range of $25\text{-}50 \mu\text{m}$, a typical value observed after finish rolling in a steel mill for a recrystallized or deformed austenite.

References

- [1] A. J. DeArdo, C. I. Garcia & E.J. Palmiere (1991) Thermomechanical Processing of Steels, Heat Treating, Vol. 4, ASM Handbook, ASM International, 237-255.
- [2] W. B. Morrison, “Microalloy steels - The beginning,” Mater. Sci. Technol., vol. 25, no. 9, pp. 1066–1073, 2009.
- [3] A. J. DeArdo, M. J. Hua, K. G. Cho, and C. I. Garcia, “On strength of microalloyed steels: An interpretive review,” Mater. Sci. Technol., vol. 25, no. 9, pp. 1074–1082, 2009.
- [4] S. Vervynckt, K. Verbeken, B. Lopez, and J. J. Jonas, “Modern HSLA steels and role of non-recrystallisation temperature,” Int. Mater. Rev., vol. 57, no. 4, pp. 187–207, 2012.
- [5] A. J. DeArdo, “Microalloyed steels: Past, present and future,” 7th Int. Conf. High Strength Low Alloy Steels, HSLA Steels 2015, Int. Conf. Microalloying 2015, Microalloying 2015 Int. Conf. Offshore Eng. Steels 2015, OES 2015, vol. 1, pp. 17–32, 2015.
- [6] Stuart, H., Metallurgical Society of AIME. (1984). *Niobium: proceedings of the international symposium*. Warrendale, Pa.: Metallurgical Society of AIME.
- [7] T. Tanaka, Thermomechanical Processing of Microalloyed Austenite: Conference proceeding, TMS-AIME, New York, 1982,
- [8] A. J. DeArdo “Fundamentals Metallurgy of Niobium in Steel” in International Symposium Niobium 2001, 2001, TMS, pp.
- [9] I. Tamura, H. Sekine, T. Tanaka, and C. Ouchi, Eds., Thermomechanical Processing of High-Strength Low-Alloy Steels. Butterworth-Heinemann, 1988.
- [10] T. Gladman, The physical metallurgy of microalloyed steels, London, Institute of Materials, 1997
- [11] L.J. Cuddy, The Effect of Microalloy Concentration on the Recrystallisation of Austenite During Hot Deformation, In Conf. Thermomechanical Processing of Microalloyed Austenite, TMS-AIME, New York, 1982, p.289
- [12] World Steel Association, World Steel Yearbook 2018
www.worldsteel.org/steel-by-topic/statistics/steel-statistical-yearbook.html
Accessed on June 20, 2019
- [13] R. Zanon, The use of heavy rolled sections in high rise buildings – current practice and future innovation, Conf. Constr Metal 2012, Accessed on June 20, 2019
- [14] B. Donnay and H. Grober, “Niobium in High Strength Weldable Beams and Other Structures” in International Symposium Niobium 2001, 2001
- [15] S. G. Jansto, L. Silvestre, and H. Wang, “Application of Niobium Low Carbon Low Alloy Structural Steel Approach,” in HSLA Steels 2015, Microalloying 2015 & Offshore Engineering Steels 2015, 2016, pp. 895–901.
- [16] S. G. Jansto, “MicroNiobium Alloy Approach in medium and high carbon steel bar, plate and sheet products,” Metall. Mater. Trans. B Process Metall. Mater. Process. Sci., vol. 45, no. 2, pp. 438–444, 2014.

- [17] S. G. Jansto, “Niobium Bearing Construction Steels and Global Applications Trends”, in Value Added Niobium Microalloyed Construction Steel Symposium, 2012,
- [18] M. Gomez, Medina, S.F., Quispe, A and Valles, P Static Recrystallisation and Precipitation in Low Nb Microalloyed Steel, ISIJ International, Vol.42 (2002), No.4, 423-431
- [19] Z. Cui, J. Patel, and E. J. Palmiere, “Thermomechanical Processing of Structural Steels with Dilute Niobium Additions,” in HSLA Steels 2015, Microalloying 2015 & Offshore Engineering Steels 2015, 2016, pp. 281–287.
- [20] C. Rhodes, Construction industry statistics and policy, Briefing Paper, House of Commons, Number 01432, October 2015 (Accessed on Dec 10, 2016, Research briefings)
- [21] Industry and Construction Statistics, Eurostat, 2018
https://ec.europa.eu/eurostat/statisticsexplained/index.php?title=Construction_of_buildings_statistics_-_NACE_Rev._2#Sectoral_analysis
 (Accessed on May 22, 2019)
- [22] J. Patel, Niobium Microalloyed High Strength Beams, Iron and Steel Review, India, December 2012, Volume 56, No. 7
- [23] S. G. Jansto, “Niobium bearing structural steels for 21st century”, in Niobium Bearing Structural Steels Conference, 2011, pp.1-27
- [24] EUROFER, “European Steel in Figures in 2018”
<http://www.eurofer.org/News%26Events/PublicationsLinksList/201806-SteelFigures.pdf>
 Accessed on Jun 20, 2019
- [25] European Commission Report, “Reference Document on Best Available Techniques in the Ferrous Metals Processing Industry”, <https://eippcb.jrc.ec.europa.eu/reference/fmp.html>
 Accessed on Jun 20, 2019
- [26] J. Patel, “China Steel Rebar: Market Overview and Latest Product Applications” in SEASI Conference, 2018
- [27] N. Baddoo, “High Strength Long Span Structural Steels (HILONG)” European Commission Technical Report, EUR 28450
- [28] M. Gkantou, Response and design of high strength steel structures employing square and rectangular hollow sections, PhD Thesis, University of Birmingham, pp.34
- [29] J. Patel, “Developing Next Generation of Cost-Effective Rebar for ASEAN Construction Market”, in SEASI Conference, 2017, pp.
- [30] Surajit Kumar Paul, Pritam Kumar Rana, Debdulal Das, Sanjay Chandra and Saurabh Kundu, High and low cycle fatigue performance comparison between micro-alloyed and TMT rebar, Construction and Building Materials, 54 (2014), 170–179
- [31] J. J. Irani, D. Burton, J. D. Jones & A. B. Rothwell (1967) Strong tough structural steels, Sp. Report 104, ISI, London, UK, 110
- [32] J. D. Jones & A. B. Rothwell (1968) Deformation under hot working conditions, Sp. Report 108, ISI, London, UK, 78.

- [33] J. Strauss and F. F. Franklin: 'Metals handbook, 485; 1948, ASM, Cleveland, OH.
- [34] J. G. Zimmerman, R. H. Aborn and E. C. Bain: Trans. ASM, 1937, 25, 755.
- [35] G. F. Comstock: Trans. ASM, 1940, 28, 608.
- [36] H. W. Gillett: 'Metals handbook', 535; 1948, ASM, Cleveland, OH
- [37] W. B. Morrison: 'HSLA steels 2000', Xi'an, China, October– November 2000, Chinese Society for Metals, 11.
- [38] G. Tither, "Progress in Niobium Market and Technology 1981-2001" in International Symposium Niobium 2001, 2001, pp.
- [39] T. M. Noren (1963) Columbium as a microalloying element in steels and its effect on welding technology, Special Report SSC-154, Ship Structure Committee, US Department of Commerce, Washington DC, USA
- [40] S.S. Hansen, J.B. Vander Sander and M. Cohen, Niobium Carbonitride Precipitation and Austenite Recrystallisation in Hot Rolled Microalloyed Steel, Metallurgical Transactions, Vol. 11A, March (1980), p,387
- [41] J. Speer and S. Hansen (1989) Austenite Recrystallisation and Carbonitride Precipitation in Niobium Microalloyed Steels, Metallurgical and Materials Transactions A, Vol. 20, No. 1, p25-38.
- [42] O. Kwon and A.J. DeArdo (1991) Interactions Between Recrystallisation and Precipitation in Hot Deformed Microalloyed Steels, Acta Metallurgica et Materialia, Vol. 39, No. 4, p529-538.
- [43] Brown, E.L, DeArdo, A.J and Bucher, J.H, The Microstructure of Hot Rolled HSLA Steels, In Conf. Hot Deformation of Ausstenite, J. Ballance, TMS-AIME, New York, 1977, p.250
- [44] J. D. Baird & R. R. Preston (1973) Processing and properties of low- carbon steel, New York, Metallurgical Society of AIME, 1-46
- [45] F. B. Pickering, "High-Strength, Low-Alloy Steels — A Decade of Progress," *Proceedings. Microalloying '75* Washington, D. C., Oct. 1–3, 1975, pp 9–32
- [46] M. Cohen and S. S. Hansen: *MICON '78: Optimization of Processing, Properties and Service Performance Through Microstructural Control*, H. Abrams, G. N. Manian, D. A. Nail, and H. D. Solomon, eds., p. 34, ASTM, Philadelphia, PA, 1979.
- [47] Underwood, E.E., Quantitative Stereology, Addison Wesley Publishing Co. Inc., 1970, p8
- [48] I. Kozasu, C. Ouchi, T. Sanpei & T. Okita (1977) Microalloying 75, Union Carbide Corporation, New York, 120-135
- [49] A. J. DeArdo (2001) Metallurgical Basis for Thermomechanical Processing of Microalloyed Steels, Journal of Ironmaking and Steelmaking, Vol. 28, 138-144
- [50] H. Sekine & T. Maruyama (1976) Trans. Iron Steel Inst. Japan., Vol. 16, 427-435

- [51] W. Roberts, A. Sandberg, T.Siwecki and T. Werlefors, Prediction of microstructure development during recrystallisation of hot rolling of Ti-V steels, Int. Conf. on HSLA Steels: Technology and Applications, 67-74, Philadelphia, PA, ASTM, 1984
- [52] T. Siwecki and G. Engberg, Thermo-Mechanical Processing in Theory, Modelling & Practice, Stockholm, Sweden, 4-6 Sept. 1996, pp.121-144 (Vanitec Publication - V0398)
- [53] T. Siwecki and B. Hutchinson, 33rd Mechanical Working and Steel Processing Conference, St. Louis, MO, 1991, Warrendale, PA, ISS-AIME, 1992, p.397
- [54] T. Tanaka (1981) Controlled Rolling of Plate & Strips, International Metallurgical Reviews, 185-207
- [55] G.R. Speich, L.J. Cuddy, C.R. Gordon and A.J. DeArdo, Phase Transformation in Ferrous Alloys, TMS-AIME, Warrendale, PA, 1984, p.341
- [56] C. Ouchi, T. Sampei and L.Kozasu, Transactions of the Iron and Steel Institute, Japan, Vol.22, 1982, p.214
- [57] J.J. Jonas, Microstructural evolution during hot rolling, Proc. Int. Symp. On Mathematical Modelling of Hot rolling of Steel, Canadian Inst of Mining and Metallurgy, Montreal, Canada, 1990, p.99-118
- [58] Pussegoda, L.N., Yue S. and Jonas, J.J. Laboratory simulation of seamless tube piercing and rolling using dynamic recrystallisation schedules, Metall. Trans. 21A, 1990, p53-64
- [59] P.D. Hodgson, J. J. Jonas and S. Yue, Evolution of microstructure in rod and bar rolling, Int. Conf. on Processing, microstructure and properties of microalloyed steels, PA, 1991
- [60] F.J. Humphreys and M. Hatherly, Recrystallisation and related annealing phenomena. 2nd ed 2004, Amsterdam; Boston: Elsevier. 628 p.
- [61] R.E. Reed-Hill (1973) Physical Metallurgy Principles, 2nd ed., Brooks/Cole Eng, p 267
- [62] S.J. Basinski and Z.S. Basinski (1966) Recrystallisation, Grain Growth and Textures, American Society for Metals, p1
- [63] Manohar, P.A., Ferry, M., & Chandra, T. Recrystallisation of Ferrite and Austenite, In Encyclopaedia of Materials: Science & Technology, (2001), pp.3019-3024
- [64] J.J. Jonas, C.M. Sellars and W.J. McG.Tegart, Metal Review, 1969, 14, 1
- [65] J.P. Shah, G.J. Richardson and C.M. Sellars, Metal Review, 1969, 8, 325
- [66] Roberts, W., H. Boden and B. Ahlblom, Dynamics Recrystallisation Kinetics, Metal Science, 1979, 13, p.195-205
- [67] T. Sakai, Dynamic recrystallisation microstructure under hot working conditions, Journal of Material Processing Technology, 53, 1195, p349-361
- [68] McQueen, H.J. and Jonas, J.J. (1975), Plastic Deformation of Materials, Vol.6, Ed. R.J. Arsenault, Academic Press, New York, 393.

- [69] A.R. Marder and J.L. Goldstein, Phase Transformation in Ferrous Alloys, TMS-AIME, Warrendale, PA, 1984, p.341/ Eric
- [70] C.M. Sellars, The Physical Metallurgy of Hot Working, In Hot Working and Forming Processes Conf., Metals Society, London, 1980, p3-15
- [71] C. Ouchi and T.Okita, Dynamic Recrystallisation Behaviour of Austenite in Nb-bearing HSLA and Stainless Steel, Trans. ISIJ, 1982, 22, p543-551
- [72] C. Rossard, Mechanical and Structural Behaviour Under Hot Working Conditions, In Microstructure and Design of Alloys, Iron Steel Inst. London, 1974, Vol. II, 175-203
- [73] LeBon. A., Rofes-Vernis. J. and Rossard. C, Mem. Sci. Rev. Met., 1973, 70, 577-588
- [74] LeBon, A., Rofes-Vernis, J.; and Rossard, C., Recrystallisation and Precipitation During Hot Working of a Nb bearing HSLA Steel, Met. Sci., 1975, 9, 36-40
- [75] Sakai, T. and Jonas, J.J. A Grain Refinement/Grain Coarsening Model for Dynamic Recrystallisation, 1986
- [76] Roberts, W. Dynamic Changes that occur during hot working and their significance during microstructural development, In Deformation Processing and Structures, ASM, Ohio, p 109-184
- [77] Sellars, C.M. and Whiteman, J.A., Recrystallisation and Grain Growth in Hot Rolling, Metals Science, 1979, 13, p187-194
- [78] C. M. Sellars, The kinetics of softening processes during hot working of austenite. Czechoslovak Journal of Physics. (1985), 35, 239-248. 10.1007/BF01605090.,
- [79] P. Dolzhenko, M. Tikhonova, R. Kaibyshev, and A. Belyakov, “Dynamically Recrystallized Microstructures, Textures, and Tensile Properties of a Hot Worked High-Mn Steel,” Metals (Basel), vol. 9, no. 1, 2019.
- [80] Barraclough, D.R. and Sellars, C.M. Static recrystallisation and restoration after hot deformation of Type 304 stainless steel, Metals Science, 1979, 13, p257-266
- [81] Morrison, W.B, J. Iron and Steel Inst, 1972, 210, p.618
- [82] G. Glover and C. M. Sellars, “Static recrystallization after hot deformation of α iron,” Metall. Trans., vol. 3, pp. 2271–2280, 1972.
- [83] J. Jonas, C. Sellars, and W. Tegart, “Strength and structure under hot-working conditions,” Metall. Rev., vol. 14, pp. 1–24, 1969.
- [84] C. Sellars and W. Tegart, “Hot Workability,” Int. Mater. Rev., vol. 17, pp. 1–24, 1972.
- [85] C. M. Sellars and W. J. McTegart, “On the mechanism of hot deformation,” Acta Metall., vol. 14, pp. 1136–1138, 1966.
- [86] B. Dutta, C.M. Sellars, Effect of Composition and Process Variables on Nb(C, N) Precipitation in Niobium Microalloyed Austenite, Mater. Sci. Technol. 3 (1987) 197–206.

- [87] Laasraoui, A. and Jonas, J.J. (1991), *Metall. Trans. A*, 22A, 151.
- [88] Medina, S.F. and Mancilla, J.E. (1993), *ISIJ Int.*, 33, 1257.
- [89] Karjalainen, L.P. and Perttula, J.S. (1996), in *Conf. Proc. "ReX '96"*, Ed. McNelly, 413.
- [90] Hodgson, P.D. and Gibbs, R.K. (1992), *ISIJ Int.*, 32, 1329.
- [91] Cho, S.H., Kim, S.I. and Yoo, Y.C. (1997); *Journal of Material Science Letters*, 16,1836.
- [92] A.I Fernandez, P. Uranga, B. Lopez and J.M. Rodriduez Ibabe, *Static Recrystallisation Behaviour of Wide Range of Austenite Grain Sizes in Microalloyed Steels*, *ISIJ International*, Vol. 40 (2000), No. 9, pp 893-901
- [93] S.S.Gorelik, *Recrystallisation in Metals and Alloys*, MIR Publisher, Moscow, 1978
- [94] R.W.K. Honeycombe, *The Plastic Deformation of Metals*, 2nd Edition, Metal Park. Ohio, ASM, 1984, p.287
- [95] G. Gottstein and L. S. Shvindlerman, *Grain Boundary Migration in Metals: Thermodynamics, Kinetics, Applications*, Second Edition, CRC Press, 2009
- [96] J.W.Marin and R.D.Doherty, *Stability of Microstructure in Metallic Systems*, Cambridge, UK, p.40
- [97] R. W. Cahn: *Recrystallisation Mechanisms In Recrystallization, Grain Growth and Textures*,(ed. H.Margulin), ASM Publication, Metals Park, Ohio, 1966. p. 99
- [98] P.A. Beck and P.R.Sperry. *Effect of recrystallisation Texture on Grain Growth*, *Transactions of the AIME*, Vol. 185 (1949), p.240
- [99] P.A. Beck and P.R.Sperry. *Strain Induced Boundary Migration in High Purity Aluminium*, *Journal of Applied Physcis*, Vol.21, (1950), p.150
- [100] J.E.Bailey and P.B.Hirsch, *The recrystallisation process in some polycrystalline Metals*, *Proceedings of Royal Society of London*, Vol. A267, (1962), p.11
- [101] W.C.. Leslie, *The Physical Metallurgy of Steels*, New York. McGraw-Hill Book Company, 1981, p.43
- [102] Zurob, H.S., Y. Brechet, and J. Dunlop. *Acta Mater*, 2006. 54: p. 3983-3990
- [103] A. Kelly and G. Groves, *Crystallography and Crystal Defects*, Reading MA, 1970, p.198
- [104] J.D.Verhoven, *Fundamental Physical Metallurgy*, New York, John Wiley Sons, 1975, p.77
- [105] H. Gleiter and B. Chalmers, *Progress in Material Science*, Vo.16, New York Pengamon Press, 1972, p.143

- [106] Keh, A.S. Dislocation Arrangements in Alpha Iron During Deformation and Recovery, In Conf. Direct Observation of Imperfections in Crystal, 1962, p.213
- [107] B. Dutta, E.J. Palmiere and C.M. Sellars, Modelling the Kinetics of Strain Induced Precipitation in Nb Microalloyed Steels, *Acta Mater.* 49 (2001) 785–794
- [108] M. Gomez, S.F. Medina, and P. Valles, Determination of Driving and Pinning Forces for Static Recrystallisation During Hot Rolling of a Nb Microalloyed Steel, *ISIJ International*, Vol.45 (2005), No.11, 1711-1720
- [109] Ruibal, E., Urcola, J. J. and Fuentes, M. Static Recrystallisation Kinetics, recrystallised grain size and growth after hot deformation of low alloy steel, *Z. Metallkde* , 1985, 76, 568-576
- [110] Lucke, K and Detert, K, A Quantitative Theory of Grain Boundary Motion and Recrystallisation in Metals in the Presence of Impurities, *Acta Metallurgica*, 1957, vol. 5, 628
- [111] Lucke, K and Stuwe, H.P, On Theory of Impurity Controlled Grain Boundary Motion, *Acta Metallurgica*, 1971, vol. 19, 1087
- [112] Cahn, R.W, The Impurity Drag Effect in Grain Boundary Motion, *Acta Metallurgica*, 1962, vol. 10, 789
- [113] Hillert, M., Monograph and Report Series No 33, Institute of Metals, 1969, 231
- [114] Hillert, M and Sundman, B, A Treatment of Solute Drag on Moving Grain Boundaries and Phase Interfaces in Binary Alloys, *Acta Metallurgica*, 1976, vol. 24, 731
- [115] Akben, M.G., Weiss, I. and Jonas, J.J. (1981), *Acta Metall.*, 29, 111.
- [116] Suehiro, M. (1998), *ISIJ Int.*, 38, 547.
- [117] A. J. Deardo, “Metallurgical basis for thermomechanical processing of microalloyed steels,” *Ironmaking and Steelmaking.*, vol. 28, no. 2, pp. 138–144, 2001.
- [118] H. Nordberg, B. Aronson, Solubility of Niobium Carbide in Austenite, *J Iron Steel Inst.* 206 (1968) 1263–1266.
- [119] P.R. Smith, The Solubility of Niobium Carbide in Gamma Iron, *Trans. Metall. Society AIME.* 236 (1966) 220.
- [120] K. Narita, Physical Chemistry of the Group IVa (Ti, Zr), Va (V, Nb, Ta) and the Rare Earth Elements in Steel, *Trans. Iron Steel Inst. Japan.* 15 (1975) 145.
- [121] T.H. Johansen, N. Christensen, B. Augland, The Solubility of Niobium (Columbium) Carbide in Gamma Iron., Technical University of Norway, Trondheim, 1967.
- [122] T. Mori, M. Tokizane, K. Yamaguchi, E. Sunami, Y. Nakazima, Thermodynamic Properties of Niobium Carbides and Nitrides in Steels, *Tetsu-to-Hagane.* 54 (1968) 763–776.
- [123] R.C. Sharma, V.K. Lakshmanan, J.S. Kirkaldy, Solubility of Niobium Carbide and Niobium Carbonitride in Alloyed Austenite and Ferrite, *Metall. Trans. A.* 15, 545–553

- [124] K. Balasubramanian, J.S. Kirkaldy, Thermodynamics of Fe-Ti-C and Fe-Nb-C Austenite and Nonstoichiometric Titanium and Niobium Carbides, in: J.D. Embury, G.R. Purdy (Eds.), *Adv. Phase Transitions*, Pergamon Press, Ontario, 1987: p.37
- [125] R.P. Smith, The Solubility of Niobium Nitride in Gamma Iron, *Trans. Metall. Society AIME*. 224 (1962) 190
- [126] M.L. Santella, PhD Thesis: Grain Growth and High-temperature Hot Rolling Behaviour of Low-alloy Steel Austenite, University of Pittsburgh, 1981
- [127] K.J. Irvine, F.B. Pickering, T. Gladman, Grain-refined C-Mn steels, *Iron Steel Inst J.* 205 (1967) 161–182
- [128] M.J. Spanraft, T.M. and Hoogendoorn, Quantifying the Effect of Microalloying Elements on Structures during Processing, in: J. Crane (Ed.), *Microalloying 75*, Union Carbide Corporation, New York, NY, 1977: pp. 75–85
- [129] L. Meyer, *Z. Metallk.*, 1967, 58, 334
- [130] E.J. Palmiere, C.I. Garcia, A.J. DeArdo, Compositional and Microstructural Changes which Attend Reheating and Grain Coarsening in Steels Containing Niobium, *Metall. Mater. Trans. A.* 25 (1994) 277–286
- [131] A. Ray, “Niobium microalloying in rail steels,” *Mater. Sci. Technol.*, vol. 33, no. 14, pp. 1584–1600, 2017.
- [132] J. Wadsworth, J. Woodhead, S. Keown, The Influence of Stoichiometry upon Carbide Precipitation, *Met. Sci.* 10 (1976) 342–348
- [133] Davenport, A.T., Miner, R.E., and Kot, R.A. (1977), in *Conf. Proc. “Hot Deformation of Austenite”*, Ed. J.B. Balance, A.I.M.E., Warrendale, 186
- [134] A. WATANABE, Y. E. SMITH, and R. D. PEHLKA: in 'Hot deformation of austenite', (ed. J. B. Ballance), 140-168, 1977, New York, The Metallurgical Society of AIME.
- [135] Hoogendoorn, T.M. and Spanraft, M.J. (1977), in *Conf. Proc. “Microalloying ‘75’*, Ed. Korchinsky et al., Union Carbide Corp., N.Y., 75
- [136] Simoneau, R., Begin, G. and Marquis, A.H. (1978), *Metal Sci.*, 12, 381
- [137] Ouchi, C., Sanpei, T., Okita, T. and Kosazu, I. (1977), in *Conf. Proc. “Hot Deformation of Austenite”*, ed. Balance, TMS-A.I.M.E., Warrendale, 316
- [138] Janampa, C.J. (1982), “The Role of Nitrogen in the Hot Working of Niobium Microalloyed Steels”, PhD Thesis, University of Sheffield
- [139] Yamamoto, S., Ouchi, C. and Osuka, T. (1982) in *Conf. Proc. “Thermomechanical Processing of Microalloyed Austenite”*, Eds. DeArdo, Ratz and Wray, The Metallurgical Society of AIME, Warrendale, 613
- [140] Fitzsimons, G., Tiitto, K., Fix, R. and DeArdo, A.J. (1984), *Metall. Trans. A*, 15A,241

- [141] Park, S.H., Yue, S. and Jonas, J.J. (1992), *Metall. Trans. A*, 23A, 1641
- [142] J. Herman, B. Donnay, V.Leroy: *ISIJ International*, 32 (1992), No.6, pp.779/85
- [143] Silveira e Silva, J.M. & Barbosa, R. (1993), *Scripta Metall. et Mater.*, 29, 881
- [144] Medina, S.F. and Quispe, A.F. (1996b), *ISIJ Int.*, 36, 1295
- [145] K.B. Kang, O. Kwon, W.B. Lee and C.G. Park, *Scripta Materialia*, Vol. 36 (1997), pp.1303-1308
- [146] Dutta, B., Valdes, E. and Sellars, C.M. (1992), *Acta Metall. Mater.*, 40, 653
- [145] Sun, W.P., Jonas, J.J., Hawbolt, I.V., Brimacombe, J.K. and Yue, S. (1994), in *Conf. Proc. "Advances in Hot Deformation Textures and Microstructures"*, Eds. Jonas, Bieler and Bowman, The Minerals, Metals & Materials Society, Warrendale, Pennsylvania,
- [147] Bai, D.Q., Yue, S., Maccagno, T. and Jonas, J.J. (1996), *ISIJ Int.*, 36, 1084
- [148] Sun, W. P., Miltzer, M., Bai, D. Q. and Jonas, J.J. (1993), *Acta Metall.*, 41, 3595
- [149] C. Zener, Private communication to C.S. Smith, *Transactions of the AIME*, Vol.175, 1949, p.15
- [150] M.F. Ashby, The influence of particles on boundary mobility, In *Recrystallisation and Grain Growth of Multiphase and Particles Containing Materials.*, 1980, p. 25
- [151] Gladman, T. (1966), On the Theory of the Effect of Precipitating Particles on Grain Growth of Metals, *Proc. Roy. Soc. A.*, Vol. 204, 298.
- [152] L.J. Cuddy, Austenite Microstructure Developed During Simulated Hot Rolling, In *Recrystallisation and Grain Growth of Multiphase and Particles Containing Materials.*, 1980, p.317
- [153] Hutchinson, W.B. and Duggan, B.J. (1978), *Metal Sci.*, 12, 372
- [154] E. J. Palmiere, C. I. Garcia, and A. J. DeArdo (1996) The Influence of Niobium Supersaturation in Austenite on the Static Recrystallisation Behaviour of Low Carbon Microalloyed Steels, *Metallurgical and Materials Transactions A*, Vol. 27, No. 4, p951-960
- [155] Orowan, E., "The Calculation of Roll Pressure in Hot and Cold Flat Rolling", *Proc. Inst. Mech. Eng.*, vol.150, 1943, p.140
- [156] Ford, H., "Researches into the Deformation of Metal by Cold Rolling", *Proc. Inst. Mech. Eng.*, vol.159, 1948, p.115
- [157] Loveday M. S., Palmiere E. J., Sellars C. M., and Winden M. R. van der "Measurement of Flow Stress in Hot Plane Strain Compression Tests, *Materials at High Temperatures*, vol. 23-2 (2006), p.85-118.

- [158] Wilbur, G.A., Bell, J.R., and Childs, W.J., “The Determination of Rapid Recrystallisation Rates of the Austenite at Temperature of Hot Deformation”, *Trans. Metall. Soc. AIME*, vol.242 (Nov 1968), p.2305
- [159] B. Lopez & L. Gutierrez (2013) Assessment of the methodologies used to determine softening and recrystallisation kinetics by mean of torsion tests, *Material Science & Engineering*, A568, 206 – 211
- [160] Santella, M.L., “Grain Growth and High Temperature Hot Rolling Behaviour of Low-Alloy Austenite”, Ph.D. Thesis, University of Pittsburgh, 1981, p.49
- [161] Palmiere, E.J., *Suppression of Recrystallisation During the Hot Deformation of Microalloyed Austenite*, Ph.D. Thesis, University of Pittsburgh, 1991, p.57
- [162] Djaic, R.A.P and Jonas, J.J., “Recrystallisation of High Carbon Steel Between Intervals of High Temperature Deformation”, *Metallurgical Transactions.*, vol.4A (Feb 1973), p.621
- [163] Petkovic, R.A., Luton, M.J., and Jonas, J.J., “Recovery and Recrystallisation of Carbon Steel between Intervals of Hot Working”, *Canadian Metall. Quarterly*, vol.14 (Nov 1975), p.137
- [164] Standard Practice for Quantitative Measurement and Reporting of Hypoeutectoid Carbon and Low Alloy, ASTM Specification, A1033-10, p8.
- [165] Mirza, M.S., and Sellars, C.M., “Modelling the hot plain strain compression test – Part I”, *Material Science and Technology*, vol.17 (Sep 2001), p1333.
- [166] Smith, E., and Nutting, J., “Direct Carbon Replicas from Metal Surface”, *Brit. Appl. Physics*, Vol 7, p.214-217, 1956
- [167] Leugen, C., “Prior Austenite Grain Size Controlled by Precipitates” Ph.D. Thesis, INSA de Lyon, 2010, English
- [168] Rao, D.V.S., Muraleedharan, K. and Humphreys, C.J., “TEM Specimen Preparation Technique, *Microscopy Science and Technology*, p.1232-1253
- [169] Morre, I., “Modelling γ ” Precipitate Nucleation, Growth and Coarsening in the Nickel-base Super alloy 625”, Ph.D. Thesis, University of Sheffield, 2017, p.92
- [170] D. B. Williams and C. B. Carter, *Transmission Electron Microscopy: A Textbook for Materials Science*. Boston, MA: Springer US, 2009.
- [171] G. Cliff and G. W. Lorimer, “The quantitative analysis of thin specimens,” *J. Microsc.*, vol. 103, no. 2, pp. 203–207, 1975.
- [172] Standard Practice for Quantitative Measurement and Reporting of Hypoeutectoid Carbon and Low Alloy, ASTM Specification, E112, p8
- [173] R. Higginson and C. M. Sellars, *Worked Examples in Quantitative Metallography*, Institute of Materials, Maney Publishing, 2003
- [174] Standard Practice for Quantitative Measurement and Reporting of Hypoeutectoid Carbon and Low Alloy, ASTM Specification, E562, p8

- [175] C. Rueden, J. Schindelin and M. Hiner, "ImageJ2: ImageJ for the next generation of scientific image data", *BMC Bioinformatics* 18:529, 2017 PMID 29187165, doi:10.1186/s12859-17-1934-z
- [176] A Guide for "Automatic Determination of Particle Size Distribution", <https://www.microscopy.ethz.ch/downloads/particle-size.pdf>, Accessed on Jan 20, 2018
- [177] Ashby, M.F. and Ebeling, R. (1966), *Trans. Metall. Soc. AIME*, 236, 1396.
- [178] Dutta B. and Palmiere E.J., "Effect of Prestrain and Deformation Temperature on the Recrystallisation Behaviour of Steels Microalloyed with Niobium", *Metallurgical and Materials Transactions A*, Vol. 34, No. 6, (2003). p1237-1247.
- [179] C. Zener and J.H. Hollomon, Effect of Strain Rate Upon Plastic Flow of Steel, *Journal of Applied Physics*, Vol. 15, (Jan 1944) p.22
- [180] G. Kurdjumov and G. Sachs, "Walz und Rekristallisationstextur von Eisenblech," (Rolling and Recrystallisation Texture of Sheet Iron), *Z. Physik*, (62) (1930), 592.
- [181] R.G. Baker and J. Nutting, "Precipitation Processes in Steels," *ISI Spec. Report No. 64*, London, (1959).
- 182 J.N. Cordeiro and Hook, Recrystallisation Behaviour in Deformed Austenite of High Strength Low Alloy Steels, *Metallurgical Transactions*, Vol. 10A, Jan 1979, p111
- 183 Stewart, M.J, The Effects of Niobium and Vanadium on the Softening of Austenite During Hot Working, In *Conf. Hot Deformation of Austenite*, J. Ballance, TMS-AIME, New York, 1977, p.233
- 184 White, M.J and Owen, W.S. Effect of V and N on Recovery and Recrystallisation During and After Hot Working Some HSLA Steels, *Metallurgical Transactions*, Vol. 11A, April 1980, p597
- 185 A. Yoshi et al Formulation of the Decrease in Dislocation Density of Deformed Austenite Due to Static Recovery and Recrystallisation, *ISIJ International*, Vol. 36 (1996), No. 4, pp. 474-480
- 186 L. Fritzmeier, M. Luton and H. McQueen. (1979), in *Conf. Proc. "Fifth International Conference on the Strength of Metals and Alloys, ICSMA5"*, 95.
- 187 P. Gong, E. Palmiere and M. Rainforth, Dissolution and precipitation behaviour in steel microalloyed with niobium during thermomechanical process. *Acta Materialia*, 97, 2015, 392-403.
- 188 Rainforth, W.M., Black, M.P., Higginson, R.L., Palmiere, E.J., Sellars, C.M., Prabst, I., Warbichler, P., Hofer, F., (2002), *Acta Mater.*, 50, 735
- 189 M.J. Luton, R. Dorvel, and R.A. Petkovic, Interaction between Deformation, Recrystallisation and Precipitation in Niobium Steels, *Metallurgical Transactions*, Vol. 11A, March 1980, pp. 411
- 190 Burke, M.G., Cuddy, L., Piller, J., and Miller, M.K. (1988), *Mater. Sci. Tech.*, 4, 113.
- 191 S.S. Brenner, M.K. Miller and M.G. Burke "Atom Probe and Electron Microscopy Analysis of Precipitates in HSLA steels", in *Proceedings of the 29th International Field Emission Symposium*, Goteborg, Sweden, 1982, pp.47

- 192 V. Nagarajan, E. J. Palmiere, and C. M. Sellars, “New approach for modelling strain induced precipitation of Nb(C,N) in HSLA steels during multipass hot deformation in austenite,” *Mater. Sci. Technol.*, vol. 25, no. 9, pp. 1168–1174, 2009.
- 193 Valdes, E. and Sellars, C.M. (1991), *Mater. Sci. Tech.*, 7, 622.
- 194 L. Sanz, B. Pereda and B. Lopez, “Analysis of Static Recrystallisation Behaviour of Nb-Ti Microalloyed Steels Including Low Strain Levels”, in THERMEC 2016 Conference, Paris
- 195 C. Ouchi, T. Sampei, and I. Kozasu: ‘The effect of hot rolling condition and chemical composition on the onset temperature of γ/α transformation after hot rolling’, *Transactions of the Iron and Steel Institute of Japan*, 1982, 22, 214–222.
- 196 K. Lee and K. Kang Proceedings of International Conference on Mathematical Modelling of Hot Rolling of Steel, 1990, pp.435
- 197 T. Abe, K. Tsukada, and I. Kozasu: ‘Role of interrupted accelerated cooling and microalloying on weldable HSLA steels’, In: J. M. Gray, T. Ko, S. Zhang, B. Wu, and X. Xie, eds. *HSLA Steels: Metallurgy and Applications*. Metals Park, Ohio, USA: ASM International, 1985:103–111.
- 198 H. Aaronson, “On the problem of definition and the mechanisms of bainitic reaction”, in *The Mechanism of Phase Transformation in Crystalline Solids*, The Institute of Metals, London, 1969, pp.270-281
- 199 P. Yan and H. Bhadeshia, The austenite–ferrite transformation in enhanced-niobium, low-carbon steel, *Materials Science and Technology*, 31, 2015, pp.1066-1076
- 200 R. Bodnar and S. Hansen,. Effects of the Austenite Grain Size and Cooling on Widmanstätten Ferrite Formation in Low Alloy Steel, *MMTA* (1994) 25: 665
- 201 G. Glover, R.B. Oldland, and G. Voight: in *High-Strength, Low-Alloy Steels*, D.P. Dunne and T. Chandra, eds., South Coast Printers, New South Wales, Australia, 1984, pp. 271–75.
- 202 J.N. Cordea: Symp. on Low Alloy High Strength Steels, The Metallurgy Companies, Nuremberg, 1970, pp.61–80.
- 203 P.R. Krahe, K.R. Kinsman, and H.I. Aaronson: *Acta Metall.*, 1972, vol. 20, pp. 1109–21
- 204 H. K. D. H. Bhadeshia: ‘Considerations of solute drag in relation to transformations in steels’, *Journal of Material Science*, 1983, 18, 1473–1481.
- 205 S. Jones, and H. K. D. H. Bhadeshia: ‘Kinetics of the simultaneous decomposition of austenite into several transformation products’, *Acta Materialia*, 1997, 45, 2911–2920.
- 206 R.L. Bodnar and S.S. Hansen, Effects of Widmanstätten ferrite on the mechanical properties of a 0.20%C -0.70% Mn Steel, *Metallurgical and Material Transactions A*, Vol.25, pp. 763, 1994
- 207 J. Patel, M. Wright and M. Rebellato, Nb Microalloyed Equal Angle Sections, Internal Technical Report – CBMM Technology Suisse S.A., 2013, Unpublished

Appendix A

Plane Strain Compression (PSC) Testing

In the year 1943, Orwan [155] in his pioneer work on “Theory of Rolling” suggested a modified compression test to simulate the material flow behaviour experienced during cold rolling of mild steel. Ford *et al.* [156] developed a first plane strain compression (PSC) test machine at the University of Sheffield based on Orwan’s suggestion to measure the yield stress characteristics of the material in cold rolling or compressive testing.

The university took this development further and built-up the first computer-controlled servo-hydraulic thermomechanical treatment simulator (TMTS) in the year 1980 to simulate hot forming behaviour of metal alloys. This successful development was achieved in close collaboration with a local company called Servotest, UK. The original equipment was used until 2002 and later dismantled for the installation of the new design. The current TMTS simulator was commissioned in 2003 with a robust control system and added new features.

In PSC, the geometry, illustrated in Figure A1, minimizes the contact friction problems because contact area increases little with strain i.e. tool width, w is constant and breadth, b only spreads to a small extent. However, when specimen thickness, h becomes very small, compared with w , the frictional constraints still become large, limiting the useful equivalent strain ranges to ~ 2.5 .

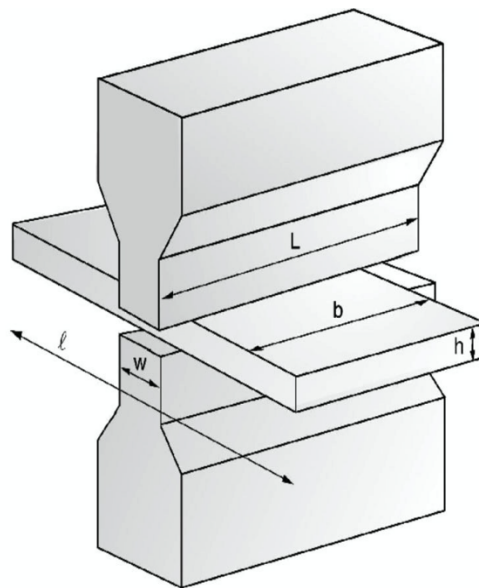


Figure A1. Geometry of PSC testing

A.1 TMTS Architecture and Control System

Figure A2 shows the schematic diagram of the TMTS simulator used in this study. The detail description and characteristics of TMTS are covered in various other works [19,178].

- **Test Furnace:** A furnace with four silicon carbide heating elements surrounding the tool provides control of the tool and test environment temperature in the range of room temperature to 1150°C. The furnace temperature is generally maintained at the same level that of deformation temperature to prevent any chilling effect between tools and PSC specimen when they make contact.
- **FTTU:** A fast-thermal treatment unit capable of controlling the temperature up to 1300°C is located exactly in front of the test furnace. This unit is used for performing the broad spectrum of reheating and cooling conditions to simulate the industrial deformation processing. The FTTU unit mainly consists of an induction heating system of 15 kW capacity (EKOHEAT, make Ambrell). The control box converts the line power to alternating current and delivers it to the work head and work coils. The work coils are water-cooled copper conductors made of copper tubing. The PSC specimen is placed in between these induction coils during hot rolling process simulations. The electromagnetic field created in the work coil induces a current in the PSC specimen which in turn generates heat in the specimen.
- **Control Cooling:** A perforate water tank placed above and below work coils is used for controlling the higher cooling rate. The high volume and low-pressure water jets are created by a pump. Compress air is used for controlling the temperature at a low cooling rate.
- **Main Actuators:** The main actuator is responsible for the control of deformation profiles with the movement of the upper tool. The servo-hydraulic controller drives the actuator with millisecond accuracy to control strain response. The main actuator has a displacement range of 0-150 mm.
- **Wedge Actuators:** A wedge actuator serves a twofold purpose in hot deformation simulation. The first it helps to control the strain profiles with accuracy in synchronization with the main actuator. Second, it acts as a safety limit preventing direct contact between the upper and lower bottom tools. The wedge actuator has a displacement range of 0-30 mm.

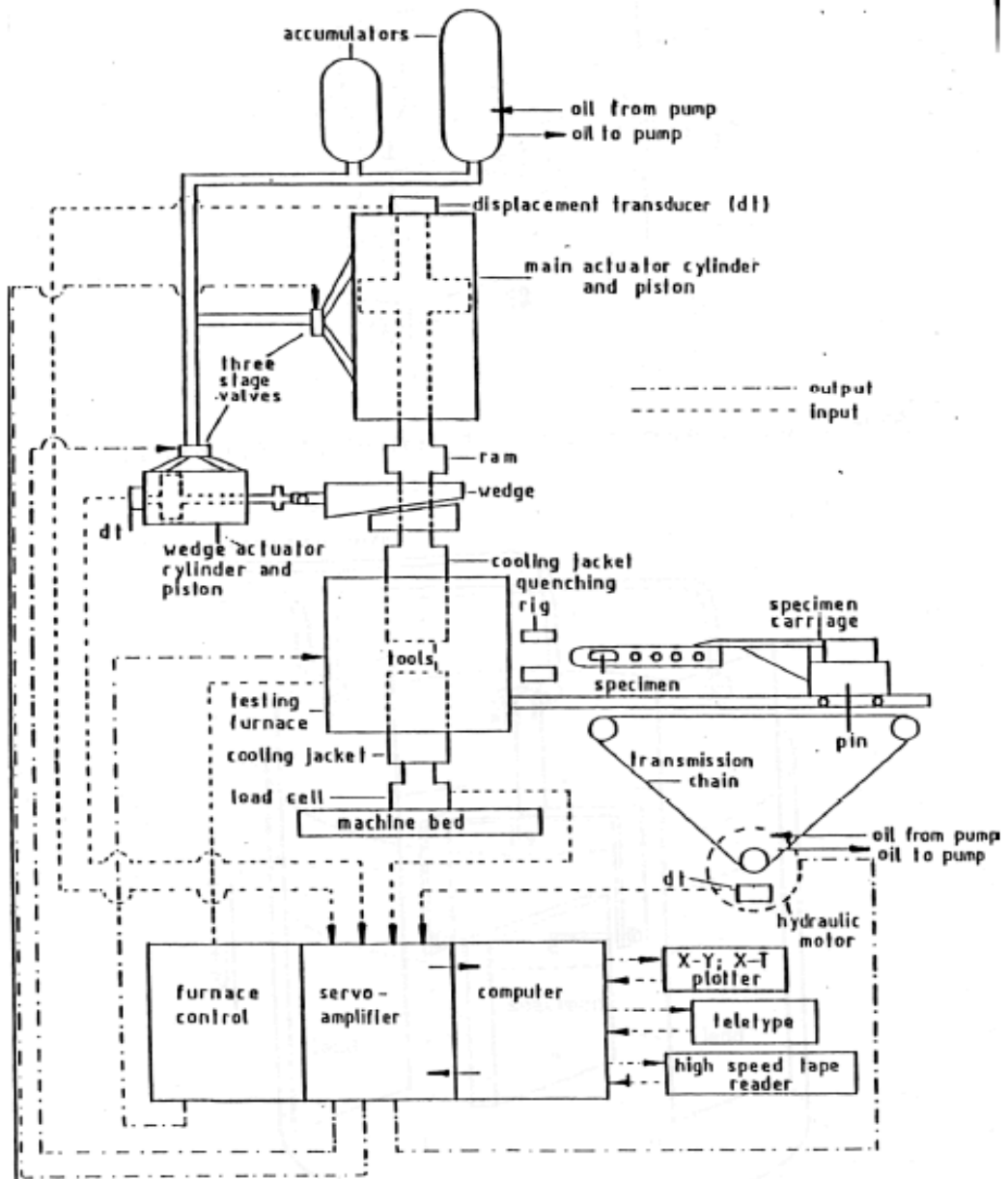


Figure A2. Schematic diagram of TMTS simulator installed in 2003

A.2 Test Control and Features

The temperature is continuously measured using an n-type thermocouple embedded into the specimen. The thermocouple hole is drilled at the half-length location, and deep up to half-width allows accurate measurement even during high strain rate deformation. The thermocouple is connected to a high speed closed loop. Its control feedback is crucial for operating in the heating and cooling part of the test in the FTTU segment.

The measurement of the tool displacement and velocity (used to calculate strain and strain rate) is difficult due to the elevated temperature of the tools and the surrounding furnace in hot PSC testing. It necessitates the control of strain and strain rate based on tool surface measurements. The main and wedge actuator is calibrated before the start of every deformation test as a standard operating procedure. For this purpose, the upper tool is moved and put in contact with a lower tool under the application of -20kN load. At this point, the displacement transducer is set to zero since the tools are in complete contact with each other. The PULSAR control system records the calibration and moves the wedge and main actuator with a calibrated reference point.

During the test, the actual deformation is governed by the displacement and velocity of the main actuator. Both are continuously measured and compensated for the machine frame compliance to get back to the tool surface measurements for controlling the test.

$$\text{sample thickness} = \text{actuator displacement} - (\text{load} \times \text{machine compliance})$$

$$\text{deformation velocity} = \text{actuator velocity} - (\text{rate of change of load} \times \text{machine compliance})$$

The high-speed data logger collects the five basic signals displacement, sample load, velocity, temperature and R-active step from individual transducer and stores it temporarily in the Digital Signal Processor (DSP) memory. The signals are recorded at the maximum frequency of 20.48kHz i.e. 80k/s during the fast deformation and at a frequency of 5 Hz during slow events like heating in FTTU. Although the datalogger can record the signal from the maximum of 32 channels, it is always important to minimize the number of recording signals to avoid overloading of the datalogger. The raw data from DSP memory is linearized and compensated for machine compliance in a post-process sequence to produce the CSV file.

A.3 Measurement of Flow Stress

Over the year, it was possible to standardize the PSC tests by coordination between different laboratories and the sharing of technical know-how. NPL has formulated a good practice guide for the measurement of flow stress in hot PSC tests in close collaboration with the University of Sheffield [157].

(a) Origin Correction: The raw displacement data need to be corrected for the zero offsets, machine compliance, and squeezing of an excess of BN lubrication during the deformation. The excel utility allows the correction of displacement where the initially recorded curve is moved to give true specimen displacement. Figure A3 shows the original load-displacement curve which was corrected for origin and machine compliance for a specimen deformed to a true strain of 1.8.

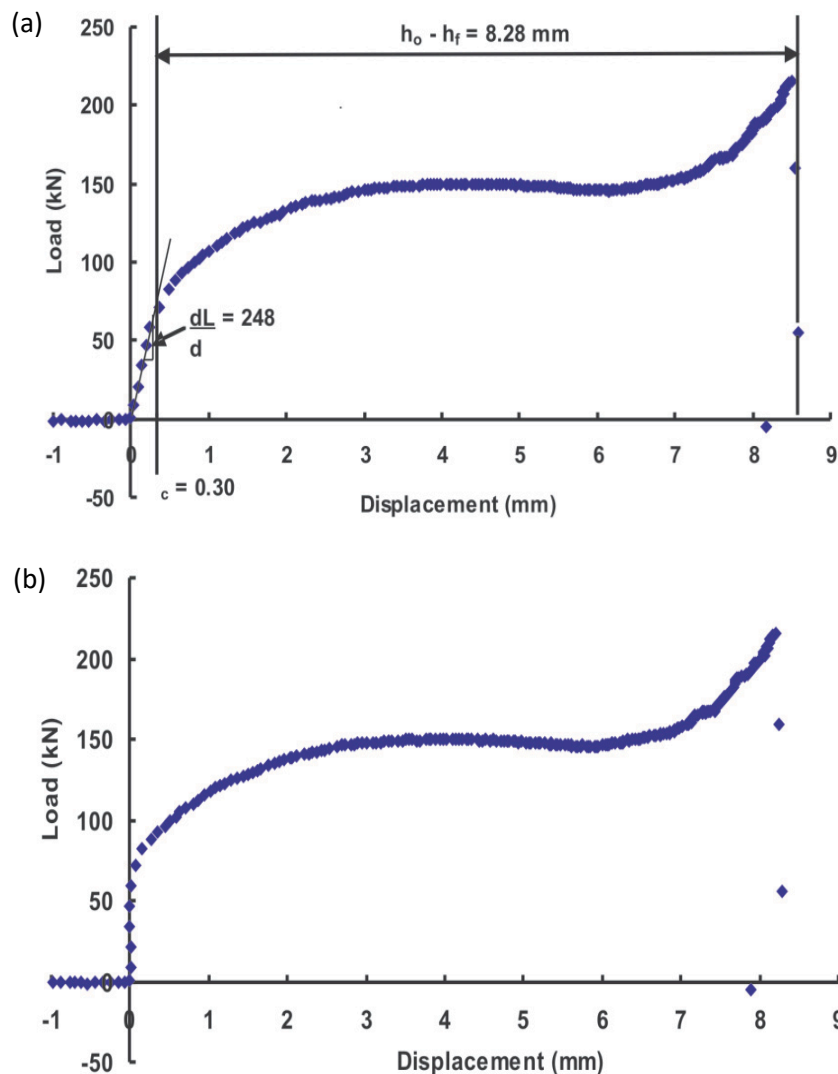


Figure A3. Load-displacement curve corrected for (a) origin and (b) machine compliance (adapted from ref [157])

(b) Equivalent Strain: In ideal plain strain condition the equivalent strain ($\bar{\epsilon}$) is directly related to thickness strain (ϵ_3). However, the lateral spread is always observed, which relaxes the frictional effects at the edges of the specimen. The equivalent strain taking into the account for lateral spread (ϵ_2).is given by:

$$\bar{\epsilon} = \frac{2}{\sqrt{3}} (\epsilon_2^2 + \epsilon_2\epsilon_3 + \epsilon_3^2)^{\frac{1}{2}} \quad (A1)$$

where $\epsilon_3 = \ln h/h_0$ and $\epsilon_2 = \ln b/b_0$ are the thickness and lateral strains, respectively.

(c) Friction Correction: The low coefficient of friction is required ideally to maintain the homogeneous deformation conditions during PSC testing. The standard practice guide has covered the effect of all frictional conditions on equivalent stress and has derived the expressions for them. The friction conditions change from (a) sliding (b) partially sticking and (c) sticking depending upon the thickness of the test piece and friction coefficient.

The function f is calculated during the post-processing of data with the following relationship: $f' = -\bar{\epsilon}/\epsilon_3$. The function $F(\mu)$ allows the friction corrections for the effect of slipping, sliding, or mixed friction conditions. The friction coefficient for BN is experimentally determined using a ring test and a value of $\mu = 0.25$ is fed into the equations.

(d) Equivalent Stress: The stress (σ) is derived from the load as follows:

$$\sigma = \frac{1}{f'} \cdot \frac{L}{bw} \cdot F(\mu) \quad (A2)$$

where f is a factor that assumes the perfect plane strain deformation occurs near the centre of specimen breadth with spread occurring a distance half of the tool width from the edges freely. Figure A4 shows the equivalent flow stress conversion from pressure and associated 2k factor.

(e) Deformation heating corrections: The instantaneous temperature of specimen rises by 30-40°C for the strain rate of $15s^{-1}$ during the deformation. The temperature rise during the deformation is not adiabatic and flow stress has to be corrected to represent isothermal test condition. The corrected isothermal stress (σ_{iso}) is given by:

$$\sigma_{iso} = \sigma + \frac{Q}{\beta R} \left(\frac{1}{T_{iso}} - \frac{1}{T_{inst}} \right) \quad (A3)$$

where Q is the activation energy of deformation (340 kJmol^{-1} in case of low carbon steel), R is the universal gas constant ($8.314 \text{ J K}^{-1} \text{ mol}^{-1}$), T_{iso} is the desired isothermal temperature and T_{inst} is the instantaneous temperature recorded using a thermocouple embedded in the specimen.

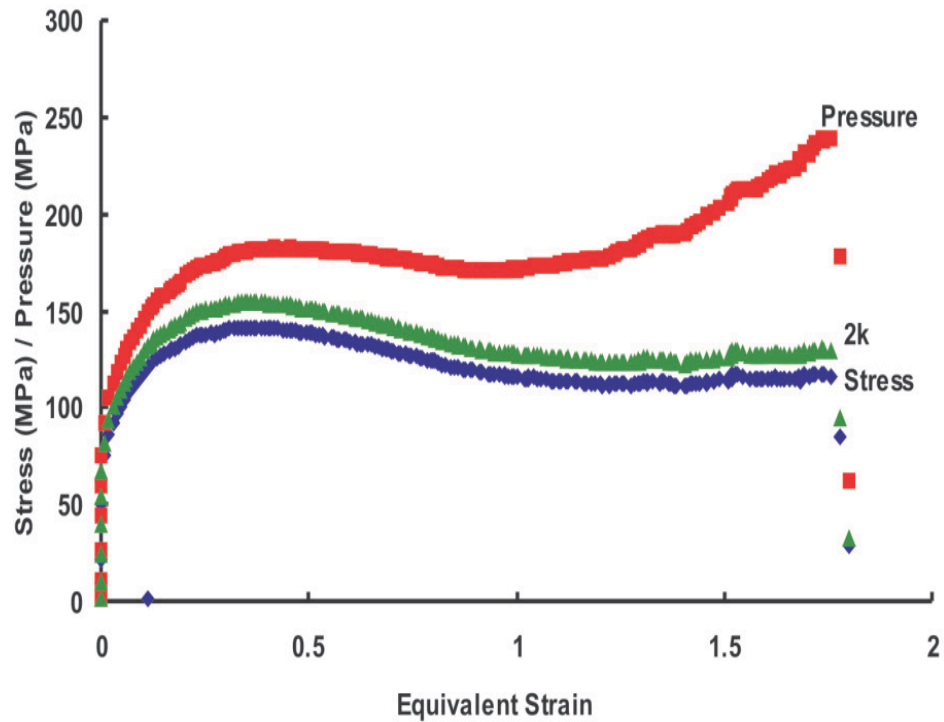
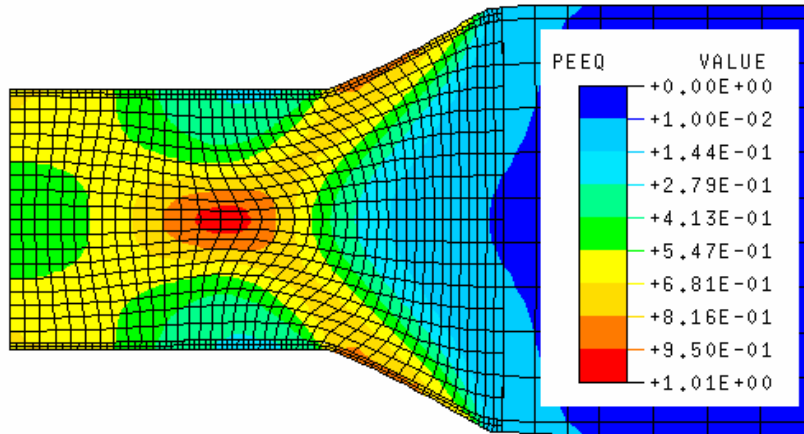


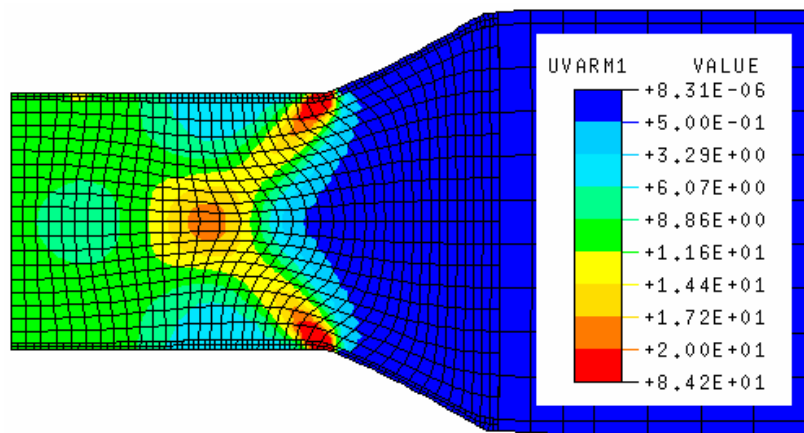
Figure A4. Equivalent stress vs strain curve with corresponding pressure and 2k factor (reproduced from ref [157])

A.4 Inhomogeneous PSC Deformation

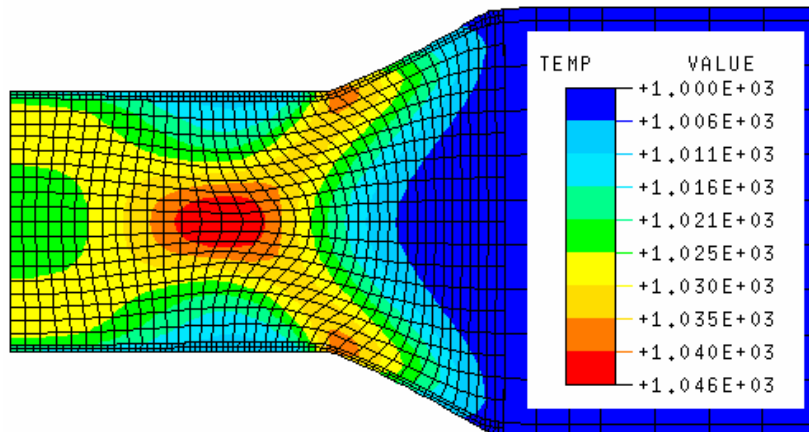
The hot deformation under PSC condition is assumed homogeneous across the specimen thickness in theory; however, inhomogeneities exist in strain, strain rate and temperature distribution. Mirza *et al.* [165] through his finite element modelling work has shown that the inhomogeneities exist due to frictional conditions and initial specimen geometry. Figure A5 shows the results of FEM modelling for 316 stainless steels. The average strain and strain rate in the central deformation region is uniform and equal to the nominal equivalent strain. The deformation regions along the diagonals from the specimen center to the edge of the tool show high strains. This strain and strain rate inhomogeneities mandate the careful selection of areas for subsequent microstructure analysis. The central deformation regions undergo the desired plastic strain; hence microstructure characterisation is focussed only on the central area of 0.5 – 1.0 mm². The strain inhomogeneities in industrial rolling conditions are far higher than the one witnessed in PSC deformation on TMTS simulator.



(a) Equivalent Plastic Strain



(b) Instantaneous Strain Rate



(c) Temperature

Figure A5. Finite element modelling analysis of deformation inhomogeneities in PSC compression testing of 316 stainless steel, tested at 1000°C, a true strain 0.40 and strain rate of 10 s⁻¹. The specimen geometry identical to that used in the present work (adapted from ref [165])

Appendix B

TEM Sample Preparation

The thin foil technique was used to obtain the orientation relationship of Nb(CN) precipitate in austenite and ferrite. The thin foil sample preparation involves the thinning of the specimen to electron transparent thickness through a combination of mechanical and electrolytic polishing. The details of sample preparation technique are as follows and illustrated in Figure B1:

- **Sectioning:** the deformed specimen was cut into a thin slice of a thickness of the order 0.70 mm with the Struers Secotom-50 precision cutting machine [Figure B1(a)]. Aluminium oxide coated blades of diameter 8'' was used for making a precise cut and to minimise the cutting damage.
- **Grinding:** the cut slice was bonded to a round aluminium holder with beehive wax to perform the mechanical grinding operation. The initial lapping was performed on coarse grinding paper #P320 to reduce the thickness and to get the parallel surface. The final lapping was done on finer grinding paper #P800 to achieve a thickness of about 200 μm . The direction of grinding was changed continuously to minimise the scratches in one direction [Figure B1(b)].
- **Disc Punching:** a disc with a diameter of 3 mm was punched using the mechanical punch cutter. The care was taken to avoid any bending or cracking of disc during punching [Figure B1(c)].
- **Disc Grinding:** the punched disc was polished down to 80-100 μm thickness using finer grinding papers #P1200 to get the final surface without scratches [Figure B1(d)]. A Gatan disc grinder, Model 623 was used to remove the material in good control from the punched disc.
- **Electrolytic Polishing:** a twinjet digitally controlled unit, Tenupol-5 (make Struers) was used to perform final thinning by electrolytic polishing [Figure B2]. The electrolyte solution of 20% Perchloric Acid (HClO_4) plus 80 % Ethanol ($\text{C}_2\text{H}_5\text{OH}$) at a temperature of -35°C was used to obtain a hole in the central region area of a disc.
- The samples were pulled out once a hole was formed. The electropolished discs were washed in fresh methanol solution and stored in glass bottles with an ethanol solution to prevent any oxidation. The thinned area around hole was observed under TEM for analysis of precipitate and microstructure analysis [Figure B1(e)].

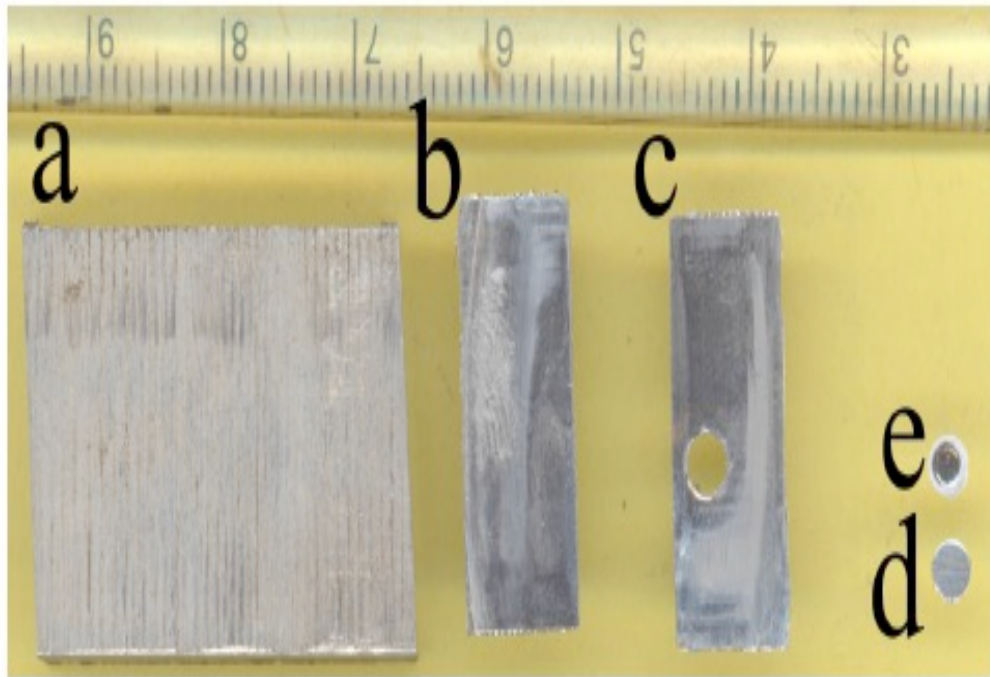


Figure B1. Stages in the TEM sample preparation from a bulk specimen. (adapted from ref [168])

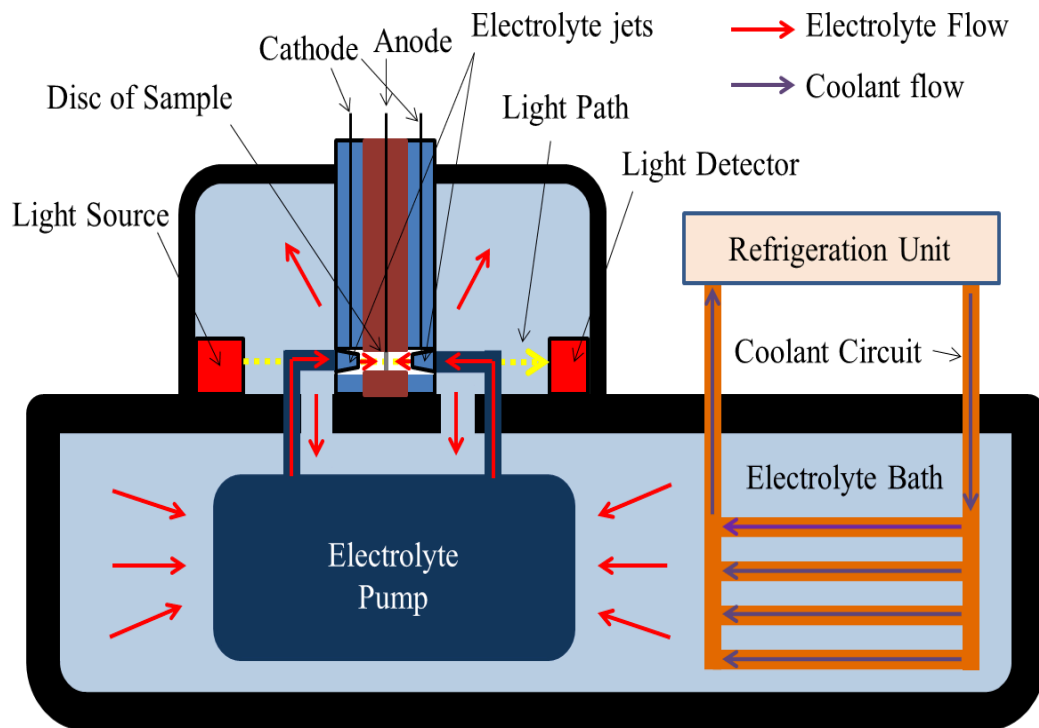


Figure B2. Schematic of a twin-jet polishing machine (TenuPol-5, make Struers) with attached refrigeration unit (adapted from ref [169])

A direct carbon extraction replicas technique is the easiest and universal method to obtain size distribution and volume fraction of second phase particles [166]. It is used as a compliant to thin foil method to quantify Nb(CN) precipitation. The five-stage process for preparing carbon extraction replica from the bulk specimen is as follows (Figure B3):

- **Polishing:** the first step was to prepare a polished surface with standard metallography procedure as described in Section 4.7. The polished surface was cleaned with isopropanol solution kept in an ultrasonic cleaner tank for 3 mins to remove any residual or loose particles from polishing operation.
- **2% Nital etch:** the freshly prepared polished surface was etched with 2% Nital solution for 3-5 secs to put the second phase Nb(CN) precipitates under relief. The etched specimen was again cleaned for 3 mins with isopropanol solution kept in an ultrasonic cleaner to remove any traces of Nital.
- **Carbon coating:** the etched surface was coated with a thin film of carbon (about 5- 10A⁰) for TEM observation. The Speedivac coating unit (Edwards High Vacuum Ltd, model 12E6/1167) was used at a potential of 30V for 2 secs to evaporate carbon on the specimen surface.
- **Extraction of replica:** the carbon film was scored into small squares of 2 x 2 mm with sharp knifepoint and was loosened from the metal surface by chemical etching in 10% Nital solution. The SIP was released from the matrix and got attached to the carbon film in their original position and orientation during the processing of the replica.
- **Lifting of replica:** the film containing particles was transferred to methanol solution, and squares of film float were collected on 400 mesh copper grids. The grid was then dried for 10 minutes and stored in specialised boxes for further examination in the electron microscope.

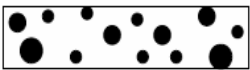
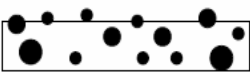
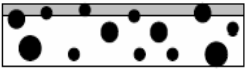
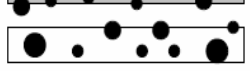
	Sample after mechanical polishing
	Nital etching to reveal precipitates
	Carbon coating
	Chemical etching of the underlying matrix
	Extraction replicas ready to be observed

Figure B3. Five stages in the TEM sample preparation from the bulk specimen (adapted from ref [167])